Dynamics of Quantum Mixtures

Nils-Eric Guenther

A thesis presented for the degree of
Doctor of Philosophy

Universitat Politècnica de Catalunya
Barcelona, Spain
June 21, 2021

Resumen

A temperaturas suficientemente bajas, un fluido compuesto por partículas bosónicas puede experimentar una transición de fase, dando lugar a un condensado de Bose-Einstein (CBE). El CBE es uno de los conceptos fundamentales en física cuántica de muchos cuerpos, suponiendo un ejemplo paradigmático de onda colectiva de materia. La pecular mezcla de comportamientos tipo fluido y tipo partícula que exhibe este estado da lugar a rasgos únicos como la cuantización de vórtices, pero también a una interacción exótica con otros tipos de materia, así como con su entorno. El objetivo de mi tesis es una investigación teórica más extensa de estas propiedades, a través de dos líneas diferentes. El manuscrito está por tanto dividido en dos partes.

En la primera parte he estudiado el problema fundamental del polarón para el caso de un baño bosónico: un CBE interactuando con una única impureza distinguible, una partícula cuántica de la misma escala que las partículas que constituyen el condensado, la cual se puede describir a menudo como una cuasipartícula 'vestida' llamada polarón. El objetivo de esta tesis tiene lugar en el contexto de un CBE diluido formado vapores de átomos ultrafríos, donde, desde un punto de vista histórico, el CBE fue observado experimentalmente por primera vez, y donde las interacciones atómicas subyacentes pueden ser controladas hasta un grado sin precedentes a través de resonancias de Feshbach. Un caso particularmente interesante es el de interacciones fuertes entre la impureza y los bosones, el régimen del límite unitario. Tales sistemas de impurezas se han observado experimentalmente en los últimos años. Sin embargo, debido a la complejidad teórica y a la riqueza del estado condensado unido a las limitaciones experimentales, la naturaleza del sistema compuesto no se entiende por completo para interacciones fuertes. En esta tesis presento dos modelos teóricos que predicen de forma cualitativa nuevos fenómenos. En el primero, extiendo un esquema usado en trabajos previos al mío, incluyendo el efecto de una temperatura finita por debajo del punto de transición para tener en cuenta la naturaleza bifluida de los bosones a tales temperaturas intermedias. Este esquema predice una separación en dos de una única rama de cuasipartículas al aumentar de la temperatura, así como una dependencia general fuerte de la temperatura sobre las propiedades de las cuasipartículas. En el segundo trabajo, desarrollo un modelo variacional diseñado para describir grandes revestimientos de la impureza. Esta estimación predice como para repulsiones intrabosónicas suficientemente débiles la impureza puede ligar una nube macroscópica pero coherente y diluida de bosones de tamaños comparables a la longitud de coherencia del condensado.

En la segunda parte de mi tesis, presento trabajos que se enfocan en la interacción entre un condensado y la geometría del recipiente que lo contiene. Algunos de los rasgos conocidos de un condensado son su superfluidez y la cuantización de la vorticidad. Considerando un superfluido contenido en una superficie bidimensional, estudio la dinámica de vórtices puntuales en superficies curvas en el contexto

de la teoría de flujo de potencial, con un enfoque en geometrías no simplemente conexas. En un trabajo presentado en esta parte de la tesis acerca de geometrías cilíndricas, derivo el potencial generador de un único vórtice puntual, prediciendo como la dinámica se ve modificada por la cuantización del flujo a lo largo de la circumferencia del cilindro. En particular, este está forzado a moverse siempre a través de su eje longitudinal, aportando un poderoso marcador de superfluidez. En otro trabajo acerca de superficies con forma de toro, así como de superficies relacionadas más generales, derivo el potencial generador tanto de un único como de múltiples pares vórtices - antivórtices y predigo un cambio significativo de dinámicas locales debido a la cuantización macroscópica del flujo y a la curvatura no-trivial de la superficie.

Abstract

At sufficiently low temperatures, fluids of bosonic particles may undergo a phase transition, below which a Bose-Einstein condensate (BEC) forms. The BEC is one of the most fundamental concepts in many-body quantum physics and provides a paradigmatic example of a collective matter wave. The distinctive mixture of fluid-like and particle-like behavior this state exhibits leads to the emergence of unique features such as vortex quantization, but also to an often exotic interaction with other matter as well as its environment. The goal of my thesis is a further theoretical investigation of the latter, along two specific lines of research. Correspondingly, this manuscript is divided into two main parts.

In the first part, I studied the fundamental polaron problem in the case of a bosonic bath: A BEC interacting with a single distinguishable impurity, a quantum particle on the same scale as the constituent particles of the condensate, which can often be described as a 'dressed' quasiparticle, called the polaron. The focus of this thesis is *dilute* BECs of ultra-cold atomic vapors, where historically the BEC state was first observed experimentally and the underlying atomic interactions can be controlled to hitherto unprecedented degree via Feshbach resonances. Of particular interest is the case of strong interactions between the impurity and the bosons, the unitary-limited regime. Such impurity systems have been first probed experimentally in recent years, however due to the theoretical complexity and physical richness of the condensate state as well as experimental limitations, the nature of the compound system is not completely understood at strong interactions. I present two theoretical models in this part of the thesis which predict qualitatively new phenomena. In the first, I extended a scheme used in previous work unrelated to me, including the effect of finite temperature below the transition point to take into account the two-fluid nature of the bosons. This scheme predicts a *splitting* of a single quasi-particle branch at zero temperature into two branches upon heating, and a general strong temperature dependence of the quasi-particle properties. In the second work, I developed a new variational ansatz tailored for describing large dressing of the impurity. This ansatz predicts that for sufficiently weak intra-bosonic repulsion the impurity can bind a *macroscopic* but coherent and dilute cloud of bosons of sizes comparable to the healing length of the condensate.

In the second part of my thesis, I present work focusing on the interplay of a condensate and the geometry of its containment. Well known features of condensates are superfluidity and the quantization of vorticity. Considering a superfluid embedded on a two-dimensional surface, I studied the dynamics of point vortices on curved surfaces in the framework of potential flow theory, with a focus on non-simply connected geometry. In a work presented in this thesis revolving around cylinder- and related geometries I derived the generating potential of a single point vortex, which predicts that the dynamics are modified by the quantization of flow around

the circumference of the cylinder. In particular, a single vortex is always forced to move along the longitudinal axis of the cylinder, providing a powerful marker for superfluidity. In a following work regarding a torus-shaped embedding as well as related more general surfaces, I derived the generating potential for a single and multiple vortex-anti vortex pairs and predicted a significant change of local dynamics due to the macroscopic quantization of flow and to the non-trivial curvature of the embedding surface.

Dedication

Für Donny, Lars, Kerstin, Jens und Olga

Declaration

This thesis is based on the following peer-reviewed articles written by me as a first author, together with various co-authors:

[1] N.-E. Guenther, P. Massignan, and A. L. Fetter, "Quantized superfluid vortex dynamics on cylindrical surfaces and planar annuli," *Phys. Rev. A*, vol. 96, p. 063608, Dec. 2017

[2] N.-E. Guenther, P. Massignan, M. Lewenstein, and G. M. Bruun, "Bose polarons at finite temperature and strong coupling," *Phys. Rev. Lett.*, vol. 120, p. 050405, Feb. 2018

[3] N.-E. Guenther, P. Massignan, and A. L. Fetter, "Superfluid vortex dynamics on a torus and other toroidal surfaces of revolution," *Phys. Rev. A*, vol. 101, p. 053606, May 2020

[4] N.-E. Guenther, R. Schmidt, G. M. Bruun, V. Gurarie, and P. Massignan, "Mobile impurity in a Bose-Einstein condensate and the orthogonality catastrophe," *Phys. Rev. A*, vol. 103, p. 013317, Jan 2021

This manuscript represents my ideas and is written in my own words, all figures and graphics are made by me. Whenever content not originally by me appears in this text, I have properly cited and referenced the original sources. Some chapters are devoted to reviewing existing literature to enhance the readability of the text. In these chapters I state explicitly that the body of the text is merely a repetition of ideas in my own words that have been previously published by others, and I properly cite and reference these publications at the beginning of the chapter. In any case, all figures appearing in this text have been produced by myself, even when they represent results by others. I declare that I never fabricated or willingly misrepresented any data or figures and that all genuinely new statements I do make are true to the best of my knowledge. I will sometimes use "we" in this text, referring to me together with my various collaborators when I feel it important to stress the collaborative effort behind the results presented. However in all such cases I was still the main contributor to these findings.

Acknowledgments

I would like to thank my supervisors Maciej Lewenstein and Pietro Massignan for their tremendous support during the entire period of my doctoral fellowship, for the guidance they provided me during times I needed it as well as the freedom they offered me in times I could afford it. I would like to thank my collaborators Victor Gurarie and Richard Schmidt, but especially Georg Bruun and Alexander Fetter, who both collaborated very closely with me during the last five years, for the countless fruitful discussions as well as the many insights I gathered from them, regarding the realm of physics and beyond. Further I would like to thank Grigori Astrakharchik for his valuable input on Bose polarons, as well as the frequent delightful lunch conversations at the UPC. I really appreciate the entire Quantum Optics Theory group, especially Daniel Gonzales-Cuadra and Alexandre Dauphin, for the collegiality I could experience and the friendships I made. Beyond my group, I would like to thank all the people in ICFO i had the possibility to discuss physics with, especially the opportunity to have an ongoing discussion with experimentalists, in particular Leticia Tarruell and Adrian Bachtold as well as members from their group.

Further I would like to extend my highest regards to the support team of ICFO, because their quick and competent handling of administrative and technical tasks. They made it not only possible for me to work in a country I did not speak the official language of when I arrived, they made life at ICFO an enjoyable and incredibly enriching experience. I would also like to thank the Fundación "la Caixa" for the generous fellowship they provided during my stay, which allowed me to focus on my research.

Finally, I would like to thank my fellow colleague and friend Donald Youmans. He always supported me during setbacks and shared genuine joy with me when something eventually worked. I found it an incredible gift to have a close friend who really understands the work I am doing.

Contents

Chapter breakdown

To give a concise overview of this thesis, the content of each chapter is briefly summarized in the following. For each chapter, it is briefly mentioned whether it directly refers to content of one of the publications [1, 2, 3, 4] or whether it merely summarizes known results produced by others. Such parts were included to improve the readability of this manuscript, fix terminology and notation according to existing conventions and give an understanding of how the publications embed in the wider fields of research of impurity physics and superfluid vortices.

Chapter 1: gives an introduction into quantum simulation with ultracold atoms. It broadly discusses the history and development of the field, it then reviews the common characteristics as well as the wide range of currently possible systems. This chapter is a review and is completely based on work not originally by me.

Chapter 2: reviews in detail two-body scattering theory as commonly used in the context of neutral ultracold gases, including a discussion of the relevant length scales, the underlying Van-der-Waals potentials and Feshbach resonances. Finally, three-body effects are shortly summarized. This chapter is mainly a review of previous results, however it contains numerical results for model scattering-potentials. These were used to obtain the results in chapter 5.

Part I

Chapter 3: gives a more specialized introduction to impurity physics and the polaron problem, from its origin in condensed matter to recent developments in ultra cold gases. This chapter is entirely a review of the results of others.

Chapter 4: reviews the most crucial elements of Green's functions as used in diagrammatic calculations. Then the $\mathcal{T}$-matrix approximation to the Bose polaron at zero temperature is reviewed. Finally the finite temperature case is discussed. This chapter contains my original results from [2]. It also contains a review of standard textbook material as well as a discussion of results from [5], where the $T = 0$ case was first discussed.

Chapter 5: discusses a variational ansatz using coherent states for the Bose-polaron problem. This chapter is based on the publication [4].

Chapter 6: summarizes the results of chapters 4 and 5, discusses further possible lines of research. Two papers by other authors published after [2] are also discussed, as they directly concern finite temperature effects in Bose polarons. This chapter is based on both [2] and [4], but also discusses work of others when it relates to these papers.

Part II

Chapter 7: reviews textbook material on superfluids and non-uniform condensates which is important to understand the theory modeling vortex dynamics in the papers [1] and [3]. This chapter is entirely a review of the results of others.

Chapter 8: discusses the vortex states and dynamics in two-dimensional superfluid films shaped as cylindrical or toroidal surfaces as well as planar annuli. This chapter is based on publications [1] and [3].

Chapter 9: summarizes the results of chapter 8. It discusses potential ways to experimentally realize the geometries and vortex states discussed and explores possible applications and further lines of research. This chapter is based on [1] and [3], but also reviews work of others.

Introduction

Chapter 1

Quantum simulation with ultracold atoms

In the first half of the twentieth century, the governing laws of non-relativistic quantum mechanics were first formulated, then empirically verified and finally consolidated into the canonical body taught today to physics students across the world. Thus, quantum mechanics today is considered an established fact, with certain key-terms and phrases such as 'Schrödinger equation' or 'Heisenberg uncertainty principle' known far beyond the scientific community and emanating into pop-culture. But even though the laws governing the dynamics of non-relativistic microscopic particles have been well known and proven correct time and again in various experiments, how they give rise to the *emergent* phenomena observable in macroscopic systems comprised of many quantum mechanical constituents, such as electrons in solid state systems, liquid Helium or other subjects of condensed matter, has occupied the majority of physicists around the world for the last seventy years. Yet, many questions first formulated in the beginnings of the field of condensed matter remain partially unanswered today, the most famous being the nature of superconductivity in its various forms [6]. Theoretical predictions in particular turned out to be only qualitatively possible for the most part, and even simplified early toy-models remain theoretically unsolved as of now [7]. Many-body quantum mechanics comes with an exponentially growing mathematical complexity in terms of particle number, which quickly makes *ab-initio* calculations completely infeasible.

Confronted with this crippling mathematical complexity, Richard Feynman was the first to put forth the idea of quantum simulation [8]. Going beyond the simulation of quantum systems with classical computers, he considered using engineered quantum systems to emulate a given quantum system of interest to predict its behavior [9]. However, no suitable candidate for such a sufficiently customizable and controllable system was available for most of the twentieth century.

This changed with the advent of quantum-degenerate atomic gases, also called *ultracold gases*: A vapor of (mostly alkali) atoms, as seen in Fig. 1.1 (left), where of paramount importance is the level-structure (Fig. 1.1 right) of the atoms, determining their optical absorption properties. Exploiting these optical properties, various cooling and trapping schemes evolved, which allows for an initial hot ensemble or even beam of atoms to be trapped in place and cooled to unbelievably low temperatures. A canonical example of cooling sequence would be the following: An initially hot atom beam is Zeeman-slowed to a standstill [10], where it is subsequently trapped

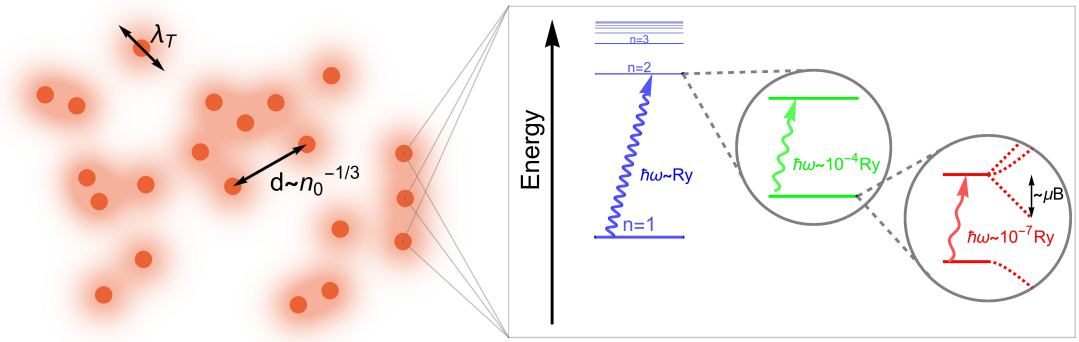

Figure 1.1: Sketch of an ultracold vapor. Each atom in the gas allows resonant absorption of photons in the optical, microwave- and radio frequency due transitions in-between the main level-, fine- and hyperfine structures respectively. Using magnetic fields, the transition energies can be further manipulated with the Zeeman effect [13, 14]. Using a series of various magneto-optical cooling techniques, the initially hot vapor reaches the degenerate regime, where the thermal de-Broglie wavelength is comparable to the classical inter-particle distance Eq. (1.1)

and Doppler cooled using a Magneto-optical Trap (MOT) to typical temperatures of several hundreds of μK at typical atomic densities of $n_0 \sim 10^{10}/cm^3$ [11]. In a last step, sub-doppler cooling techniques are used, the most prevalent being evaporative cooling [12]. The vapor then reaches the degenerate regime at densities of $n_0 \sim 10^{13}/cm^3$ and temperatures in the order of $T \sim 100nK$. At this stage, the inter-particle distance $\sim n_0^{-1/3}$ is in the same order of magnitude as the thermal de-Broglie wavelength $\lambda_T = \hbar/\sqrt{2\pi m k_B T}$, with m the mass of the atomic species, such that

$$n_0 \lambda_T^3 \sim 1. \tag{1.1}$$

This is the classical criterion for quantum effects to play a significant role in the dynamics.

The development of this series of techniques culminated in two almost simultaneous experiments, realizing the first observable Bose-Einstein Condensates (BECs), in a cloud of Rubidium [11] and Sodium atoms [15] respectively, in 1995.

Since this discovery, atomic vapors proliferated tremendously and today they provide *the* canonical example of quantum engineering. The optical properties of the atoms can be used to cool, trap and image the atomic cloud. But with the use of lasers and magnetic fields, clouds can also be confined to almost arbitrary trap geometries, from a uniform box potential [16], to quasi-two- and one-dimensional systems, periodic optical lattices [17] and disordered potentials, allowing to investigate the physics of Anderson- and many-body localization, as well as spin glasses [18]. As discussed in chapter 2, the interaction between atoms can be controlled using magnetic Feshbach resonances in the ultra cold regime. Clouds can be prepared in one or various spin states to observe the dynamic of mixtures of several distinguishable species [19]. They can even be excited to Rydberg states, such that many-body systems with long-range interaction can be realized [20]. Ultracold gases with strong dipolar interaction have also been realized [21]. Recent experiments can

even prepare true mixtures of different atoms in the same trap simultaneously, allowing for mixtures with different atomic masses as well as different statistics, i.e. Bose-Bose [22], Fermi-Fermi [23] or Bose-Fermi [24] mixtures. New publications stretching these possibilities further appear at break-neck pace, and an exhaustive list of all realizable systems is near-impossible as well as quickly out-of-date.

The framework of cold atoms is indeed very successful to simulate quantum systems of interest according to Feynman's vision and new insights into the nature of emergent quantum phenomena have been gained. I like to briefly describe just a few examples to highlight the fruitfulness of this approach in the last decades. For example, the experimental realization of the BEC-BCS crossover in the context of fermionic mixtures showed that the two classical theories of superfluidity, Bogoliubov theory [25] and BCS theory [26], are limiting cases connected by an entire regime of superfluid states, the most exotic and novel being the unitary Fermi gas [27]. Another example are Bose-Droplets, a completely novel self-bound superfluid state of matter stabilized by quantum fluctuations [28]. This state can also be realized with dipolar gases, where even a transition to a supersolid state has been reported [29, 30, 31], a state theorized to exist since 1970 [32]. A last example I find particularly striking is the realization of the Bose-Hubbard model, first in an ultracold gas of Rubidium confined in an optical lattice [33], that shows a quantum phase transition between a superfluid and an insulating phase.

A single distinguishable particle interacting with a quantum bath, often referred to as the polaron problem, is one of the simplest realizations of a non-trivial quantum many-body system. Yet such fundamental physics problem eludes a solution since the formative days of Quantum mechanics, and it is the main focus of the first part of my thesis, presented in part I. The concept can be applied to better understand a wide range of systems, including metals and dielectric materials [34], semiconductors [35], ^{3}He-^{4}He mixtures [36], and high-T_c superconductors [37]. In certain limits, polarons provide a paradigmatic realization of Landau's fundamental concept of a quasiparticle.

Polaron physics received renewed attention with the advent of ultracold atoms experiments, and it has been extensively studied especially in the case of the majority atoms being fermionic, but also more recently in the bosonic analogue, which exhibits particularly rich physics. I give a quick review of the recent theoretical and experimental advances in polaron physics with ultracold atoms in chapter 3. In the remainder of part I, I present the results of my two publications [2] and [4] in chapters 4 and 5 respectively. Both are theoretical models of the Bose polaron, predicting a strong and non-trivial temperature dependence as well as the possibility of the impurity to loosely bind large numbers of bosons.

Another exciting possibility enabled by ultracold atoms is the quantum simulation of superfluid flow dynamics. A particularly interesting and well known feature of superfluids is the emergence of quantized vortices in the fluid. This was first observed in the context of liquid helium in 1961 [38], but has also been directly observed in ultracold condensed gases more recently [39]. The dynamics of vortices of superfluids are generally well understood, especially in the case of point vortices in a quasi-two-dimensional superfluid film. Cases investigated however mostly focused on flat geometries, films on simply connected but curved surfaces have been investigated [40]. In part II of this thesis, I present the results of my publications [1]

and [3], which go one step further and consider cylinder- and torus-shaped films, having a non-trivial topology. In chapter 7, I briefly review the standard theory of superfluid point vortices and its regime of validity, before presenting the curved-film results in chapter 8.

Chapter 2

Interactions in ultracold atoms

The interaction between two atoms in a cold gas forms a fundamental building block for the complex many-body phenomena witnessed in such experiments. In this chapter we will review the microscopic origin of the interaction between neutral alkali atoms and their basic properties.

We will discuss the two-atom scattering properties of such potentials and why it is sufficient and often of advantage in effective theories to describe interactions in terms of low-energy scattering properties instead of the bare potential. Further, we will discuss how Feshbach resonances can be exploited to effectively control these properties in experiments due to the multi-channel nature of the scattering processes. Finally, we will also talk about processes involving more than two particles, and how they lead to losses over time in experiments. We will briefly sketch other effects of few-body processes, such as Effimov trimers.

2.1 Van der Waals interaction

Typical ultracold gases consist of neutral alkali atoms, and in general a gas can be a mixture of different elements, isotopes of atoms. We will loosely refer to the collection of these internal degrees of freedom as a *species* of particles, in the sense that each species is *indistinguishable* in the quantum mechanical sense, as discussed in chapter IX of [14], as long as they have identical internal degrees of freedom, such as spin.

The defining characteristic of alkali atoms is a single valence electron, which dominates most chemical properties and plays a central role in inter-atom interactions. At typical temperatures of most cold gas experiments, in the range from several mK to several μK [41], the atoms can be considered in their electronic ground state and the only relevant degree of freedom are the different hyperfine states. In the alkali case, this corresponds to an electron orbital of type s.

Due to the large mass difference between nucleus and electrons, of 3 to 5 orders of magnitude, dynamics of electrons happen on much smaller time scales than dynamics of nuclei and in comparison can be considered instantaneous to good approximation. The electronic interaction potential $U(\boldsymbol{r})$ between two atoms can then in principle be determined by solving the ground state of the few-electron problem in the Born-Oppenheimer approximation [14].

At long distances, this Born-Oppenheimer potential is attractive, which can be understood as induced dipole-dipole interactions of the Van-der-Waals type [42],

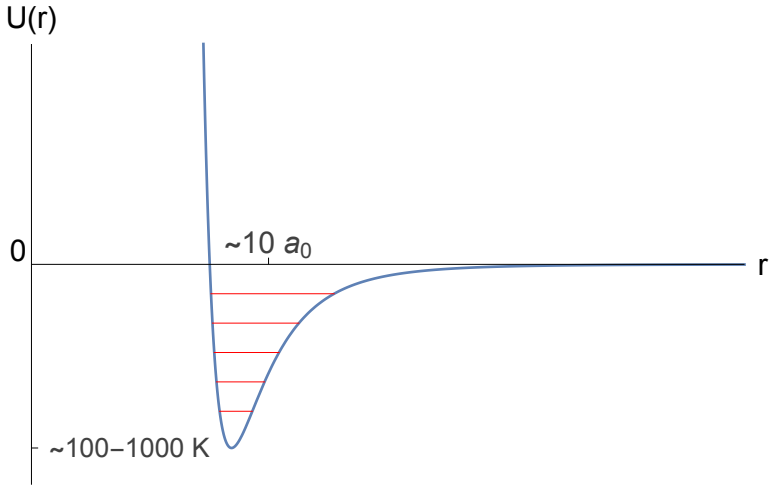

Figure 2.1: Sketch of a typical potential $U(r)$ between two alkali atoms at separation r. The potential has a range in the order of Bohr radii a_0, with a minimum at typical lengths of about $\sim 10a_0$ and a variable depth in the order of $\sim 100K$ up to several $\sim$ 1000K, depending on species and spin configuration of the valence electrons. Typically, these potentials support tens or even hundreds of two-body bound states. The attractive tail is given by the Van der Waals interaction Eq. (2.1) and scales as $\sim r^6$, the repulsive core has been modeled by a $\sim r^{12}$ term.

dominated by the polarization of the valence electron clouds:

$$U(r) \simeq -\frac{C_6}{r^6}. \tag{2.1}$$

This attraction is isotropic, depending only on the magnitude $r = |\boldsymbol{r}|$ of the separation. The parameter C_6 is dependent on the species of the two atoms involved and has units of energy times length to the power six. We can associate a length scale R_{vdW}, called the Van-der-Waals length, to the interaction, by equating $U(R_{vdW})$ from Eq. (2.1) with a kinetic term $\hbar^2/2m_r R_{vdW}^2$, see [43]:

$$R_{vdW} = \frac{1}{2}\left(\frac{2m_r C_6}{\hbar^2}\right)^{1/4}, \tag{2.2}$$

where $m_r = m_1 m_2/(m_1 + m_2)$ is the reduced mass of the two atoms. Note that in atomic units, with lengths measured in Bohr radii a_0 and energy in units of the Hatree energy $E_h = \hbar^2/2m_e a_*^2$, the interaction parameter C_6 is typically very large for alkali atoms, in the order of $10^3 - 10^4$, and as such typical Van-der-Waals lengths are much larger than a_0. Typical values are of the order of $R_{vdW} \sim 100a_0$, or of about $\sim$ 5nm [44].

At smaller separations on the other hand, the valence electrons will experience a stronger repulsive exchange interaction, forming a very hard barrier at small distances [42]. Both factors combine to a spherically symmetric potential $U(r)$ with a potential minimum, as sketched in Fig. 2.1. For typical alkali atoms, this potential well is deep in the sense that it supports actually tens or even hundreds of bound states.

2.2 Dilute gases and scattering theory

In typical experiments with alkali gases, the density n_0 of particles is in the order of 10^{12} to 10^{15} particles per cm^3, leading to average inter-particle distances $\sim n_0^{-1/3} \simeq 0.1 - 1\mu$m, much smaller than the typical range of interactions given by the Van-der-Waals length R_{vdW}. We will refer to this as a *dilute* gas, and two particles will only rarely be close to other particles on average, with more particles an even rarer occasion. Interaction effects in a dilute gas can be thought of in terms of a series of scattering events between such few particles.

For completeness, we will briefly review the relevant parts of two-body scattering theory in this section. A more thorough discussion can be found in chapter X of [45], or chapter XVII of [14].

2.2.1 Two-body scattering problem

Given an inter-atomic potential $U(r)$ with a tail as in Eq. (2.1), the stationary Schroedinger equation for the relative wave function $\psi(\boldsymbol{r})$ in the relative coordinate $\boldsymbol{r}$ of two distinguishable atoms is

$$\left(-\frac{\hbar^2}{2m_r}\Delta_{\boldsymbol{r}} + U(r)\right)\psi(\boldsymbol{r}) = E\psi(\boldsymbol{r}). \tag{2.3}$$

We are interested in the stationary scattering states, where $E > 0$ and which can be labeled by their wave vector $\mathbf{k}$. We set $E = \hbar^2 k^2/2m_r$ with $k = |\mathbf{k}|$. Since $U(r)$ is spherically symmetric, we can expand the wavefunction in Legendre polynomials

$$\psi_{\mathbf{k}}(\boldsymbol{r}) = \sum_n c_{k,l} P_l(\cos\theta)\,\frac{u_{k,l}(r)}{r}, \tag{2.4}$$

where $c_{k,l}$ are general coefficients, θ is the angle between $\mathbf{k}$ and $\boldsymbol{r}$, and $u_{k,l}$ is the radial wave function, fulfilling the radial Schroedinger equation

$$\left(\frac{2m_r}{\hbar^2}U(r) + \frac{l(l+1)}{r^2} - k^2\right)u_{k,l}(r) - u''_{k,l}(r) = 0. \tag{2.5}$$

Since $U(r)$ falls off as r^{-6} at long distances, the radial wave function will asymptotically connect to a free solution, of $k^2 u_{k,l}(r) - u''_{k,l}(r) = 0$, its asymptotic limit can hence be expressed as

$$u_{k,l} \simeq_{r\to\infty} \sin\left(kr - l\pi/2 + \delta_{k,l}\right), \tag{2.6}$$

up to normalization and a global phase factor. In this convention, the k-dependent $\delta_{k,l}$ is called phase shift for the l-th partial wave. The phase shifts $\delta_{k,l}$ determine completely the asymptotic form of any wave packet scattering at the potential $U(r)$.

However, scattering properties are usually discussed in terms of the scattering amplitude $f_k(\theta)$, defined through the asymptotic form

$$\psi_{\mathbf{k}}(\boldsymbol{r}) \simeq e^{i\mathbf{k}\cdot\boldsymbol{r}} + f_k(\theta)\frac{e^{ikr}}{r}, \tag{2.7}$$

at large distances. It is related to the scattering cross section via

$$\frac{d\sigma}{d\Omega} = |f_k(\theta)|^2, \tag{2.8}$$

with $d\Omega = 2\pi \sin\theta d\theta$ the solid angle. It is a measure of collision rates mediated by the interaction. To express the scattering amplitude in terms of the phase shifts $\delta_{k,l}$, we expand the plane wave $e^{i\mathbf{k}\cdot\boldsymbol{r}}$ in partial waves, similarly to Eq. (2.4) (compare with [45])

$$e^{i\mathbf{k}\cdot\boldsymbol{r}} = \sum_l i^l (2l+1) j_l(kr) P_l(\cos\theta), \tag{2.9}$$

where $j_l(x)$ is the spherical Bessel function, as discussed for example in chapter XVII of [46], which behaves as $j_l(x) \sim \sin(x - l\pi/2)/x$ for large x. We can also expand $f_k(\theta) = \sum_l f_{k,l} P_l(\cos\theta)$. Equating Eq. (2.7) and Eq. (2.4) while using Eq. (2.9) fixes the coefficients $c_{k,l}$ and $f_{k,l}$. As discussed in [45], one finds:

$$f_{k,l} = \frac{2l+1}{k} e^{i\delta_l} \sin\delta_l, \quad c_{k,l} = i^l \frac{2l+1}{k} e^{i\delta_l}. \tag{2.10}$$

Using the partial wave expansion of $f_k(\theta)$ in the expression Eq. (2.8), we find for the total cross section σ after integrating:

$$\sigma = \frac{4\pi}{k^2} \sum_{l=0}^{\infty} (2l+1) \sin(\delta_{k,l})^2, \tag{2.11}$$

which follows from the orthogonality of the Legendre polynomials $\int_{-1}^{1} dx P_l(x) P_m(x) = \delta_{l,m} 2/(2l+1)$.

All scattering properties discussed above assume distinguishable particles . In the case of indistinguishable bosons (fermions), with the required (anti-) symmetrization of the asymptotic form Eq. (2.7) leads to a modified differential cross-section Eq. (2.8):

$$\frac{d\sigma}{d\Omega} = |f_k(\theta)^2 \pm f_k(\pi - \theta)^2|. \tag{2.12}$$

Correspondingly, in the total cross section, only even (odd) partial waves contribute in the sum in Eq. (2.11). This gives the total cross sections $\sigma_b(\sigma_f)$ for indistinguishable bosons (fermions)

$$\sigma_b = \frac{8\pi}{k^2} \sum_{l \,\in\, \text{even}} (2l+1) \sin(\delta_{k,l})^2, \quad \sigma_\text{f} = \frac{8\pi}{k^2} \sum_{l \,\in\, \text{odd}} (2l+1) \sin(\delta_{k,l})^2. \tag{2.13}$$

2.2.2 Low-k limit: s-wave scattering

Given typical temperatures of cold gases in the sub-millikelvin regime, typical relative wave vectors $k \sim \sqrt{2m_r k_b T}/\hbar$ are of order $10^{-4} a_0^{-1}$ to $10^{-6} a_0^{-1}$ for alkali species. This is much smaller than the relevant scale $R_{vdW}^{-1} \sim 10^{-2} a_0^{-1}$ of the inter-atomic potential, and the relevant information is the scattering amplitude $f_k(\theta)$ in the low-k limit.

The centrifugal barrier term in Eq. (2.5) suppresses $\delta_{k,l}$ for small k and higher l. In particular, the phase shifts scale as $\delta_{k,l} \sim k^{2l+1}$ for small k, as discussed in detail in §132 of [14]. Correspondingly, in our regime the $l \neq 0$ terms can be neglected and $f_k(\theta) \to f_{0,0}$. This limit is called s-wave scattering. We define $\delta_{k,0} \to -ak$ in the low-k limit, where the proportionality factor a is called the s-wave scattering length. From Eq. (2.10) with $l = 0$, it follows that $f_0 \to \delta_{k,0}/k = -a$ for $k \to 0$. Then, the stationary scattering state $\psi_{\mathbf{k}}(\boldsymbol{r})$ takes the asymptotic form

$$\psi_{\mathbf{k}}(\boldsymbol{r}) \simeq 1 - \frac{a}{r}, \tag{2.14}$$

for $r \gg R_{vdW}$. In particular, this means that identical fermions, which do not scatter in s-wave, will have strongly suppressed collisions at low temperatures, which can often be neglected.

The s-wave scattering length a can be extracted directly from the asymptotic form Eq. (2.6) of the s-wave radial solution $u_{k,0}$. Plugging $\delta_{k,0} = -ak$ into Eq. (2.6) for $l = 0$, we find in the region $kR_{vdW} \lesssim kr \lesssim \delta_{k,0}$ the relation

$$\frac{u'_{k,0}(r)}{u_{k,0}(r)} \to k \cot(\delta_{k,0}). \tag{2.15}$$

In the limit $k \to 0$, this reduces to

$$\frac{u'_{0,0}(r)}{u_{0,0}(r)} \to -\frac{1}{a}, \tag{2.16}$$

for $R_{vdW} \lesssim r \lesssim a$. The last equation is known as the Bethe-Peierls condition, first discussed in the context of neutron scattering [47].

In chapter 5, we are also interested in the first k-dependent correction to Eq. (2.16):

$$k \cot \delta_{k,0} = -\frac{1}{a} + \frac{1}{2} r_e k^2 + \mathcal{O}(k^4), \tag{2.17}$$

where r_e is called the effective range, and which can be given explicitly if $u_{0,0}$ is known, following [48]. Consider a solution u_0 of Eq. (2.5) for $l = 0$ and $k = 0$. Choose a normalization such that for $r \gg R_{vdW}$ it approaches $u_0 \to 1 - r/a$, making it a-dimensional. Then r_e is given by

$$r_e = 2 \int_0^\infty dr \left[(1 - r/a)^2 - u_0(r)^2 \right] \tag{2.18}$$

2.2.3 Feshbach resonances

In the last section, we neglected the internal spin degrees of the atoms. In principle, a separate interaction $U(\boldsymbol{r})$ must be considered for every possible spin combination of atoms. Typically, these potentials still conform to the general shape shown in Fig. 2.1, with varying depth and shape of the potential around the minimum, however the van-der-Waals tail Eq. (2.1) is spin-independent, and only determined by the atomic species of the scattering atoms. Spin-exchange interactions can also couple the initial spin configuration to different outgoing configurations. Therefore one should consider a full spin-dependent matrix potential, turning scattering into a *multi-channel* problem.

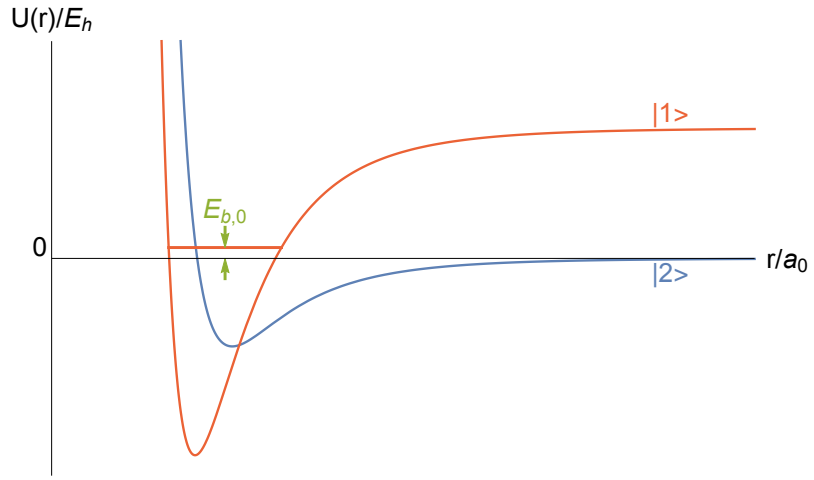

Figure 2.2: Sketch of an uncoupled two-channel potential configuration typically found in a Feshbach resonance. The closed channel (red), with spin character $|1\rangle$, has a potential which supports a bound state, with energy $E_{b,0}$ very close to the threshold of the open channel (blue), with spin character $|2\rangle$. Other bound states both in the closed and open channel are not depicted for clarity.

Of great experimental importance are so called Feshbach resonances, which lead to strong renormalization of spin-conserving scattering by resonant coupling to other spin-channels. An in-depth discussion of the subject can be found in [43], a qualitative understanding however can be gained from a two-channel picture, which we shall briefly discuss here.

One starts with two bare, uncoupled channels: The *closed* channel where the atoms are in spin configuration $|1\rangle$ and interacting through Hamiltonian $\hat{H}_1$, and a similar second *open* channel for a different spin configuration $|2\rangle$ with interaction $\hat{H}_2$. The first channel is called *closed* since the associated threshold energy, when the atoms are far apart and interactions are negligible, for configuration $|1\rangle$ is larger than the threshold energy of $|2\rangle$, which we will put to 0 in the following. A single bound state $|\psi_b\rangle_0$ of the closed channel has a binding energy $E_{b,0}$ very close to the open channel threshold. A sketch of a typical configuration is shown in Fig. 2.2.

Upon introducing a cross-channel interaction $\hat{H}_{12}$, the eigenstates of $\hat{H}_1$ and $\hat{H}_2$ will be mixed. Especially the low-lying continuum states $|\psi_{\mathbf{k}}\rangle_0$ of $\hat{H}_2$ and the bound state $|\psi_b\rangle_0$ of $\hat{H}_1$ will be dressed strongly, since their energies are near degenerate. This can be seen by the breakdown of first order perturbation theory for the states:

$$\begin{aligned} |\psi_{\mathbf{k}}\rangle_1 =& |\psi_{\mathbf{k}}\rangle_0 + |\psi_b\rangle_0 \frac{\langle\psi_b|\hat{H}_{12}|\psi_{\mathbf{k}}\rangle_0}{k^2/2m_r - E_{b,0}} \\ |\psi_b\rangle_1 =& |\psi_b\rangle_0 + \sum_{\mathbf{k}} |\psi_{\mathbf{k}}\rangle_0 \frac{\langle\psi_{\mathbf{k}}|\hat{H}_{12}|\psi_b\rangle_0}{E_{b,0} - k^2/2m_r}. \end{aligned} \tag{2.19}$$

Even if $|\langle\psi_{\mathbf{k}}|\hat{H}_{12}|\psi_b\rangle_0|$ is small, corrections might be large due to the small denominator in Eq. (2.19). Here we neglected the presence of continuum states in the closed channel and other bound states in either channel, since their contribution will in general be negligible compared to the ones indicated in Eq. (2.19).

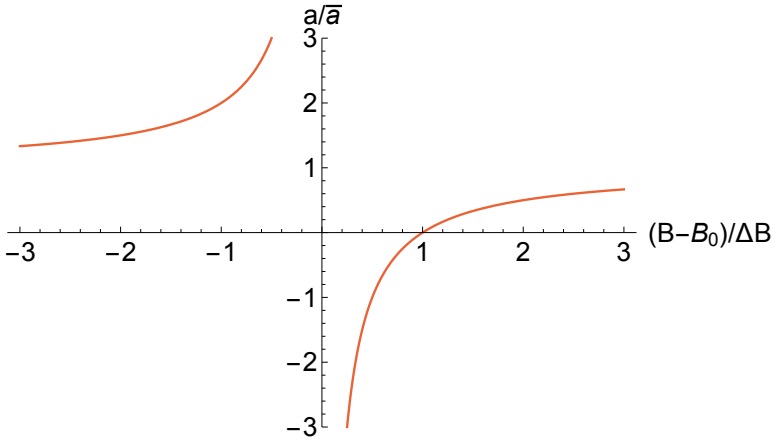

Figure 2.3: The open channel scattering length a across a magnetic Feshbach resonance described by a two-channel model, as in Eq. (2.21). Close to the resonance, the scattering length a diverges.

In some configurations, the energy difference $E_{b,0}$ can be controlled externally, for example magnetically if the configurations $|1\rangle$ and $|2\rangle$ have different magnetic moments μ_1 and μ_2.The classical example would be $|1\rangle$ corresponding to the singlet state of the valence pair and $|2\rangle$ to the triplet state. Upon applying an external magnetic field B, the thresholds of $|1\rangle$ and $|2\rangle$ will shift differently under the Zeeman effect and $E_{b,0} \sim B(\mu_1 - \mu_2)$; the system can be thus tuned across the resonance experimentally by changing B.

To properly understand this resonance phenomenon, a full diagonalization of the subspace $|\psi_{\mathbf{k}}\rangle_0 \otimes |\psi_b\rangle_0$ of the Hamiltonian $\hat{H}_1 + \hat{H}_2 + \hat{H}_{12}$ is needed. Such a procedure is discussed in [49], giving the fully dressed scattering states $|\psi_{\mathbf{k}}\rangle$ and bound state $|\psi_b\rangle$, with an eigenenergy E_b generally different from the bare energy E_{b_0} due to the dressing.

As discussed around Eq. (2.6), associated to the asymptotic behavior of the bare scattering states $|\psi_{\mathbf{k}}\rangle_0$ are s-wave phase shifts, i.e. $\langle \boldsymbol{r}|\psi_{\mathbf{k}}\rangle_0 \simeq \sin(kr + \delta_{k,0})$ for large r. The fully dressed states $|\psi_{\mathbf{k}}\rangle$ behave similarly, but acquire an additional phase shift in s-wave due to the resonance

$$\langle \boldsymbol{r}|\psi_{\mathbf{k}}\rangle \simeq \sin(kr + \delta_{k,0} + \delta_{k,res}), \tag{2.20}$$

which depends on the complicated details of the microscopic coupling. Instead a phenomenological description, based on experimentally accessible parameters, is more convenient. In the low-k limit, with the asymptotic behavior $\delta_{k,0} + \delta_{k,res} = -ka$, the effective scattering length a can be expressed to good approximation with the formula

$$a = \bar{a}\left(1 - \frac{\Delta B}{B - B_0}\right), \tag{2.21}$$

which is shown in Fig. 2.3. Here $\bar{a}$ is the scattering length associated with the bare open channel, i.e. $\delta_{k,0} = -k\bar{a}$ for $k \to 0$, B_0 is the properly renormalized magnetic field-strength at which the resonance occurs and ΔB is called the 'width' of the

resonance. On resonance $B = B_0$, the scattering length Eq. (2.21) diverges. In this case, the s-wave phase shift is actually $\pi/2$, called the unitary limit.

Similarly, the effective range Eq. (2.18) also is affected by the resonance. Unlike the scattering length however, the effective range varies less across the resonance and does not diverge but takes a finite value at $B = B_0$. At resonance, the effective range is completely determined by the van-der-Waals length R_{vdW} and the resonance length $R^* = \hbar^2/(2m_r a_0 \Delta\mu \Delta B)$ [43, 22, 50]:

$$r_e(B_0) = -2R^* + \frac{2}{3\pi}\Gamma(1/4)^2 R_{vdW}. \tag{2.22}$$

Note that R^* is always positive.

The dressed states $|\psi_b\rangle$ and $|\psi_{\mathbf{k}}\rangle$ will in general be in a superposition of the bare channel configurations $|1\rangle$ and $|2\rangle$. We can decompose the states into the two components:

$$\langle \boldsymbol{r}|\psi_b\rangle = \chi_b(\boldsymbol{r})|1\rangle + \sqrt{Z_b}\psi_{b_0}(\boldsymbol{r})|2\rangle, \tag{2.23}$$

$$\langle \boldsymbol{r}|\psi_{\mathbf{k}}\rangle = \chi_{\mathbf{k}}(\boldsymbol{r})|1\rangle + \sqrt{Z_{\mathbf{k}}}\psi_{b_0}(\boldsymbol{r})|2\rangle, \tag{2.24}$$

where ψ_{b_0} is the normalized wave function of the bare bound state $\langle \boldsymbol{r}|\psi_b\rangle_0$. We assume $|\psi_b\rangle$ and $|\psi_{\mathbf{k}}\rangle$ to be normalized[1] and therefore $Z_{b,\mathbf{k}} + \int d^3|\chi_{b,\mathbf{k}}(\boldsymbol{r})|^2 = 1$ and $0 < Z_{b,\mathbf{k}} < 1$. Both $Z_{\mathbf{k}}$ (for small k) and Z_b are useful to discuss the level of the admixture of the closed channel configuration into both states due to dressing.

Z_b changes strongly across the resonance and $Z_b \ll 1$ close to $B = B_0$ where $|a|$ is large, implying that the bound state has entirely open channel character [43]. If this is the case and if the binding energy of the dressed dimer state is below the open channel threshold $E_b < 0$, it takes the form

$$E_b = -\frac{\hbar^2}{2m_r a^2}, \tag{2.25}$$

which is energetically accessible via near-threshold scattering. In this universal regime, the dressed bound state $|\psi_b\rangle$ has a spatial extension of linear size a, much larger than deep bound states of size R_{vdW}, and it is completely independent of the microscopic properties of the closed channel. This feature is entirely quantum in nature, and due to the large extension of the state they have been referred to as "halo dimers", a term originally coming from nuclear physics [51]. An extensive review of the universal quantum halo phenomenon is found in Ref. [52].

The behavior of $Z_b, Z_{\mathbf{k}}$ across the resonance can be roughly classified by the a-dimensional resonance strength [43]:

$$s_{res} = \frac{4\pi}{\Gamma(1/4)^2}\frac{R_{vdW}}{R^*}, \tag{2.26}$$

linking them to the resonance length R^*. Two regimes can be distinguished:

[1] For example, by using a quantization volume V for the states $|\psi_{\mathbf{k}}\rangle$ and taking the limit $V \to \infty$ at the end.

- $s_{res} \gg 1$: In this regime typically $Z_b, Z_{\mathbf{k}} \ll 1$ in a large domain around the resonance, both bound state and scattering states have negligible admixture of the closed channel configuration $|2\rangle$. Correspondingly the bound state energy of the universal form Eq. (2.25) for $E_b < 0$ is valid for this large domain. This regime is called *open channel dominated*. Such resonances are sometimes called *broad*, since a large width $|\Delta B|$ is often associated in this regime. Because $R_{vdW} \gg R^*$, it follows from Eq. (2.22) that $r_e(B_0)$ is positive and of order R_{vdW}.

- $s_{res} \ll 1$: In the opposite regime one has $Z_b \ll 1$ only in a very small window close to the resonance. Away from it the bound state loses any open channel dressing quickly and $Z_b \to 1$. This regime is called *closed channel dominated*. Since $R_{vdW} \ll R^*$, the effective range $r_e(B_0)$ is negative and of order R^*. As often small $|\Delta B|$ coincides with large R^*, such resonances are conventionally called *narrow*.

Since the states in open-channel dominated resonances have negligible admixture of the $|2\rangle$ configuration for most relevant B values in an experiment, they can be well described with just an effective single channel model recovering the relevant scattering parameters. In the remainder of this work, we will focus on this case.

2.2.4 Effective single-channel models

In the last section, we established that open channel dominated resonances, with $s_{res} \gg 1$, can be well described with an effective single channel model and a simplified model potential $U(\boldsymbol{r})$. A physically realistic potential in the shape of Fig. 2.1 is unpractical, since due to its many bound states and steep repulsive barrier, small numerically errors can propagate to large errors in the s-wave scattering properties.

Especially in chapter 5, we will use explicit single channel model potentials. Their relevant s-wave scattering properties can be extracted from the solution of the radial s-wave Schroedinger equation Eq. (2.5) at zero energy:

$$-u''(r) + \left(\frac{2m_r}{\hbar^2}U(r)\right)u(r) = 0 \tag{2.27}$$

We consider isotropic model potentials characterized by a length scale r_0. Recasting the potential in the form $U(r) = \hbar^2 U_0 \bar{U}(r/r_0)/2m_r r_0^2$, with the adimensional height U_0, we can make the substitution $\rho = r/r_0$ in Eq. (2.27) and recover the adimensional equation

$$-u_k''(\rho) + U_0\bar{U}(\rho)u(\rho) = 0, \tag{2.28}$$

As model potentials, we use an attractive Gaussian, exponential and spherical well potential:

$$\bar{U}_G = -\,e^{-\rho^2}, \tag{2.29}$$

$$\bar{U}_{\text{Exp}} = -\,e^{-\rho}, \tag{2.30}$$

$$\bar{U}_{\text{Box}} = \begin{cases} -1 & \rho < 1 \\ 0 & \rho > 1 \end{cases}. \tag{2.31}$$

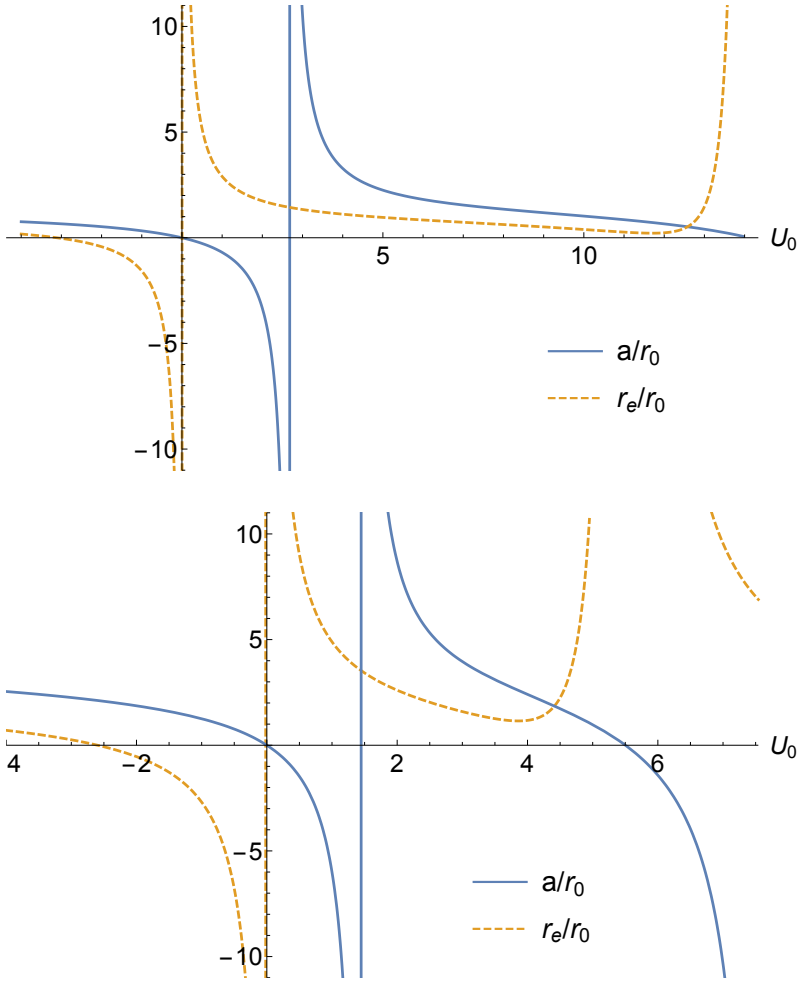

Figure 2.4: Relation between the height U_0 and the scattering length a in units of r_I for the Gaussian potential (top) in Eq. (2.29) and the exponential potential (bottom) in Eq. (2.30).

With the box potential Eq. (2.31), Eq. (2.28) can easily be solved analytically, and using Eqs. (2.34) and (2.18), one finds the well known results (compare with [45]):

$$\frac{a}{r_0} = 1 - \frac{\tan\sqrt{U_0}}{\sqrt{U_0}}, \tag{2.32}$$

$$\frac{r_e}{r_0} = 1 + \frac{3\tan\sqrt{U_0} - \sqrt{U_0}(3+U_0)}{3\sqrt{U_0}\left(\sqrt{U_0} - \tan\sqrt{U_0}\right)^2} \tag{2.33}$$

Correspondingly, at $U_0 = (2n-1)^2\pi^2/4$ the n-th bound state appears for the spherical well.

Eq. (2.28) with the Gaussian potential Eq. (2.29) cannot be solved analytically. Since Eq. (2.29) is regular at $r = 0$, we choose the boundary conditions $u(0) = 0$ and $u'(0) = 1$ and integrate Eq. (2.28) outward with standard methods. The phase shift appears in the asymptotic shape Eq. (2.6) of u_0 for $\rho \gg 1$, and in the limit $k \to 0$ one can extract the scattering length via

$$\frac{a}{r_0} = \lim_{\rho\to\infty}\left(\rho - \frac{u_0(\rho)}{u_0'(\rho)}\right), \tag{2.34}$$

as discussed for example in [53]. Given a, the effective range r_e can be computed via Eq. (2.18). Numerically computed scattering lengths and effective ranges are shown in Fig. 2.4 (top). The first bound state appears at $U_0 \approx 2.684$, reproducing the result in [53].

The exponential potential Eq. (2.30) admits an analytic solution in terms of Bessel functions of the first kind $J_0(x)$[2]. The resonance points take an easy analytical form: $U_0^{(n)} = j_n^2/4$ marks the appearance of the n-th bound state, where $j_n = (2.405, 5.520, \ldots)$ are the positive roots of the Bessel function $J_0(x)$. However, an analytic description is cumbersome and we rather solve Eq. (2.28) numerically. The numerically computed scattering lengths and effective ranges are shown in Fig. 2.4 (bottom).

2.2.5 Zero-range model

While the single-channel model potentials discussed in the previous section are a significant simplification compared to the full multi channel picture, they still involve the small length scale r_0 and therefore introduce microscopic two-body correlations of atoms on the same length scale.

In the context of dilute gases however, these short range correlations often form an unnecessary complication. A way to simplify the description further is to introduce zero-range models where the bare interaction range r_0 as well as potential strength are eliminated directly in terms of their scattering properties. To this end, in this section we consider a Dirac-delta potential:

$$U(\hat{r}) = g\delta(\hat{r}), \tag{2.35}$$

which has no physical range r_0 left. We will review its scattering properties. Due to its singular nature, it is convenient to study it via the T-matrix formalism, which we will introduce in the following.

Consider the Schroedinger equation Eq. (2.3) for a continuum state $|\psi_\mathbf{k}\rangle$ in operator form:

$$\left(\frac{\hat{p}^2}{2m_r} + \hat{U}\right)|\psi_\mathbf{k}\rangle = \frac{\hbar^2 k^2}{2m_r}|\psi_\mathbf{k}\rangle. \tag{2.36}$$

We introduce the operator $\hat{G}_k$, which is defined by the operator equation

$$\left(\frac{\hbar^2 k^2}{2m_r} - \frac{\hat{p}^2}{2m_r}\right)\hat{G}_k = \hat{1}, \tag{2.37}$$

where $\hat{1}$ is the identity matrix. By projecting Eq. (2.37) on the eigenstates $|\mathbf{p}\rangle$ of the momentum operator $\hat{\mathbf{p}}$, we find

$$\langle\mathbf{p}|\hat{G}_k|\mathbf{p}'\rangle = \delta_{p,p'}\frac{2m_r}{\hbar^2}\frac{1}{k^2 - p^2} \quad \rightarrow \quad \langle\boldsymbol{r}|\hat{G}_k|\boldsymbol{r}'\rangle = -\frac{m_r}{2\pi\hbar^2}\frac{e^{ik|\mathbf{r}-\mathbf{r}'|}}{|\mathbf{r}-\mathbf{r}'|}, \tag{2.38}$$

where the latter equation follows from Fourier transforming $\langle\mathbf{p}|\hat{G}_k|\mathbf{p}'\rangle$. Since $(\hbar^2k^2 - \hat{p}^2)|\mathbf{k}\rangle = 0$, it follows that

$$|\psi_\mathbf{k}\rangle = |\mathbf{k}\rangle + \hat{G}_k\hat{U}|\psi_\mathbf{k}\rangle, \tag{2.39}$$

[2]The Bessel function of the first kind $J_\alpha(z)$ can be defined via the contour integral $J_\alpha(z) = \frac{1}{2\pi i}\oint \exp\left[(z/2)(t-1/t)\right]t^{\alpha-1}dt$

solves the Schroedinger equation Eq. (2.36). Eq. (2.39) can be iteratively put into itself, i.e.

$$\begin{aligned}|\psi_{\mathbf{k}}\rangle &= |\mathbf{k}\rangle + \hat{G}(\hat{U} + \hat{U}\hat{G}_k\hat{U} + \ ...)|\mathbf{k}\rangle \\ &= |\mathbf{k}\rangle + \hat{G}_k\hat{T}|\mathbf{k}\rangle,\end{aligned} \tag{2.40}$$

which implicitly defines the T-matrix operator. Projecting Eq. (2.40) on $|\boldsymbol{r}\rangle$, one finds

$$\psi_{\mathbf{k}}(\boldsymbol{r}) = e^{i\mathbf{kr}} - \frac{m_r}{2\pi\hbar^2}\int d^3r' \frac{e^{ik|\mathbf{r}-\mathbf{r}'|}}{|\mathbf{r}-\mathbf{r}'|}\langle \boldsymbol{r}'|\hat{T}|\mathbf{k}\rangle \tag{2.41}$$

For large $\mathbf{r}$ one can safely assume $\mathbf{r} \gg \mathbf{r}'$ for all $\mathbf{r}'$ in the integral. By using $|\mathbf{r}-\mathbf{r}'| \approx r - \boldsymbol{r}\cdot\mathbf{r}'/r$ in that limit, we find

$$\psi_{\mathbf{k}}(\boldsymbol{r}) = e^{i\mathbf{kr}} - \frac{m_r}{2\pi\hbar^2}\frac{e^{ikr}}{r}\int d^3r' \ e^{i\mathbf{k}'\boldsymbol{r}'}\langle \boldsymbol{r}'|\hat{T}|\mathbf{k}\rangle, \tag{2.42}$$

where $\mathbf{k}' = k\boldsymbol{r}/r$ is a wave vector of magnitude k and in the direction of $\boldsymbol{r}$. Comparing with Eq. (2.7), we can identify the scattering amplitude

$$f_k(\theta) = -\frac{m_r}{2\pi\hbar^2}\int d\mathbf{r}' e^{i\mathbf{k}'\boldsymbol{r}'}\langle \boldsymbol{r}'|\hat{T}|\mathbf{k}\rangle = -\frac{m_r}{2\pi\hbar^2}\langle \mathbf{k}'|\hat{T}|\mathbf{k}\rangle. \tag{2.43}$$

In the case of a delta potential Eq. (2.35), where $\langle \mathbf{k}'|U|\mathbf{k}\rangle = g\delta_{\mathbf{k},\mathbf{k}'}$ is particularly simple, the T-matrix becomes a geometric series in k space:

$$\begin{aligned}\langle \mathbf{k}'|\hat{T}|\mathbf{k}\rangle &= \langle \mathbf{k}'|(\hat{U} + \hat{U}\hat{G}_k\hat{U} + ...)|\mathbf{k}\rangle \\ &= g\delta_{k,k'}\sum_{n=0}^{\infty}\left(g\frac{2m_r}{\hbar^2}\int\frac{d^3p}{(2\pi)^3}\frac{1}{k^2-p^2}\right)^n \\ &= \frac{\delta_{k,k'}}{g^{-1} - \frac{2m_r}{\hbar^2}\int\frac{d^3p}{(2\pi)^3}\ \frac{1}{k^2-p^2}}.\end{aligned} \tag{2.44}$$

In the low-k limit, where $f_k(\theta) \to -a$, this defines the relation between scattering length and the bare coupling g:

$$g^{-1} = \frac{m_r}{2\pi\hbar^2 a} - \frac{2m_r}{\hbar^2}\int\frac{d^3p}{(2\pi)^3}\frac{1}{p^2}. \tag{2.45}$$

Note that the integral in the second term of Eq. (2.45) is ultraviolet divergent, a consequence of the zero-range nature of the potential Eq. (2.35). Therefore the physical scattering length for a Dirac potential vanishes for any g. However, we can 'regularize' the delta-potential by introducing an ultraviolet cutoff Λ in the integral in Eq. (2.45):

$$g^{-1} = \frac{m_r}{2\pi\hbar^2 a} - \frac{2m_r}{\hbar^2}\int_{p\leq\Lambda}\frac{d^3p}{(2\pi)^3}\frac{1}{p^2}. \tag{2.46}$$

This ensures that the pair g, Λ corresponds to a unique, finite scattering length a. Reinserting Eq. (2.46) into Eq. (2.44), one can safely take the limit $\Lambda \to \infty$ and finds

$$f_k(\theta) = -\frac{1}{a^{-1} - ik}, \tag{2.47}$$

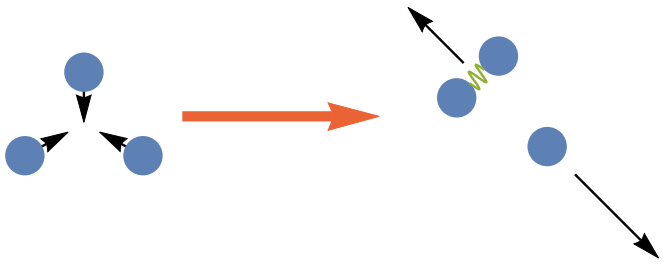

Figure 2.5: Typical three body recombination event: three incoming particles undergo a collision, where two particles form a deeply bound molecule supported by the two-body potential, as indicated in Fig. 2.1. The released binding energy results in a large kinetic energy for both the dimer and the third particle after the collision, and typically both escape the trap holding the gas.

which is valid for all k, and which is the proper s-wave limit of the scattering amplitude incorporating the optical theorem [3]. Thus the regularized delta-potential creates an effective scattering which is always s-wave and where all higher-order k corrections, such as the effective range r_e in Eq. (2.16), are zero. This is often called the zero-range limit.

While this treatment seems technical, the simple form of the Dirac potential in Fourier space can simplify many-body treatments dramatically. In section 4.1.1, we will see this for the particular case of the many-body T-matrix. A cutoff dependent Dirac potential is just one of many possible, properly regularized zero-range models. Other methods, such as the direct implementation of Bethe-Peierls contact conditions (2.16) or non-local pseudo-potentials, are also often used [41], however in this work, we will only employ the regularization procedure Eq. (2.46).

2.3 Three-body processes

Beyond two-body collisions, also three- and larger few-body encounters can occur. While the microscopic nature of these processes are not the focus of this thesis, we shall give a brief overview of two aspects of great experimental and conceptual importance, three-body recombination and Efimov physics.

2.3.1 Three-body recombination

Three-body recombination plays an important role in losses of ultracold atoms from the trap, depleting the gas over time. In a typical event, two of the three incoming particles form a molecule, supported by the two-body potential sketched in Fig. 2.1, after the collision. The released binding energy results in large kinetic energy for both the dimer and the remaining particle, with velocities so high that they generally escape the trap.

Three-body channels involving identical fermions are Pauli-suppressed in s-wave, however for mixtures or bosons, these processes often determine the lifetime of the gas. The recombination rate is drastically enhanced if the two-body interaction of any possible pairing has a large scattering length a, due to a resonantly tuned

[3] A more detailed discussion of the optical theorem can be found in §125 in [14]

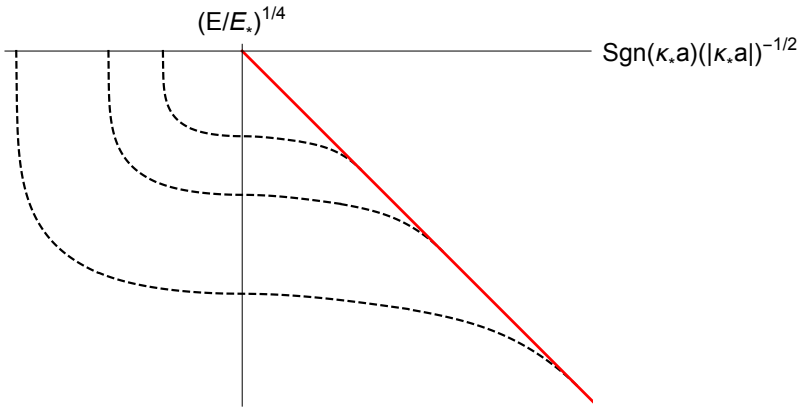

Figure 2.6: Sketch of the Efimov trimer energies $E_{3,n}$ (black dashed lines) of three identical bosons with mass m and pair-wise scattering length a, in units of $E_* = \hbar^2\kappa_*^2/m$ for $n = 0, 1, 2$. To make the plot more accessible and reduce the spacing between levels, computations of $E_{3,n}$, as discussed in [59], were performed with $s_0 = 3$ instead of the true value $s_0 \approx 1.006$. The solid red line marks the universal two-body binding energy Eq. (2.25)

Feshbach resonance for example, and generally scales as $\sim a^4$ [54] for identical bosons or Bose-Fermi mixtures. This has been experimentally confirmed for both homo- and heteronuclear gases [55, 56]. For resonant two component Fermi gases, Pauli blocking theoretically suppresses three body recombination at zero temperature, but in real experiments at finite temperature, losses can still be large given the right circumstances [57].

Thus spin polarized fermionic gases and two-component Fermi fluids typically remain stable at strong interactions and low enough temperatures. On the other hand, mixtures involving bosonic or more than two fermionic species have severely limited lifetimes for strong interactions [58].

2.3.2 Efimov states

In two-body scattering, the zero-range limit is well-defined by fixing a single parameter, the scattering length a, connected to a universal bound state with energy Eq. (2.25). However, for more than two particles, this universality is broken and an additional parameter must be introduced for a well-defined zero-range limit [60, 61]. From an ultracold dilute gas perspective, this parameter will have a sizable impact on the dynamics as well in the many-body context, as long as more-than-two-body processes are not suppressed by quantum statistics.

Often this parameter is defined over the binding energy of so-called Efimov states, first discussed in [62]. If one considers three identical bosons of mass m, interacting pairwise with an interaction characterized by a scattering length a, then a series of three-body bound states can appear if a is larger than the typical interaction range, R_{vdW} in the case of alkali atoms. The binding energies $E_{3,n}$, can be described by the Efimov equation, as discussed in Refs. [63, 59, 64]. Exactly at resonance $1/a = 0$, they follow the simple scaling:

$$E_{3,n} = -\frac{\hbar^2\kappa_*^2}{m} e^{-2\pi n/s_0}, \tag{2.48}$$

for large n. Here n is an integer, $s_0 \approx 1.0065$ and the binding wave number κ_* fixes an *arbitrary* energy $E_{3,0}$ in the series at resonance. In the zero range limit, an infinite number of evermore deeply bound Efimov states exists at resonance, however for alkali atoms with finite interaction range, this series terminates once the supposed Efimov bound state has a linear size comparable to R_{vdW}. For the lowest and lower bound states, the universal scaling Eq. (2.48) is then only approximate due to finite range effects. For $1/a \neq 0$, a sample of universal Efimov binding energies is shown in Fig. 2.6. For $a < 0$, the n-th bound state still exists until a threshold value $a_{n,-}$, such that Efimov states still exist even if the two-body interaction does not support one. On the other hand for large $a > 0$, the trimers are more deeply bound than a dimer with energy Eq. (2.25) plus a free third particle, until a critical value $a_{n,+}$ where they merge into the dimer spectrum.

By fixing κ^*, the entire zero-range scattering problem is determined. For identical bosonic alkali atoms on resonance, the binding wave number is related to the Van-der-Waals length, with measured values of the order $\kappa_* \sim 0.1-0.2R_{vdW}^{-1}$, however the origins and validity of this relatively narrow window is subject to ongoing scientific debate [65]. For heterogeneous systems, Efimov physics also exist and lead to similar phenomena, as long as Pauli blocking cannot suppress three-body events.

Remarkably, for more than three particles, a and κ^* seem sufficient to determine completely 4-body clusters as well, and there is indication that indeed all possible N-body clusters can be fixed in the zero-range limit just by a and κ_* [61].

Part I

Impurities in Bose gases

Chapter 3

A quick review of polaron physics

The polaron concept originated in the investigation of self-trapping of electrons in polarizable solids by induced deformation of the surrounding lattice, started by a short paper of Landau [66]. In this context, Pekar first described the electron dressed by the local lattice deformation as a quasi-particle, the polaron [67], which could have effective masses several orders of magnitude higher than the bare electron [68]. The polaron has been considered important for the understanding of polar and dielectric materials and was quickly elaborated further theoretically, among others by Fröhlich [69, 70], who established the contemporary picture of the polaron as an electron interacting with a phonon bath. Other important contributions were made by Lee and Pines [71], Feynman [72] as well as Holstein [73]. From these beginnings, the field of polaron physics in solids has been an active field of research for almost a century now. It has seen many extensions [74], among them additional degrees of freedom of bath and impurity [75, 76]. Polarons have been observed in a large variety of materials, [77, 78, 79] being some examples, and have even been observed with different quasi-particles acting as the base impurity [80]. As an underlying concept, polarons play a fundamental role in the functioning of state-of-the-art technological applications, such as OLEDS [81] and Lithium-ion batteries [82].

The polaron concept proved very successful in the qualitative understanding of diverse phenomena in dielectric materials. However, the basic models proposed in the 1950s proved very hard to solve theoretically beyond the mean-field level. Moreover a quantitative comparison to real materials is often futile since their real-world complexity, with a plethora of effects and parameters at play at once, makes isolating polaron physics from other phenomena challenging. The advent of ultracold gases made it possible to realize polaron physics with as-of-yet unprecedented conceptual simplicity and experimental access.

Within the ultracold gas community, the so called Fermi polaron was the first impurity problem investigated [83]: In a cloud of spin-polarized fermions at ultracold temperatures, a tiny fraction of particles is flipped into a different spin state via a coherent radio-frequency pulse. Particles in this population are now distinguishable from the surrounding majority population, their interaction with the bath controllable via a magnetic Feshbach resonance, as described in section 2.2.3. On the other hand, interaction effects within both majority and minority spin species are negligible due to Pauli blocking and the resulting suppression of s-wave scattering, see Eq. (2.13). In the limit of a vanishing number of minority particles, finite density effects can be ignored and the system properties can be described by the

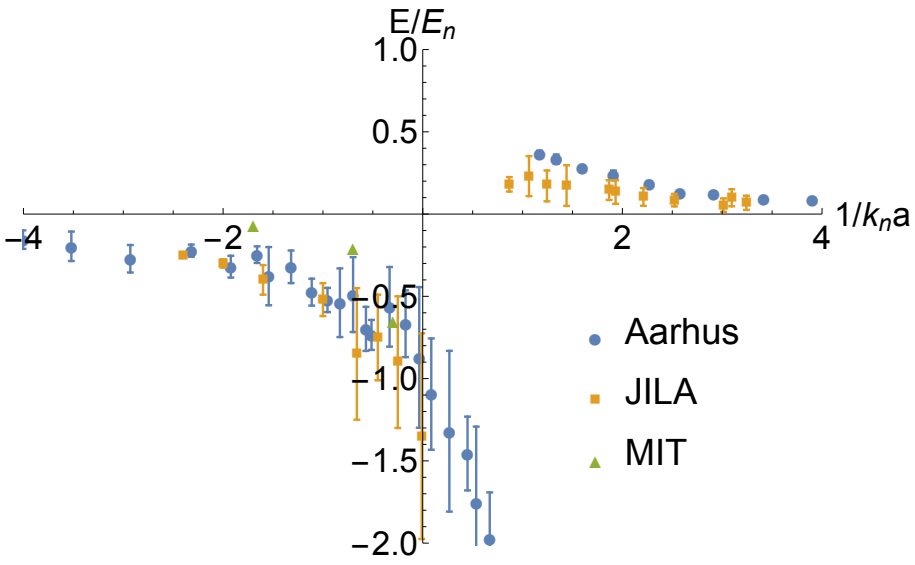

Figure 3.1: Experimental data on the Bose-polaron quasi-particle energies across a Feshbach-resonance, showing both the repulsive (right) and attractive branch (left). Data taken from the three experiments at Aarhus [87], JILA [88] and MIT [89]

physics of a single impurity interacting with a bath of ideal fermions. This realizes the polaron problem as envisioned by Fröhlich, with a fermionic bath instead of phonons. In a series of closely-interwoven experimental and theoretical works, the ultracold Fermi polaron is now understood to astounding precision with excellent agreement between theory and experiment [84, 85, 86].

The ultracold Bose polaron, the analogue with a bosonic bath, is experimentally much more challenging to realize since the presence of three-body losses in bosonic gases tremendously shortens lifetimes of the gaseous state [87, 88]. In particular the minority particles are lost from the trap quickly whenever the inter-species interaction is close to resonance, and thus experiments need to accommodate for strong losses. Recently, two almost simultaneous publications [87, 88] provided first experimental data on the groundstate properties of the Bose polaron via injection spectroscopy as a function of the inter-species scattering length a. A similar work using ejection spectroscopy [89] was published shortly after. However in all experiments, spectral data obtained is significantly broadened in the strongly interacting regime due to three-body losses, as discussed in section 2.3.1, so that the experimental access to the Bose polaron has been limited so far. Across experiments, two distinct branches of spectral peaks were found, corresponding to quasiparticle states. Fig. 3.1 shows the extracted quasiparticle energies across a Feshbach resonance for these three experiments.

The problem is considerably richer than the Fermi analogue, since more-than-two body interactions are not suppressed, allowing for potentially larger dressing. This complicates the theoretical description of the problem considerably even in this idealized scheme. On the one hand, computationally very costly Quantum Monte-Carlo approaches [90, 91] were employed to tackle the problem, on the other hand a large number of publications employ various approximations [92, 5, 93, 94, 95, 96] to account for the complicated more-than-two-body physics needed to properly describe the polaron properties. While these publications mostly focused on the case

of few bosonic excitations bound to the impurity, in chapter 5 I present my study of a novel variational ansatz tailored to describe the as-of-yet poorly understood regime where the polaron dressing can be macroscopic. Additionally, the problem is complicated by a phase transition of the bosonic bath to a BEC at low temperatures, and the nature of the phonon modes present below the transition strongly depends on the temperature of the bath. The temperature of the bath is difficult to control experimentally, and only one experiment [89] was able to extrapolate the temperature dependence of the problem by measuring the polaron energy spatially resolved within the non-homogeneous boson cloud: This varies the density-dependent critical temperature T_C for Bose condensation in the problem, and therefore the a-dimensional temperature T/T_C. However, this approach is limited: By varying the density in the experiment, the relevant a-dimensional length scales $k_n a$ and $k_n a_{BB}$ describing inter- and intra-species scattering are changed as well. Extrapolation of the independent temperature dependence only works if one can either neglect or predict the energy change due to the other parameters sufficiently. But until now the Bose-polaron problem is lacking a complete theoretical picture including temperature effects, such that any assumption might lead to biased data.

Finite temperature effects were first studied in [97] for weak boson-impurity coupling. The first published work considering finite temperatures in the strongly interacting regime was by me, and is presented in chapter 4. A later work by other authors showed qualitatively similar behavior using a variational approach [98]. With the Fermi polaron being the historical starting point of impurity physics in the ultracold gases community, the discussion of the Bose polaron inherited unit conventions established for the Fermi case. Given the density n_0 of the Bose condensate, the wave vector

$$k_n = (6\pi^2 n_0)^{1/3} \tag{3.1}$$

is defined in analogy to the Fermi momentum, which in this case can be understood simply as a scale associated to the classical mean inter-boson distance in the gas. The associated energy scale is defined as

$$E_n = \frac{\hbar^2 k_n^2}{2m}, \tag{3.2}$$

where the mass m is typically chosen from the impurity mass m_I, the Bose mass m_B, or the reduced mass $m_r = m_B m_I/(m_I + m_B)$ in various works, depending on their focus. In chapter 4 and the associated publication [2], the focus was put on the equal mass case $m_B = m_I$, and $m = m_B$ was chosen in Eq. (3.2). However, in chapter 5 and the work [4], various impurity masses including the limit $m_I \to \infty$ were considered, and the choice $m = m_r$ in Eq. (3.2) proved beneficial.

Chapter 4

Diagrammatic ladder approximation

One technique especially suited to the discussion of impurities in dilute media, covered in-depth in this chapter, is the ladder or $\mathcal{T}$-matrix approximation. We shall briefly review the Green's function formalism underlying the $\mathcal{T}$-matrix in section 4.1. In section 4.2 we will introduce the $\mathcal{T}$-matrix and review earlier results established with it for impurities in a three-dimensional, zero-temperature bosonic bath. Finally in section 4.4, we will extend the common ladder approximation to finite temperatures, including new diagrams describing important processes in thermal BECs. This last section is adapted from [2].

4.1 Green's functions and diagrammatics

The $\mathcal{T}$-matrix is an approximation within the diagrammatic approach to many-body physics, relying heavily on the concept of *Green's functions*, also called *propagators*. This formalism, originally developed in the context of high-energy physics [99] and later adopted to many-body systems, is highly technical and elaborate. In this section, we shall briefly recall the basic tenets of the concept as well as the aspects relevant to the application of the $\mathcal{T}$-matrix approach to impurities and its relation to physical observables. A complete discussion of diagrammatic quantum-many-body theory can be found in [100], on which this section is largely based.

4.1.1 Ground state Green's function

Consider a single species of identical particles of mass m in free space interacting pairwise through a two-body potential V. In second quantization, the corresponding Hamiltonian $\hat{H}$ can be expressed as

$$\hat{H} = \int d^3x\ \hat{a}^\dagger_{\mathbf{x}} \frac{-\hbar^2}{2m} \Delta_{\mathbf{x}} \hat{a}_{\mathbf{x}} + \frac{1}{2} \int d^3x d^3y\ \hat{a}^\dagger_{\mathbf{x}} \hat{a}^\dagger_{\mathbf{y}} U(\mathbf{x}-\mathbf{y}) \hat{a}_{\mathbf{y}} \hat{a}_{\mathbf{x}}, \tag{4.1}$$

where the fields $a_{\mathbf{x}}$ associated to the particle species fulfill the canonical (anti-) commutation relations

$$\left[\hat{a}_{\mathbf{x}}, \hat{a}^\dagger_{\mathbf{y}}\right]_{\mp} = \delta(\mathbf{x}-\mathbf{y}), \tag{4.2}$$

if the particle species is bosonic (fermionic). Due to translational invariance of the Hamiltonian in Eq. (4.1), the dual base of fields in $\mathbf{k}$-space will also be important

$$\begin{aligned}\hat{a}^\dagger_{\mathbf{k}} &= \int \frac{d^3x}{(2\pi)^3}\, e^{i\mathbf{k}\cdot\mathbf{x}}\hat{a}^\dagger_{\mathbf{x}} \\ \hat{a}_{\mathbf{k}} &= \int \frac{d^3x}{(2\pi)^3}\, e^{-i\mathbf{k}\cdot\mathbf{x}}\hat{a}_{\mathbf{x}}\end{aligned} \tag{4.3}$$

We assume a normalized ground state $|\Psi_0\rangle$ of Eq. (4.1) with N particles. Considering a Heisenberg picture with time-dependent fields $\hat{a}_{\mathbf{x}}(t) = \exp(i\hat{H}t/\hbar)\hat{a}_{\mathbf{x}}\exp(-i\hat{H}t/\hbar)$, the Green's function is defined as

$$iG_{\mathbf{x},\mathbf{y}}(t,s) = -i\langle\Psi_0|\mathbf{T}\left[\hat{a}_{\mathbf{x}}(t)\hat{a}_{\mathbf{y}}(s)^\dagger\right]|\Psi_0\rangle = \begin{cases}\langle\Psi_0|\hat{a}_{\mathbf{x}}(t)\hat{a}_{\mathbf{y}}(s)^\dagger|\Psi_0\rangle, & t > s \\ \pm\langle\Psi_0|\hat{a}_{\mathbf{y}}(s)^\dagger\hat{a}_{\mathbf{x}}(t)|\Psi_0\rangle, & t < s\end{cases}, \tag{4.4}$$

for bosons (fermions), such that the operator $\mathbf{T}$ orders the canonical fields left to right with descending time variables. Note that the case $t = s$ is not defined, only limits of the kind $t - s \to 0^\pm$ will be considered. We consider henceforth a system invariant under translations in time and space, correspondingly the Green's function is only dependent on the relative spatial and temporal coordinates $G = G(t - s, \mathbf{x} - \mathbf{y})$. Associated is the Green's function in momentum and frequency space $G(\omega, \mathbf{k})$, obtained via a double Fourier transform. In particular, in $\omega, \mathbf{k}$-space the Green's function has the informative *Lehmann representation*

$$G(\omega,\mathbf{k}) = \sum_n \frac{|\langle\Psi_n|\hat{a}^\dagger_{\mathbf{k}}|\Psi_0\rangle|^2}{\omega - (E_n - E_0)/\hbar + i0^+} \mp \frac{|\langle\Psi_n|\hat{a}_{\mathbf{k}}|\Psi_0\rangle|^2}{\omega + (E_n - E_0)/\hbar - i0^+}, \tag{4.5}$$

for bosons (opposite sign terms) and fermions (same sign terms), as is derived in detail in [100]. Here $|\Psi_n\rangle$ is the full set of energy eigenstates of the Hamiltonian Eq. (4.1) with energies E_n and 0^+ is an infinitesimal real and positive number. Clearly, the expectation values $\langle\Psi_n|\hat{a}^\dagger_{\mathbf{k}}|\Psi_0\rangle(\langle\Psi_n|\hat{a}_{\mathbf{k}}|\Psi_0\rangle)$ in the first (second) term (4.5) are only non-vanishing when Ψ_n contains $N + 1(N - 1)$ particles with a total momentum of $\mathbf{k}(-\mathbf{k})$. Consider now the simplest case where $N = 0$,such that $|\Psi_0\rangle$ is the vacuum. The second term in Eq. (4.5) vanishes and the first term connects only to the free single-particle state with momentum $\mathbf{k}$, such that the *vacuum* Green's function reads

$$G_0^{vac}(\omega,\mathbf{k}) = \frac{1}{\omega - \omega_{\mathbf{k}} + i0^+}, \tag{4.6}$$

with $\omega_{\mathbf{k}} = \hbar k^2/2m$. In particular, in the case where $m = m_I$, Eq. (4.6) describes a free impurity. On the other hand, in the thermodynamic limit with N large, if there is a well defined chemical potential μ, we can write $E_n - E_0 = \hbar\omega_n + \mu(\hbar\omega_n - \mu)$ in the denominator of the first (second) term. Then, $\hbar\omega_n$ corresponds to the *excitation energy* of a single particle in the macroscopic ensemble. Level spacings between eigenenergies typically become too small to be resolved individually and it is convenient to define *spectral functions*

$$\begin{aligned}A(\omega,\mathbf{k}) &= \sum_n |\langle\Psi_n|\hat{a}^\dagger_{\mathbf{k}}|\Psi_0\rangle|^2\delta\left(\omega - \omega_n + \mu/\hbar\right), \\ B(\omega,\mathbf{k}) &= \sum_n |\langle\Psi_n|\hat{a}_{\mathbf{k}}|\Psi_0\rangle|^2\delta\left(\omega - \omega_n - \mu/\hbar\right),\end{aligned} \tag{4.7}$$

which can be considered continuous functions instead of delta-type distributions in most practical purposes, in particular when the system is interacting and $a^\dagger_{\mathbf{k}}|\Psi_0\rangle$ and $\hat{a}_{\mathbf{k}}|\Psi_0\rangle$ will not be eigenstates. The Green's function then reads

$$G(\omega, \mathbf{k}) = \int d\omega' \left(\frac{A(\omega', \mathbf{k})}{\omega - \omega' + i0^+} \mp \frac{B(\omega', \mathbf{k})}{\omega + \omega' - i0^+} \right). \tag{4.8}$$

Following the definition Eq. (4.7), the spectral functions A, B are positive. From the canonical relations Eq. (4.2) it follows further that $\int d\omega \left(A(\omega, \mathbf{k}) \mp B(\omega, \mathbf{k})\right) = 1$ for bosons (fermions).

The spectral function $A(\omega, \mathbf{k})$ in Eq. (4.7) is proportional to the energy-resolved cumulative overlap between the state $\hat{a}^\dagger|\Psi_0\rangle$, the interacting N particle ensemble with a single particle plane-wave state of momentum $\mathbf{k}$ on top, which will be called the plane-wave-like state in the following, and any true eigenstate $|\Psi_n\rangle$ of the interacting $N+1$ ensemble. As such it allows inference of the level density in the following sense:

- $A(\omega, \mathbf{k})$ large: In the case where A is large for a given frequency interval, the system *must* have many eigenstates $|\Psi_n\rangle$ with eigenenergies in the corresponding energy window and a large portion of them has significant overlap with the state $\hat{a}^\dagger_{\mathbf{k}}|\Psi_0\rangle$, implying resemblance to a plane-wave-like state.
- $A(\omega, \mathbf{k})$ small: In the opposite case, either the general level density of eigenstates is very low, or most eigenstates in the interval are (almost)-orthogonal to the plane-wave-like state $\hat{a}^\dagger_{\mathbf{k}}|\Psi_0\rangle$.

Loosely speaking, the spectral function $A(\omega, \mathbf{k})$ measures the level density of "plane-wave like" single particle excitations. Conversely, the spectral function $B(\omega, \mathbf{k})$ measures the level density of "plane-wave like" hole excitations.

For non-interacting particles, spectral functions can be easily identified and the corresponding free Green's functions read

$$G_0^B(\omega, \mathbf{k}) = \frac{1}{\omega - \omega_k + i0^+} + N_B\delta(k)\left(\frac{1}{\omega + i0^+} - \frac{1}{\omega - i0^+}\right), \tag{4.9}$$

$$G_0^F(\omega, \mathbf{k}) = \frac{\theta(k - k_F)}{\omega - \omega_k + i0^+} + \frac{\theta(k_F - k)}{\omega + \omega_k - i0^+}, \tag{4.10}$$

$$\tag{4.11}$$

for bosons and fermions respectively. Here k_F is the Fermi momentum and N_B the total number of bosons.

4.1.2 Green's function of a weakly interacting condensate

While the ideal Bose case Eq. (4.9) is an easy model for a condensate, it lacks important phenomena present in physical condensates, such as low-lying sound modes and a critical velocity. Of critical experimental importance to describe these features in a Bose condensate is the weak intra-boson repulsion characterized by a scattering length a_B.

Consider a bosonic species with mass m_B and associated canonical fields $b_{\mathbf{k}}, b^\dagger_{\mathbf{k}}$. The system can most efficiently be described using the classical treatment of Bogoliubov [25], replacing the zero mode operators in Eq. (4.1) by a classical number

$\hat{b}_0, \hat{b}_0^\dagger \to N_0^{1/2}$ and neglecting terms growing smaller than N_0. This simplified Hamiltonian can be diagonalized exactly using the famous Bogoliubov transformation to a new set of canonical fields $\hat{\beta}_{\mathbf{k}}, \hat{\beta}_{\mathbf{k}}^\dagger$

$$\hat{b}_{\mathbf{k}} = u_k \hat{\beta}_{\mathbf{k}} - v_k \hat{\beta}_{-\mathbf{k}}^\dagger \quad , \quad \left[\hat{\beta}_{\mathbf{k}}, \hat{\beta}_{\mathbf{k}'}^\dagger\right]_- = \delta_{\mathbf{k},\mathbf{k}'}, \tag{4.12}$$

where u_k, v_k are defined by a set of well-known relations:

$$\begin{aligned} u_{\mathbf{k}}^2 - v_{\mathbf{k}}^2 = 1 \quad &, \quad u_{\mathbf{k}}^2 = \frac{1}{2}\left(\frac{\epsilon_{\mathbf{k}} + \mu_B}{E_{\mathbf{k}}} + 1\right) \\ \mu_B = n_0 \frac{\hbar^2 4\pi a_B}{m_B} \quad &, \quad E_{\mathbf{k}} = \sqrt{\epsilon_{\mathbf{k}}(\epsilon_{\mathbf{k}} + 2\mu_B)}. \end{aligned} \tag{4.13}$$

Here $\epsilon_{\mathbf{k}} = \hbar^2 k^2 / 2m_B$ is the dispersion relation of the free bosons and $n_0 = N_0/V$ is the condensate density. Up to a constant energy shift, the resulting Hamiltonian then reads

$$H_{Bog} = \frac{1}{2} \sum_{\mathbf{k}} E_k \left(\hat{\beta}_{\mathbf{k}}^\dagger \hat{\beta}_{\mathbf{k}} + \hat{\beta}_{-\mathbf{k}}^\dagger \hat{\beta}_{-\mathbf{k}}\right), \tag{4.14}$$

where the sum of $\mathbf{k}$ from now on is implicitly assumed to exclude the $\mathbf{k} = 0$ mode. This Hamiltonian describes a gas of non-interacting quasi-particles, in particular the ground-state is the vacuum state $|0\rangle_\beta$ associated to the Bogoliubov operators $\beta_{\mathbf{k}}, \beta_{\mathbf{k}}^\dagger$.

The spectral functions of the associated Green's function can then be found using the definition Eq. (4.7) and Eq. (4.12):

$$\begin{aligned} A(\omega, \mathbf{k}) &= \sum_n |\langle \Psi_n | b_{\mathbf{k}}^\dagger | 0 \rangle_\beta|^2 \delta(\omega - \omega_n) = u_{\mathbf{k}}^2 \delta(\omega - E_{\mathbf{k}}/\hbar) \\ B(\omega, \mathbf{k}) &= \sum_n |\langle \Psi_n | b_{\mathbf{k}} | 0 \rangle_\beta|^2 \delta(\omega - \omega_n) = v_{\mathbf{k}}^2 \delta(\omega - E_{\mathbf{k}}/\hbar). \end{aligned} \tag{4.15}$$

Then the Green's function reads:

$$G_B(\omega, \mathbf{k}) = \frac{u_{\mathbf{k}}^2}{\omega - E_{\mathbf{k}}/\hbar + i0^+} - \frac{v_{\mathbf{k}}^2}{\omega + E_{\mathbf{k}}/\hbar - i0^+}. \tag{4.16}$$

Since the Bogoliubov Hamiltonian Eq. (4.14) does not commute with the number operator $N_B = N_0 + \sum_{\mathbf{k}} b_{\mathbf{k}}^\dagger b_{\mathbf{k}}$, the number of bosons is not conserved in this approach.

Note that in principle this allows for non-trivial *anomalous* propagators of the type $G_{\downarrow\downarrow} = \langle \Psi_0 | \mathbf{T}\left[b_{\mathbf{x}}(t) b_{\mathbf{y}}(s)\right] | \Psi_0 \rangle$ and $G_{\uparrow\uparrow} = \langle \Psi_0 | \mathbf{T}\left[b_{\mathbf{x}}^\dagger(t) b_{\mathbf{y}}^\dagger(s)\right] | \Psi_0 \rangle$ as depicted in Fig. 4.1. They can play an important role in describing interacting ensembles. However they play no role in the $\mathcal{T}$-matrix approximation and its extended variant discussed in sections 4.2 and 4.4, as such they will not be discussed further here.

4.1.3 Green's function of an impurity in a weakly repulsive condensate

The impurity problem consists of a single particle of species I with mass m_I, the impurity, with associated operators $\hat{c}^\dagger, \hat{c}$, immersed in a weakly repulsive Bose condensate of bosonic species B, as discussed in the previous subsection, interacting

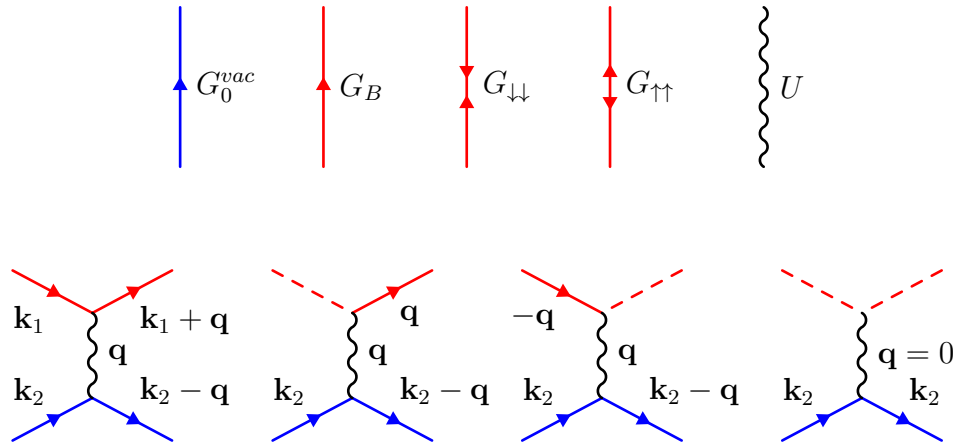

Figure 4.1: The four possible interaction nodes (**bottom row**) in Feynman diagrams, generated by the terms in Eq. (4.18). All nodes conserve four momenta $(\omega, \mathbf{k})$ between incoming and outgoing lines (depicted only for momenta for visual clarity). They are connected via the interaction and various propagators (**top row**) for the impurity (blue) and the bosons (red). The dashed lines represent the factor $\sqrt{n_0}$ appearing in terms in Eq. (4.18), connecting to bosons in the condensate mode. The two right most propagators are the anomalous propagators mentioned just below Eq. (4.16). Within the $\mathcal{T}$-matrix approximations discussed in this chapter, no diagrams including anomalous propagators are included however.

through a short range potential U:

$$\hat{H} = \underbrace{\sum_{\mathbf{k}} \frac{\hbar^2 k^2}{2m_I} \hat{c}^\dagger_{\mathbf{k}} \hat{c}_{\mathbf{k}}}_{\hat{H}_I} + \hat{H}_{Bog} + \underbrace{\frac{1}{V} \sum_{k_1,k_2,q} \hat{b}^\dagger_{\mathbf{k}_1+\mathbf{q}} \hat{c}^\dagger_{\mathbf{k}_2-\mathbf{q}} U(\mathbf{q}) \hat{b}_{\mathbf{k}_1} \hat{c}_{\mathbf{k}_2}}_{H_{\text{Int}}}, \tag{4.17}$$

where $U(\mathbf{q})$ is the potential in Fourier space. Note that the interaction term actually decomposes into four distinct terms when inserting the Bogoliubov approximation $\hat{b}^\dagger_0, \hat{b}_0 \to N_0^{1/2}$:

$$\begin{aligned} \hat{H}_{\text{Int}} =& \frac{1}{V} \sum_{\mathbf{k}_2,\mathbf{k}_1+\mathbf{q}\neq 0,\mathbf{k}_1\neq 0} \hat{b}^\dagger_{\mathbf{k}_1+\mathbf{q}} \hat{c}^\dagger_{\mathbf{k}_2-\mathbf{q}} U(\mathbf{q}) \hat{b}_{\mathbf{k}_1} \hat{c}_{\mathbf{k}_2} + \frac{\sqrt{n_0}}{\sqrt{V}} \sum_{\mathbf{k}_2,\mathbf{q}\neq 0} \hat{b}^\dagger_{\mathbf{q}} \hat{c}^\dagger_{\mathbf{k}_2-\mathbf{q}} U(\mathbf{q}) \hat{c}_{\mathbf{k}_2} \\ &+ \frac{\sqrt{n_0}}{\sqrt{V}} \sum_{\mathbf{k}_2,\mathbf{q}\neq 0} \hat{c}^\dagger_{\mathbf{k}_2-\mathbf{q}} U(\mathbf{q}) \hat{b}_{-\mathbf{q}} \hat{c}_{\mathbf{k}_2} \quad + \quad n_0 U(0) \sum_{\mathbf{k}_2} \hat{c}^\dagger_{\mathbf{k}_2} \hat{c}_{\mathbf{k}_2}. \end{aligned} \tag{4.18}$$

We are interested in the energy spectrum of this interacting ensemble. It can be accessed via the spectral function of the impurity Green's function: Consider a ground state $|\Psi_0\rangle$, containing exactly $N_I = 0$ impurities and N_B bosons on average. The associated Green's function for the impurity has the spectral representation

$$G_I(\omega, \mathbf{k}) = \int d\omega' \frac{A(\omega', \mathbf{k})}{\omega - \omega' + i0^+} \quad , \quad A(\omega, \mathbf{k}) = \sum_n |\langle \Psi_n | \hat{c}^\dagger_{\mathbf{k}} | \Psi_0 \rangle|^2 \delta(\omega - \omega_n), \tag{4.19}$$

since the second spectral function B in Eq. (4.7) must vanish due to $|\Psi_0\rangle$ containing no impurities. Since $\Im\{1/(x - i0^+)\} \to \pi\delta(x)$ in the distributional sense for x real,

the impurity spectral function is proportional to the imaginary part of the Green's function

$$A(\omega, \mathbf{k}) = -\frac{\Im\{G_I(\omega, \mathbf{k})\}}{\pi}. \tag{4.20}$$

Green's functions are commonly used because the interacting system can be related to non-interacting Green's functions via a convenient perturbative expansion in terms of $\hat{H}_{\text{Int}}$ in Eq. (4.17). A detailed discussion of this expansion and the associated Wick's theorem is beyond the scope of this thesis, but can be found for example in [100] for a single species. Here we simply recollect the most important results for the particular case of the impurity problem as a reference for the calculations following in this chapter.

The impurity Green's function for the interacting system can be given via the *Dyson equation*:

$$G_I(\omega, \mathbf{k})^{-1} = G_0^{vac}(\omega, \mathbf{k})^{-1} - \Sigma(\omega, \mathbf{k}), \tag{4.21}$$

where G_0 is the vacuum propagator for the impurity, Eq. (4.6) which is now and in the following always assumed to be with $m = m_I$. We refer to Σ as the impurity *self energy*, even though it is a frequency. It can formally described by a perturbative series in terms represented by *Feynman diagrams*:

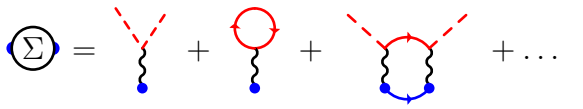

(4.22)

The diagrams are generated and translated into mathematical expressions given by the following rules:

- Each term in the expansion is presented by a single, topologically distinct diagram.
- Diagrams are generated by connecting every possible combination of nodes with the allowed propagators for each node, as is summarized in Fig. 4.1, such that two connecting legs for the impurity propagator (blue) remain. These are represented as blue dots in Eq. (4.22) and in following graphical depictions.
- Diagrams must be *irreducible*: upon cutting any single propagator line from the diagram, the whole diagram stays connected.
- Each propagator line represents the associated Green's function $G(\omega, \mathbf{k})$ as a simple multiplicative factor. Correspondingly, each interaction line represents a factor $U(\mathbf{q})/\hbar$. At all nodes, four momenta of incoming and outgoing lines (indicated by arrows), are conserved. The dashed lines represent bosons in the quasi-classical condensate mode with a simple factor $\sqrt{n_0}$, and have an associated four momentum of zero.
- All independent internal four momenta of a diagram are integrated over via $\int d\omega \; d^3k/(2\pi)^4$.

The single terms or diagrams can be thought of as the energy contribution due to different scattering processes depicted by the diagrams. For example the first and the second diagram depicted explicitly on the right side of Eq. (4.22) represent the mean-field energy shift in Born approximation the impurity experiences due to bosons in- and out-of-the-condensate respectively.

The expansion in Eq. (4.22) is formally exact, however its radius of convergence is not obvious. In practice calculations can only be performed by assuming an ordering of diagrams leading to an asymptotically convergent series, or by approximating the series in Eq. (4.22) by considering only a certain subset of diagrams.

4.2 Zero temperature $\mathcal{T}$-matrix

The $\mathcal{T}$-matrix- or *ladder* diagrams are one such classical approach to approximate the series in Eq. (4.22). It was first discussed in the context of relativistic quantum field theory in [101] and has hence been applied to many different areas, including the many-body context. Crucial is the so-called $\mathcal{T}$-matrix, a generalized interaction node described by an infinite series of four-legged diagrams

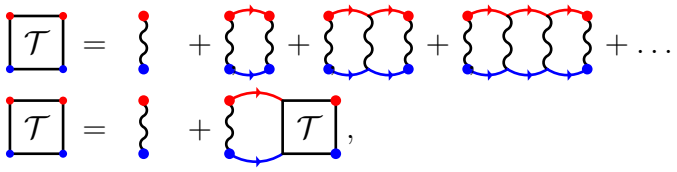

(4.23)

where the second line is an often-used implicit definition analogous to the ladder approximation in the *Bethe-Salpeter equation*. The $n-$th term in the series can be thought of as an n-times repeated scattering process between the impurity and one particular boson, involving intermediate states in different $\mathbf{k}$ modes. An approximate impurity self energy can then be generated by closing the bosonic legs of the $\mathcal{T}$-matrix:

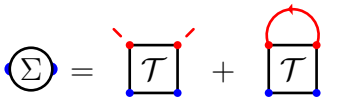

(4.24)

The first (second) term in Eq. (4.24) represent the energy contribution due to repeated scattering with a single boson from the condensate mode (out-of-condensate modes). The $\mathcal{T}$-matrix neglects processes involving more than two particles, which are expected to scale with higher powers of the Bose density n_0. As such it is a natural approximation for *dilute* atomic vapors with n_0 small. Note however that these higher order terms might still contribute significantly or even dominantly in special cases, unlike in the Fermi analogue, where such processes are strongly suppressed due to Pauli blocking. This feature is at the core of the work discussed in chapter 5.

The infinite series in Eq. (4.23) involves arbitrary powers of the potential $U(q)$, hence the self energy Eq. (4.24) can picture strong interaction effects. Above all, the series in Eq. (4.23) can be summed up analytically for the right choice of $U(\mathbf{q})$, as we shall briefly show in the following, making calculations with the $\mathcal{T}$-matrix practically feasible.

As discussed in chapter 2, in the context of cold and dilute gases the most important aspect of the interaction potential $U(\mathbf{q})$ are its low-$\mathbf{k}$ scattering properties,

encapsulated by the s-wave scattering length a, while the microscopic details of $U(\mathbf{q})$ are not important. As such, a particularly convenient choice is the zero-range model Eq. (2.35) simply giving:

$$U(\mathbf{q}) = g, \tag{4.25}$$

as long as $\mathbf{q} \leq \Lambda$, with Λ the necessary cut-off discussed above Eq. (2.46). With this simple model potential, the $\mathcal{T}$-matrix diagrams in Eq. (4.23) all become dependent on the total 4-momentum $\Omega, \mathbf{q}$ of both particles. Further, each term in Eq. (4.23) becomes factorisable, yielding:

$$\mathcal{T}(\Omega, \mathbf{q}) = \frac{g}{\hbar} \sum_{n=0}^{\infty} \left(\underbrace{\frac{g}{\hbar} \int_{k \leq \Lambda} \frac{d^3k \; d\omega}{(2\pi)^4} G_0^{vac}(\omega, \mathbf{k}) G_B(\Omega - \omega, \mathbf{q} - \mathbf{k})}_{= \tilde{\Pi}_\Lambda(\Omega, \mathbf{q})} \right)^n, \tag{4.26}$$

where the bracketed integral is called the bare pair propagator $\tilde{\Pi}_\Lambda$, with G_0 and G_B defined by Eqs. (4.6) and (4.16) respectively. Note that it becomes divergent in the limit $\Lambda \to \infty$, since the integrand scales only as $\sim -2m_r/(\hbar k)^2$ for large k. The geometric series in Eq. (4.26) can be summed analytically

$$\mathcal{T}(\Omega, \mathbf{q}) = \frac{1}{(g/\hbar)^{-1} - \tilde{\Pi}_\Lambda(\Omega, \mathbf{q})}. \tag{4.27}$$

We can regularize the cut-off dependence by inserting the relation Eq. (2.46) and rearranging Eq. (4.27)

$$\mathcal{T}(\Omega, \mathbf{q})^{-1} = \mathcal{T}_v^{-1} - \Pi_\Lambda(\Omega, \mathbf{q}), \tag{4.28}$$

where $\mathcal{T}_v = 2\pi\hbar^2 a/m_r$ and the last term in Eq. (2.46) is now included in the modified pair propagator Π_Λ. Note that this term exactly cancels the divergence of the bare pair propagator for large k, such the limit $\Lambda \to 0$ can be safely taken. The resulting regularized pair propagator will be simply called $\Pi(\Omega, \mathbf{q})$ in the following:

$$\begin{aligned} \Pi(\Omega, \mathbf{q}) &= \int \frac{d^3k}{(2\pi)^3} \left(\int \frac{d\omega}{2\pi} G_0^{vac}(\omega, \mathbf{k}) G_B(\Omega - \omega, \mathbf{q} - \mathbf{k}) + \frac{2m_r}{\hbar k^2} \right), \\ &= \int \frac{d^3k}{(2\pi)^3} \left(\frac{u_{\mathbf{k}}^2}{\Omega - \omega_{\mathbf{k}+\mathbf{q}} - E_{\mathbf{k}}/\hbar + i0^+} + \frac{2m_r}{\hbar k^2} \right) \end{aligned} \tag{4.29}$$

Remarkably, the integrals in Eq. (4.29) can be performed analytically in terms of the roots of a 4th order polynomial, as was first described in [5]. A step-by-step derivation following this approach is presented in Appendix A.1. Given the $\mathcal{T}$-matrix, the two diagrams in Eq. (4.24) translate as

$$\Sigma(\Omega, \mathbf{q}) = n_0 \mathcal{T}(\Omega, \mathbf{q}) + \int \frac{d^3k \; d\omega}{(2\pi)^4} \mathcal{T}(\omega, \mathbf{k}) G_B(\Omega + \omega, \mathbf{q} + \mathbf{k}) \tag{4.30}$$

However, for typically small na_B^3, the number of out-of-condensate bosons is very small and correspondingly the contribution of the second term in Eq. (4.30) can be

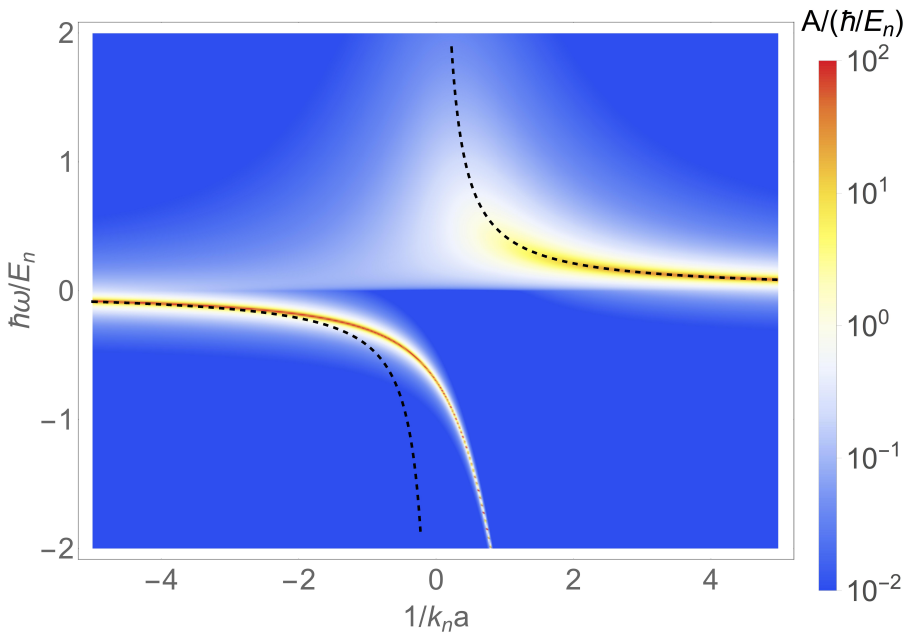

Figure 4.2: The spectral function $A(\omega, \mathbf{k} = 0)$ of the impurity, with the self energy given by Eq. (4.30), with respect to the energy $\hbar\omega/E_n$ and the interaction strength $1/k_n a$, for $m_I = m_B$ and $k_n a_B = 0.01$. For clarity, we have added an artificial tiny width of $0.01E_n$ to the spectral lines. Two branches of high spectral density can be distinguished, at positive and negative energies respectively. At small $|k_n a|$ these branches both converge to the first order result given by Eq. (4.32), depicted as a black dashed line

neglected in comparison to the first term as a first approximation. By using the Dyson equation Eq. (4.21) with the first term in Eq. (4.30)

$$G_I(\omega, \mathbf{k}) = \frac{1}{\omega - \omega_{\mathbf{k}} - n_0 \mathcal{T}(\omega, \mathbf{k}) + i0^+}. \tag{4.31}$$

For small $|n_0 a^3|$, the $\mathcal{T}$-matrix can be expanded to first order in a to give $\mathcal{T} \to \mathcal{T}_v$ and the corresponding mean-field self energy $n_0 \mathcal{T}_v$, a real number independent of ω, with the corresponding spectral function.

$$A_{I,0}(\omega, \mathbf{k}) = \delta(\omega - \omega_{\mathbf{k}} - n_0 \mathcal{T}_v). \tag{4.32}$$

In this mean-field regime, the interacting impurity behaves simply as a free impurity with energies shifted by the mean-field term $n_0 \mathcal{T}_v$. For stronger interactions, the pair-propagator starts to play a role in the self energy, leading to a finite imaginary part and a corresponding broadening of the spectrum. In Fig. 4.2, a numerical evaluation of the spectral function via Eq. (4.20) is presented, with respect to different interaction strengths $k_n a$ and an impurity at rest $\mathbf{k} = 0$.

Even beyond the validity of the approximation Eq. (4.32), the spectral function remains strongly peaked around a certain frequency for a given $k_n a$, and in the unitary regime both branches seem to exist simultaneously. This justifies the application of the well-known *quasiparticle* concept, as discussed for example in [102] in the context of propagators and spectral functions.

For any fixed $\mathbf{k}$, in regions of the spectrum with a single well defined peak the spectrum can be locally approximated by a Cauchy-distribution. This corresponds to an interacting Green's function locally taking the form of a modified *vacuum* Green's function as in Eq. (4.6), shifted by a generally complex frequency

$$G_I \approx \frac{Z_0}{\omega - \omega_0 + i\gamma_0} \quad \text{for} \quad \omega \sim \omega_0. \tag{4.33}$$

Here ω_0 is the center location of the Cauchy-curve and γ_0 the width, with Z_0 a scaling factor. Physically, this means that the system supports a meta-stable state with eigenfrequency ω_0 and an inverse lifetime γ_0. Z_0 is the overlap squared between this state and the state $\hat{c}^\dagger_{\mathbf{k}}|\Psi_0\rangle$. For a set of several quasiparticle branches, this process repeats for each nth branch present and the entire Green's function can be decomposed as

$$G_I(\omega, \mathbf{k}) = \sum_j \frac{Z_j(\mathbf{k})}{\omega - \omega_j(\mathbf{k}) + i\gamma_j(\mathbf{k})} + \int d\omega' \frac{A^*(\omega', \mathbf{k})}{\omega - \omega' + i0^+}, \tag{4.34}$$

where the auxiliary spectral function A^* is chosen such that it vanishes at the quasi-particle peaks ω_j. When the imaginary part of Σ is small compared to its real part in a given region, the quasi particle properties can be found to good approximation by finding the root

$$\omega_j(\mathbf{k}) = \omega_{\mathbf{k}} + \Re\{\Sigma(\omega_j(\mathbf{k}), \mathbf{k})\}, \tag{4.35}$$

giving correspondingly

$$Z_j(\mathbf{k}) = \frac{1}{1 - \partial_\omega \Re\{\Sigma(\omega, \mathbf{k})\}|_{\omega=\omega_j(\mathbf{k})}} \quad , \quad \gamma_j(\mathbf{k}) = -2Z_j(\mathbf{k})\Im\{\Sigma(\omega_j(\mathbf{k}), \mathbf{k})\}, \tag{4.36}$$

for the residue and inverse lifetime. This is consistent as long as $|\omega_{j,k}| >> \gamma_{j,k}$.

In the case of the Bose polaron within the $\mathcal{T}$-matrix approximation, clearly two quasi-particle branches can be distinguished from Fig. 4.2. They are referenced as the 'attractive' ('repulsive') polaron branch, given their negative (positive) energy shift and their correspondence to an attractive (repulsive) impurity-Bose interaction far away from the Feshbach-resonance. This picture resembles closely the one elaborated in the case of the previously discussed Fermi polaron, which is by now experimentally and theoretically well understood [84, 86]. While the repulsive polaron washes out close to resonance, the attractive polaron crosses over to the universal bound state associated to the resonance, indicated by its energy converging to the universal bound state energy Eq. (2.25) and the overlap with a free wave Z_- vanishing for increasingly off-resonance values.

In principle, the previous discussion of the spectral function at $\mathbf{k} = 0$ can be repeated for finite $\mathbf{k}$ as well. An analysis of the $\mathbf{k}$ dependency of the spectrum and related concepts such as the effective mass of the polarons are of great importance. A discussion of the effective mass as well as the effect of the second term in Eq. (4.30) and also the more elaborate self-consistent $\mathcal{T}$-matrix approach are discussed in [5]. However the focus of this work, as is discussed in the next section, was the effect of finite temperature, and for this purpose we choose to focus first on the fundamental case of quasi-particle properties at rest.

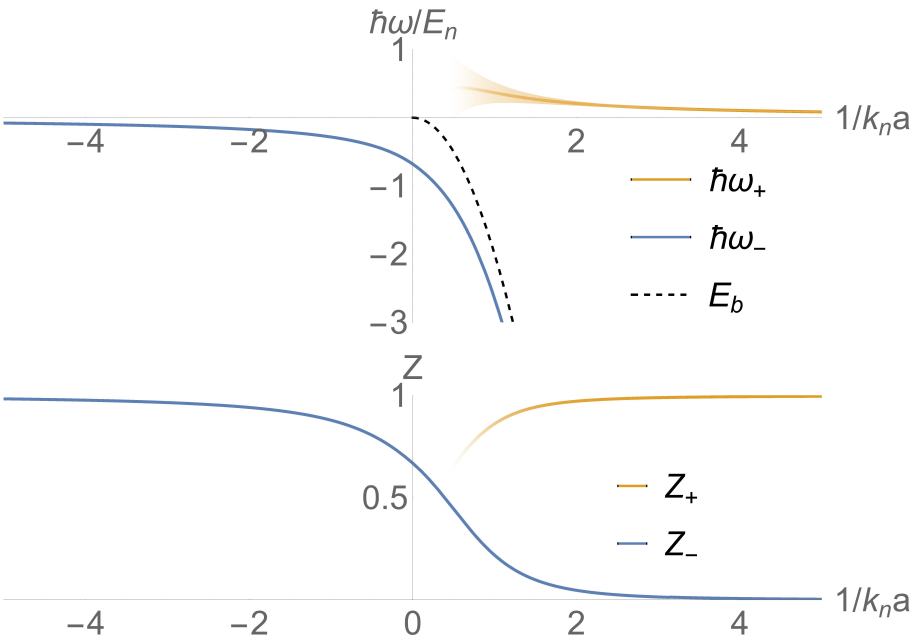

Figure 4.3: Polaron energy and residue given by Eqs. (4.35) and (4.36), for $\mathbf{k} = 0$. The broadening of the repulsive ω_+ peak, given by the inverse lifetime γ_+ and indicated by shading, becomes comparable to ω_+ for $k_n a \sim 1$, and the quasi-particle picture looses its validity. The attractive ω_- branch has a negligible inverse lifetime across the entire resonance, and it converges to the molecular state E_b defined in Eq. (2.25) for small positive $k_n a$.

4.3 Thermal Green's functions

A powerful feature of the diagrammatic approach to Green's functions is that it can be quite easily extended to thermal quantum ensembles. As in section 4.1, we shall quickly review the features of finite temperature Green's functions most relevant to us, again a detailed and comprehensive discussion can be found in [102].

4.3.1 Real- and imaginary time thermal Green's functions

In section 4.1.1, the Green's function with respect to the groundstate was discussed, and how it can be used to extract the relevant excitation spectrum of the impurity at $T = 0$. Correspondingly, at finite temperature the Green's function must be extended to the thermal ensemble average. It is more convenient to work in the grand canonical ensemble. For enhanced readability and brevity, we introduce the grand canonical Hamiltonian simply through the implicit substitution $\hat{H} \to \hat{H} - \mu\hat{N}$, where now the chemical potential μ is fixed instead of N. It is useful to introduce the density matrix:

$$\hat{\rho} = \frac{1}{\mathcal{Z}} e^{-\beta \hat{H}}, \tag{4.37}$$

$$\mathcal{Z} = \mathrm{Tr}\{e^{-\beta \hat{H}}\}, \tag{4.38}$$

where $\beta = 1/k_B T$ is the inverse temperature and $\mathrm{Tr}\{\ \}$ denotes the trace. Then one can define the thermal Greens' function as

$$\begin{aligned} iG_{\mathbf{x}-\mathbf{y}}(t-s) =& -i\mathrm{Tr}\{\hat{\rho}\mathbf{T}\left[\hat{a}_{\mathbf{x}}(t)\hat{a}_{\mathbf{y}}(s)^\dagger\right]\}, \\ =& \sum_n \frac{-ie^{-\beta E_n}}{\mathcal{Z}} \langle\Psi_n|\mathbf{T}\left[\hat{a}_{\mathbf{x}}(t)\hat{a}_{\mathbf{y}}(s)^\dagger\right]|\Psi_n\rangle, \end{aligned} \tag{4.39}$$

where we assumed translational and temporal invariance immediately to reduce the number of independent arguments of $\mathcal{G}$. The second line, the trace in the eigenbasis $|\Psi_n\rangle$ of $\hat{H}$, makes clear that the thermal Green's function is just a weighted average of Green's functions with respect to a single state, as discussed in section 4.1. Correspondingly, the entire preceding analysis applies term by term in Eq. (4.39), where $|\Psi_0\rangle$ must be replaced with $|\Psi_n\rangle$ when appropriate. In particular the Lehmann representation Eq. (4.5) applies term by term, giving

$$\begin{aligned} G(\omega,\mathbf{k}) =& \sum_{n,m} \frac{e^{-\beta E_n}}{\mathcal{Z}} \left(\frac{|\langle\Psi_m|\hat{a}^\dagger_{\mathbf{k}}|\Psi_n\rangle|^2}{\omega - (E_m - E_n)/\hbar + i0^+} \mp \frac{|\langle\Psi_m|\hat{a}_{\mathbf{k}}|\Psi_n\rangle|^2}{\omega + (E_m - E_n)/\hbar - i0^+} \right) \\ =& \sum_{n,m} \frac{|\langle\Psi_m|\hat{a}^\dagger_{\mathbf{k}}|\Psi_n\rangle|^2}{\mathcal{Z}} \left(\frac{e^{-\beta E_n}}{\omega - (E_m - E_n)/\hbar + i0^+} \mp \frac{e^{-\beta E_m}}{\omega - (E_m - E_n)/\hbar - i0^+} \right), \end{aligned} \tag{4.40}$$

where the second line results from a reordering of indices possible since N is no longer held fixed. In an analogous fashion to the discussion before Eq. (4.7), the overlaps in the first (second) term in Eq. (4.40) are only non-vanishing if the $|\Psi_m\rangle$ contain one more particle then $|\Psi_n\rangle$, such that we can write $E_m - E_n = \hbar\omega_{mn} + \mu$, with ω_{mn} the transition frequency between states. It is convenient to define the thermal spectral function as

$$A(\omega,\mathbf{k}) = \sum_{n,m} \frac{e^{-\beta E_n}}{\mathcal{Z}} |\langle\Psi_m|\hat{a}^\dagger_{\mathbf{k}}|\Psi_n\rangle|^2 \left(1 \mp e^{-\beta\hbar\omega}\right) \delta(\omega - \omega_{mn} + \mu/\hbar), \tag{4.41}$$

which corresponds to the spectral representation

$$G(\omega,\mathbf{k}) = \int d\omega' \left(\frac{1}{1 \mp e^{-\beta\hbar\omega'}} \frac{A(\beta,\omega',\mathbf{k})}{\omega - \omega' + i0^+} + \frac{1}{1 \mp e^{\beta\hbar\omega'}} \frac{A(\beta,\omega',\mathbf{k})}{\omega - \omega' - i0^+} \right), \tag{4.42}$$

of the Green's function. The spectral function $A(\omega,\mathbf{k})$ can be interpreted similarly to the $T = 0$ case in the first line of Eq. (4.7), but with respect to the thermal average and not the ground state. Unfortunately however, there is not a straight-forward way to compute the real-time thermal Green's function in interacting systems.

This is why 'imaginary-time' Green's functions, as discussed below, are of fundamental importance. These propagators can be used to access the spectral distribution A in Eq. (4.41) as well, and there exists a way to practically compute it in the interacting case via a series of Feynman diagrams, as discussed later in section 4.3.3.

Inspired by proper time-evolved operators, one can define the two operators

$$\begin{aligned} \hat{a}_{\mathbf{k}}(\tau) =& e^{\tau\hat{H}/\hbar}\hat{a}_{\mathbf{k}}e^{-\tau\hat{H}/\hbar} \\ \hat{a}_{\mathbf{k}}(\tau)^\dagger =& e^{\tau\hat{H}/\hbar}\hat{a}^\dagger_{\mathbf{k}}e^{-\tau\hat{H}/\hbar}, \end{aligned} \tag{4.43}$$

which are only *true* adjoints when $\tau = it$ is purely imaginary, we will assume however that τ is real, often referred to as 'imaginary time'. We can define an analogue to the thermal Green's function in imaginary time by writing:

$$\mathcal{G}_{\mathbf{x}-\mathbf{y}}(\tau - \sigma) = -\operatorname{Tr}\{\hat{\rho}\mathbf{T}\left[\hat{a}_{\mathbf{x}}(\tau)\hat{a}_{\mathbf{y}}(\sigma)^{\dagger}\right]\}, \tag{4.44}$$

where $\mathbf{T}$ orders the operators from left to right in descending imaginary time, and again temporal and translational invariance was assumed. For τ real, the imaginary time-evolution operator closely resembles the density matrix $\sim \exp(-\beta\hat{H})$ and it can be shown that this results in the Green's function being (anti-)periodic in τ with period $\beta\hbar$

$$\mathcal{G}_{\mathbf{x}}(\tau) = \pm\mathcal{G}_{\mathbf{x}}(\tau + \beta\hbar) \tag{4.45}$$

for bosonic (fermionic) operators. One can thus show that $\mathcal{G}$ can be described by discrete Fourier coefficients:

$$\mathcal{G}_{\mathbf{x}}(\tau) = \frac{1}{\beta\hbar}\sum_{n} e^{-i\omega_n\tau}\mathcal{G}_{\mathbf{x}}(i\omega_n), \tag{4.46}$$

$$\mathcal{G}_{\mathbf{x}}(i\omega_n) = \int_0^{\beta\hbar} d\tau e^{i\omega_n\tau}\mathcal{G}_{\mathbf{x}}(\tau). \tag{4.47}$$

Here $\omega_n = n\pi/\beta\hbar$ are the Matsubara frequencies, where

$$\begin{cases} n \text{ even} & \text{for bosons} \\ n \text{ odd} & \text{for fermions} \end{cases}. \tag{4.48}$$

The imaginary-time Green's function is useful because it has a Lehmann representation closely related to the real-time equivalent:

$$\mathcal{G}(i\omega_n, \mathbf{k}) = \sum_{m,n} \frac{|\langle\Psi_m|\hat{a}^{\dagger}_{\mathbf{k}}|\Psi_n\rangle|^2}{\mathcal{Z}} \frac{e^{-\beta E_n} \mp e^{-\beta E_m}}{i\omega_n - (E_m - E_n)/\hbar}, \tag{4.49}$$

and $\mathcal{G}$ can be reconstructed with the *same* spectral data as the real-time spectral function

$$\mathcal{G}(i\omega_n, \mathbf{k}) = \int d\omega' \frac{A(\omega', \mathbf{k})}{i\omega_n - \omega'}. \tag{4.50}$$

For completely non-interacting systems, $\mathcal{G}$ can be calculated by straight forward algebra to be

$$\mathcal{G}_0^{vac}(i\omega_n, \mathbf{k}) = \frac{1}{i\omega_n - \omega_{\mathbf{k}} + \mu/\hbar}, \tag{4.51}$$

for both fermions and bosons. In contrast to the real-time Green's function, there *does* exist a convenient way to compute $\mathcal{G}$ for interacting systems via a diagrammatic expansion from the non-interacting case. As before however, the condensed weakly interacting Bose gas needs careful treatment, discussed in the next section.

4.3.2 Green's function of a weakly interacting condensate at finite temperatures

The treatment of the Bose propagators in section 4.1.2 needs to be revisited with care at finite temperature, since in the substitution $\hat{b}_0^\dagger, \hat{b}_0 \to \sqrt{n_0}$ of the Bogoliubov approximation, the condensate fraction n_0 itself will depend on temperature. In a zero-order approximation, we describe the condensate fraction n_0 in terms of the temperature dependence of an ideal Bose gas

$$n_0(T) = n\left(1 - \left(\frac{T}{T_C}\right)^{3/2}\right), \tag{4.52}$$

where n is the overall density of bosons and $T_C = [4/(3\sqrt{\pi}\zeta(3/2))]^{2/3} E_n/k_B$ is the critical temperature. Any corrections to Eq. (4.52) in terms of $k_n a_B$ beyond the ideal result are subject to a longstanding scientific debate and will not be considered further here. Nonetheless in the regime where $k_n a_B \ll 1$, Eq. (4.52) should be a very good approximation as long as $T \ll T_C$, when the out-of-condensate fraction due to interactions in the Bogoliubov Hamiltonian is still much smaller than the thermal depletion. With the condensate fraction set, $\mathcal{G}_B$ can be calculated using Eqs. (4.12),(4.14) as well as $\mathrm{Tr}\{\hat{\rho}\hat{\beta}_{\mathbf{k}}^\dagger\hat{\beta}_{\mathbf{k}}\} = 1/(e^{\beta E_{\mathbf{k}}} - 1)$ directly in Eqs. (4.44) and (4.47):

$$\mathcal{G}_B(i\omega_n, \mathbf{k}) = \frac{u_{\mathbf{k}}^2}{i\omega_n - E_{\mathbf{k}}/\hbar} - \frac{v_{\mathbf{k}}^2}{i\omega_n + E_{\mathbf{k}}/\hbar}, \tag{4.53}$$

where the coherence factors as well as the dispersion relation

$$\begin{aligned} u_{\mathbf{k}}^2 - v_{\mathbf{k}}^2 = 1 \quad &, \quad u_{\mathbf{k}}^2 = \frac{1}{2}\left(\frac{\epsilon_{\mathbf{k}} + \mu_B}{E_{\mathbf{k}}} + 1\right) \\ \mu_B = n_0(T)\frac{\hbar^2 4\pi a_B}{m_B} \quad &, \quad E_{\mathbf{k}} = \sqrt{\epsilon_{\mathbf{k}}(\epsilon_{\mathbf{k}} + 2\mu_B)}. \end{aligned} \tag{4.54}$$

are now explicitly temperature dependent. Above T_c the condensate disappears, the excitations become free bosons, $E_{\mathbf{k}} = \epsilon_{\mathbf{k}}$, and the chemical potential reduces to that of an ideal Bose gas. Correspondingly $\mathcal{G}_B$ reduces to the Green's function of free bosons Eq. (4.51)

4.3.3 The impurity Green's function and Dyson equation

Since we are working in the grand canonical ensemble with a variable particle number, the case of a single impurity must be understood as the limit of vanishing density n_I of the impurity species, and hence $-\mu_I \to -\infty$ for both fermionic and bosonic impurities [1]. For practical purposes, we will consider $-\mu_I$ to be finite but larger than all other energy scales in the system, in particular $-\mu_I\beta \gg 1$.

An extended Wick's theorem can be derived for imaginary-time Green's functions and a diagrammatic expansion from the noninteracting system via the interaction

[1] For ideal bosons (fermions) in three dimensions , the overall density is $n_I = \int d^3k/(2\pi)^3(\exp[\beta(\hbar\omega_{\mathbf{k}} - \mu_I)] \mp 1)^{-1} = \pm(\hbar^2\beta/2m\pi)^{-3/2}\mathrm{Li}_{3/2}(\pm\exp[\beta\mu_I])$, where $\mathrm{Li}_s = \sum_{n=1}^{\infty} z^n/n^s$ is the polylogarithm of order s. In both cases, n_I vanishes for $\mu \to -\infty$

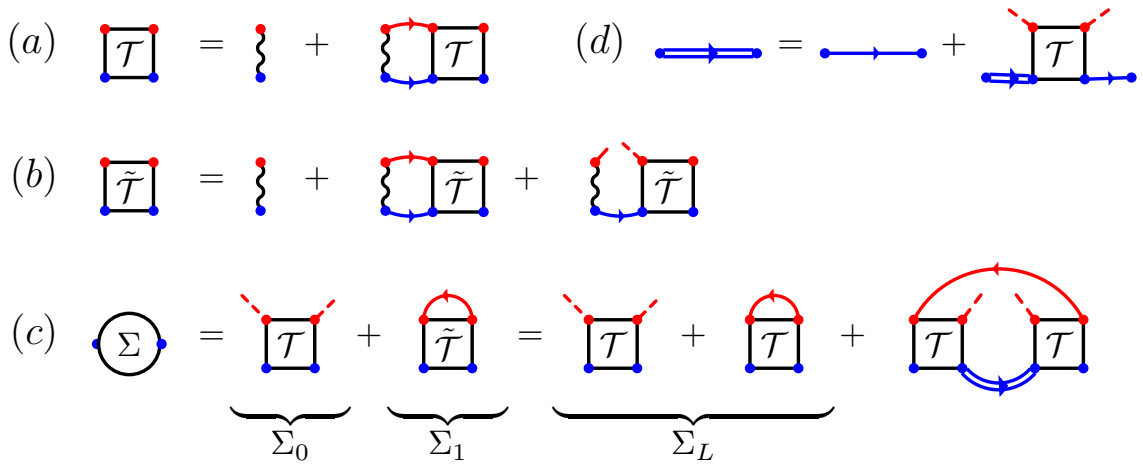

Figure 4.4: Feynman diagrams yielding the self energy Σ within the "extended" ladder approximation. Thin blue lines represent the bare impurity propagator, solid red lines are Bogoliubov propagators, dashed red lines are condensate bosons, and wavy lines represent the vacuum scattering matrix $\mathcal{T}_v$. The ladder self energy is indicated by Σ_L, and the double blue line is an impurity dressed by the condensate only.

Hamiltonian in Eq. (4.18) exists for $\mathcal{G}_I$. In fact, due to the similarity between the imaginary-time evolution $e^{-\tau\hat{H}/\hbar}$ and the thermal density matrix Eq. (4.37), this expansion has *exactly the same algebraic structure* as for the $T = 0$ Green's function. Thus a Dyson equation analogous to Eq. (4.21) holds in imaginary time:

$$\mathcal{G}_I(i\omega_n, \mathbf{k})^{-1} = \mathcal{G}_0^{vac}(i\omega_n, \mathbf{k})^{-1} - \mathbf{\Sigma}(i\omega_n, \mathbf{k}). \tag{4.55}$$

The thermal self energy $\mathbf{\Sigma}$ has the same expansion in Feynman diagrams as in Eq. (4.22), the Feynman rules are only slightly altered:

- replace G_0^{vac} with $\mathcal{G}_0^{vac}$ and G_B with $\mathcal{G}_B$
- replace integrals $\int d\omega/2\pi$ with Matsubara frequency sums $(\beta\hbar)^{-1}\sum_{\omega_n}$.

With this, the $\mathcal{T}$-matrix model can be extended to finite temperatures.

4.4 Finite temperature $\mathcal{T}$-matrix

Within the framework of thermal Green's functions discussed in the previous section, the $\mathcal{T}$-matrix model can be extended to finite temperatures below and above the transition temperature T_C, a work not done previously to my publication [2], which also forms the basis of this section.

Again, we will base our model of $\mathbf{\Sigma}$ on the $\mathcal{T}$-matrix. Using finite temperature Feynman rules and evaluating the Matsubara sums via contour integration, we find

the standard scattering matrix $\mathcal{T}(i\Omega_j, \mathbf{q}) = 1/\left[\mathcal{T}_v^{-1} - \mathbf{\Pi}(i\Omega_j, \mathbf{q})\right]$, where now

$$\begin{aligned}
&\mathbf{\Pi}(i\Omega_j, \mathbf{q}) \\
=&\int \frac{d^3k}{(2\pi)^3}\left(\frac{u_{\mathbf{k}}^2(1+f_{\mathbf{k}})}{i\Omega_j + \mu_I/\hbar - E_{\mathbf{k}}/\hbar - \omega_{\mathbf{k}+\mathbf{q}}} + \frac{v_{\mathbf{k}}^2 f_{\mathbf{k}}}{i\Omega_j + \mu_I/\hbar + E_{\mathbf{k}} - \omega_{\mathbf{k}+\mathbf{q}}} + \frac{2m_r}{k^2}\right), \\
=&\Pi(i\Omega_j, \mathbf{q}) + \int \frac{d^3k f_{\mathbf{k}}}{(2\pi)^3}\left(\frac{u_{\mathbf{k}}^2}{i\Omega_j + \mu_I/\hbar - E_{\mathbf{k}}/\hbar - \omega_{\mathbf{k}+\mathbf{q}}} + \frac{v_{\mathbf{k}}^2}{i\Omega_j + \mu_I/\hbar + E_{\mathbf{k}} - \omega_{\mathbf{k}+\mathbf{q}}}\right),
\end{aligned} \tag{4.56}$$

is the renormalized pair propagator at finite temperatures. Here $f_{\mathbf{k}} = 1/[\exp(\beta E_{\mathbf{k}}) - 1]$ is the Bose distribution, and the first term in the second line is exactly Eq. (4.29), but with the temperature dependent Bogoliubov dispersions Eqs. (4.54). The remaining integral in Eq. (4.56) needs to be computed numerically.

In the zero temperature case, we neglected the second term in Eq. (4.30), since only very few bosons are out-of-condensate due to interactions. At finite temperature this term becomes more important, since thermal depletion gives rise to a way larger out-of-condensate population. Additionally, a recent perturbative analysis [97] showed that events where the impurity scatters excited bosons into the BEC are important at finite temperatures. To include these events, which are not contained in the ladder approximation, we introduce the "extended" scattering matrix $\tilde{\mathcal{T}}$ shown in Fig. 4.4 (b), and given by

$$\tilde{\mathcal{T}}(i\Omega_j, \mathbf{q}) = \frac{1}{\mathcal{T}_v^{-1} - \mathbf{\Pi}(i\Omega_j, \mathbf{q}) - n_0 \mathcal{G}_0^{vac}(i\Omega_j, \mathbf{q})}. \tag{4.57}$$

Compared to the standard ladder approximation $\mathcal{T}$, graphically shown in Fig. 4.4 (a), the denominator of $\tilde{\mathcal{T}}$ contains the additional term $n_0\mathcal{G}_0^{vac}(i\Omega_j, \mathbf{q})$, which describes pair propagation where the entire momentum is carried by the impurity while the boson is in the condensate mode. This process is represented by the third term in Fig. 4.4 (b).

As shown in Fig. 4.4 (c), within the extended scheme the impurity self-energy is $\mathbf{\Sigma} = \mathbf{\Sigma}_0 + \mathbf{\Sigma}_1$, where

$$\mathbf{\Sigma}_0(i\Omega_j, \mathbf{q}) = n_0 \mathcal{T}(i\Omega_j, \mathbf{q}), \tag{4.58}$$

is the energy shift experienced by the impurity through interactions with the condensate only, and

$$\begin{aligned}
\mathbf{\Sigma}_1(i\Omega_j, \mathbf{q}) = \int \frac{d^3k}{(2\pi)^3}\Big[&u_{\mathbf{k}}^2 f_{\mathbf{k}} \tilde{\mathcal{T}}(i\Omega_j + E_{\mathbf{k}}/\hbar, \mathbf{k}+\mathbf{q}) \\
&+ v_{\mathbf{k}}^2(1+f_{\mathbf{k}})\tilde{\mathcal{T}}(i\Omega_j - E_{\mathbf{k}}/\hbar, \mathbf{k}+\mathbf{q})\Big],
\end{aligned} \tag{4.59}$$

is the energy shift coming from interactions with bosons excited out of the BEC. Note that replacing $\mathcal{T}$ with $\tilde{\mathcal{T}}$ in Σ_0 is not allowed, since this would lead to double counting of diagrams. As shown in Fig. 4.4 (c), Σ_1 may be decomposed in two contributions: one where the impurity scatters a boson from an excited state to another (second diagram), and one where the excited bosons are scattered virtually back into the BEC (last diagram). An approximation similar to ours was used in Ref. [103] for analyzing Bose-Fermi mixtures, while the ladder approximation Σ_L (considered at $T = 0$ in Ref. [5]) is recovered by replacing $\tilde{\mathcal{T}}$ with $\mathcal{T}$ in Eq. (4.59), which is equivalent to neglecting the rightmost diagram in Fig. 4.4 (c).

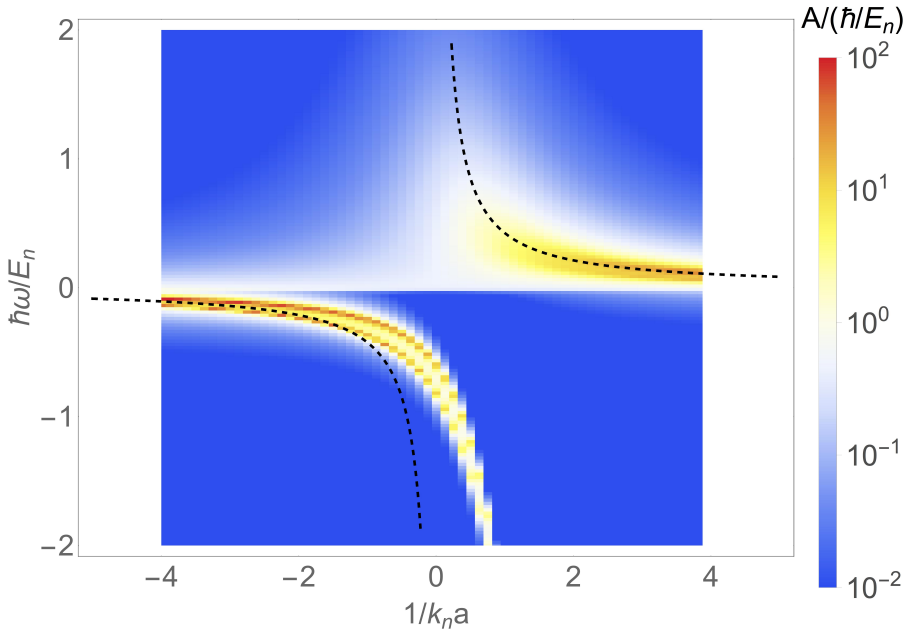

Figure 4.5: The spectral function $A(\omega, \mathbf{q} = 0)$ in Eq. (4.60), with the self energy terms given by Eqs. (4.58) and (4.59), with respect to the energy $\hbar\omega/E_n$ and the interaction strength $1/k_n a$ for $m_I = m_B$, $k_n a_B = 0.01$ and $T = 0.2T_C$. The black dashed line represents the zero temperature first order result $n_0\hbar^2 2\pi a/m_B$ for the polaron energy. The attractive polaron branch is now split into two branches for intermediate $k_n a$, however the two peaks eventually wash out for $k_n a \to 0^-$. The onset of splitting is discussed in more detail in Fig. 4.9 and the corresponding text.

4.4.1 Spectral function

Eqs. (4.58) and (4.59) are well defined not just for imaginary $i\Omega_j$, but actually for any complex number in the frequency argument. We can hence analytically continue $\Sigma(i\Omega_j, \mathbf{q})$ and, via the Dyson equation (4.55), $\mathcal{G}_I(i\Omega_j)$ in a unique fashion to the complex plane, $\mathcal{G}_I(i\Omega_j, \mathbf{q}) \to \mathcal{G}_I(z, \mathbf{q})$. Because of Eq. (4.50), we can find the spectral function through

$$A(\omega, \mathbf{q}) = -\Im\{\mathcal{G}_I(\omega - \mu_I/\hbar + i0^+, \mathbf{q})\}/\pi, \tag{4.60}$$

where we have chosen μ_I as the reference point of the energy scale. We now analyze the properties of the dressed impurity. For concreteness, we show results for $m_I = m_B$, corresponding to the impurity and the bosons being different spin states of the same atom as in the Aarhus experiment [87]. Having this experiment in mind, we also focus on zero momentum polarons and, unless otherwise specified, we set $k_n a_B = 0.01$. For small but finite temperature $T = 0.2T_C$, the spectral function is shown in Fig. 4.5. While the repulsive polaron branch is generally broadened compared to the $T = 0$ case depicted in Fig. 4.2, intriguingly the attractive branch is now split into two peaks instead of one. In the following, we will discuss the temperature dependence in more detail, separately for the original attractive and repulsive branches.

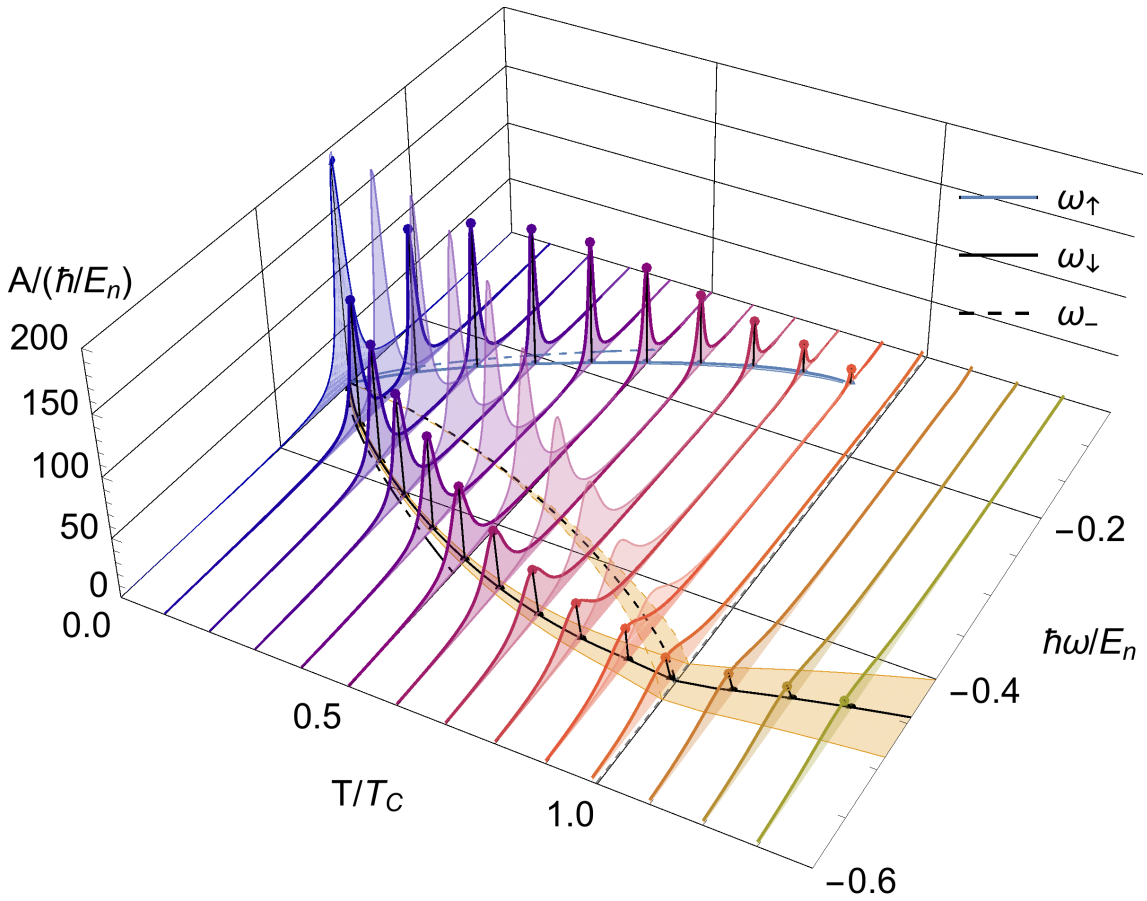

Figure 4.6: Spectral function $A(\omega, \mathbf{q} = 0)/(\hbar/E_n)$ versus T/T_C at $k_n a_B = 0.01$ and $k_n a = -1$, computed using the ladder approximation (dashed lines and lighter shading) and our extended model (thick lines and darker shading). For clarity, we have added an artificial tiny width of $0.01E_n$ to the spectral lines. The thick solid lines in the plane show the polaron energies, as given by Eq. (4.35), and the width of their shading gives the damping γ in Eq. (4.36). The dash-dotted lines are the low temperature result $\omega_0(1 \pm \sqrt{Z_0 n_{\rm ex}/n_0})$.

4.4.2 Attractive polaron and quasiparticle splitting

The impurity spectral function is shown in Fig. 4.6 as a function of temperature for $k_n a = -1$. The solid lines with dark shading are obtained from the extended scheme whereas the dashed lines with lighter shading are the ladder approximation. For $T = 0$, the two schemes give essentially the same result: The spectral function exhibits a single narrow peak corresponding to a quasiparticle, the attractive polaron, with energy $\omega \simeq -0.3E_n$. This is not surprising, since $k_n a_B = 0.01 \ll 1$ and very few bosons are excited out of the BEC at $T = 0$, so that Σ_1 is negligible in both the ladder and the extended scheme.

Significant differences between the two approximations appear however for $T > 0$. As shown in Fig. 4.6, while the spectral function in the ladder approximation exhibits a single polaron peak, corresponding to a single quasiparticle solution ω_- of Eq. (4.35), the extended approximation yields *two quasiparticle peaks* in the spectral function. Correspondingly, there are *two* quasiparticle (polaron) solutions to (4.35), $\omega_\uparrow$ and $\omega_\downarrow$. Just above $T = 0$, the two sharp polaron peaks emerge symmetrically

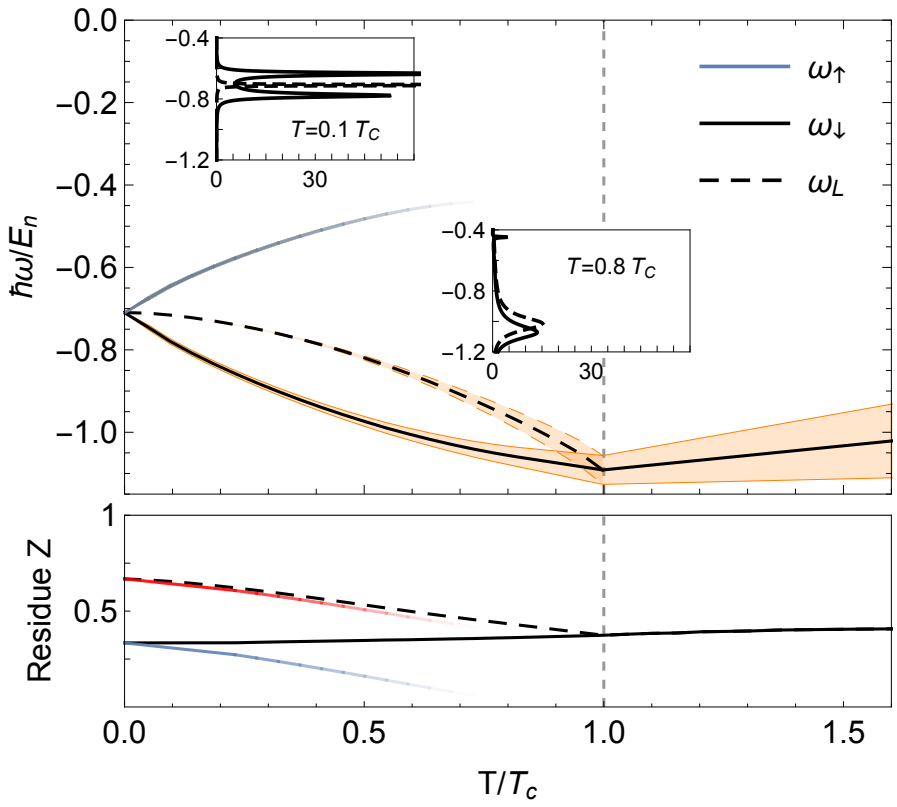

Figure 4.7: Energies (top) and residues (bottom) of the attractive polarons for $1/k_n a = 0$ in the ladder approximation (dashed line) and from our extended model (solid lines). The width of the shading around the energies gives the damping Γ. We stop plotting $\omega_\uparrow$ when its residue is below 5%. The insets depict the spectral function $A(\omega, \mathbf{k} = 0)$ at $T = 0.1T_c$ (left) and $T = 0.8T_c$ (right). The red line shows $Z_\uparrow + Z_\downarrow$.

out of the ladder polaron with similar spectral weight. In fact, their residues $Z_\uparrow$ and $Z_\downarrow$ are both close to $Z_-/2$. Both features can be explained by a pole expansion valid for $k_n a_B \ll 1$, discussed in Appendix A.2. For weak coupling, $\omega_{\uparrow,\downarrow} \simeq \omega_0(1 \pm \sqrt{Z_0 n_{\rm ex}/n_0})$, where $\omega_0 = n_0 \mathcal{T}_v$ is the energy of a zero momentum impurity dressed by the condensate only, $Z_0 = Z_-[T = 0]$, and $n_{\rm ex} = n - n_0(T)$ is the density of bosons excited out of the condensate thermally, as discussed in the Appendix A.2. The energy of the upper polaron $\omega_\uparrow$ increases with T, but its spectral weight drops to zero as T_C is approached. The energy of the lower polaron $\omega_\downarrow$ instead decreases with temperature, reaching a minimum at T_C, after which it increases. For $T \geq T_C$ there is no BEC, here the extended- and ladder approximation coincide. The width of the lower polaron peak increases with temperature reflecting increased damping due to the scattering on thermally excited bosons. Eventually, the polaron becomes ill-defined for $T \gg T_C$.

In Fig. 4.7, we show the quasiparticle spectrum and residues at unitarity $1/k_n a = 0$, obtained by solving (4.35). This shows the same physics as we found for $k_n a = -1$, but scaled to larger binding energies.

It is interesting to consider the fate of the polaron at very high temperatures $T \gg T_C$. Using a virial expansion to compute the self-energy for $T \gg T_c$, and

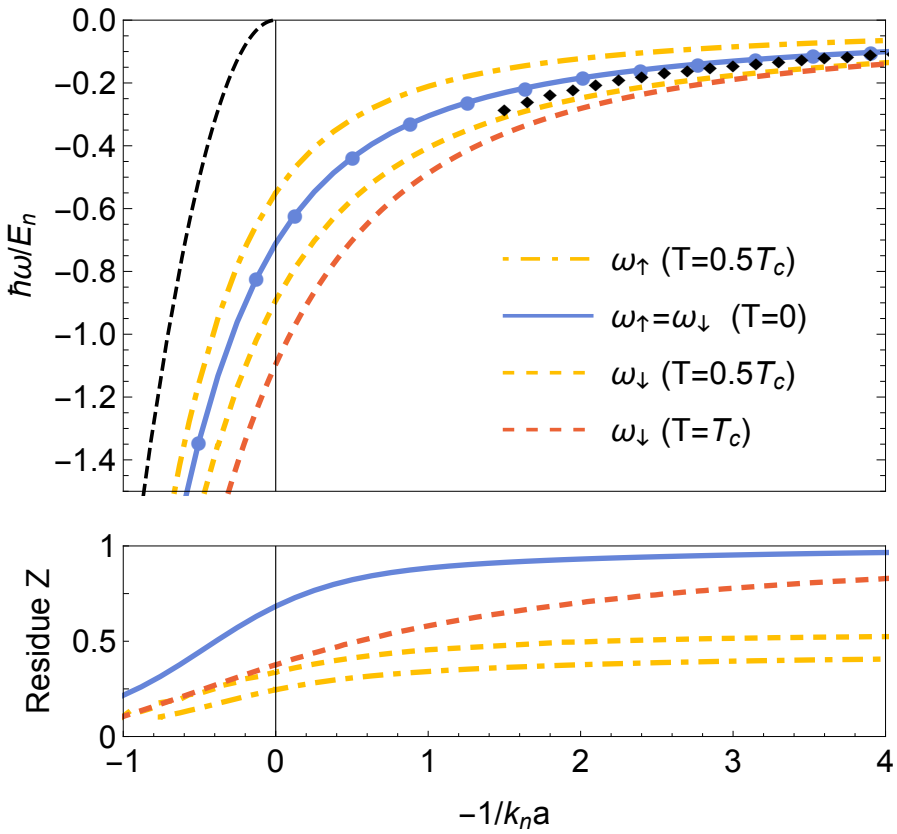

Figure 4.8: Energy (top) and residue (bottom) of the attractive polarons versus interaction strength, at $T = 0$ (blue), $T = 0.5T_c$ (yellow), and $T = T_c$ (red). The filled blue circles in the energy plot indicate the results of the ladder approximation at $T = 0$, the black filled diamonds are the mean field result $\omega = 2\pi\hbar a/m_r$ (right) and the dashed line the molecular binding energy Eq. (2.25).

assuming also $k_BT \gg \hbar^2/m_r a^2$, we obtain

$$\mathbf{\Sigma}(0,0) \approx -i\frac{4E_n}{3\pi^{3/2}\hbar}\left(\frac{m_B}{m_r}\right)^2\sqrt{\frac{E_n}{k_BT}}. \tag{4.61}$$

Thus, at high temperature the polaron energy approaches zero, and the quasiparticle becomes overdamped. Our numerical results converge to (4.61) for $T \gg T_c$, although such high temperatures are not shown in Figs. 4.6 and 4.7.

In Fig. 4.8 we plot the energy of the attractive polaron as a function of the interaction strength $1/k_na$, for $k_na_B = 0.01$ and at various temperatures. For all coupling strengths $a \gtrsim a_B$, we observe that the single attractive polaron present at $T = 0$ splits into two polarons at intermediate temperatures, of which only the lower one survives at $T \geq T_c$.

To analyze the origin of the splitting, in Fig. 4.9 we plot $\mathrm{Re}[\Sigma(\omega)]$ for $k_na = -0.1$ and various values of k_na_B and T/T_c. Graphically, the quasiparticle solutions Eq. (4.35) are given by the crossing of $\mathrm{Re}[\mathbf{\Sigma}(\omega)]$ with the diagonal dashed line giving ω, provided the imaginary part of the self-energy is small. Focus first on the purple lines relevant for a very small value of k_na_B. For $T = 0$ (purple dotted line, almost horizontal) there is only one solution close to ω_0. However, at finite temperatures

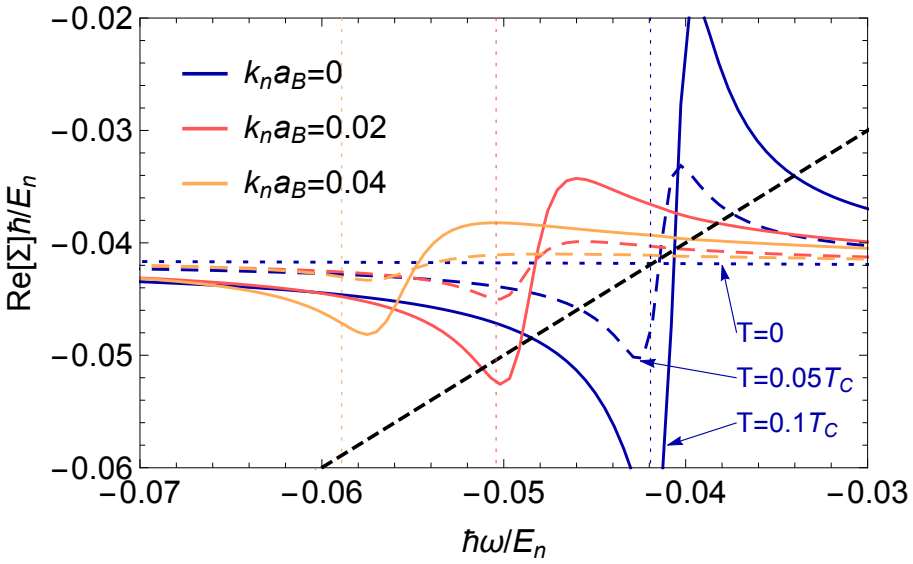

Figure 4.9: Real part of the self-energy $\mathbf{\Sigma}(\mathbf{p}=0,\omega)$ for $k_n a = -0.1$, at $T=0$ (purple dotted line, almost horizontal), $T=0.05T_c$ (dashed) and $T=0.1T_c$ (solid). The different colors correspond to various values of $k_n a_B$. The diagonal black line represents ω, and the vertical lines denote $n_0(\mathcal{T}_v - \mathcal{T}_B)$.

$\Sigma_1(\omega)$ develops a resonance structure around ω_0 and two further crossings appear. At the middle crossing (the one with $\partial_\omega \mathrm{Re}[\Sigma] > 0$) the self-energy has a large imaginary part, so that this does not correspond to a well-defined excitation; as a consequence, the spectrum contains now *two* quasiparticle solutions. The resonance at $\sim \omega_0$ arises because the pole $\tilde{\omega}_p$ of the extended matrix $\tilde{\mathcal{T}}$ in Eq. (4.57) fulfills $\tilde{\omega}_p = \epsilon_{\mathbf{p}} + \Sigma_0(\omega, \mathbf{p})$, the polaron dressed only with the condensate [shown as a double line in Fig. 4.4 (d)]. At $T=0$ the number of excited bosons is negligible, $n_{\mathrm{ex}} \ll n$, so that Σ_1 can be neglected and $\omega_0 \approx \tilde{\omega}$. Looking at the integral expression for Σ_1 in Eq. (4.59) for $\omega \sim \tilde{\omega}$, however, one can see that for finite T the combination of the infra-red divergence of the Bose distribution $f_{\mathbf{k}}$ and the pole of the $\tilde{\mathcal{T}}$ matrix being close to the $\mathbf{k} \to 0$ end of the integration range makes the infrared part of Eq. (4.59) very large and switching sign around $\omega \sim \tilde{\omega} \approx \omega_0$. The result is the resonance structure shown in Fig. 4.9, a completely non-perturbative feature of the extended scheme. The energy splitting between $\omega_\uparrow$ and $\omega_\downarrow$ increases with temperature, since more particles are thermally excited out of the BEC leading to a more pronounced resonance structure. This explains the behavior seen in Figs. 4.6 to 4.7.

The physical interpretation of the resonance feature of $\tilde{\mathcal{T}}$ is that the coupling between the impurity and the low-lying Bogoliubov modes gets strongly enhanced by the presence of the macroscopically occupied condensate mode. The coupling to the BEC itself however is via the usual ladder scattering matrix $\mathcal{T}$. At finite temperatures $0 < T < T_C$, the impurity couples to both the BEC and a macroscopic amount of excited bosons, and the hybridization between these two terms leads to the emergence of two quasiparticles.

Increasing $k_n a_B$ has two main effects on the resonance structure of Σ. First, it becomes less pronounced, since the low-energy density-of-states of the BEC decreases due to the stiffening of the Bogoliubov dispersion. Second, it moves to lower energies because of the increased effect of the coherence factors $u_{\mathbf{k}}, v_{\mathbf{k}}$. Indeed, in the weak

coupling limit the resonance is approximately located at $n_0(\mathcal{T}_v - \mathcal{T}_B)$, as is also discussed in more detail in Appendix A.2. These energies are plotted as vertical dashed lines in Fig. 4.9. It follows from these two effects that at low temperatures only *one* quasiparticle solution (the upper polaron) survives in the limit of weak impurity-bath coupling $|a| \lesssim a_B \ll 1/k_n$, and the energy of this solution approaches the first order result $n\mathcal{T}_v$, in agreement with perturbation theory (compare with Eq. (A.21)).

4.4.3 Repulsive polaron

Here, we briefly analyze the effects of temperature on the repulsive polaron, i.e. the quasiparticle branch present at positive energies for positive scattering lengths a in Figs. 4.2 and 4.5. As shown in Fig. 4.10, within our formalism the quasiparticle peak in the spectral function for $k_n a = 1$ broadens rapidly as T increases, and it disappears completely well below T_c. The spectral function instead exhibits a broad continuum, which is peaked at $\omega = 0$. This continuum consists of the impurity having momentum $\mathbf{k}$ and a Bogoliubov mode having momentum $\mathbf{k}$, and the contribution of the $\mathbf{k} \to 0$ states is large due to the infrared divergence in the Bose distribution function. The peak diverges at $T = T_c$ due the change in the $k \to 0$ dispersion, from linear to quadratic. At $T > T_c$ the zero-frequency peak disappears and the spectral function becomes approximately Lorentzian with a width given by (4.61) for $T \gg T_c$ and $k_B T \gg \hbar^2/ma^2$. Note that these effects are due to the repulsive polaron sitting in the middle of a continuum starting at zero energy. This is however an artifact of the approximation used. Physically, the low energy threshold of the continuum should lie at the energy of the zero momentum repulsive polaron and not at zero energy, since an impurity with momentum $\mathbf{k}$ is also in a repulsive polaron state. This will change the behavior of the repulsive polaron. To include this effect, one could use a self-consistent approximation, as was done for example at zero temperature in Ref. [5]. A self-consistent treatment at finite temperatures goes beyond the scope of the present work, and it constitutes an interesting future project.

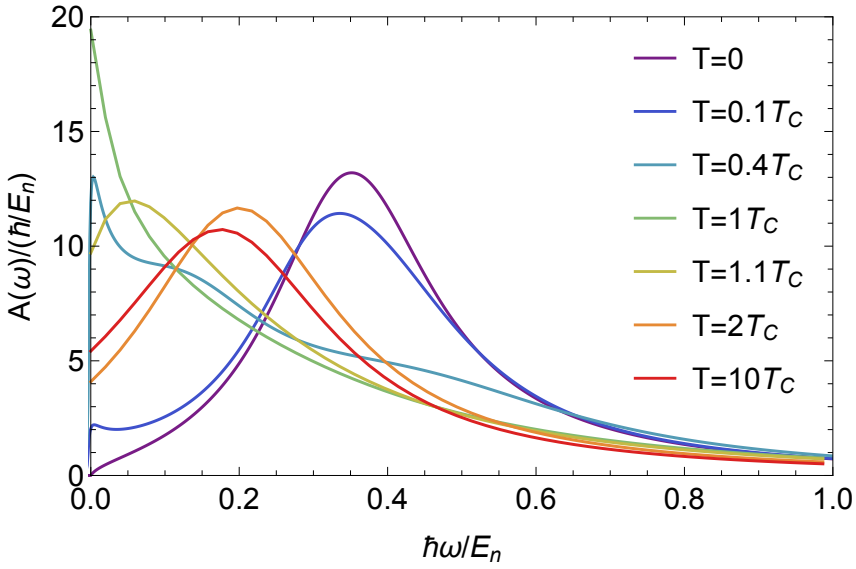

Figure 4.10: Spectral function $A(\omega, \mathbf{q} = 0)$ for $k_n a = 1$, $k_n a_B = 0.01$, and various temperatures T.

Chapter 5

Coherent state ansatz for zero temperature Bose impurities

In the previous chapter, the diagrammatic $\mathcal{T}$-matrix approach only allowed for up to one bosonic excitation being close to the impurity at the same time. This approach already shows reasonable agreement with experiment, and allowed to focus on the extension to finite temperatures. However, more-body effects are important in interacting Bose gases. In contrast to the Fermi case, where Pauli-blocking suppresses three-body effects, they feature in Bose gases and play a large role in the loss dynamics with strongly interacting impurities [87, 88], as discussed also in section 2.3.1. Beyond few-body physics, experimental Bose gases often have miniscule intra-bosonic repulsion $k_n a_B$ and Bose statistics allow for bunching of particles, thus a dressing of the impurity by many bosons and even macroscopic cloud sizes could be possible under the right conditions. The most extreme case imaginable is the limit $k_n a_B \to 0$, when the condensate becomes infinitely compressible. What is the ground state of such a fragile system?

In this chapter, we carefully analyze this question with a completely different angle than diagrammatic expansions, using a variational ansatz instead. First, we show analytically how, for a static impurity in an ideal BEC, the ground state overlap with the non-interacting state vanishes as a stretched exponential with particle number, leading to a bosonic orthogonality catastrophe (OC). We then develop a variational ansatz, which allows for a macroscopic dressing of the impurity, including the back-action on the BEC as well as boson-boson repulsion beyond the Bogoliubov approximation. The ansatz, which recovers the exact result for a static impurity, predicts that the OC also occurs for an impurity with *finite* mass when the Bose gas becomes non-interacting. A physical picture emerges where the BEC scatters coherently with the impurity, and a large number of bosons builds a macroscopic but very dilute dressing cloud. Intriguingly, the properties of the polaron are demonstrated analytically to be given by expressions similar to those obtained from perturbation theory, even in the regime governed by the OC at small boson-boson repulsion. Finally, we show how our ansatz recovers experimental observations.

5.1 A static impurity in an ideal BEC: orthogonality catastrophe

We start by analyzing a static impurity at zero temperature in an ideal gas of N identical bosons of mass m_B within a sphere of radius R, a case which is analytically tractable. For vanishing boson-boson interaction the ground state is simply the product $\prod_{j=1}^{N}\psi(\boldsymbol{r}_j)$ of the lowest energy single-particle wave function. In absence of the impurity, the single particle wave function is $\psi_0(\boldsymbol{r}) = (2\pi R)^{-1/2}\sin(k_0 r)/r$ where $k_0 = \pi/R$. Upon introducing an impurity in the center that interacts with the bosons via a potential of the form $U(r)$ with short range $r_0 \ll R$, the problem can be discussed within two-body scattering theory as in chapter 2. The normalized single-particle wave functions for $r \gg r_0$ become

$$\psi_1(r) = \frac{1}{\sqrt{2\pi R}\sqrt{1+\frac{\sin(2\delta)}{2(\pi-\delta)}}}\frac{\sin\left(k_1 r+\delta\right)}{r}, \tag{5.1}$$

where $k_1 = k_0 - \delta/R$, and the phase shift $\delta = -\arctan(ak_1)$ is determined by the boson-impurity scattering length a. In the thermodynamic limit where $N, R \to \infty$ at fixed density, both $k_0, k_1 \to 0$, and for any finite $a < 0$ one has $\delta \approx -ak_0 \ll 1$. The difference ΔE in ground state energies defines the polaron energy [104]

$$\Delta E_0 = N\frac{\hbar^2\left(k_1^2-k_0^2\right)}{2m_B} = N\frac{\hbar^2 k_0^2}{m_B}\frac{a}{R} = \frac{2\pi\hbar^2 a}{m_B}n_0, \tag{5.2}$$

where $n_0 \equiv N|\psi_0(0)|^2 = \pi N/2R^3$ is the BEC density in the center in absence of the impurity.

The overlap between the ground states with and without the impurity is quantified by the residue $Z_0 = |\langle\Psi_0|\Psi_1\rangle|^2 = |\langle\psi_0|\psi_1\rangle|^{2N}$. Introducing $k_n = (6\pi^2 n_0)^{1/3}$, we obtain

$$Z_0 = \left[1-\alpha(k_n a)^2/(2N^{2/3})\right]^{2N} \to e^{-\alpha N^{1/3}(k_n a)^2}, \tag{5.3}$$

in the thermodynamic limit, where $\alpha \equiv (\pi^2/3+1/4)/(3\pi^3)^{2/3}$. Thus, the residue vanishes as a stretched exponential with increasing particle number, giving rise to a *bosonic orthogonality catastrophe* (bosonic OC). This behavior is even more drastic than the one Anderson predicted for a fermionic bath [105], where the overlap vanishes as a slower power law, due to an infinity of particle-hole excitations in the Fermi sea. The bosonic OC emerges instead because the ideal BEC is infinitely compressible, so that a macroscopic dressing cloud can gather around the impurity. Here and in the following, we will limit our discussion to static properties of the impurity-bath system. Dynamical aspects of the origin of the OC have been investigated in various other works, such as for example Refs. [106, 107, 108, 109].

5.2 A mobile impurity in an interacting BEC

We now explore how a finite impurity mass and boson-boson repulsion affect the OC. Taking a mobile impurity of mass m_I, the Hamiltonian is

$$\hat{H} = \int d^3r \left[\hat{b}^\dagger_{\boldsymbol{r}} \left(-\frac{\hbar^2 \nabla^2_{\boldsymbol{r}}}{2m_B} + \frac{\mathcal{T}_B}{2} \hat{b}^\dagger_{\boldsymbol{r}} \hat{b}_{\boldsymbol{r}} - \mu \right) \hat{b}_{\boldsymbol{r}} \right.$$
$$\left. + \hat{a}^\dagger_{\boldsymbol{r}} \left(-\frac{\hbar^2 \nabla^2_{\boldsymbol{r}}}{2m_I} \right) \hat{a}_{\boldsymbol{r}} + \int d^3s \; \hat{b}^\dagger_{\boldsymbol{r}} \hat{b}_{\boldsymbol{r}} U(\boldsymbol{r} - \boldsymbol{s}) \hat{a}^\dagger_{\boldsymbol{s}} \hat{a}_{\boldsymbol{s}} \right], \tag{5.4}$$

where $\hat{a}^\dagger_{\boldsymbol{r}}$ and $\hat{b}^\dagger_{\boldsymbol{r}}$ create an impurity and a boson, respectively, at position $\boldsymbol{r}$, and μ is the chemical potential of the bosons. The interaction between bosons is given by the regularized potential $\mathcal{T}_B = 4\pi\hbar^2 a_B/m_B$ where a_B is the boson-boson scattering length, which is consistent as long as $n(\boldsymbol{r})a_B^3 \ll 1$ at any point $\boldsymbol{r}$ in the BEC. As before, the interaction between the bath and the impurity is modeled through a short-ranged potential $U(\mathbf{r}) = U(r)$. We now introduce a variational ansatz for the ground state of Eq. (5.4), which smoothly connects to the exact result for a static impurity in an ideal BEC. The ansatz includes finite mass effects and accounts for the boson-boson repulsion beyond the Bogoliubov approximation. To this end, consider the state

$$|\Psi\rangle = \int \frac{d^3r}{\sqrt{V}} \; \hat{a}^\dagger_{\boldsymbol{r}} \exp\left(\int d^3s \; \phi(\boldsymbol{r} - \boldsymbol{s}) \hat{b}^\dagger_{\boldsymbol{s}} - c.c. \right) |0\rangle$$
$$= \int \frac{d^3r}{\sqrt{V}} |\boldsymbol{r}\rangle |\phi(\boldsymbol{r})\rangle, \tag{5.5}$$

where V is the system volume. It describes a BEC given by the coherent state $\hat{b}_{\boldsymbol{s}}|\phi(\boldsymbol{r})\rangle = \phi(\boldsymbol{r} - \boldsymbol{s})|\phi(\boldsymbol{r})\rangle$, which adjusts to the position of the impurity. It follows that $\langle \hat{n}_I(\boldsymbol{r}) \hat{n}_B(\boldsymbol{r} + \boldsymbol{s}) \rangle \sim |\phi(\boldsymbol{s})|^2$, such that ϕ can be regarded as the impurity-bath density-density correlation function. Assuming a spherically symmetric ground state $\phi(\boldsymbol{r}) = \phi(r)$, the expectation value of Eq. (5.4) with respect to the state Eq. (5.5) reads

$$\langle \hat{H} \rangle = \int d^3r \; \phi^*(r) \left[-\frac{\hbar^2 \nabla^2_{\boldsymbol{r}}}{2m_r} + U(r) + \frac{\mathcal{T}_B}{2} |\phi(r)|^2 - \mu \right] \phi(r), \tag{5.6}$$

as shown in Appendix B. Here $m_r^{-1} = m_B^{-1} + m_I^{-1}$ is the reduced mass. Minimizing Eq. (5.6) gives

$$\left[-\frac{\hbar^2 \nabla^2_{\boldsymbol{r}}}{2m_r} + U(r) + \mathcal{T}_B |\phi(r)|^2 \right] \phi(r) = \mu \phi(r). \tag{5.7}$$

Eq. (5.7) is remarkably simple: The mobile impurity is described by a modified Gross-Pitaevskii equation (GPE) where the kinetic term contains the reduced mass, and the bosons scatter collectively on the impurity. Note that the back-action on the BEC due to the dressing cloud around the impurity and boson-boson interactions are naturally included in the GPE, an effect that is not fully accounted for in a Bogoliubov approach to the problem that expands in fluctuations around a homogeneous BEC [95, 110]. We note that Eq. (5.7) was derived long ago following a very different strategy by Gross in [111]. For infinite impurity mass we have $m_r = m_B$,

and Eq. (5.7) reduces to the standard GPE for a static potential $U(r)$. If, moreover, $a_B = 0$ it reduces to the one-body Schrödinger equation thereby recovering the exact results for the bosonic OC described above.

To investigate the ground state of the impurity, we solve Eq. (5.7) subject to the condition $\mu = n_0 \mathcal{T}_B$, which ensures that the density far away from the impurity converges to the density n_0 of the BEC in absence of the impurity. Introducing the dimensionless quantities $\mathbf{x} = \boldsymbol{r}/\xi$, $\tilde{\phi}(x) = \phi(x\xi)/\sqrt{n_0}$ and $\tilde{U}(x) = 2m_r\xi^2 U(x\xi)/\hbar^2$ with $\xi = (8\pi n_0 a_B m_r/m_B)^{-1/2}$, Eq. (5.7) becomes

$$\left[-\nabla_x^2 + \tilde{U}(x) + |\tilde{\phi}(x)|^2 - 1\right]\tilde{\phi}(x) = 0, \tag{5.8}$$

showing that the generalized healing length ξ is the natural length scale of the problem.

The polaron energy is the energy shift ΔE away from the solution with $\tilde{U} = 0$. Using Eq. (5.8) in EQ. (5.6), one finds

$$\Delta E = -\frac{E_\xi}{2}\int d^3x\ (|\tilde{\phi}(x)|^4 - 1), \tag{5.9}$$

where $E_\xi = \hbar^2 n_0 \xi/2m_r$. Again, Z is the squared overlap between ground states of the gas with and without impurity. With the coherent ansatz one finds

$$Z = |\langle\Psi_0|\Psi_1\rangle|^2 = e^{-N_\xi \int d^3x\ |\tilde{\phi}(x)-1|^2}, \tag{5.10}$$

where we defined $N_\xi = n_0\xi^3$. This shows that changes in the condensate mode cause an exponential suppression of the overlap. Finally, the number ΔN of bosons in the dressing cloud around the impurity is

$$\Delta N = N_\xi \int d^3x\ (|\tilde{\phi}(x)|^2 - 1). \tag{5.11}$$

The condensate wave function $\phi(\mathbf{x})$ is obtained numerically. In our computation we employ three attractive potentials: a square well $U_w\Theta(1-r/r_0)$, a Gaussian $U_g \exp(-r/r_0)^2$, and an exponential $U_e \exp(-r/r_0)$, which give rise to effective ranges $r_e \sim r_0$, mimicking open-channel dominated resonances [112]. We tune their depth U and characteristic size r_0 independently, so that we can model different scattering lengths a at fixed effective range r_e. Within the wide range of parameters explored, the results given by these three potentials differ by less than the width of the lines in all figures, demonstrating an effective two-parameter universality (given by the scattering length a and range r_e) governing this problem. Note that in general one cannot use a zero-range potential for both the boson-boson and the boson-impurity interaction, because in that case Eq. (5.7) admits only a zero-energy polaron solution.

Numerically, the problem needs careful treatment, because next to the impurity the wave function varies on scales comparable to r_e, while further away it evolves on a scale set by $\xi \gg r_e$. To achieve sufficient accuracy despite this large separation of scales, we discretize the integral in Eq. (5.6) on a non-uniform grid featuring an exponentially-growing lattice spacing in the outward radial direction containing several thousand points both inside and outside the potential. For all computational results presented here, we used a grid with maximal radius $R = 100\xi$, and boundary condition $\phi(R) = \sqrt{n_0}$.

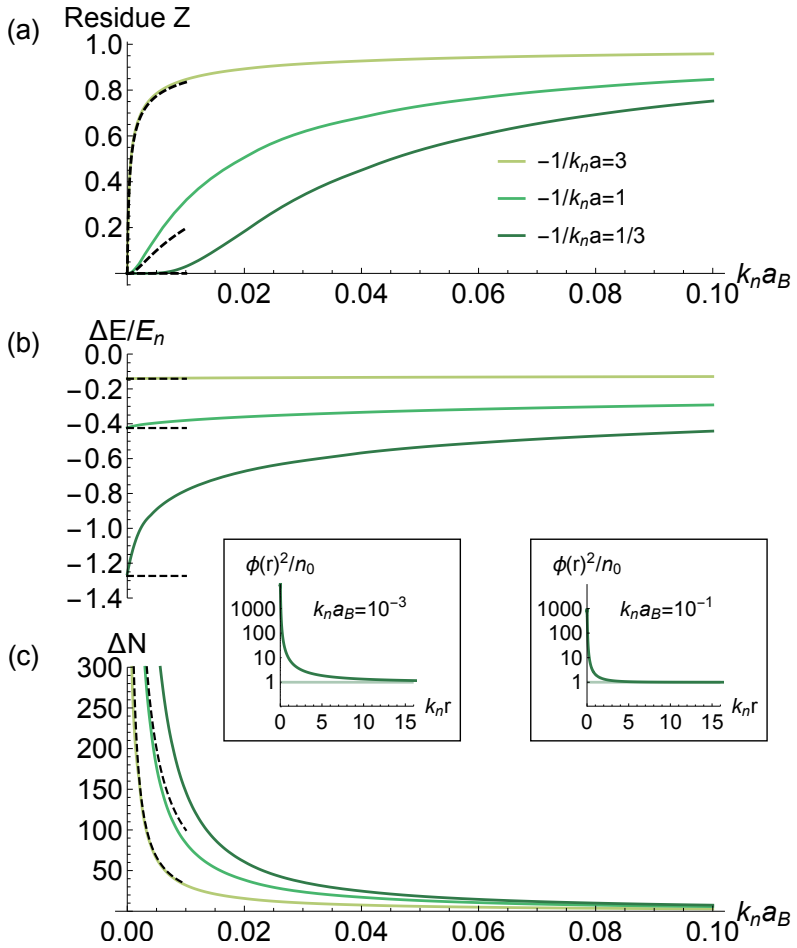

Figure 5.1: **Polaron properties:** (a) The residue and (b) the energy (in units $E_n = \hbar^2 k_n^2/2m_B$) of the polaron, as well as (c) the number of particles in the dressing cloud as a function of $k_n a_B$ for $-1/k_n a = (3, 1, 1/3)$ (light green to darker green lines). In all panels, $m_I = m_B$ and $k_n r_e = 0.05$. The dashed lines are the perturbative expressions Eqs. (5.13)-(5.15). The insets show $|\phi(r)|^2$ for $-1/k_n a = 1/3$ and for two values of $k_n a_B$, corresponding to $k_n \xi \approx 70$ (left) and $k_n \xi \approx 7$ (right).

In Fig. 5.1 we plot the residue and energy of the polaron as well as the number of particles in its dressing cloud as a function of the boson-boson scattering length a_B for various impurity-boson interaction strengths. Fig. 5.1 (a) shows that, in contrast to fermions, the OC persists even for mobile impurities when the BEC becomes ideal. A related finding was discussed in Refs. [95, 96]. In this limit, the residue Z vanishes and the number of particles ΔN in the dressing cloud diverges for $k_n a_B \to 0_+$, see Fig. 5.1 (b). The bosonic OC is cured when the bosons start to repel which leads to a suppression of particles in the dressing cloud.

Equation (5.8) can be solved analytically for $|a|^3 \ll \xi^2 r_0$, as discussed in more detail in [113]. Under this condition, which is fulfilled for any finite $|a|$ when $a_B \to 0$, one obtains for $x \gtrsim r_0/\xi$ the Yukawa solution

$$\tilde{\phi}(x) = 1 - (a/\xi) e^{-\sqrt{2}x}/x. \tag{5.12}$$

Using this in Eqs. (5.9)-(5.11) gives

$$\Delta E = 4\pi E_\xi a/\xi \qquad = 2\pi\hbar^2 a n_0/m_r, \tag{5.13}$$

$$\log Z = -\sqrt{2}\pi N_\xi a^2/\xi^2 = -\sqrt{2}\pi n_0 \xi a^2, \tag{5.14}$$

$$\Delta N = -4\pi N_\xi a/\xi \qquad = -a m_B/2a_B m_r. \tag{5.15}$$

These expressions, which are recovered by our numerical results when $k_n a_B \to 0$ (so that $a/\xi \to 0$) as shown in Fig. 5.1, analytically describe how the Bose polaron disappears in the limit of an ideal Bose gas. In particular, the residue vanishes exponentially with $\log Z \propto -1/\sqrt{a_B}$ and the number of particles in the polaron cloud grows as $\Delta N \propto 1/a_B$ when the BEC looses its stiffness, leading to the build-up of a macroscopic screening cloud around the impurity and causing the bosonic OC. Intriguingly, Eqs. (5.13) and (5.14) have the same functional form as those obtained from an expansion in $k_n a$ [94, 114], even though they are valid close to the bosonic OC, which must be expected to be well beyond the radius of convergence of perturbation theory.

The insets in Fig. 5.1 display $|\phi(r)|^2$ for $1/k_n a = -1/3$ at boson-boson scattering lengths $k_n a_B = 0.001$ and 0.1. They show how the bosons pile up around the impurity in a macroscopic dressing cloud of size $\sim \xi$. Importantly, in this case the local gas parameter $|\phi(r)|^2 a_B^3$ remains small *everywhere*, even close to the impurity. In the most strongly interacting case, the unitary limit $|k_n a| \to \infty$, we found it to vanish as $\propto k_n a_B (a_B/r_e)^{4/3}$ when $k_n a_B \to 0$. This ensures that the assumption of a contact potential for the boson-boson interaction in Eq. (5.4) is consistent. It also shows that the large number of bosons in the dressing cloud is due to a large radius $\sim \xi$ and not to an exceedingly large density.

Comparison with experiment.– We now compare the predictions of our ansatz with experiments. Close to a Feshbach resonance, the effective range r_e, defined through the low-energy expansion of the phase shift $k \cot\delta = -1/a + r_e k^2/2 + O(k^2)$, varies slowly around its value right at resonance [112, 116, 50, 22]

$$r_e = -2R^* + 2\Gamma(1/4)^2 R_{\rm vdW}/(3\pi), \tag{5.16}$$

Here, $R^* = \hbar^2/(2m_r a_{\rm bg}\delta\mu\,\Delta B)$, $\Gamma(x)$ is the Gamma function, and $R_{\rm vdW}$ is the Van-der-Waals radius. For open-channel dominated resonances, one has $R_{vdW} \gg R^*$ such that $r_e \sim R_{vdW} \ll \xi$ in typical experiments. For example, the experiments in Aarhus [87], JILA [88], and MIT [89], featured $k_n\xi = 21.7,\ 8,\ 9.6$, respectively, giving $r_e/\xi = 0.002,\ 0.02,\ 0.01$ (using data from Refs. [22, 50, 117]).

Our numerical results for ΔE are shown in Fig. 5.2 together with the measurements from the experiments reported in Refs. [87, 88], which had mass ratios $m_I/m_B = 1$ and 40/87, respectively. Corresponding QMC results of Refs. [115, 91] are also displayed. The coherent state ansatz shows good agreement with the experimental data, even for impurities with mass comparable to m_B or lighter. Our ansatz predicts large dressing clouds at unitarity, containing $20-180$ bosons for the JILA and Aarhus case, respectively. This strong dressing, however, is accompanied by an extremely small residue Z at resonance and therefore a very small spectral weight of the ground state in the experimental radio-frequency spectrum at odds with other theories that recover the experimentally measured spectrum [5, 93].

Contact.– We finally examine Tan's contact parameter, which quantifies the short-range correlations between the impurity and the atoms in the BEC. It can

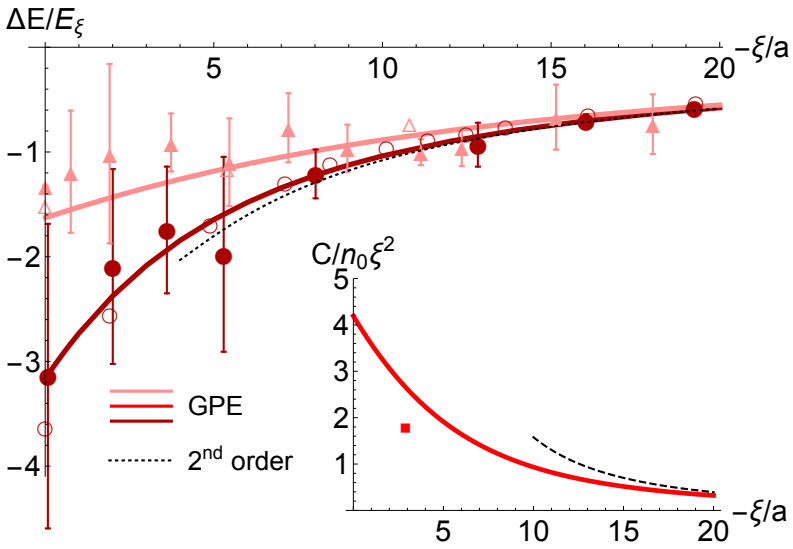

Figure 5.2: **Polaron energy and contact.** Polaron energy ΔE in units of $E_\xi = \hbar^2 n_0 \xi / 2m_r$ as a function of $-\xi/a$. The solid lines are the results of our ansatz obtained for effective ranges $r_e/\xi = 0.002$ (pink) and 0.02 (dark red), corresponding respectively to the experimental conditions of Aarhus [87] and JILA [88]. Filled symbols are the experimental data from Aarhus (triangles) and JILA (circles), and empty symbols are the corresponding QMC data from [115, 91]. The black dotted line is the second order perturbative result $\Delta E = 4\pi(a/\xi)(1 + \sqrt{2}a/\xi)E_\xi$ [114, 94]. The inset shows Tan's contact C of a single impurity given by Eq. (5.17), as a function of $-\xi/a$ for the effective range $r_e/\xi = 0.01$. The red point is the measurement reported by the MIT group [89] at lowest temperature and closest to unitarity, using a resonance with a comparable ratio r_e/ξ. The dashed line is the perturbative result, Eq. (5.18).

be obtained from Tan's adiabatic theorem [118, 119, 120, 121, 122]

$$C = -\frac{8\pi m_r}{\hbar^2}\frac{\partial(\Delta E)}{\partial(1/a)} = -4\pi n_0 \xi^2 \frac{\partial(\Delta E/E_\xi)}{\partial(\xi/a)}. \tag{5.17}$$

Our ansatz gives to leading order in a/ξ

$$C_1 = (4\pi a/\xi)^2 n_0 \xi^2 = 16\pi^2 n_0 a^2, \tag{5.18}$$

which agrees with the leading order result of perturbation theory. In the inset of Fig. 5.2 we show the dependence of the contact as function of $-\xi/a$ for ratios r_e/ξ and mass ratios appropriate for the experiment at MIT [89]. In this experiment the contact, shown as a red square, was obtained from the tail of the radio-frequency response at finite temperatures.

Chapter 6

Discussion and Outlook

In chapter 4, I showed how the proper extension of the two-body $\mathcal{T}$-matrix to finite temperature leads to a splitting of the attractive polaron branch into two new quasi-particles at finite temperatures, with a symmetric splitting of quasi-particle weight for $T/T_C \to 0$. The diagrammatic reason for this lies in the two-fluid nature of the BEC at intermediate temperatures below T_C: Both the discrete condensate mode and the continuum of out-of condensate modes are macroscopically populated. Low-energy scattering of out-of-condensate bosons with the impurity are thus massively altered due to exchange effects associated with bosons in the condensate. The resulting splitting is a non-perturbative effect and is predicted to persevere even for relatively small inter-species scattering lengths. Both the occupation of the continuum and the condensate as well as the dispersion of the out-of-condensate Bogoliubov modes themselves are strongly temperature dependent, this results in significant energy shifts associated with the splitting even at intermediate temperatures.

Theoretically, an important question concerns whether three-body losses wash out the effect of the splitting. Three-body losses were investigated in the Aarhus and JILA experiments. Both groups found that they have surprisingly small effects, in the sense that the observed spectra could be explained theoretically without introducing three-body losses. Since temperature shifts and splittings predicted by the extended $\mathcal{T}$-matrix have the same order of magnitude as the polaron energy at $T = 0$, we conclude that their observation is likely robust towards three-body losses.

Note that the physical mechanism underlying the strong temperature dependence and the quasiparticle splitting, is generic: both effects are caused by the condensed Bose gas breaking a continuous symmetry below T_c, so that a gapless mode appears, leading to a dramatic change in the low energy density of states to which the impurity couples. Our findings are therefore relevant to a wide class of systems consisting of an impurity immersed in a medium breaking a continuous symmetry. This includes impurities in liquid Helium [36], normal and high-T_c superconductors [37], ultracold Fermi superfluids [123], and quantum magnets [124]. In high energy physics, a similar splitting of a fermionic quasiparticle into two modes due to the coupling to a linear bosonic spectrum has indeed been predicted in hot quark-gluon plasmas, and in Yukawa and QED theories [125, 126, 127, 128]. Due to its collective nature, the emergent quasiparticle in this context was dubbed *plasmino* [129]. Our results therefore provide an avenue to study this interesting prediction in the controlled environment of a quantum gas.

After the publication of our work, new experimental data on the T/T_C-dependence of the attractive Bose-polaron ground-state has been published using spatially-resolved ejection spectroscopy of impurity atoms dispersed inside a inhomogeneous BEC [89]. The ground-state energy reported is not in agreement with the lower branch $\omega_\downarrow$ of our theory, when adjusted to the experimental parameters, i.e. a mass imbalance of $m_B/m_I = 40/23$ and the various interaction parameters $k_n a$ reported. It should be noted however that in this experiment, the controlled parameter is the bosonic density, not the temperature directly, and as such T/T_C in this experiment cannot be controlled independently from $k_n a$, as shown in Fig. S7 in [130]. Yet a linearly growing polaron binding energy is found for increasing T/T_C at resonant interactions, qualitatively similar to our theory.

Another theoretical work appearing after our initial publication aimed to replicate and extend our results using a variational ansatz for the thermal density matrix of the system [131], an approach completely different from the $\mathcal{T}$-matrix. This ansatz allows to incorporate the effect of two-,three-, and more-body-scattering processes on the finite temperature spectrum of the system. Only including two-body processes, they report a spectrum identical to the one obtained with the extended $\mathcal{T}$-matrix approach, while including three-body processes leads to a splitting of the $T = 0$ polaron into *three* new quasi-particles. They argue heuristically that including the n-th body scattering process leads to a spectrum with n polaron branches, merging into a broad continuum for the complete series at $n \to \infty$.

In chapter 5, I showed how a coherent ansatz can describe the macroscopic dressing of the impurity and the back-action on the BEC including the boson-boson repulsion beyond the Bogoliubov approximation, as first discussed in our original work [4]. We carefully analyzed the fate of the polaron with decreasing boson-boson interaction. We showed that the polaron disappears for $a_B \to 0$ resulting in a bosonic orthogonality catastrophe also when it has a finite mass.

Strikingly, the ansatz predicts that the properties of the polaron are accurately described by expressions similar to perturbation theory even in a regime where the polaron picture ceases to be valid, and perturbation theory becomes formally invalid. It would be very interesting to examine this experimentally for instance using a Feshbach resonance to tune a_B, and employing Rabi [132] or Ramsey [133, 107, 134] spectroscopy. Also, the predicted large dressing clouds suggest potentially strong induced impurity-impurity interactions, which could affect the spectrum even for small impurity concentrations [135, 136]. It remains to understand how the coherent picture is affected by three-body losses, especially since in cases close to the orthogonality catastrophe, where Z is small, the relaxation into the new ground-state upon sweeping into the resonant regime can be expected to be very slow. Relaxation times could be possibly larger than the lifetime of the resonant mixture .

Concluding, my research presented in the last chapters suggests exciting rich physical phenomena associated with resonant impurities within a condensate environment, beyond the intriguing few-body physics that were the focus in the first works on Bose polarons.

Part II

Vortices on multiply-connected surfaces

Chapter 7

Superfluid vortices

In this chapter, I briefly introduce the core concept of vortices in a BEC, as discussed in many books and reviews, for example [137, 44, 100, 18]. To this end, we will review the derivation of the static Gross-Pitaevskii equation for non-uniform condensate modes, discuss the central role of the healing length, as well as the Thomas-Fermi limit.

In the next section, I will discuss the time-dependent Gross-Pitaevskii equation, its hydrodynamic reformulation and the resulting quantization of vorticity. From the general case, we discuss the limiting case of potential flow, well known from the study of hydrodynamics in classical fluids [138]. These flow potentials form the basis of the original works [1, 3].

Finally I will review the vortex state in condensates, its typical size and its flow potential. Further I will introduce the point vortex model, and discuss briefly the vorticity equation and the resulting reduction of the vortex time dynamics to a discrete set of partial differential equations.

7.1 Non-uniform condensates

The experimental observation of Bose-Einstein Condensation (BEC) in ultracold atomic vapors [11, 15] is predated by a decades long discussion of bosonic gases in the condensed matter community, with the primary experimental platform being superfluid helium. In particular, the theory of weakly bosonic gases was developed already in the 1950s by, among others, Bogoliubov, Pitaevskii, Gross and Beliaev [25, 139, 111]. In the original condensed matter context, this formed only the starting point for the as-of-now still not completely resolved description of liquid helium, where strong interactions and large densities typically place the system far away from the weakly interacting regime. In contrast, ultracold bosonic gases first provided a clean and accessible experimental system to verify the theoretical advancements of the 1950s.

In this new context, the theory of weakly interacting Bose gases proved able to properly describe experiments to very high accuracy. A centerpiece of this development is the Gross-Pitaevskii equation (GPE), which was found to excellently describe the spatial shape of the non-uniform condensates appearing in modern experiments due to the trapping potentials [137].

In addition to BECs in traps and optical potentials, a paradigmatic example of a non-uniform condensate is the one that contains a vortex or many vortices. Such

states of BEC were introduced by Gross [140] and Pitaevskii [141], which originally led to the formulation of the GPE. A way to derive the static GPE is briefly outlined below.

7.1.1 Bogoliubov-de-Gennes approach

One canonical example is the Bogoliubov-de-Gennes (BdG) approach, which will be quickly reviewed here, following closely [18]. Consider the Gibbs-Hamiltonian, describing the Bose gas in the external potential $V(\mathbf{x})$ in the second quantized form

$$H = \int d^d r \left(+\frac{\hbar^2}{2m_B} \partial_{\mathbf{r}} \hat{\phi}^\dagger \partial_{\mathbf{r}} \hat{\phi} + [V(\mathbf{r}) - \mu] \hat{\phi}^\dagger \hat{\phi} + \frac{g}{2} \hat{\phi}^\dagger \hat{\phi}^\dagger \hat{\phi} \hat{\phi} \right), \tag{7.1}$$

where μ is the chemical potential and d is the spatial dimension. the coupling constant g is typically determined by the two-body scattering in vacuum $g = \mathcal{T}_B = \hbar^2 4\pi a_B / m_B$ [102], but can be also chosen more phenomenologically. Assuming a condensate is present, it is convenient to expand the fields around the average $\phi_0 = \langle \hat{\phi} \rangle$, replacing $\hat{\phi} \to \phi_0 + \delta\hat{\phi}$. Here the fluctuation fields $\delta\hat{\phi}$ and $\delta\hat{\phi}^\dagger$ fulfill the canonical bosonic commutation relations and are typically considered small, i.e. $|\langle \delta\hat{\phi} \rangle| \ll |\phi_0|$. Inserting into Eq. (7.1) and ordering by powers of $\delta\hat{\phi}$

$$\hat{H} = H_0(\phi_0) + H_1(\phi_0, \delta\hat{\phi}) + H_2(\phi_0, \delta\hat{\phi}) + \mathcal{O}(\delta\hat{\phi}), \tag{7.2}$$

yields in particular the zero order mean field term

$$H_0(\phi_0) = \int d^d r \left(+\frac{\hbar^2}{2m_B} \partial_{\mathbf{r}} \phi_0^\dagger \partial_{\mathbf{r}} \phi_0 + [V(\mathbf{r}) - \mu] |\phi_0|^2 + \frac{g}{2} |\phi_0|^4 \right). \tag{7.3}$$

Assuming that $\langle \delta\phi \rangle$ is small compared to ϕ_0, we can minimize H_0 separately from H_1 and H_2 to fix ϕ_0. A standard calculation yields

$$\mu\phi_0 = \left(-\frac{\hbar^2}{2m} \nabla_{\mathbf{r}}^2 + V(\boldsymbol{r}) + g|\phi_0|^2 \right) \phi_0, \tag{7.4}$$

the famous stationary Gross-Pitaevskii equation. With ϕ_0 fulfilling (7.4), H_1 in Eq. (7.2) actually vanishes, and H_2 reads:

$$\begin{aligned} H_2 = \int d^d r \Bigg[& \frac{\hbar^2}{2m_B} \partial_{\mathbf{r}} \delta\hat{\phi}^\dagger \partial_{\mathbf{r}} \delta\hat{\phi} + (V(\mathbf{r}) - \mu) \delta\hat{\phi}^\dagger \delta\hat{\phi} \\ & - \frac{g}{2} (4 |\phi_0|^2 \delta\hat{\phi}^\dagger \delta\hat{\phi} + \phi_0^2 \delta\hat{\phi}^\dagger \delta\hat{\phi}^\dagger + (\phi_0^*)^2 \delta\hat{\phi} \delta\hat{\phi}) \Bigg], \end{aligned} \tag{7.5}$$

the Bogoliubov-de-Gennes (BdG) Hamiltonian. The quadratic Hamiltonian can be easily diagonalized in the homogeneous case, using the Fourier and Bogoliubov transforms, yielding the well known Bogoliubov eigenmodes already discussed in chapter 4. In the non-homogeneous case, such as in a trapped condensate, the diagonalization is typically technically much more involved. The corresponding eigenmodes describe quasi-particles, in the sense that creation of such quasi-particle is a superposition of creation of a real particle with the annihilation of a real particle

accompanied by the creation of two condensate particles. Since the Bogoliubov approach breaks the $U(1)$ symmetry of the model, one of the BdG modes corresponds to a gapless Nambu-Goldstone mode, that restores the symmetry in a finite system [142, 143]. In this reading, the GPE is the zero-th order result in a systematic expansion in the number-fluctuations of the Bose gas. It defines the shape of the condensate mode and is needed to determine the Bogoliubov eigenmodes in the next step. In the remainder of this part, all quantitative discussions will remain on the zero order level of the GPE. Occasionally, we will mention qualitative effects arising from the presence the Bogoliubov excitations given by the associated Hamiltonian Eq. (7.5).

7.1.2 Healing length

Consider a region with no local variation in the potential landscape, i.e. $V(\boldsymbol{r}) \approx V_0$, and without loss of generality consider $V_0 = 0$. It is clear that the term $\sim g|\phi_0|^2$ in Eq. (7.4) favors homogeneously spreading boson density over the entire region to minimize the cost in repulsive energy. Consider a point $\boldsymbol{r}_0$ deep within this region, such that $\phi_0(\boldsymbol{r}_0)$ is locally flat and the kinetic term in Eq. (7.4) becomes negligible. We can re-express the chemical potential as

$$\mu = n_0 g, \tag{7.6}$$

where $n_0 = |\phi_0|^2$ is the bulk density associated with the region. With the substitution $\tilde{\phi}_0 = \phi_0/\sqrt{n_0}$ and $\boldsymbol{s} = \boldsymbol{r}/\xi$, where $\xi = \hbar/\sqrt{2m_B n_0 g}$, the general GPE (7.4) can be brought to a-dimensional form

$$\tilde{\phi}_0(\boldsymbol{s}) = \left(-\nabla_{\boldsymbol{s}}^2 + |\tilde{\phi}_0(\boldsymbol{s})|^2 + \tilde{V}(\boldsymbol{s})\right)\tilde{\phi}_0. \tag{7.7}$$

Here $\tilde{V}$ is an appropriately rescaled potential. This shows that the length scale ξ, called the healing length, is the typical length scale of deformations of the condensate at the edges of such bulk regions. Inserting $g = \mathcal{T}_B$ yields the canonical form

$$\xi = \frac{\hbar}{\sqrt{8\pi n_0 a_B}}, \tag{7.8}$$

in the cold gas context. Note that the concept of the healing length is often generalized to systems beyond the weakly interacting regime where $n_0^{1/3} a_B \ll 1$, such as superfluid Helium. In this case ξ is the fundamental parameter accessible in experiments, and a phenomenological modeling of such a superfluid with the GPE can be achieved to some degree by simply choosing g to get the experimental ξ.

7.1.3 Thomas-Fermi limit

Ultracold bosonic gases are typically created in a regime called the "Thomas-Fermi limit" [144]: Variations of the trapping potential $V(\boldsymbol{r})$ are of a length scale much larger than the healing length ξ, such that the kinetic term in Eq. (7.4) is negligible almost everywhere. In this regime the local density $n(\boldsymbol{r}) = |\phi_0(\boldsymbol{r})|^2$ is approximated well by the Thomas-Fermi profile

$$n(\boldsymbol{r}) = \frac{\mu - V(\boldsymbol{r})}{g}\,\theta\left[\mu - V(\boldsymbol{r})\right], \tag{7.9}$$

where θ is the step function. Note that the Thomas-Fermi profile is inaccurate close to regions where $n(\boldsymbol{r})$ is vanishes, since here the repulsive term $\sim g|\phi_0|^2$ in Eq. (7.4) vanishes as well and the kinetic term must be taken into account.

Paradigmatic is the harmonic oscillator potential, which is typical in ultracold gas experiments and can also locally approximate wells in a more complex potential landscape. Given

$$V_{osc}(\mathbf{r}) = \frac{m_B}{2} \sum_{j=x,y,z} \omega_j^2 j^2, \tag{7.10}$$

Eq. (7.9) yields for the Thomas-Fermi profile

$$n(\boldsymbol{r}) = n_0 \left(1 - \frac{x^2}{R_x^2} - \frac{y^2}{R_y^2} - \frac{z^2}{R_z^2}\right). \tag{7.11}$$

Here $n_0 = \mu/g$ is the central density at the point $\boldsymbol{r} = 0$ where $V(\boldsymbol{r}) = 0$. $R_j^2 = 2\mu/(m_B\omega_j^2)$ are the squared condensate radii in the three cardinal directions. As per the stepfunction in Eq. (7.9), the density $n(\boldsymbol{r})$ is to be set to zero when the RHS of Eq. (7.11) becomes negative.

The length scales associated with the harmonic potentials are the oscillator lengths $d_j = \sqrt{\hbar/m_B\omega_j}$, and for the Thomas-Fermi profile to be valid one must thus have $d_j \gg \xi$ for $j \in \{x, y, z\}$. Comparing with R_j, it follows that

$$\xi \ll d_j \ll R_j \text{ for } j \in \{x, y, z\}, \tag{7.12}$$

which is found verified in most cases of interest.

7.1.4 Confinement to lower dimensions

We are particularly interested in condensates in two-dimensions. Such clouds can be achieved by very steep potential confinement locally in one direction, which we will call z in this section. Approximating such confinement as a harmonic potential with frequency ω_z and associated oscillator length d_z, this realizes the opposite case where $\xi \gg d_z$. In this regime, the discrete spectrum of the oscillator must be taken into account. If the temperature T of the condensate is such that $k_B T \ll \hbar\omega_0$, only the groundstate $\psi_0(z)$ of the oscillator can be populated in this cardinal direction and the system can be considered locally two dimensional. Applying the GPE in two dimensions for the remaining degrees of freedom $\boldsymbol{r} = \{x, y\}$, the full three-dimensional density of the system is

$$n_{3D}(\boldsymbol{r}, z) = |\psi_0(z)|^2 \underbrace{|\phi_0(\boldsymbol{r})|^2}_{=n_{2D}(\boldsymbol{r})} \tag{7.13}$$

In the following, we always consider cases where the superfluid is locally two-dimensional everywhere and assume that the systems we consider are created experimentally with an appropriate confining trap.

7.2 Time-dependent Gross-Pitaevskii equation

The time-dependent GPE can be derived similarly to section 7.1.1, but using the action instead of the Hamiltonian. One starts from the Lagrangian in the second

quantized form and applies the same expansion in powers of $\delta\hat{\phi}$ to obtain the zero-order action [145]:

$$S = \int d^d r dt \left[\frac{i\hbar}{2}(\phi_0^* \partial_t \phi_0 - \phi_0 \partial_t \phi_0^*) + \frac{\hbar^2}{2m_B} \partial_{\mathbf{r}} \phi_0^* \partial_{\mathbf{r}} \phi_0 - V(\boldsymbol{r})|\phi_0|^2 - \frac{g}{2}|\phi_0|^4 \right], \quad (7.14)$$

where $\phi_0(\boldsymbol{r}, t)$ is now the time-dependent condensate mode. Applying the principle of stationary action to the above functional we obtain that the stationary configurations of the fields fulfill the time dependent Gross-Pitaevskii equation (tGPE) [137]

$$i\hbar \partial_t \phi_0(\boldsymbol{r}, t) = \left[-\frac{\hbar^2}{2m_B} \nabla_{\boldsymbol{r}}^2 + V(\boldsymbol{r}) + g|\phi_0(\boldsymbol{r}, t)|^2 \right] \phi_0(\boldsymbol{r}, t). \quad (7.15)$$

From this it is clear that solutions ϕ_0 of the stationary GPE Eq. (7.4) are eigenmodes of Eq. (7.15) with frequency $\mu/\hbar$.

7.2.1 Hydrodynamic picture

It is convenient to study the tGPE in Eq. (7.15) in the so called hydrodynamical picture, which highlights how closely related the dynamics generated by Eq. (7.15) are to classical hydrodynamics. Central is the Madelung transformation, which splits the complex-valued ϕ_0 into two real fields n and φ

$$\phi_0(\boldsymbol{r}, t) = \sqrt{n(\boldsymbol{r}, t)} \exp\left[i\varphi(\boldsymbol{r}, t) \right], \quad (7.16)$$

the magnitude and phase of ϕ respectively. Now consider the standard current density

$$\boldsymbol{j} = \frac{\hbar}{2m_B i} (\phi_0^* \boldsymbol{\nabla} \phi_0 - \phi_0 \boldsymbol{\nabla} \phi_0^*) = n \frac{\hbar \boldsymbol{\nabla} \varphi}{m_B}. \quad (7.17)$$

We can define the local velocity $\boldsymbol{v}$ via $\boldsymbol{j} = n\boldsymbol{v}$, such that

$$\boldsymbol{v}(\boldsymbol{r}, t) = \frac{\hbar}{m_B} \boldsymbol{\nabla} \varphi(\boldsymbol{r}, t) \quad (7.18)$$

is determined entirely by the gradient of the phase φ. It follows that so that the "superfluid velocity" $\boldsymbol{v}$ is irrotational

$$\nabla \times \boldsymbol{v} = 0, \quad (7.19)$$

except when φ is singular, where additional care must be taken. Consider now the "circulation" κ, defined at a given instant of time in terms of the line integral $\kappa = \oint_{\mathcal{C}} d\boldsymbol{l} \cdot \boldsymbol{v}$ around an arbitrary closed path $\mathcal{C}$. Substitution of Eq. (7.18) yields

$$\kappa = \frac{\hbar}{m_B} \oint_{\mathcal{C}} d\boldsymbol{l} \cdot \boldsymbol{\nabla} \varphi = \frac{\hbar}{m_B} \Delta\varphi, \quad (7.20)$$

where $\Delta\varphi$ is the change in the phase upon following $\mathcal{C}$ once. For the condensate wave function to be single valued and sufficiently smooth at any given point, this quantity must be a multiple of 2π, therefore the circulation around any closed loop in a superfluid must be quantized in units of $2\pi\hbar/m_B$ [146, 8]:

$$\oint_C d\boldsymbol{l} \cdot \boldsymbol{v} = \frac{2\pi\hbar}{m_B} n, \; n \in \mathcal{Z} \quad (7.21)$$

To describe the dynamics of $\boldsymbol{v}$ in a closed form, substitute Eq. (7.16) into the time-dependent GP equation (7.15) and decompose into imaginary and real parts respectively to get the two real-valued equations

$$0 = \frac{\partial n}{\partial t} + \boldsymbol{\nabla} \cdot (n\boldsymbol{v}), \tag{7.22}$$

$$0 = \frac{m_B}{2}\boldsymbol{v}^2 + V(\boldsymbol{r}) - \frac{\hbar^2}{2m_B\sqrt{n}}\nabla^2\sqrt{n} + ng + \hbar\partial_t\varphi. \tag{7.23}$$

Eq. (7.22) is a canonical continuity equation as appearing in most field theories. Applying $\nabla/m_B\cdot$ on both sides of Eq. (7.23) and substituting Eq. (7.18) gives after some elementary reordering

$$m_B \underbrace{(\partial_t \boldsymbol{v} + (\boldsymbol{v}\cdot\boldsymbol{\nabla})\,\boldsymbol{v})}_{=D\boldsymbol{v}/Dt} = -\underbrace{\boldsymbol{\nabla}\left(ng - \frac{\hbar^2}{2m_B\sqrt{n}}\nabla^2\sqrt{n}\right)}_{=\nabla P(r)/n} + \underbrace{(-\boldsymbol{\nabla}V(\boldsymbol{r}))}_{=f(r)}, \tag{7.24}$$

which is analogous to the Euler equation of classical hydrodynamics, describing an inviscid fluid [138]. Here the first term on the right-hand side corresponds to a pressure term in the Euler equation with a generalized pressure $P(r)$, the second term $f(r)$ is a conservative force due to the potential. The material derivative $\frac{D}{Dt}\cdot = (\partial_t + \boldsymbol{v}\cdot\nabla)\cdot$ on the left side describes the temporal change of a field while being transported by the velocity field $\boldsymbol{v}$. Note the two contributions to the pressure P in Eq. (7.24). The repulsive term $\sim ng$ is a classical mean field term. However the second term, arising from the kinetic term $\sim \nabla|\phi_0|$ in the original tGPE Eq. (7.15), is purely quantum in nature and is hence often called the *quantum pressure term* [44].

Eqs. (7.22) and (7.24) together form a closed set of differential equations for $\{n(\boldsymbol{r},t), \boldsymbol{v}(\boldsymbol{r},t)\}$. The dynamics generated by the tGPE Eq. (7.15) are thus equivalent to a classical inviscid and irrotational flow with the additional condition of quantized circular currents Eq. (7.21).

7.2.2 Potential flow

The equations (7.22),(7.24) and (7.21) describe compressible superfluid flow, as can be expected ab initio in experimental ultracold BECs. Whenever the system is in the Thomas-Fermi limit (see section 7.1.3) however, spatial variations in the density n are typically very small away from the boundary region [144]. They can thus be neglected in Eq. (7.22). Consider now the particular case of a trapping potential $V_{\mathcal{R}}(\boldsymbol{r})$ that confines the superfluid uniformly to a region $\mathcal{R}$, i.e.

$$V_{\mathcal{R}}(\boldsymbol{r}) = \begin{cases} 0 & \text{if } \boldsymbol{r} \in \mathcal{R} \\ \infty & \text{else} \end{cases} \tag{7.25}$$

When in the TF limit, variations of the density will be significant only at the edges of the fluid and will be on the order of the healing length ξ, everywhere else the density will be simply constant, $n(\boldsymbol{r},t) = n_0$. Hence, for flow on length scales much larger than ξ, the system can be considered *incompressible* to good approximation. In this case, Eq. (7.22) reduces to

$$\boldsymbol{\nabla}\cdot\boldsymbol{v} = 0 \tag{7.26}$$

Inserting $\boldsymbol{v} \sim \nabla\varphi$ results in the Laplace equation for the phase

$$\Delta\varphi = 0, \tag{7.27}$$

which given sufficient boundary conditions *completely* determines φ. Therefore a direct solution of the quantum-Euler equation Eq. (7.24) is no longer needed for steady flow configurations. Apart from the phase, one can show from Eq. (7.26) that the velocity can also be re-expressed as the curl of a scalar function, the stream function $\chi(\boldsymbol{r})$:

$$\boldsymbol{v} = (\hbar/m_B)\,\hat{\boldsymbol{n}} \times \boldsymbol{\nabla}\chi, \tag{7.28}$$

where $\hat{\boldsymbol{n}} = \hat{\mathbf{x}} \times \hat{\mathbf{y}}$ is the unit vector normal to the plane. It follows from Eq. (7.28) that lines where $\chi = \textit{constant}$ are tangential to $\boldsymbol{v}$. Hence lines of $\chi = \textit{constant}$ are often called stream lines, as they describe trajectories of test particles advected by the fluid.

A fluid showing both *irrotational* and *incompressible* as well as frictionless flow is called a perfect fluid, a fundamental model in the field of hydrodynamics [138]. Significant simplifications of the dynamics can be achieved in this case. Given the two equations (7.18) and (7.28), we find for the components of the velocity

$$v_x = \frac{\hbar}{m_B}\frac{\partial\varphi}{\partial x} = -\frac{\hbar}{m_B}\frac{\partial\chi}{\partial y} \quad \text{and} \quad v_y = \frac{\hbar}{m_B}\frac{\partial\varphi}{\partial y} = \frac{\hbar}{m_B}\frac{\partial\chi}{\partial x}. \tag{7.29}$$

These equations are equivalent to the Cauchy-Riemann equations of a complex function where $z = x + iy$. They give the compact representation of the hydrodynamic flow velocity components

$$\Omega(z) = v_y + iv_x = (\hbar/m_B)\,F'(z) \tag{7.30}$$

in terms of the first derivative $F'(z)$ of the complex potential. F(z) has real and imaginary values identical to the condensate phase and the stream function respectively:

$$F(x + iy) = \chi(\boldsymbol{r}) + i\varphi(\boldsymbol{r}) \tag{7.31}$$

This allows to use the tremendous power of complex analysis on hydrodynamical properties. Note that *any* meromorphic complex function by definition fulfills the Cauchy-Riemann equations, and with this the conditions for irrotational and incompressible flow.

7.3 Quantized superfluid vortices

This section follows the presentation from Ref. [147]. I will briefly discuss the basic solution of the GP-equation Eq. (7.4) containing a two-dimensional vortex and the resulting length scales associated with a vortex. In cases where the extent of the vortex can be neglected compared to other length scales, it can be considered a point and I will discuss the basic point vortex model forming the basis of the subsequent work discussed in the following chapter 8.

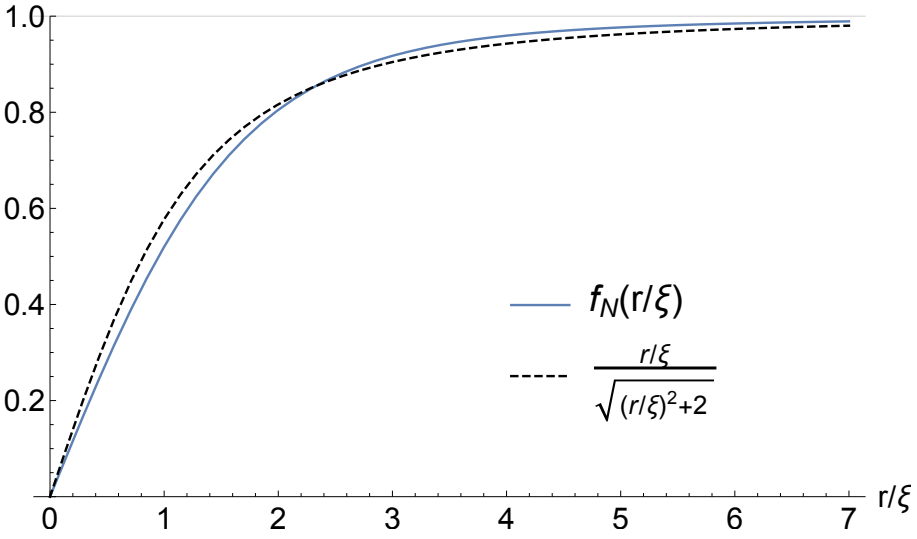

Figure 7.1: Numerical solution f_N of Eq. (7.34) with boundary conditions $f(0) = 0$ and $f(\infty) = 1$. The solution f_N depicted here was found via the shooting method, implemented with the "NDSolve" routine of Mathematica. The dashed line represents a common approximation of the true solution, see [147, 44]

7.3.1 Size of a single vortex

Consider the case of a single vortex in a two-dimensional unbound condensate of bulk density n_0,such that $\mu = n_0 g$, with bosons of mass m_B. A convenient ansatz for the condensate wave function is

$$\phi_0(\boldsymbol{r}) = \sqrt{n_0} e^{i\theta} f(r/\xi), \tag{7.32}$$

with r, θ polar coordinates, such that the vortex core is at the origin $r = 0$. ξ is the healing length as in Eq. (7.8) and f is an a-dimensional function describing the density deformation around the vortex core. Since the vortex should have a finite extend, we assume that $f \to 1$ for $r \to \infty$. Using Eq. (7.18), we find the velocity field

$$\boldsymbol{v}(\boldsymbol{r}) = \frac{\hbar}{m_B r} \hat{\boldsymbol{\theta}}, \tag{7.33}$$

where $\hat{\boldsymbol{\theta}}$ is the azimuthal unit vector, and which fulfills Eq. (7.21) for $n = 1$ on any radial curve $r = \textit{constant}$. Inserting ansatz Eq. (7.32) into the stationary GP equation, we retain the equation governing f, which can be expressed in a-dimensional form using the substitution $\boldsymbol{s} = \boldsymbol{r}/\xi$:

$$\left(-\partial_s^2 - \frac{1}{s}\partial_s + \frac{1}{s^2} - 1 + f^2 \right) f = 0. \tag{7.34}$$

Note the centrifugal barrier term induced by the azimuthal rotation Eq. (7.33). For $s \to 0$, f must scale at least linearly in s such that the second and third term in (7.34) cancel. Therefore $f(0) = 0$, and together with $f(\infty) = 1$ this sets the necessary boundaries to uniquely determine the solution of Eq. (7.34). A numerical solution can be seen in Fig. 7.1, together with a common approximation $s/\sqrt{s^2+2}$ [147]. It

is clear from Fig. 7.1 that the vortex core is indeed of an extent of the order of the healing length ξ.

Of interest is also the energy of the vortex, that is the energy difference between the vortex state Eq. (7.32) and a uniform condensate $\phi_0 = \sqrt{n_0}$, for example by subtracting Eq. (7.3) for both states. The dominant contribution comes from the azimuthal flow Eq. (7.33), which leads to a logarithmically divergent contribution at larger $|r|$. Therefore, one considers the condensate to be of finite radial size R and finds for the vortex energy

$$E_{vortex} = \pi \frac{\hbar^2 n_0}{m_B} \ln\left(\frac{R}{\xi}\right) + E_{core}\{f\}, \tag{7.35}$$

where E_{core} describes the additional contribution from the region $r \lesssim \xi$, where $f < 1$. Numerically one finds

$$E_{core}\{f_N\} \approx \pi \frac{\hbar^2 n_0}{m_B} \underbrace{\ln(1.464)}_{\approx 0.381}, \tag{7.36}$$

as first reported in [148]. For a more detailed discussion, see also [44].

7.3.2 The point vortex model

In many cases, and in all cases of interest in this thesis, all relevant length scales of the system determining the geometry of the condensate, are much larger than the healing length ξ. In this case, one can neglect the region $r \lesssim \xi$ altogether and consider the vortex to be a 'point'. In this picture, the only relevant property of the vortex state in a plane Eq. (7.32) is the azimuthal velocity Eq. (7.33). The flow-field of the vortex can then be re-expressed with a complex flow potential

$$F_{\text{vortex}}(z) = \ln(z) \tag{7.37}$$

, where it can be easily verified, that Eq. (7.37) inserted into Eq. (7.30) yields Eq. (7.33). The strength of the potential picture is that it can be easily expanded by simply adding different potential terms. For example, Eq. (7.37) can be easily extended to any possible vortex configuration in the plane. Writing the vortex positions $\boldsymbol{r}_n = \{x_n, y_n\}$ of the n-th vortex as $z_n = x_n + iy_n$, the velocity potential of the entire configuration is simply the sum of the single potentials

$$F(z) = \sum_n q_n \ln(z - z_n), \tag{7.38}$$

where $q_n = \pm 1$, the 'charge' of the vortex, describes whether a given vortex rotates clock- or counterclockwise.

7.3.3 Dynamics of point vortices

Since the GP equation can be re-expressed in a quasi-classical hydrodynamic picture (see Eqs. (7.24) and (7.22)), all the classical results on vortex dynamics in an irrotational fluid automatically hold for any vortex configuration in a dilute BEC. Particularly useful properties concern the so-called vorticity $\boldsymbol{\omega}$ of the flow-field:

$$\boldsymbol{\omega} = \nabla \times \boldsymbol{v} \tag{7.39}$$

For a two-dimensional flow $\boldsymbol{v}$ in the x, y-plane, $\boldsymbol{\omega}$ always is perpendicular to the plane, and it is enough to consider the scalar $\omega = \boldsymbol{\omega}_z$. In particular, for a vortex configuration as in Eq. (7.38), the vorticity is a series of delta functions:

$$\omega = \left(\frac{\hbar}{m_B}\right) \sum_n q_n \delta(\boldsymbol{r} - \boldsymbol{r}_n). \tag{7.40}$$

By applying $\nabla \times \cdot$ on both sides of the Euler equation Eq. (7.24) and inserting Eq. (7.39), one can find the *vorticity equation* that directly describes the evolution of the vorticity ω [149]. In the case of an incompressible flow with $\nabla \cdot \boldsymbol{v} = 0$, the vorticity equation simplifies tremendously in the two-dimensional case and simply reads:

$$\frac{D\omega}{Dt} = 0, \tag{7.41}$$

where $D \cdot /Dt$ is the material derivative as discussed below Eq. (7.24). Therefore the vorticity is simply *advected* by the velocity field. In the particular case of point vortices Eq. (7.40), the vortex cores $\boldsymbol{r}_n$ are advected by the 'local' velocity $\boldsymbol{v}(\boldsymbol{r}_n)$. However this is ill-defined, since both the velocity $\boldsymbol{v}$ diverges at $\boldsymbol{r}_n$ and the fluid density vanishes, as described in Fig. 7.1. A way to approach the problem is considering the movement of a small ring of fluid around the vortex core: Consider an average over a ring $\bigcirc(\boldsymbol{r}_n, \epsilon)$ of infinitesimal radius ϵ around the position $\boldsymbol{r}_n$:

$$\langle g(\boldsymbol{r}) \rangle_{\boldsymbol{r}_n} = \lim_{\epsilon \to 0} \left(\frac{1}{2\pi\epsilon} \int_{\bigcirc(\boldsymbol{r}_n, \epsilon)} d\boldsymbol{r} g(\boldsymbol{r}) \right), \tag{7.42}$$

where $g(\boldsymbol{r})$ is an arbitrary test function. Using Eq. (7.42), $\langle \boldsymbol{v} \rangle_{\boldsymbol{r}} = \boldsymbol{v}(\boldsymbol{r})$ anywhere where $\boldsymbol{v}$ is regular, but at $\boldsymbol{r} = \boldsymbol{r}_n$ the divergent $\sim 1/r$ contribution in Eq. (7.33) is averaged out to zero radially. With this, the equations of motion for the vortex cores are simply given as

$$\dot{\boldsymbol{r}}_n = \langle \boldsymbol{v} \rangle_{\boldsymbol{r}_n}. \tag{7.43}$$

For the example of a vortex configuration as in Eq. (7.38), using the complex notation $\Omega = v_y + i v_x$ as in Eq. (7.30), the velocity Ω_m of the m-th vortex at any given moment is given by

$$\begin{aligned} \Omega_m =& \frac{\hbar}{m_B} \sum_{n \neq m} \frac{q_n}{z_m - z_n} \\ =& \frac{\hbar}{m_B} \lim_{z \to z_m} \left(F'(z) - \frac{1}{z - z_m} \right) \end{aligned} \tag{7.44}$$

In effect, a given vortex experiences the entire velocity field, except for the local divergent part induced by itself.

Chapter 8

Superfluid vortices on multiply-connected surfaces

8.1 Introduction

Chapter 7 reviewed the general theory of vortices in planar superfluids as known in standard textbook material. In contrast, this chapter presents and closely follows the new results of the publications [1] and [3]. Central to both is the question of how the flow field induced by vortices as well as their dynamics are affected when the embedding superfluid is non-simply connected. As will be seen, the quantization condition Eq. (7.21) imposes additional constraints on the flow field to ensure the coherence of the condensate.

The first paper [1] discusses quantized superfluid vortex dynamics on cylindrical surfaces and planar annuli. The surface of a cylinder is locally flat [150], which allows to focus entirely on the quantization constraint Eq. (7.21) for paths around the cylinder circumference. I present the derivation of the flow-field potentials and the discussion of the resulting vortex dynamics as presented in the manuscript. In particular, section 8.2 discusses the situation on an infinite cylinder, section 8.3 the finite analogue, and section 8.4 the planar annulus, which is easily mapped to a cylinder surface.

The second paper [3] focuses on vortex dynamics on a torus as well as more generalized toroidal surfaces. In contrast to the cylinder case, the torus surface is boundary-less and has a finite area. As such it only allows configurations of vortices with zero net vorticity. We derived analytic expressions for the flow field, the total energy, and the time-dependent dynamics of the vortex cores, which I present in section 8.5 for a torus surface. In section 8.6 I present how the torus results can be easily generalized using an extended version of the conformal map discussed in section 8.5.1.

Note that all calculations performed in this chapter assume point vortices, the condensate wave function is only important in terms of its phase φ. Therefore, the letter ϕ will denote angles in various geometric description in the following chapter.

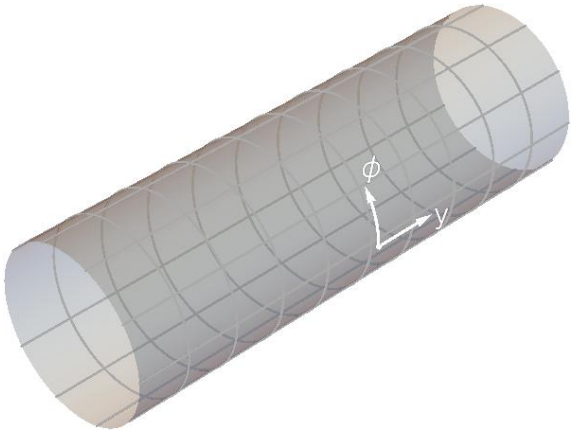

Figure 8.1: surface of a cylinder parametrized by a length y and angle ϕ.

8.2 Superfluid vortices on an infinite cylinder

In this section I present the flow-field configurations induced by, as well as the dynamics of, point vortices embedded in a thin superfluid film on a cylindrical surface of radius R. I start by briefly discussing the parametrization of such an infinite cylinder in the following section. Then, I present the derivation of the flow potential of a single vortex as well as more general vortex configurations on such a cylinder, discuss the flow field and the vortex core dynamics generated by it.

8.2.1 Coordinate set

Points $\boldsymbol{s}$ on the surface of an infinite cylinder with a radius R can be described with the parametrization

$$\boldsymbol{s}(y,\phi)\begin{cases} R\cos\phi \\ R\sin\phi \\ y, \end{cases} \tag{8.1}$$

which is presented schematically in Fig. 8.1. The corresponding line element is

$$ds^2 = R^2 d\phi^2 + dy^2 \tag{8.2}$$

which can be trivially brought to isothermal form with the variable $x = R\phi$, such that

$$ds^2 = dx^2 + dy^2. \tag{8.3}$$

The cylinder surface is simply "unrolled" onto a flat, infinite strip with coordinates $-\pi R < x < \pi R$ and $-\infty \leq y \leq \infty$, however the boundaries are identified, i.e. $x = -\pi R \equiv \pi R$.

8.2.2 Single point vortex

The periodic cylinder surface can be thought of as an infinite plane with periodic repetitions of a strip of width $2\pi R$ along $\hat{\boldsymbol{x}}$. We can find the appropriate flow

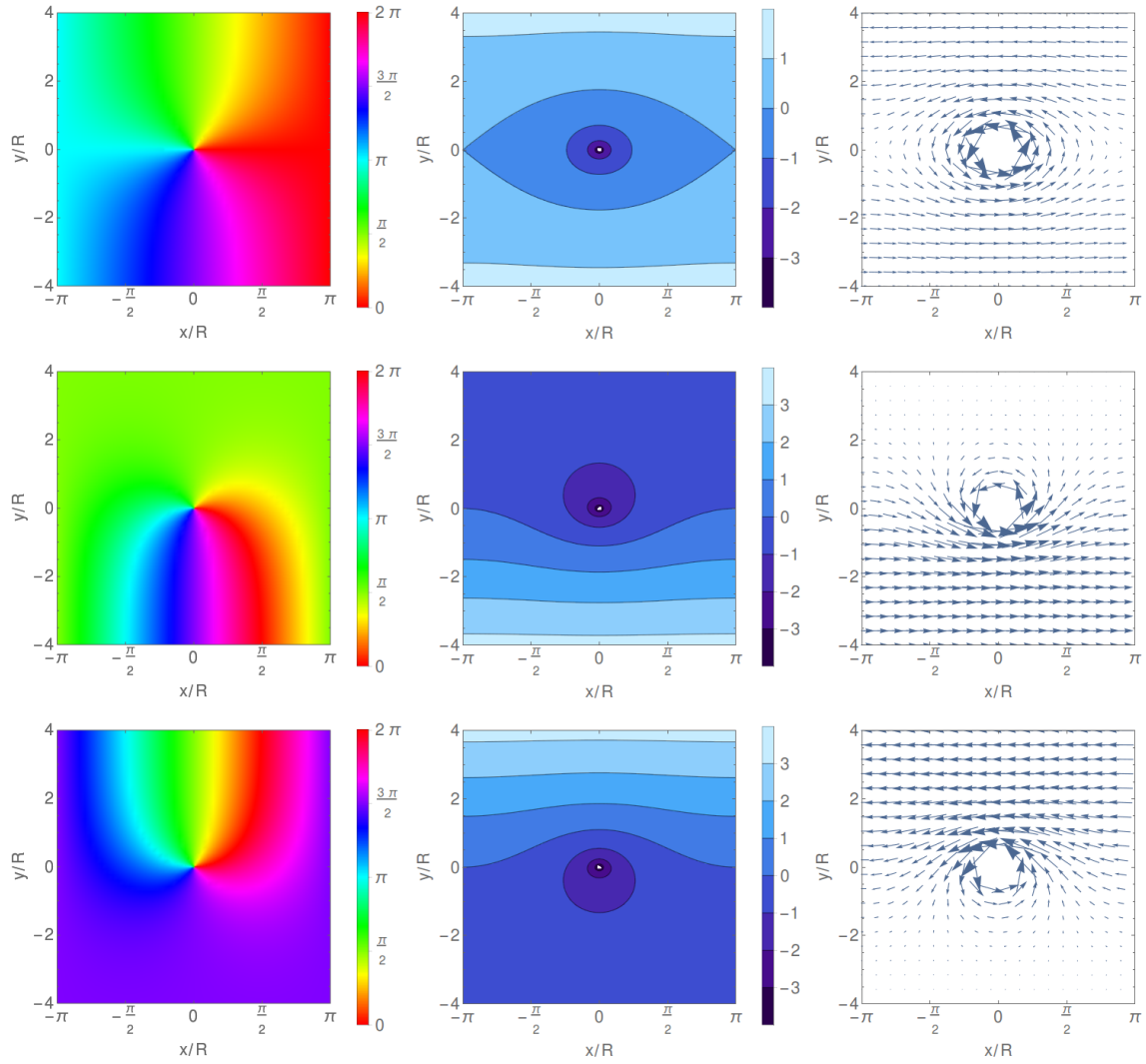

Figure 8.2: Phase φ (left), streamlines (center), and flow-field (right) for single point vortex on an infinite cylinder. Top: No additional uniform flow; since the phases at $x = \pm\pi/R$ differ by π, this is not an acceptable solution for a quantum superfluid. Middle and bottom: Additional uniform flow specified by $C = 1/2$ and $C = -1/2$, respectively (or, equivalently, $n_\uparrow = 0$ and $n_\uparrow = -1$)

.

potential using the method of images, adding virtual vortices along the strip every $2\pi R$. With the complex notation $z = x + iy$, we find

$$\begin{aligned} F(z) &= \sum_{n\in\mathcal{Z}} \ln\left(z - 2\pi R n\right) \\ &= \ln\left[\prod_{n\in\mathcal{Z}} (z - 2\pi R n)\right] \\ &= \ln\left[z \prod_{n=1}^{\infty} \left(z^2 - 4\pi^2 R^2 n^2\right)\right]. \end{aligned}$$

Note that $F(z)$ is defined only up to a constant, since terms independent of z have no effect on the generated flow-field in Eq. (7.30). The same way, the condensate phase $\varphi = \Re F$ also only carries information up to a constant. One can then write:

$$\begin{aligned} F(z) &= \ln\left[\frac{z}{2R}\prod_{n=1}^{\infty}\left(1-\frac{(z/2R)^2}{\pi^2 n^2}\right)\right] + \textit{constant} \\ &= \ln\left[\sin\left(\frac{z}{2R}\right)\right] + \textit{constant}, \end{aligned} \tag{8.4}$$

where the product expansion of the sin function was used [46]. At first sight, this complex potential should represent a single superfluid vortex at the origin of an infinite cylinder. Note, however, that $\sin(z/2R)$ changes sign for $z \to z + 2\pi R$. Therefore, by Eq. (7.31) the phase $\varphi(\boldsymbol{r}) = \Im F(z)$ would not be single-valued over the entire cylinder, since $e^{i\varphi(\boldsymbol{r})}$ remains unchanged only for $x \to x + 4\pi R$. To fix this, one has to introduce an additional linear term

$$F(z) = \ln\left[\sin\left(\frac{z}{2R}\right)\right] + i\,C\frac{z}{R}, \tag{8.5}$$

where C is a dimensionless real constant. This corresponds to adding a constant flow around the cylinder circumference, with uniform velocity $(\hbar/m_B R)\,C\hat{\boldsymbol{x}}$ according to Eq. (7.30). As a result, the previous expression for φ acquires the additional term Cx/R. The additional net phase change on going once around the cylinder is $2\pi C$. Thus merely adjusting the value C can yield any desired phase change; for example, the choice $C = 1/2$ would give zero total phase change for $y > 0$ and 2π total phase change for $y < 0$. In general, $C = j/2$ with $j \in \mathcal{Z}$ ensures a single valued φ. This behavior can be considered the hydrodynamic analog of the Bohm-Aharonov effect. Note that this a quantum effect only necessary in a coherent superfluid. In a 'classical' perfect fluid, φ carries no physical significance and is just a mathematical tool.

Fig. 8.2 (middle and bottom) shows the phase pattern for a single positive point vortex with additional flow velocity $C = \pm 1/2$. These choices ensure that the lines of constant phase all collect into the lower (upper) part of the cylinder for $C = 1/2\,(-1/2)$ leaving the fluid asymptotically at rest in the upper (lower) end of the cylinder. In these special cases, the net change in phase upon once encircling the cylinder now will be 0 or $\pm 2\pi$, merely by counting the phase lines crossing the path. Note that the two solutions may be mapped onto each other by a rotation of 180°, which effectively interchanges the two ends of the cylinder. Focus on the two simplest cases with $C = \pm 1/2$, in which case the flow vanishes as $y \to \pm\infty$ [see Fig. 8.2 (middle and bottom)]. The corresponding complex potential becomes

$$F_{\pm}(z) = \ln\left[\sin\left(\frac{z}{2R}\right)\right] \pm \frac{iz}{2R} = \ln\left(e^{\pm iz/R} - 1\right) + \text{const.} \tag{8.6}$$

Apart from the additive constant, this complex potential is just that considered by Ho and Huang [151] as the two possible conformal transformations from a plane to a cylinder (corresponding to the choice $\pm i$). This connection clarifies the special role of the two values $C = \pm 1/2$.

8.2.3 Single vortex: velocity field

The stream function $\chi(\boldsymbol{r}) = \Re F(z)$ provides a clear picture of the hydrodynamic flow through its contour plots and it is helpful to calculate it explicitly. The stream

function for one vortex on the surface of a cylinder of radius R is

$$\begin{aligned}\chi(\boldsymbol{r}) &= \Re\left\{\ln\left[\sin\left(\frac{z}{2R}\right)\right] + iC\frac{z}{R}\right\} \\ &= \frac{1}{2}\ln\left|\sin\left(\frac{x+iy}{2R}\right)\right|^2 - C\,\frac{y}{R}.\end{aligned} \tag{8.7}$$

Familiar complex trigonometric identities give

$$\begin{aligned}\chi(\boldsymbol{r}) &= \frac{1}{2}\ln\left[\sin^2\left(\frac{x}{2R}\right) + \sinh^2\left(\frac{y}{2R}\right)\right] - C\,\frac{y}{R} \\ &= \frac{1}{2}\ln\left[\frac{1}{2}\cosh\left(\frac{y}{R}\right) - \frac{1}{2}\cos\left(\frac{x}{R}\right)\right] - C\,\frac{y}{R},\end{aligned} \tag{8.8}$$

where each form is useful in different contexts. A contour plot is shown in Fig. 8.2 (middle) for $C = 0$ (top), $C = 1/2$ (middle) and $C = -1/2$ (bottom).

This stream function has the proper periodicity in x and reduces to the result $\frac{1}{2}\ln[(x^2+y^2)/4R^2] - Cy/R = \ln(r/2R) - Cy/R$ for a single vortex at the origin when $r \ll R$. In contrast, for $|y| \gg R$, the stream function has the very different and asymmetric behavior $\chi(\boldsymbol{r}) \approx |y|/(2R) - Cy/R$, independent of x. Correspondingly, $\boldsymbol{\nabla}\chi(\boldsymbol{r}) \approx \hat{\boldsymbol{y}}\,[\mathrm{sgn}(y)/(2R) - C/R]$ in this limit, and the hydrodynamic flow velocity reduces to a uniform flow (from C) plus an antisymmetric uniform flow: $\boldsymbol{v}(\boldsymbol{r}) = (\hbar/m_B)\,\hat{\boldsymbol{n}} \times \boldsymbol{\nabla}\chi(\boldsymbol{r}) \approx -\hat{\boldsymbol{x}}\,[(\hbar/2m_BR)\,\mathrm{sgn}(y) - \hbar C/m_BR]$.

With standard trigonometric identities, onr can find the hydrodynamic flow velocity induced by the single positive vortex at the origin on the surface of a cylinder:

$$\begin{aligned}\boldsymbol{v}(\boldsymbol{r}) &= \frac{\hbar}{m_B}\,\hat{\boldsymbol{n}} \times \boldsymbol{\nabla}\chi(\boldsymbol{r}), \\ &= \frac{\hbar}{2m_BR}\,\hat{\boldsymbol{n}} \times \left[\frac{\hat{\boldsymbol{x}}\sin(x/R) + \hat{\boldsymbol{y}}\sinh(y/R)}{\cosh(y/R) - \cos(x/R)} - C\hat{\boldsymbol{y}}\right], \\ &= \frac{\hbar}{2m_BR}\left[\frac{-\hat{\boldsymbol{x}}\sinh(y/R) + \hat{\boldsymbol{y}}\sin(x/R)}{\cosh(y/R) - \cos(x/R)} + C\hat{\boldsymbol{x}}\right].\end{aligned} \tag{8.9}$$

The resulting flow pattern is shown in Fig. 8.2 (right) for $C = 0$ (top), $C = 1/2$ (middle) and $C = -1/2$ (bottom). For $|x| \ll R$ and $|y| \ll R$, the hydrodynamic flow field reduces to Eq. (7.33), if θ describes the polar angle in the $\{x, y\}$-plane. For large $|y|/R$ on a cylinder, in contrast, the flow velocity reduces to a constant $\boldsymbol{v}(x, y) \approx -(\hbar/2m_BR)\,\hat{\boldsymbol{x}}\,\mathrm{sgn}(y)$. In this region the periodicity around the cylinder dominates the flow pattern, rather than the single vortex. Interesting is the velocity of the vortex core itself, as in Eq. (7.44). All terms except the linear term $\sim C$ average to zero and one finds for $C = +1/2$:

$$\boldsymbol{v}_{core} = \frac{\hbar}{4m_BR}\hat{\boldsymbol{x}}, \tag{8.10}$$

so that the core spins with exactly half the quantization velocity around the cylinder. Note that only due to the quantization condition Eq. (7.21), the vortex always has to move.

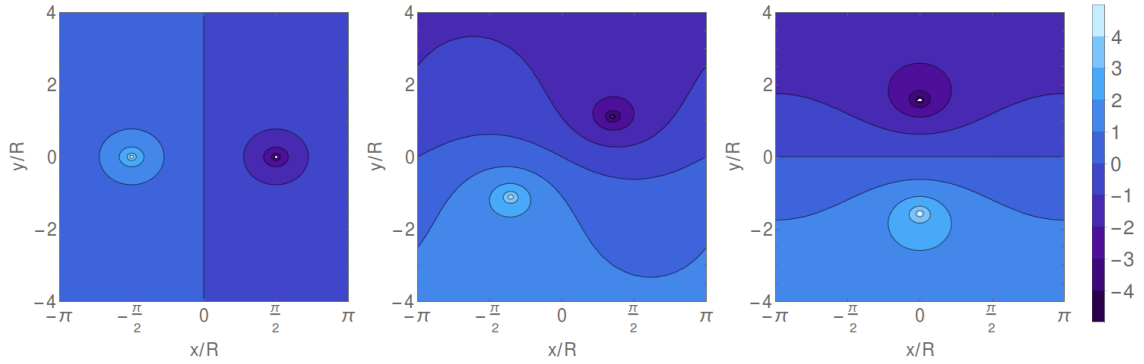

Figure 8.3: Hydrodynamic streamlines for vortex dipole $q_1 = -q_2 = 1$ on a cylinder of radius R, for various orientations of the dipole axis.

8.2.4 Multiple vortices on a cylinder

It is now straightforward to generalize the previous discussion to the case of N vortices on an infinite cylinder, each located at complex position z_n and with charge $q_n = \pm 1$ $(n = 1, \ldots, N)$, just as in Eq. (7.38). As in the previous chapter, the complex potential for multiple vortices on the cylindrical surface is simply the sum of the complex potentials of the individual vortices, always with the option of adding a uniform flow of the form iCz/R.

$$F^{(N)}(z) = i\frac{iCz}{R} + \sum_n q_n F(z - z_n) = i\frac{iCz}{R} + \sum_n q_n \ln\left[\sin\left(\frac{z - z_n}{2R}\right)\right]. \tag{8.11}$$

For an even number of vortices, this term is unnecessary, else one must have $C = j/2$ with $j \in \mathcal{Z}$ to ensure a single-valued phase φ of the condensate. In the remainder of this section and unless stated otherwise, C is taken to be zero when allowed by the quantization rule and $C = 1/2$ if not.

8.2.5 Induced motion of two vortices on a cylinder

As a special case of Eq. (8.11), consider the two vortices with charges q_1 and q_2. An example of a resulting stream function is shown in Fig. 8.3. As discussed in section 7.3.3, the motion of each vortex arises is given by the local velocity at the vortex core after regularizing the divergent contribution of the core itself. From Eq. (7.30) and Eq. (8.11), it follows that

$$\dot{y}_1 + i\dot{x}_1 = \frac{\hbar}{m_B R}\frac{q_2}{2}\cot\left(\frac{z_1 - z_2}{2R}\right), \tag{8.12}$$

$$\dot{y}_2 + i\dot{x}_2 = -\frac{\hbar}{m_B R}\frac{q_1}{2}\cot\left(\frac{z_1 - z_2}{2R}\right). \tag{8.13}$$

It is helpful to return to a vector notation to better understand the dynamics generated by Eqs. (8.12) and (8.13). For the two vortices at $\boldsymbol{r}_1$ and $\boldsymbol{r}_2$, let $\boldsymbol{R}_{12} = \frac{1}{2}(\boldsymbol{r}_1 + \boldsymbol{r}_2)$ be the centroid and $\boldsymbol{r}_{12} = \boldsymbol{r}_1 - \boldsymbol{r}_2$ be the relative position (note that the vector $\boldsymbol{r}_{12}$ runs from 2 to 1). As a result [compare Eq. (8.9)], one finds the

appropriate dynamical equations

$$\dot{\boldsymbol{R}}_{12} = \frac{\hbar}{m_B R}\left(\frac{q_1 - q_2}{4}\right)\left[\frac{\hat{\boldsymbol{x}}\sinh(y_{12}/R) - \hat{\boldsymbol{y}}\,\sin(x_{12}/R)}{\cosh(y_{12}/R) - \cos(x_{12}/R)}\right], \tag{8.14}$$

$$\dot{\boldsymbol{r}}_{12} = \frac{\hbar}{m_B R}\left(\frac{q_1 + q_2}{4}\right)\left[\frac{-\hat{\boldsymbol{x}}\sinh(y_{12}/R) + \hat{\boldsymbol{y}}\,\sin(x_{12}/R)}{\cosh(y_{12}/R) - \cos(x_{12}/R)}\right]. \tag{8.15}$$

When the vortices have opposite orientation, say $q_1 = -q_2 = q$, one has $\dot{\boldsymbol{r}}_{12} = \boldsymbol{0}$. The centroid on the other hand moves with uniform translational velocity

$$\begin{aligned}\dot{\boldsymbol{R}}_{12} &= \frac{q\hbar}{2m_B R}\left[\frac{\hat{\boldsymbol{x}}\sinh(y_{12}/R) - \hat{\boldsymbol{y}}\,\sin(x_{12}/R)}{\cosh(y_{12}/R) - \cos(x_{12}/R)}\right] \\ &= \underbrace{-\frac{\hbar}{m_B}\hat{\boldsymbol{n}}\times\boldsymbol{\nabla}\chi(\boldsymbol{r}_{12})}_{=\boldsymbol{v}(\boldsymbol{r}_{12})},\end{aligned} \tag{8.16}$$

since $\boldsymbol{r}_{12}$ is constant under dynamics. Two limits are of particular interest:

1. If $|y_{12}| \ll R$, and additionally $|x_{12}| \ll R$, the translational velocity approaches that of a vortex dipole on a plane [147]:

$$\dot{\boldsymbol{R}}_{12} = \frac{q\hbar}{m_B}\frac{\hat{\boldsymbol{x}}\,y_{12} - \hat{\boldsymbol{y}}\,x_{12}}{x_{12}^2 + y_{12}^2} = -\frac{q\hbar}{m_B}\frac{\hat{\boldsymbol{n}}\times\boldsymbol{r}_{12}}{r_{12}^2}. \tag{8.17}$$

2. If $|y_{12}| \gg R$, the term $\cosh(y_{12}/R)$ will suppress the term $\sim \hat{\boldsymbol{y}}$, and the $\hat{\boldsymbol{x}}$ component simplifies to

$$\dot{\boldsymbol{R}}_{12} = \frac{q\hbar}{2m_B R}\hat{\boldsymbol{x}}\,\mathrm{sgn}(y_{12}). \tag{8.18}$$

   In this limit each vortex is in the far-field of the other, and dynamics are dominated by the image vortices ensuring the periodic boundaries, as discussed in section 8.2.2. In this limit, the vortex dipole will circle the cylinder in a time $4\pi m_B R^2/\hbar$ independent of its angle towards the $\hat{\boldsymbol{y}}$ axis. Note that this motion is the same as that induced for one vortex with $C = \pm 1/2$, discussed in Sec. 8.2.2.

In the case of two vortices with the same orientation ($q_1 = q_2 = q$), conversely $\dot{\boldsymbol{R}}_{12}$ vanishes in Eq. (8.14), so that the centroid of the two vortices remains fixed. In contrast Eq. (8.15) becomes

$$\begin{aligned}\dot{\boldsymbol{r}}_{12} &= \dot{x}_{12}\,\hat{\boldsymbol{x}} + \dot{y}_{12}\,\hat{\boldsymbol{y}} \\ &= \frac{q\hbar}{m_B}\left[\frac{-\hat{\boldsymbol{x}}\sinh(y_{12}/R) + \hat{\boldsymbol{y}}\,\sin(x_{12}/R)}{\cosh(y_{12}/R) - \cos(x_{12}/R)}\right] \\ &= \underbrace{\frac{q\hbar}{m_B}\hat{\boldsymbol{n}}\times\boldsymbol{\nabla}\chi(\boldsymbol{r}_{12})}_{=\boldsymbol{v}(\boldsymbol{r}_{12})}.\end{aligned} \tag{8.19}$$

In this case the dynamics of R_{12} and r_{12} are now reversed. Note that the motion is non-trivial this time since r_{12} appears on both sides of Eq. (8.19). Incidentally, the motion of the relative coordinate in Eq. (8.19) is equivalent to the motion of a test particle at position r_{12} in the flow field of a single vortex on a cylinder. Hence the streamlines in Fig. 8.2 (central column) completely characterize the motion also of this vortex dipole configuration. Three regimes can be distinguished:

1. When $x_{12}^2 + y_{12}^2 \ll R^2$, the two positive vortices simply circle in the positive sense around their common center $\boldsymbol{R}_{12}$. The motion is the same as it would be on a flat plane.

2. If $\sin^2(x_{12}/2R) + \sinh^2(y_{12}/2R) < 1$, the two vortices execute closed orbits in the positive sense around their common center $\boldsymbol{R}_{12}$, but the general orbits are not circular [by definition, they remain inside the separatrix in Fig. 8.2 (top row, central column)].

3. If $\sin^2(x_{12}/2R) + \sinh^2(y_{12}/2R) > 1$, the two vortices move in opposite directions, executing periodic closed orbits around the cylinder with unit winding number. The upper vortex moves monotonically to the left and the lower vortex moves monotonically to the right, as seen in Fig. 8.2 (top row, central column), and they remain outside the separatrix. For relatively large $|y_{12}|/R$, an expansion of the above equation yields the approximate form

$$\dot{\boldsymbol{r}}_{12} \approx \frac{q\hbar}{m_B R}\left\{-\mathrm{sgn}(y_{12}/R)\left[1 - 2\cos(x_{12}/R)\, e^{-|y_{12}|/R}\right]\hat{\boldsymbol{x}} + 2\sin(x_{12}/R)\, e^{-|y_{12}|/R}\,\hat{\boldsymbol{y}}\right\}. \quad (8.20)$$

Asymptotically for $|y_{12}| \gg R$, the variable x_{12} varies linearly in time. The leading correction to this uniform horizontal motion is a small periodic modulation for both $\hat{\boldsymbol{x}}$ and $\hat{\boldsymbol{y}}$ components.

8.2.6 Energy of two vortices

The stream function $\chi(\boldsymbol{r})$ determines not only the hydrodynamic flow velocity $\boldsymbol{v}(\boldsymbol{r})$, as in Eq. (7.28). As shown below, the stream function also determines the interaction energy E_{12} between two point vortices through Eq. (8.24). Here we present a straightforward analysis that gives the interaction energy E_{12} of two vortices by integrating the kinetic-energy density, which is proportional to the squared velocity field.

In the present model, the total energy of two vortices at $\boldsymbol{r}_n$ $(n = 1, 2)$ with unit charge $q_n = \pm 1$ is the spatial integral of the kinetic-energy density

$$\begin{aligned} E_{\mathrm{tot}} &= \tfrac{1}{2} n_0 m_B \int d^2r\, [q_1\, \boldsymbol{v}(\boldsymbol{r} - \boldsymbol{r}_1) + q_2\, \boldsymbol{v}(\boldsymbol{r} - \boldsymbol{r}_2)]^2 \\ &= \tfrac{1}{2} n_0 m_B \int d^2r\, [|\boldsymbol{v}(\boldsymbol{r} - \boldsymbol{r}_1)|^2 + |\boldsymbol{v}(\boldsymbol{r} - \boldsymbol{r}_2)|^2 \\ &\quad + 2q_1 q_2\, \boldsymbol{v}(\boldsymbol{r} - \boldsymbol{r}_1) \cdot \boldsymbol{v}(\boldsymbol{r} - \boldsymbol{r}_2)] \end{aligned} \quad (8.21)$$

over the surface of the cylinder. Here, $\boldsymbol{v}(\boldsymbol{r})$ is the hydrodynamic velocity field of a single positive unit vortex at the origin, as per Eq. (8.9).

Interaction energy

As noted in Sec. 8.2.2, for large $|y|/R$, the asymptotic velocity field of a single vortex on a cylinder is uniform and finite on at least one side. Therefore the kinetic energy of any single vortex diverges linearly as the upper and lower integration boundaries on the cylinder become large (namely $|y| = Y \to \infty$). As a result, each term in the above kinetic energy of two vortices on a cylinder separately diverges. The only case

with a finite total kinetic energy is the vortex dipole with (say) $q_1 = 1$ and $q_2 = -1$, since the two asymptotic flow-fields then cancel.

It is convenient to use the stream function to characterize the local fluid velocity of the nth vortex: $\boldsymbol{v}(\boldsymbol{r} - \boldsymbol{r}_n) = (\hbar/m_B)\hat{\boldsymbol{n}} \times \boldsymbol{\nabla}\chi_n$, where $\chi_n = \chi(\boldsymbol{r} - \boldsymbol{r}_n)$ [compare Eq. (8.9)]. The operation $\hat{\boldsymbol{n}}\times$ simply rotates the following vector through $\pi/2$ and we find

$$\begin{aligned} E_{\rm tot} &= \tfrac{n_0\hbar^2}{2m_B}\int d^2r\,(q_1\boldsymbol{\nabla}\chi_1 + q_2\boldsymbol{\nabla}\chi_2)^2 \\ &= \tfrac{n_0\hbar^2}{2m_B}\int d^2r\,\{\boldsymbol{\nabla}\cdot[(\chi_1 + q_1q_2\chi_2)\,\boldsymbol{\nabla}\,(\chi_1 + q_1q_2\chi_2)] \\ &\quad - \chi_1\nabla^2\chi_1 - \chi_2\nabla^2\chi_2 - q_1q_2\left(\chi_1\nabla^2\chi_2 + \chi_2\nabla^2\chi_1\right)\}. \end{aligned} \tag{8.22}$$

The two-dimensional surface integral runs over the region $-\pi R \le x \le \pi R$ and $-Y \le y \le Y$, where $Y \to \infty$.

The first term above involves the divergence of the total derivative $\frac{1}{2}\boldsymbol{\nabla}\,(\chi_1 + q_1q_2\chi_2)^2$, and the divergence theorem reduces it to an integral on the boundary with outward unit normals. The contributions from the vertical parts at $x = \pm\pi R$ cancel because the integrand is periodic with period $2\pi R$. In general, the contributions from the horizontal parts at $y = \pm Y$ separately diverge linearly, except for the special case of a vortex dipole with $q_1q_2 = -1$. The quantity of importance is $\frac{1}{2}\partial_y(\chi_1 - \chi_2)^2$ for large $|y|$. Eq. (8.8) gives

$$\begin{aligned} \chi_1 - \chi_2 &= \frac{1}{2}\ln\left[\frac{\sin^2[(x-x_1)/2R] + \sinh^2[(y-y_1)/2R]}{\sin^2[(x-x_2)/2R] + \sinh^2[(y-y_2)/2R]}\right] \\ &\approx \frac{|y-y_1| - |y-y_2|}{2R} + \cdots \\ &= \text{constant} + \cdots \text{ for } |y| \to \infty, \end{aligned} \tag{8.23}$$

where the corrections are exponentially small for large $|y|$. It is now clear that each horizontal contribution vanishes for the present case of a vortex dipole, reflecting the overall charge neutrality.

It remains to evaluate the second line of Eq. (8.22). We already noted that $\nabla^2\chi_j = \nabla^2\chi(\boldsymbol{r}-\boldsymbol{r}_j) = 2\pi\delta^{(2)}(\boldsymbol{r}-\boldsymbol{r}_j)$, and the interaction energy (the terms involving the cross product of χ_1 and χ_2) thus becomes

$$E_{12} = -(2\pi n_0\hbar^2/m_B)\,q_1q_2\,\chi(\boldsymbol{r}_{12}), \tag{8.24}$$

for general choice of q_1q_2.

Self energy of one vortex

Eq. (8.22) also contains two self energy terms, one for each vortex. Consider the first vortex to be at the origin, then the self energy reads

$$\begin{aligned} E_1 &= \frac{n_0\hbar^2}{2m_B}\int d^2r\,\boldsymbol{\nabla}\chi(\boldsymbol{r})\cdot\boldsymbol{\nabla}\chi(\boldsymbol{r}) \\ &= \frac{n_0\hbar^2}{2m_B}\int d^2r\,\left\{\boldsymbol{\nabla}\cdot[\chi(\boldsymbol{r})\boldsymbol{\nabla}\chi(\boldsymbol{r})] - \chi(\boldsymbol{r})\nabla^2\chi(\boldsymbol{r})\right\}. \end{aligned} \tag{8.25}$$

To approach the self energy terms (those involving $-\chi_j \nabla^2 \chi_j$) in Eq. (8.22) one can cut off the singularity at ξ, which only neglects the small contribution E_{core} in Eq. (7.35) which stem from the finite size-shape of the core. In any case, these are independent of the geometry and the same for each vortex, and will only change the energy up to a constant . Using a cutoff gives

$$E_1 = \frac{\pi n_0 \hbar^2}{m_B} \ln\left(\frac{2R}{\xi}\right). \tag{8.26}$$

The finite total energy of a vortex dipole is simply the sum of the interaction energy and the two self energies

$$E_{\rm tot} = E_{12} + 2E_1 = \frac{2\pi n_0 \hbar^2}{m_B}\left[\chi(\boldsymbol{r}_{12}) + \ln\left(\frac{2R}{\xi}\right)\right]. \tag{8.27}$$

Note that this total vortex energy reduces to the familiar $\ln(r_{12}/\xi)$ for small r_{12}. Otherwise it has a very different form and grows linearly for $|y_{12}| \gg R$ (see Fig. 8.4). This interaction energy was previously discussed in previous studies of Berezinskii-Kosterlitz-Thouless behavior for a thin cylindrical film [152], and of vortex dipoles on capped cylinders [40].

8.2.7 Energy of multiple vortex dipoles

As follows from the discussion in section 8.2.4, the stream function for a set of N vortices on an infinite cylinder is the sum of individual terms $\chi = \sum_{i=n} \chi_n$, where we assume N is even. The total kinetic energy of the vortices is proportional to $\int d^2r |\boldsymbol{\nabla}\chi|^2$ over the area of the cylinder. The calculation is analogous to the version for a single pair discussed in the previous section 8.2.6, just with all possible pairings at once. The energy of multiple pairs of point vortices on the infinite cylinder is then the sum over all pairs plus the sum over all self energies

$$\begin{aligned} E_{\rm tot} = E_{\rm int} + E_{\rm self} &= \sum_{n<m} E_{nm} + \sum_{n}^{N} E_n \\ &= -\sum_{n<m} q_n q_m \frac{2\pi n_0 \hbar^2}{m_B}\chi(\boldsymbol{r}_{nm}) + N\frac{\pi n_0 \hbar^2}{m_B}\ln\left(\frac{2R}{\xi}\right). \end{aligned} \tag{8.28}$$

If the system is overall neutral, then the total energy is finite; otherwise, there are divergent constant terms that do not affect the dynamics of individual vortices. Similar divergences appear in two-dimensional electrostatics unless the total electric charge vanishes. Eqs. (8.9), (8.11) can be combined with Eq. (8.28)) to give the general dynamical equations

$$q_k \dot{x}_k = \frac{1}{2\pi\hbar}\frac{\partial E_{tot}}{\partial y_k} \quad \text{and} \quad q_k \dot{y}_k = -\frac{1}{2\pi\hbar}\frac{\partial E_{tot}}{\partial x_k}, \tag{8.29}$$

These equations resemble canonical Hamiltonian dynamics, with E_{tot} playing the role of the "Hamiltonian". The canonical variables are (x_k, y_k), and they determine the motion of the vortices on the cylinder.

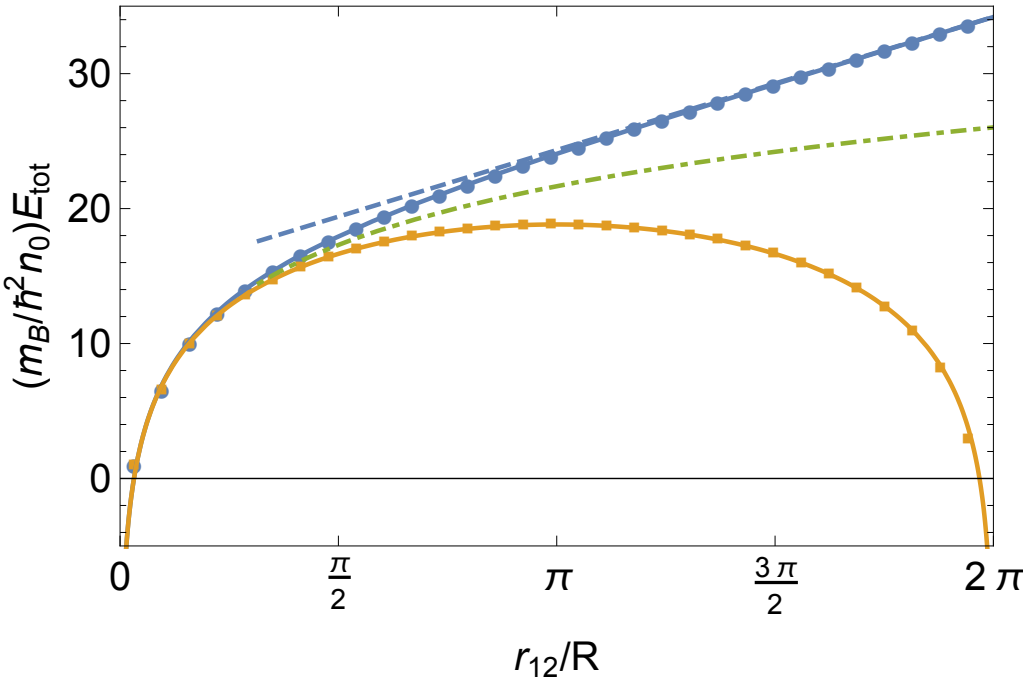

Figure 8.4: Energy of a vortex dipole on an infinite cylinder, as a function of the inter-vortex separation r_{12}, for a dipole oriented along the axis of the cylinder and moving along the equatorial direction (dark blue), and for a vortex dipole oriented along the equator and moving along the axial direction (light orange). The vortex core size is set to $\xi = R/10$. Symbols display the numerical evaluation of Eq. (8.22), and solid lines show the analytical result in Eq. (8.27). The dot-dashed green line is the usual result on the plane, $E_{\rm tot} = (2\pi\hbar^2 n_0/m_B)[\ln(r_{12}/2R) + \ln(2R/\xi)]$, and the dashed line is the asymptotic behavior for large axial separation $y_{12} \gg R$, $E_{\rm tot} = (2\pi\hbar^2 n_0/m_B)[y_{12}/(2R) + \ln(R/\xi)]$.

8.3 Vortices on a cylinder of finite length

This section considers a vortex on a finite cylinder of length L, where the method of images provides an exact solution in terms of the first Jacobi ϑ function [153]. It is structured very similar to the previous section 8.2, and allows to consider an experimentally more realistic setting. Further, the energy of a single vortex on such a finite system is also finite, and we discuss its form. Also, we discuss how the results of the previous section 8.2 are recovered in the limit $L \to \infty$.

8.3.1 Single vortex

As seen in the previous sections, the complex potential generated by a single positive vortex located at the origin of a cylinder with radius R and of infinite length, is

$$F(z) = \ln\left[\sin\left(\frac{z}{2R}\right)\right], \tag{8.30}$$

up to the linear flow needed to ensure single-valuedness. The corresponding solution on a cylinder with finite length L (with $0 \le y \le L$) follows with the method of

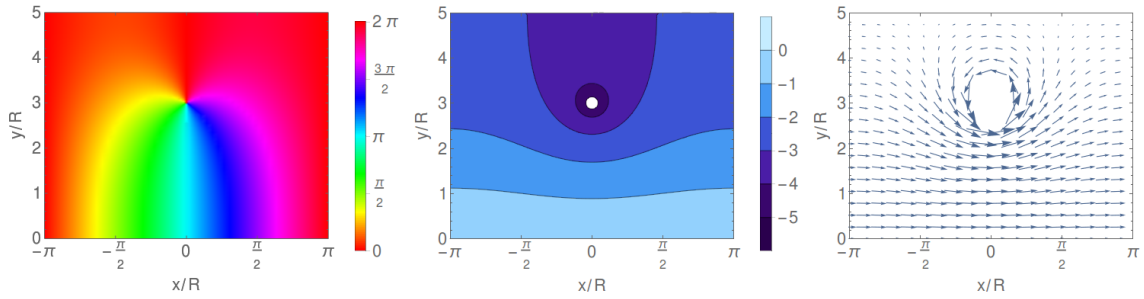

Figure 8.5: Single vortex on a finite cylinder of length $L = 5R$, located at $y_0 = 3R$. From left to right, plots show: the phase φ, the stream function χ, and the velocity field $\boldsymbol{v}$.

images. Consider a physical vortex located at $z_0 = (x_0 + iy_0)$ with $0 < y_0 < L$. Reflect the potential of the unbounded solution along the planes $y = iL$ and $y = 0$ and reverse the charge of successive image vortices. This procedure creates an infinite set of positive vortices at positions $z_{(n,+)} = z_0 + 2inL$ and negative vortices at $z_{(n,-)} = z_0^* + 2inL$. It ensures, that the flow-field is perpendicular at the boundary. We find

$$\begin{aligned} F_L(z) &= \sum_{n\in\mathbb{Z}} \left\{ \ln\left[\sin\left(\frac{z - z_{(n,+)}}{2R}\right)\right] - \ln\left[\sin\left(\frac{z - z_{(n,-)}}{2R}\right)\right] \right\} \\ &= \ln\left[\prod_{n\in\mathbb{Z}} \left(\frac{\sin(z_+/R - i\beta n)}{\sin(z_-/R - i\beta n)}\right)\right], \end{aligned} \tag{8.31}$$

where $z_+ = (z - z_0)/2$, $z_- = (z - z_0^*)/2$, and $\beta = L/R$.

Examine the infinite product in Eq. (8.31) in detail:

$$\begin{aligned} \prod_{n\in\mathbb{Z}} \left(\frac{\sin(z_+/R - i\beta n)}{\sin(z_-/R - i\beta n)}\right) =& \frac{\sin(z_+/R)}{\sin(z_-/R)} \prod_{n=1}^{\infty} \left(\frac{\sin(z_+/R - i\beta n)\sin(z_+/R + i\beta n)}{\sin(z_-/R - i\beta n)\sin(z_-/R + i\beta n)}\right) \\ =& \frac{\sin(z_+/R)}{\sin(z_-/R)} \prod_{n=1}^{\infty} \left(\frac{2\cos(2z_+/R) - q^{2n} - q^{-2n}}{2\cos(2z_-/R) - q^{2n} - q^{-2n}}\right) \\ =& \frac{\vartheta_1(z_+/R, q)}{\vartheta_1(z_-/R, q)}, \end{aligned} \tag{8.32}$$

where $q = e^{-\beta} = e^{-L/R}$. $\vartheta_1(z, q)$ is the first Jacobi ϑ function, defined by either its product form or its series form [46]:

$$\begin{aligned} \vartheta_1(z, q) =& 2q^{1/4} \sin(z) \prod_{n=1}^{\infty} (1 - q^{2n})(1 - 2q^{2n}\cos(2z) + q^{4n}) \\ =& 2\sum_{n=0}^{\infty} (-1)^n q^{(n+1/2)^2} \sin\left[(2n+1)z\right]. \end{aligned} \tag{8.33}$$

This function has simple zeros at the complex points $z = m\pi + n\pi\tau$, where $m, n \in \mathbb{Z}$ and τ is a complex number with positive imaginary part. In addition, the parameter

$q = e^{i\pi\tau}$ obeys the condition $|q| < 1$. Here, $\tau = i\beta/\pi = iL/\pi R$, such that $q = e^{-L/R}$. The final potential for a vortex located at z_0 on a cylinder of length L and radius R has then the analytic form

$$F_L(z) = \ln\left[\frac{\vartheta_1\left(\frac{z-z_0}{2R}, e^{-L/R}\right)}{\vartheta_1\left(\frac{z-z_0^*}{2R}, e^{-L/R}\right)}\right]. \tag{8.34}$$

Figure 8.5 shows the phase $\Phi(\boldsymbol{r}) = \Im F_L(z)$, the stream function $\chi(\boldsymbol{r}) = \Re F_L(z)$, and the vector velocity field $\boldsymbol{v}(\boldsymbol{r})$ obtained from $v_y + iv_x = (\hbar/m_B)F_L'(z)$. These plots may be compared to the analogous ones for an infinite cylinder shown in Fig. 8.2 (middle row)

8.3.2 Velocity of the vortex core

Regularizing the core velocity as in Eq. (7.43) is straight forward. Combining Eqs. (8.34), (7.30) and (7.43), one finds the core velocity expressed in complex form

$$\Omega_0 = \frac{\hbar}{m_B}\lim_{z\to z_0}\left(F_L'(z) - \frac{1}{z-z_0}\right) = -\frac{\hbar}{2Rm_B}\frac{\vartheta_1'\left(iy_0/R, e^{-L/R}\right)}{\vartheta_1\left(iy_0/R, e^{-L/R}\right)}, \tag{8.35}$$

where $\vartheta'(z,q)$ indicates the derivative of ϑ with respect to its variable z. This function is purely imaginary, indicating that the vortex moves solely along the $\hat{\boldsymbol{x}}$ direction, and its velocity diverges as it approaches either end of the cylinder, and therefore one of the image charges, as shown in Fig. 8.6. If the vortex is located at the middle of the cylinder at $z_0 = x_0 + iL/2$, one may use the property $\vartheta_1'(iu/2, e^{-u}) = -i\vartheta_1(iu/2, e^{-u})$ (valid for generic real $u > 0$) to show that it moves uniformly around the cylinder with speed

$$\dot{x}_0 = \hbar/2m_BR \quad \text{when} \quad y_0 = L/2, \tag{8.36}$$

as seen in Fig. 8.6. Here the rightward motion arises because we chose to pair the vortex with its image in the lower boundary of the cylinder. Had we instead used the image in the upper boundary at $z_0^* + 2iL$, the motion would have been to the left with the same magnitude. This broken symmetry is just that seen in section 8.2 associated with the choice $C = \pm 1/2$.

8.3.3 Analytical limits for long and short cylinders

When $L \gg R$, the parameter q is small, so that we may approximate $\vartheta_1(z,q) \approx 2q^{1/4}\sin(z)$. For a vortex at the complex position z_0, let $z \approx z_0 + z'$, where $z' = z - z_0$ is small. Hence the previous $F_L(z)$ becomes

$$F_L(z) \approx \ln\left[\frac{\sin(z'/2R)}{\sin\left(2iy_0/2R + z'/2R\right)}\right], \tag{8.37}$$

where we assume $z_0 = iy_0$. It is convenient to take $y_0 = L/2$, placing the vortex at the center of the cylinder.

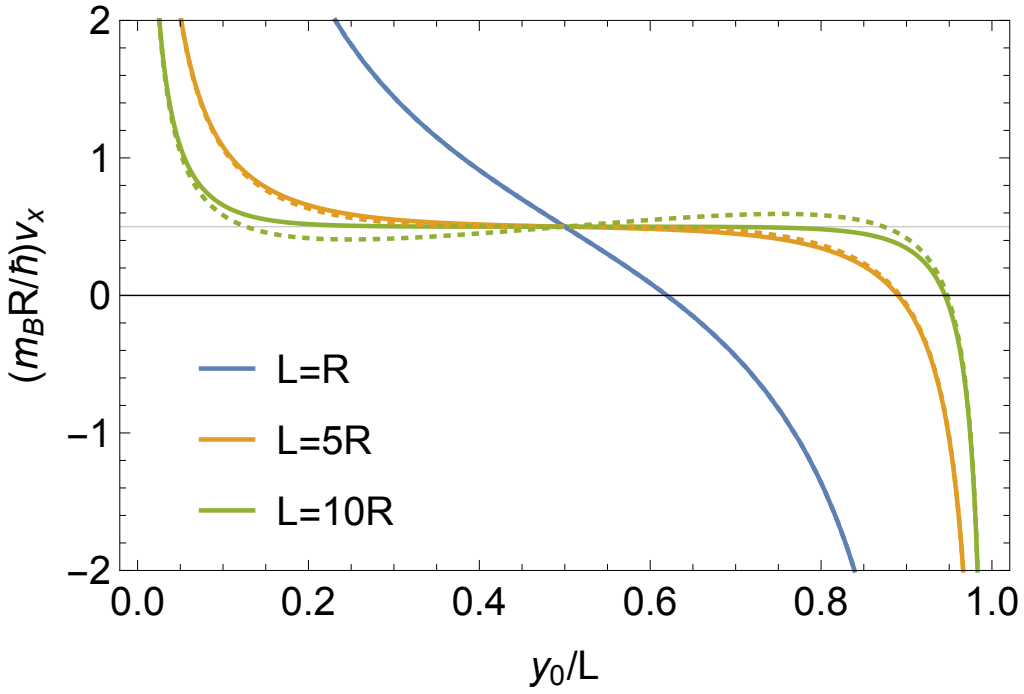

Figure 8.6: Velocity of the vortex core as a function of its vertical coordinate y_0, for various cylinder lengths L (from top to bottom, on the left side, the lines represent $L = R, 5R, 10R$). The dotted lines are the approximate results, valid in the limit $L \lesssim \pi R$, obtained from Eq. (8.41). The blue dotted line is indistinguishable from the solid one.

In this case, the denominator here can be expanded as $\sin(iL/2R + z'/2R) \approx i\frac{1}{2}e^{L/2R}(1 - iz'/2R)$. As a result, we find the approximate expression

$$F_L(z) \approx \ln \sin\left(\frac{z'}{2R}\right) + \frac{iz'}{2R} - \frac{L}{2R} - \frac{i\pi}{2} + \ln 2. \tag{8.38}$$

Apart from the additive constant terms, this result is precisely that found in section 8.2 for an infinite cylinder with a vortex at the origin and zero velocity flow on its (distant) upper rim.

When we have the opposite limit $L \ll R$, we may use the Jacobi imaginary transformation that relates a theta function with parameter τ to one with parameter $\tau' = -1/\tau$ (see for example [46]). Here, $\tau' = i\pi R/L$ and $q' = e^{i\pi\tau'} = e^{-\pi^2 R/L}$ is now small. The relevant transformation formula becomes

$$\vartheta_1\left(\frac{z}{R}, e^{-L/R}\right) = i\sqrt{\frac{\pi R}{L}}\, e^{-z^2/RL}\, \vartheta_1\left(\frac{z\pi}{iL}, e^{-\pi^2 R/L}\right). \tag{8.39}$$

In this way we find

$$\begin{aligned} F_{L\ll R}(z) &= \ln\left[\frac{e^{-[(z-z_0)^2/4RL]}\,\vartheta_1\left(\frac{\pi(z-z_0)}{2iL}, e^{-\pi^2 R/L}\right)}{e^{-\left[\left(z-z_0^*\right)^2/4RL\right]}\,\vartheta_1\left(\frac{\pi(z-z_0^*)}{2iL}, e^{-\pi^2 R/L}\right)}\right] \\ &\approx \ln\left[\frac{\sinh\left(\frac{\pi(z-z_0)}{2L}\right)}{\sinh\left(\frac{\pi(z-z_0^*)}{2L}\right)}\right] + i\frac{y_0}{L}\frac{z-x_0}{R}. \end{aligned} \tag{8.40}$$

For a short cylinder, the result converges to the complex potential generated by a row of positive vortices located at positions $z_0 + 2imL$, together with a row of negative ones at positions $z_0^* + 2imL$ (with $m \in \mathbb{Z}$).

As in Eq. (7.44), the velocity of the vortex core on a short cylinder is found by regularizing:

$$\begin{aligned}\frac{im_B\dot{x}_0}{\hbar} &= \lim_{z\to z_0}\left(F'_{L\ll R}(z) - \frac{1}{z-z_0}\right)\\ &= -\frac{\pi}{2L}\coth\left(\frac{i\pi y_0}{L}\right) + i\frac{y_0}{LR} = \frac{i\pi}{2L}\cot\left(\frac{\pi y_0}{L}\right) + i\frac{y_0}{LR}.\end{aligned} \tag{8.41}$$

For a vortex at the center of the cylinder with $y_0 = L/2$, this equation gives the familiar quantized circulating motion $\dot{x}_0 = \hbar/2m_BR$, in agreement with the result from section 8.2 for $C = 1/2$.

8.3.4 Energy of a vortex on a finite cylinder

The following very physical approach clarifies the basic physics underlying the total energy of a vortex at position z_0. Consider a larger surface $-L \le y \le L$ which includes both the original vortex and its vortex image, forming a dipole. The superfluid flow is symmetric in y, so that the energy of this extended region is twice the original energy. The complex potential on a finite cylinder (and the corresponding stream function) may be decomposed in two contributions, one coming from the vortex itself, and one from the image vortex. The notation $\mathcal{L}(z) = \ln|\vartheta_1(z/2R, q)|$ denotes the part of the stream function due to the original vortex (and not to its image), and note that $\mathcal{L}(z) \approx \ln|\eta z/2R|$ for small z, with $\eta \equiv \vartheta_1'(0, q)$. To be very specific, the stream function obtained from $F_L(z)$ is $\chi(\boldsymbol{r}, \boldsymbol{r}_n) = \mathcal{L}(z-z_n) - \mathcal{L}(z-z_n^*)$.

In complete analogy with Eq. (8.28), the total energy on the extended cylinder due to the original vortex and its image contains the core energies of the two vortices, given by the stream function $\mathcal{L}$ evaluated at the core radius, $E_{\text{core}} \equiv -\frac{1}{2}[2\pi\mathcal{L}(\xi)] \approx \pi\ln(2R/\eta\xi)$, plus the stream function $\mathcal{L}$ evaluated for the relative separation of the two vortices. By symmetry, the resulting energy is half the total energy of the flow field:

$$\begin{aligned}2E_{\text{tot}} &= \left(\frac{n_0\hbar^2}{2m_B}\right)\left(2\pi\mathcal{L}(z\to z_0+\xi) + 2\pi\mathcal{L}(z_0 - z_0^*)\right)\\ &= \left(\frac{n_0\hbar^2}{2m_B}\right)\left(2\pi\ln\left(\frac{2R}{\eta\xi}\right) + 2\pi\ln\left|\vartheta_1\left(\frac{iy_0}{R}, q\right)\right|\right)\end{aligned} \tag{8.42}$$

8.4 Single vortex on a planar annulus

The surface of a cylinder of finite length is topologically equivalent to that of a planar annulus, and therefore we expect that the vortex dynamics will be very similar in the two cases. To derive the dynamics on the annulus, the simplest way to proceed is to apply a conformal mapping as discussed in the following.

As seen in Sec. 8.3, the complex potential for a vortex located at z_0 on a cylinder

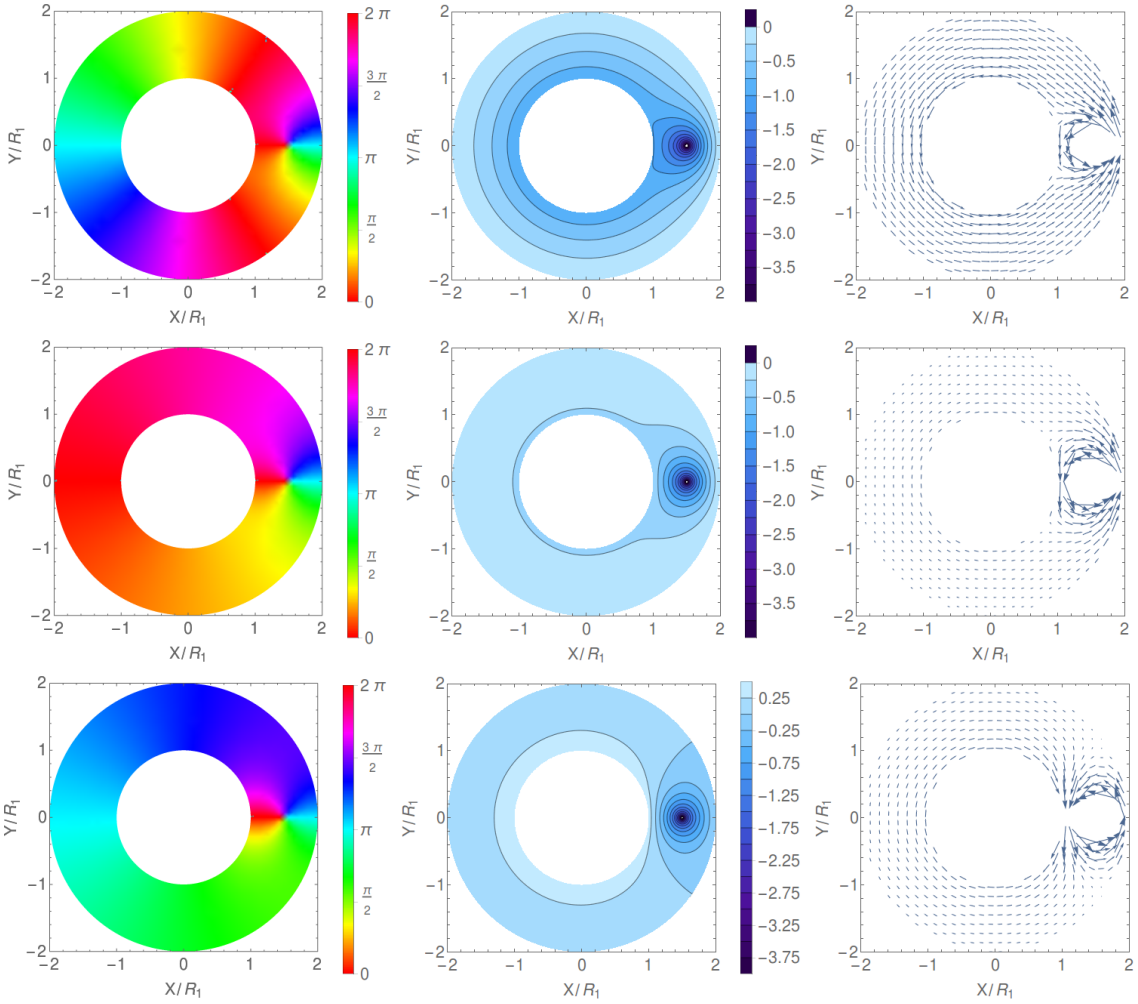

Figure 8.7: Single vortex on an annulus: (top) $n_1 = 1$, (center) $n_1 = 0$, and (bottom) $n_1 = -1$. In all cases, the vortex is located at $z_0 = 1.5R_1$, and the outer radius is $R_2 = 2R_1$. From left to right, plots show: the phase φ, the stream function χ, and the velocity flow.

of length L and radius R reads

$$F_L(z) = \ln\left[\frac{\vartheta_1\left(\frac{z-z_0}{2R}, e^{-L/R}\right)}{\vartheta_1\left(\frac{z-z_0^*}{2R}, e^{-L/R}\right)}\right] + n_\uparrow \frac{i\,z}{R}, \tag{8.43}$$

where we have allowed for the possibility of having additional quantized flow on the upper rim of the cylinder, controlled by the integer number $n_\uparrow = C - 1/2$.

A convenient conformal mapping from the finite cylinder of radius R to the annulus of radii $R_1 = R_2 \exp(-L/R)$ and R_2 is

$$z = -iR\ln(Z/R_2), \tag{8.44}$$

where Z is the Cartesian coordinate on the plane containing the annulus. This mapping sends the lower rim of the cylinder ($y = 0$) to R_2, the upper rim ($y = L$) to R_1, and maintains the orientation, so that anti-clockwise rotation around

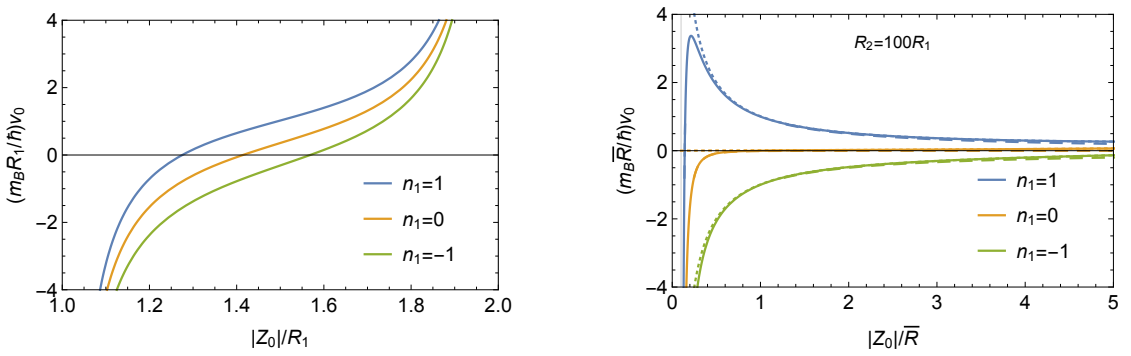

Figure 8.8: Velocity of the vortex core on an annulus. Left: results for an outer radius $R_2 = 2R_1$, and for various values of the flow circulation around the inner radius (from top to bottom, $n_1 = 1, 0, -1$). Right: wide annulus limit ($R_2 \gg R_1$); $\bar{R} = \sqrt{R_1 R_2}$ is the geometric mean of the radii, and the dotted and dashed lines show the limiting cases $R_1 \to 0$ and $R_2 \to \infty$, respectively given by Eq. (8.48) and (8.49).

the cylinder (increasing x) maps onto anti-clockwise rotation around the annulus (increasing polar angle). Applying this mapping to Eq. (8.43) yields the potential

$$\begin{aligned} F_{\rm ann}(Z) &= F_{\rm circ}(Z) + F_{\rm images}(Z) \qquad (8.45)\\ &= n_\uparrow \ln\left(\frac{Z}{R_2}\right) + \ln\left[\frac{\vartheta_1\left(-\frac{i}{2}\ln\left(\frac{Z}{Z_0}\right), \frac{R_1}{R_2}\right)}{\vartheta_1\left(-\frac{i}{2}\ln\left(\frac{ZZ_0^*}{R_2^2}\right), \frac{R_1}{R_2}\right)}\right], \end{aligned}$$

where n_1 now determines the quantized flow circulation around the inner radius R_1 of the annulus. The first term arises from the quantized flow around the inner boundary and the second arises from the images in both the inner and outer boundaries of the annulus.

The phase φ, the stream function χ and the velocity flow are shown in Fig. 8.7 for $n_1 = 0$ and $n_1 = \pm 1$. The plots for non-zero circulation $n_1 = \pm 1$ clearly indicate that the multiply connected geometry of the planar annulus (and of the cylinder) allows for the presence of two distinguishable and independent phase windings: the one around the vortex, and the one around the inner boundary.

A vortex on a planar annulus precesses around the center of the system, similar to the case of the cylindrical surface. A detailed calculation akin to Eq. (7.44) gives the tangential velocity of the vortex core

$$v_0 = \frac{\hbar}{m_B|Z_0|}\left[n_\uparrow - \frac{1}{2} + \frac{i}{2}\frac{\vartheta_1'\left(-i\ln\left(\frac{|Z_0|}{R_2}\right), \frac{R_1}{R_2}\right)}{\vartheta_1\left(-i\ln\left(\frac{|Z_0|}{R_2}\right), \frac{R_1}{R_2}\right)}\right]. \qquad (8.46)$$

When $|Z_0| = \bar{R} \equiv \sqrt{R_1 R_2}$ (the geometric mean of the inner and outer radii), the identity $\vartheta_1'\left(-i\ln\sqrt{q}, q\right) = -i\vartheta_1\left(-i\ln\sqrt{q}, q\right)$ valid for any real q $(0 < q < 1)$ immediately yields the simple result for the precessional velocity

$$v_0 = n_\uparrow(\hbar/m_B\sqrt{R_1 R_2}). \qquad (8.47)$$

It is intriguing to note that the mapping transforms the circle of radius $\bar{R}$ onto the circle $y = L/2$ going round a finite cylinder at half its length. As such, the latter result is the direct analog of Eq. (8.36). Note, however, there is an important difference: when $n_1 = 0$, a vortex along this line is stationary on the annulus, but it moves on the cylinder.

The series expansion of ϑ_1 for small q may now be used: $\vartheta_1(\alpha, q) = 2q^{1/4}(\sin\alpha - q^2 \sin 3\alpha) + \mathcal{O}(q^{25/4})$. Retaining only the lowest order, we find the limiting behavior for $R_1 \to 0$,

$$v_0 = \frac{\hbar}{m_B|Z_0|}\left(n_\uparrow + \frac{|Z_0|^2}{R_2^2 - |Z_0|^2}\right). \tag{8.48}$$

When $n_1 = 0$, one recovers the well-known result for a vortex in a trapped disk-shaped BEC [44]. To take the limit $R_2 \to \infty$ while retaining a dependence on $|Z_0|$, one needs instead to expand both ϑ_1 functions to order $q^{9/4}$. Doing so gives a rather complicated expression. In the limit $R_2 \to \infty$, one finds

$$v_0 = \frac{\hbar}{m_B|Z_0|}\left(n_\uparrow - \frac{R_1^2}{|Z_0|^2 - R_1^2}\right), \tag{8.49}$$

which is a known result for a vortex outside a cylinder of radius R_1 [149]. Finally in the limit $R_1 \ll |Z_0| \ll R_2$, one finds $v_0 = n_\uparrow\hbar/m_B|Z_0|$.

Figure 8.8 shows the various results found above for the precession velocity of a vortex on an annulus.

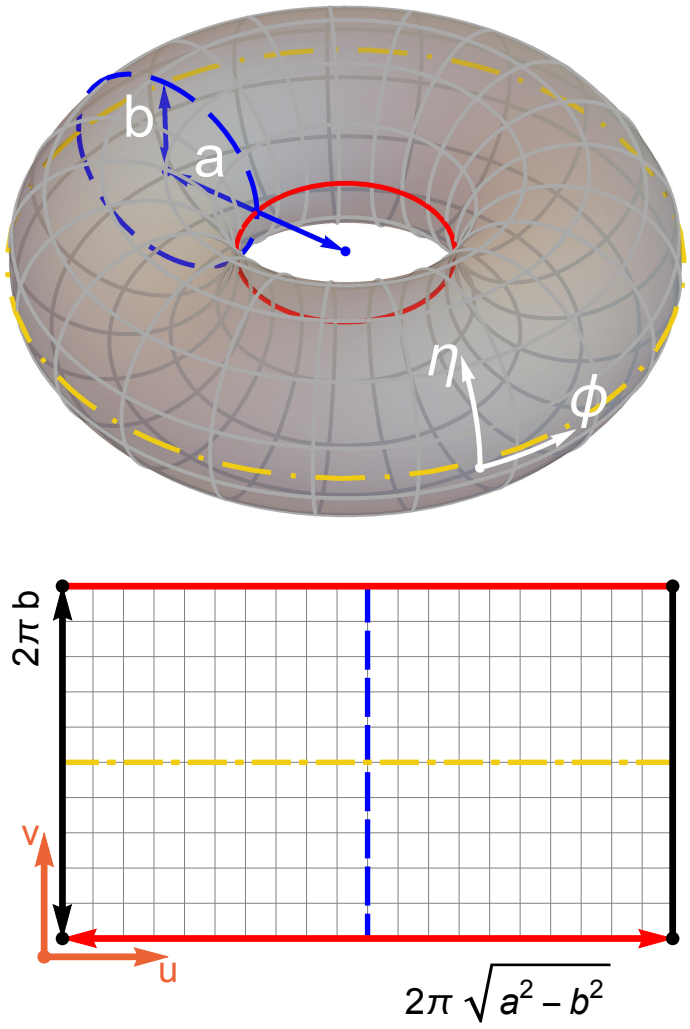

Figure 8.9: The surface of a torus with major radius a and minor radius b (top panel) can be conformally mapped to a doubly periodic cell with sides $2\pi\sqrt{a^2-b^2}$ and $2\pi b$ (bottom panel). The red, blue and yellow orbits on the torus surface appear as straight lines in the $\{u, v\}$ cell.

8.5 Superfluid vortices on a torus

In comparison to a cylinder, a torus surface has not only more quantized flow conditions Eq. (7.21) for various paths around its two circumferences, it is also not locally flat, but has a varying Gaussian curvature. To apply potential flow theory on a torus surface, one therefore has to be careful with the coordinate set, as discussed in the following subsection 8.5.1. Also, explicit curvature effects appear, as was discussed in detail in [154] in the context of superfluid vortices. Apart from this, a method of images procedure similar to the previous sections 8.2 and 8.3 can be applied, which is presented in section 8.5.2. The energy of these configurations as well as the resulting core dynamics are presented in sections 8.5.3 and 8.5.4 respectively.

8.5.1 Isothermal coordinates

A torus has a major radius a and a minor radius b, with $a \geq b$, as shown in the top panel of Fig. 8.9. Every point $\boldsymbol{s}$ on its surface can be parameterized in terms of two

angles $\phi, \eta \in \{-\pi, \pi\}$ in Cartesian coordinates:

$$\boldsymbol{s}(\phi, \eta) = \begin{cases} x = (a + b\cos\eta)\cos\phi \\ y = (a + b\cos\eta)\sin\phi \\ z = b\sin\eta, \end{cases} \tag{8.50}$$

where ϕ is the "toroidal" angle and η is the "poloidal" angle. Correspondingly, the squared line element $ds^2 = dx^2 + dy^2 + dz^2$ on the surface becomes

$$ds^2 = \underbrace{(a + b\cos\eta)^2}_{=\lambda_\phi^2} d\phi^2 + \underbrace{b^2}_{=\lambda_\eta^2} d\eta^2. \tag{8.51}$$

The coordinate set $\{\phi, \eta\}$ is curvilinear, since physical distances are related to infinitesimal elements $d\phi$ and $d\eta$ through the local scale factors λ_ϕ and λ_η. This metric distorts the gradients appearing in Eq. (7.30), precluding a formulation in terms of a complex function $F(\phi + i\eta)$ of a complex variable $\phi + i\eta$.

Such formulation is still possible, however, if one finds a suitable set of *isothermal* coordinates $\{u, v\}$ with squared line element

$$ds^2 = \lambda^2 \left(du^2 + dv^2\right), \tag{8.52}$$

which ensures that the coordinates $\{u, v\}$ are a conformal parametrization of the surface. Kirchhoff already gave such an isothermal coordinate system for a torus in 1875 [155] in the context of electro-hydrodynamics on two-dimensional surfaces:

$$\phi = \frac{u}{c}, \quad \tan\left(\frac{\eta}{2}\right) = \sqrt{\frac{a+b}{a-b}} \tan\left(\frac{v}{2b}\right), \tag{8.53}$$

with $c = \sqrt{a^2 - b^2}$. Lengthy but elementary algebra shows that $\{u, v\}$ are indeed isothermal and satisfy Eq. (8.52) with local scale factor

$$\lambda = \frac{c}{a - b\cos(v/b)}. \tag{8.54}$$

In the $\{u, v\}$ plane, these coordinates vary in a rectangular cell of dimensions $\{-\pi c, \pi c\} \times \{-\pi b, \pi b\}$ with opposite edges identified. The bottom panel of Fig. 8.9 illustrates this situation. In section 8.6, we derive the transformation given in Eq. (8.53), where we extend the analysis to more general toroidal surfaces of revolution.

8.5.2 Complex flow potential of vortex configurations

With the isothermal coordinate set $\{u, v\}$ established in the last section, we can find the flow field in terms of a complex potential function. Define the complex coordinate $w = u + iv$ describing the point $\boldsymbol{s}$ on the torus' surface and call $F(w)$ the complex flow potential associated with a set of N vortices at positions w_n with charges $q_n = \pm 1$, $n \in \{1, \ldots, N\}$. Close to each vortex core w_n the flow field must behave just as in the flat plane, as described in Chapter IV of Ref. [138]:

$$F(w) = q_n \log(w - w_n) + \mathcal{O}(w - w_n). \tag{8.55}$$

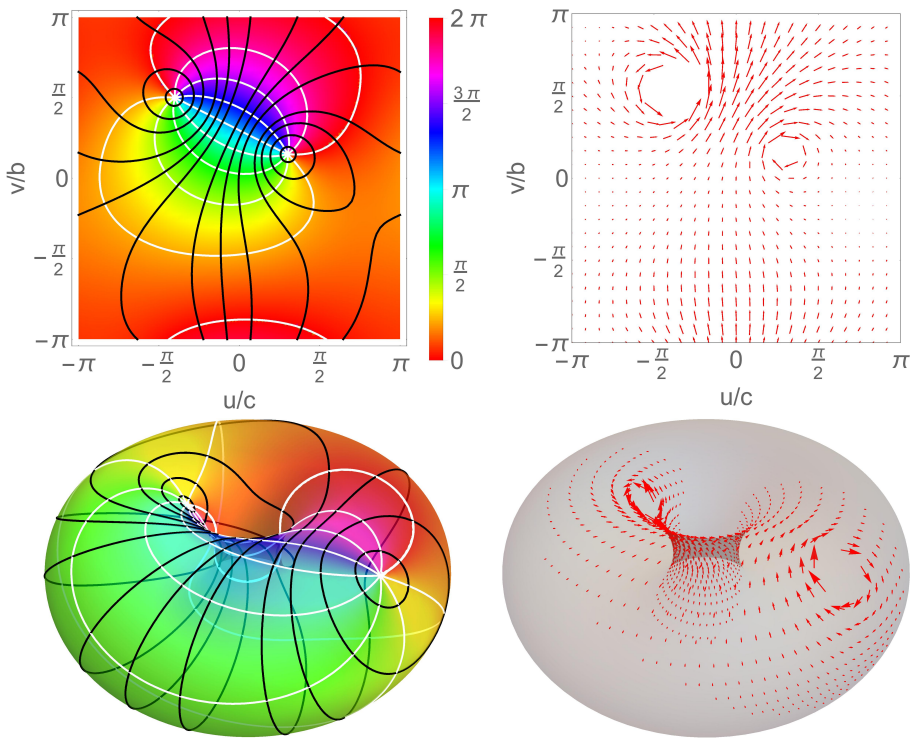

Figure 8.10: Phase (left panels) and corresponding flow field (right panels) for a torus with major radius a and minor radius b such that $a = \sqrt{2}b$, depicted in the $\{u, v\}$ coordinate set (top panels) and schematically mapped to the surface of the torus (bottom panels). The black lines in the left panels indicate stream lines, the white lines curves of constant phase. For clarity, the right panels omit points too close to the vortex cores, as well as regions with vanishing velocity.

Additionally from Eq. (7.21), the superfluid phase $\varphi = \Im\{F\}$ must wind in integer multiples (k, m) of 2π upon traversing the cell in either direction:

$$\begin{aligned} \Im\{F(w + 2\pi c)\} &= \Im\{F(w)\} + 2\pi k, \\ \Im\{F(w + i\,2\pi b)\} &= \Im\{F(w)\} + 2\pi m. \end{aligned} \tag{8.56}$$

We can distinguish two classes of functions $F(w)$ fulfilling Eq. (8.56). The first class contains simple linear functions of the form $F_{k,m}(w) = w\,(ik/c + m/b)$ with integer coefficients k, m. These potentials represent uniform flows with k elementary quanta of circulation around the toroidal direction, and m quanta along the poloidal one. The second class consists of specific complex functions that are doubly periodic within the elementary cell. These are the *elliptic functions* [46], specifically θ_1 defined in Eq. (8.33). The following property of all elliptic functions is crucial: *The sum of all residues of a doubly periodic function at its poles within any elementary cell is zero* (see Sec. 20.12 of Ref. [153]). It follows from Eq. (8.55) that the net vorticity in the system is zero: $\sum_n q_n = 0$. In particular the simplest possible configuration is a *vortex dipole* with $\{q_1 = 1, q_2 = -1\}$, which we consider in the next section.

Vortex dipoles

As seen in the bottom panel of Fig. 8.9, the elementary cell in the $\{u, v\}$ plane is a rectangle with periodic boundary conditions. To satisfy these boundary conditions, imagine tiling the whole plane with replicas of the original elementary cell complete with the vortex dipole. As discussed already in section 8.3 Specifically, in terms of the complex variable $w = u + iv$ with dimension of a length, consider a vortex dipole with a positive vortex at w_1 and a negative vortex at w_2 in the elementary cell. Analogous to the calculation presented in Eqs. (8.31) and (8.32), this yields a 'classical' flow-potential in terms of the theta function ϑ_1:

$$F_{\rm cl}(w) = \log\left[\frac{\vartheta_1\left[(w-w_1)/2c, p\right]}{\vartheta_1\left[(w-w_2)/2c, p\right]}\right] \tag{8.57}$$

As shown below, however, $F_{\rm cl}(w)$ does not yield a periodic condensate wave function, similar to the cylinder case in section 8.2. The function ϑ_1 has the quasiperiodic properties $\vartheta_1(\zeta+\pi, p) = -\vartheta_1(\zeta, p)$ and $\vartheta_1(\zeta+\pi\tau, p) = -p^{-1}e^{-2i\zeta}\vartheta_1(\zeta, p)$. A detailed analysis shows that $\Im\{F_{\rm cl}\} \to \Im\{F_{\rm cl}\} + \Re\{w_{12}\}/c$ for $v \to v + 2\pi b$, namely one revolution along the v axis, where $w_{12} = w_1 - w_2$. This behavior violates Eq. (8.56). An additional linear term ensures that the order parameter is indeed single valued:

$$F(w) = \log\left[\frac{\vartheta_1\left[(w-w_1)/2c, p\right]}{\vartheta_1\left[(w-w_2)/2c, p\right]}\right] - \frac{\Re\{w_{12}\}}{2\pi bc}w. \tag{8.58}$$

This added linear term arises from the phase coherence of the superfluid across the entire torus' surface and is wholly quantum in nature. Note that unlike the corresponding term in Eq. (8.5), this term is dependent upon te vortex dipole separation w_{12}.

The velocity field $\mathbf{w}$ of the superfluid at a point $\boldsymbol{s}(w)$ on the torus can be evaluated in the local tangent space of the surface at that point. Points at infinitesimally changed coordinates $\boldsymbol{s}(w + dw)$ correspond to points at physical distances $|ds| = \lambda|dw|$ around it; specifically the basis vectors 1 and i in the complex plane $w = u+iv$ are equivalent to the set of local dimensionless tangent vectors $\boldsymbol{u} = \partial\boldsymbol{s}/\partial u$ and $\boldsymbol{v} = \partial\boldsymbol{s}/\partial v$, with norm $|\boldsymbol{u}| = |\boldsymbol{v}| = \lambda$. In this basis, the local gradient $\boldsymbol{\nabla}$ is $\boldsymbol{\nabla} = \tilde{\boldsymbol{\nabla}}/\lambda$, where

$$\tilde{\boldsymbol{\nabla}} = \boldsymbol{u}\,\partial_u + \boldsymbol{v}\,\partial_v.\tilde{\boldsymbol{\nabla}}, \tag{8.59}$$

Eqs. (7.18) and (7.28) then become

$$\mathbf{w} = \frac{\hbar}{m_B\lambda}\tilde{\boldsymbol{\nabla}}\Phi(\boldsymbol{s}) \tag{8.60}$$

$$\mathbf{w} = \frac{\hbar}{m_B\lambda}\hat{\boldsymbol{n}} \times \tilde{\boldsymbol{\nabla}}\chi(\boldsymbol{s}), \tag{8.61}$$

which can be combined in the complex form

$$\Omega = \mathbf{w}_v + i\mathbf{w}_u = \frac{\hbar}{m_B}\frac{F'(w)}{\lambda}. \tag{8.62}$$

Here Ω denotes the complex representation of the velocity field $\mathbf{w}$. Fig. 8.10 gives an example of a vortex-dipole configuration and the corresponding phase pattern,

streamlines and flow field, both in the $\{u, v\}$ coordinate set (top panels) and mapped to the surface of a torus (bottom panels).

By construction, the imaginary part of Eq. (8.58) is doubly periodic, as is evident from the colors in the upper left panel of Fig. 8.10. In contrast, the real part is only quasiperiodic:

$$F(w + 2\pi ck + i\,2\pi bm) = F(w) - k\frac{\Re\{w_{12}\}}{b} - m\frac{\Im\{w_{12}\}}{c}, \tag{8.63}$$

with integers k and m. Nevertheless, the physical velocity field in Eq. (8.62) is doubly periodic, as is clear from its representation in terms of the gradient of the doubly periodic phase function $\Phi = \Im\{F\}$. Since $\chi = \Re\{F\}$, streamlines $\chi = c_1$ that extend to the boundary of the $\{u, v\}$ cell must be identified with other streamlines $\chi = c_1 + k\Re\{w_{12}\}/b + m\Im\{w_{12}\}/c$, with $k, m \in \mathbb{Z}$. Hence, these curves might wind several times around the torus before closing on themselves, as can be seen in the lower left panel of Fig. 8.10.

In the limit of large major radius, $a/b \gg 1$, we expect the torus to approximate the simpler geometry of an infinite cylinder with radius b. The theta function Eq. (8.33) has the remarkable imaginary transformation $(-i\tau)^{1/2}\vartheta_1(\zeta, q) = -i\exp(i\tau'\zeta^2/\pi)\vartheta_1(\zeta\tau', q')$, with $\tau' = -1/\tau$ and $q' = \exp(i\pi\tau') = e^{-\pi c/b}$. In the infinite-cylinder limit, where $c/b \to \infty$, one finds $q \to 1$ and correspondingly $q' \to 0$. The series Eq. (8.33) for the transformed theta function with parameter q' then terminates converges to the first term in the limit $a/b \to \infty$ and gives

$$F_{\text{cyl}}(w) = \log\left[\frac{\sin[i(w - w_1)/2b]}{\sin[i(w - w_2)/2b]}\right]. \tag{8.64}$$

This recovers Eq. (8.6) for a net charge zero dipole, provided one identifies u with the coordinate along the axis of the cylinder, and v with the azimuthal coordinate around its radius. In particular, the linear term in Eq. (8.58) disappears in this limit.

Flux quanta on the torus and "winding" of single vortices

The function $F(w)$ also has quasiperiodic properties in terms of the positions w_1, w_2 of the two vortices. For example, consider $w_1 \to w_1 + 2\pi c\,k + i\,2\pi b\,m$ with k, m integer. Using the properties of the Jacobi theta function we find

$$F(w) \to F(w) + q_1\left(\frac{m}{c} + i\frac{n}{b}\right)w. \tag{8.65}$$

Winding a single vortex once in the toroidal direction along u with $n = 1$ and $m = 0$ introduces an elementary quantum of flux around the poloidal direction along v, and vice versa. When $w_1 = w_2$, the complex potential defined in Eq. (8.58) reduces to $F(w) = 0$. According to Eq. (8.65), if one creates an infinitesimal vortex-antivortex pair and then annihilates it after "winding" one of its members around the torus, the superfluid initially at rest acquires an elementary flux quantum for flow in the orthogonal direction around the torus. When a poloidal winding generates a flux in the toroidal direction, the two-dimensional vortex dipole can be considered the entry and exit point of a single flux line crossing into the inside of the torus. This model realizes the classic picture of phase slippage in ring-shaped superfluids, as discussed by Anderson in Ref. [156].

Multipole configurations

The extension to cases with more than two vortices is straightforward. Defining

$$F(w, w_n) = \log\left[\vartheta_1\left(\frac{w - w_n}{2c}, p\right)\right] - \frac{\Re\{w_n\}}{2\pi bc} w, \tag{8.66}$$

we can write Eq. (8.58) as

$$F(w) = \sum_n q_n F(w, w_n). \tag{8.67}$$

Every neutral set of $2N$ vortices with elementary charges $q_n = \pm 1$ can be organized into a set of N dipoles. In this way, Eq. (8.67) describes every possible neutral set of vortices on a torus. Correspondingly, we define $f(w, w_n) = \partial_w F(w, w_n)$, which explicitly gives

$$f(w, w_n) = \frac{1}{2c} \frac{\vartheta_1'\left[(w - w_n)/2c, p\right]}{\vartheta_1\left[(w - w_n)/2c, p\right]} - \frac{\Re\{w_n\}}{2\pi bc}. \tag{8.68}$$

The complex velocity field $\Omega(w)$ then becomes

$$\Omega(w) = \frac{\hbar}{m_B} \frac{1}{\lambda} \sum_n q_n f(w, w_n). \tag{8.69}$$

An individual term $q_n F(w, w_n)$ in Eq. (8.67) can be interpreted as the complex potential of a single vortex on the torus, but this picture applies only for an ensemble of vortices with zero net charge. Otherwise $F(w, w_n)$ alone does not fulfill the conditions Eqs. (8.56) and (8.55).

8.5.3 Energy of vortex configurations

The energy of a vortex configuration is given by the kinetic energy of the flow field

$$E = \frac{1}{2} m_B n_0 \int_A du\, dv\, \lambda^2 |\mathbf{w}|^2, \tag{8.70}$$

with A the appropriate integration region. Before proceeding, we need to define carefully the region A.

On first impression, A denotes the $\{u, v\}$ elementary cell $\{-\pi c, \pi c\} \times \{-\pi b, \pi b\}$, but close to each vortex core w_n, the squared velocity $|\mathbf{w}|^2 \sim 1/|w - w_n|^2$ diverges. As a result, the integral must exclude a small disk around each core center to reflect the finite *physical* core size ξ on the torus. As long as ξ is much smaller than the smallest geometrical scale of the system, the vortex is still effectively point-like, and the torus' surface can be considered locally flat across the vortex core. In the $\{u, v\}$ plane, however, the physical length scale ξ appears locally rescaled. Specifically, the original disk of physical radius ξ on the torus becomes a disk with radius $\xi_n = \xi/\lambda_n$ in $\{u, v\}$ coordinates, where $\lambda_n = \lambda(u_n, v_n)$ is the scale factor evaluated at the vortex core. Fig. 8.11 illustrates this transformation for a vortex dipole.

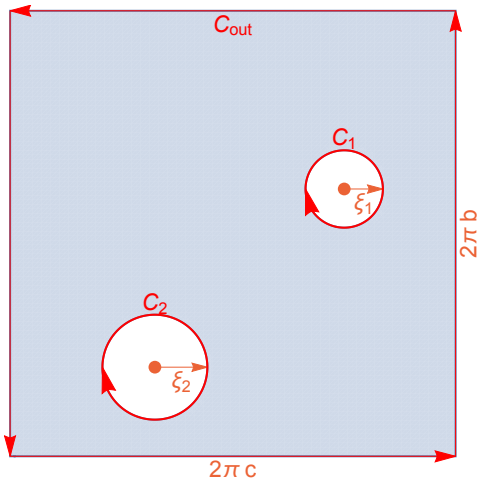

Figure 8.11: Region of integration A in the $\{u, v\}$ plane for the surface integral in Eq. (8.70) determining the kinetic energy for a vortex dipole on a torus. On the torus' surface, a small disk of physical size ξ around each vortex center must be excluded from the area of integration. In the curvilinear $\{u, v\}$ plane, this physical size is locally rescaled with the factor $\lambda(v) = c/[a - b\cos(v/b)]$. As a result, the excluded disk now has a radius $\xi_n = \xi/\lambda(v_n)$, where v_n is the v-coordinate of the nth vortex core. Green's theorem in two dimensions leads to a corresponding boundary integral (red arrows) that can be separated into two small circles $C_{1,2}$ and one outer boundary C_{out}.

In the curvilinear $\{u, v\}$ coordinates, the flow of the stream function acquires a scaling factor: $\mathbf{w} = \hbar/(m_B\lambda)\,\hat{\boldsymbol{n}} \times \tilde{\boldsymbol{\nabla}}\chi$, where $\tilde{\boldsymbol{\nabla}}$ is defined in Eq. (8.59). Consequently, the scale factors in Eq. (8.70) cancel and we find

$$\begin{aligned} E =& \frac{n_0\hbar^2}{2m_B}\int_A du\; dv\; (\tilde{\boldsymbol{\nabla}}\chi)\cdot(\tilde{\boldsymbol{\nabla}}\chi) \\ =& \frac{n_0\hbar^2}{2m_B}\int_A du\; dv\; \left[\tilde{\boldsymbol{\nabla}}\cdot\left(\chi\tilde{\boldsymbol{\nabla}}\chi\right) - \chi\tilde{\nabla}^2\chi\right] \\ =& \frac{n_0\hbar^2}{2m_B}\left(\int_{\partial A} d\boldsymbol{s}\times\hat{\boldsymbol{n}}\cdot\chi\tilde{\boldsymbol{\nabla}}\chi - \int_A du\; dv\; \chi\tilde{\nabla}^2\chi\right), \end{aligned} \tag{8.71}$$

where integration by parts in the first step and Green's theorem in two dimensions in the second were used. One can write $\chi = \sum_n q_n\chi_n$ with $\chi_n = \Re\{F(w, w_n)\}$. It is straightforward to confirm that $\tilde{\nabla}^2\chi = 2\pi\sum_n q_n\delta(u - u_n)\delta(v - v_n)$, with the Dirac delta function δ. Hence the second term in Eq. (8.71) vanishes because the region A excludes all vortex centers.

The first term in Eq. (8.71) is a boundary integral that separates into a counterclockwise (positive) loop around the outer boundary of the elementary cell and clockwise (negative) loops of radius ξ_n around each vortex center w_n. The integral around the outer boundary of the elementary cell vanishes because of the quasiperiodic properties of the complex potential in Eq. (8.67). The remaining parts are the

small circles C_n around each vortex core:

$$\begin{aligned} E_{tot} =& \frac{\hbar^2 n_0}{2m_B} \sum_n \int_{C_n} d\boldsymbol{s} \times \hat{\boldsymbol{n}} \cdot \chi \tilde{\boldsymbol{\nabla}} \chi \\ =& \frac{\hbar^2 n_0}{2m_B} \sum_{n,m,k} q_m q_k \int_{C_n} d\boldsymbol{s} \times \hat{\boldsymbol{n}} \cdot \chi_m \tilde{\boldsymbol{\nabla}} \chi_k, \end{aligned} \tag{8.72}$$

where $\tilde{\boldsymbol{\nabla}}$ acts on the first variable of $\chi_k = \Re\{F(w, w_k)\}$

Near the nth vortex, it is convenient to introduce the local vector $\boldsymbol{\delta} = (u - u_n)\,\boldsymbol{u} + (v - v_n)\,\boldsymbol{v}$, of length $|\boldsymbol{\delta}| = \xi$, for points w on C_n. Correspondingly, the local stream function behaves like $\chi_n \approx \log \delta$ apart from an additional constant. Most terms appearing in Eq. (8.72) will be negligible because of the small length $2\pi\xi$ of each curve C_n. The dominant contributions come from terms with $k = n$, since the singular behavior of $\tilde{\boldsymbol{\nabla}} \chi_n \approx \hat{\boldsymbol{\delta}}/\delta$ cancels the small circumference on C_n.

For $m \neq n$, the function χ_m reduces to the constant

$$\chi_{nm} = \Re\{F(w_n, w_m)\}, \tag{8.73}$$

apart from small corrections of order ξ/b. Terms with $m = n$ require special care, however, because of the logarithmic behavior of $\chi_n \approx \log \delta$. On the curve C_n, we can set $\boldsymbol{\delta} = \xi_n \cos\theta\ \boldsymbol{u} + \xi_n \sin\theta\ \boldsymbol{v}$ and define

$$\chi_{nn} = \log\left(\frac{\vartheta_1' \xi_n}{2c}\right) - \frac{\Re\{w_n\}^2}{2\pi bc}, \tag{8.74}$$

where $\vartheta_1' = \partial\vartheta_1(\zeta, p)/\partial\zeta\big|_{\zeta=0}$ is a constant. We can then write the dominant contributions in Eq. (8.72) in the compact form

$$\frac{2m_B E_{tot}}{\hbar^2 n_0} = -2\pi \sum_{n,m} q_n q_m \chi_{nm}. \tag{8.75}$$

Note that this expression involves a double sum over χ_{nm} and takes the same form as that for a set of vortices in the plane. Omitting the constant core-energy term in Eq. (8.74), we can group the terms in Eq. (8.75) into three categories according to their physical origin:

$$\begin{aligned} \frac{2m_B E_{tot}}{n_0 \hbar^2} =& E_{\text{class}} + E_{\text{curv}} + E_{\text{quant}} \\ =& -2\pi {\sum_{n,m}}' q_n q_m \log\left|\vartheta_1\left(\frac{w_n - w_m}{2c}, p\right)\right| \\ &+ 2\pi \sum_n \log \lambda_n \\ &+ \sum_{n,m} q_n q_m \frac{u_n u_m}{bc}, \end{aligned} \tag{8.76}$$

where the primed double sum omits terms with $n = m$. The *classical* term E_{class} gives the energy of point vortices in a classical inviscid, incompressible fluid contained in the elementary cell with a constant metric, which we may call a "flat" torus. The *curvature* term E_{curv} represents changes in the kinetic energy due to the

curvature of the torus induced by the locally distorted metric Eq. (8.52) and would not be present for a flat metric. In the context of simply connected two-dimensional superfluids, these terms have been discussed extensively in [40]. Finally, as discussed in the previous section and, the *quantum* term E_{quant} arises from the need to ensure that the superfluid order parameter is single valued and hence represents a purely quantum contribution. The next section shows how these terms generate distinct contributions to the vortex-core dynamics.

8.5.4 Vortex dynamics

The time-dependent evolution of the flow field, described by the motion of the vortex cores according to section 7.3.1, needs considerable care due to the inhomogeneous scale factor λ. This will be discussed in the case of general isothermal coordinate set with some scale factor λ in the following section, before applying it to the torus specifically

Local flow field at a vortex core

Consider a two-dimensional surface with an isothermal parametrization $\boldsymbol{s} = \{u, v\}$ [compare Eq. (8.52)] and metric parameter $\lambda(\boldsymbol{s})$. It is convenient to start from the corresponding full complex potential $F(w)$, which is logarithmically singular near the complex coordinate $w_n = u_n + iv_n$. Separating out this singular part gives the residual regular part

$$F_n^{\text{reg}}(w) = F(w) - q_n \log(w - w_n) \tag{8.77}$$

near w_n.

For a general system of well-separated vortices, we now assume that the complex potential $F(w)$ is a sum over individual vortices, as in Eq. (8.67). In the vicinity of the nth vortex $w \approx w_n$, all terms for $m \neq n$ remain finite. Thus the regular contribution to the complex potential near w_n has the intuitive form

$$\begin{aligned} F_n^{\text{reg}}(w) = &\sum_{m \neq n} q_m F(w, w_m) \\ &+ q_n \left[F(w, w_n) - \log(w - w_n)\right]. \end{aligned} \tag{8.78}$$

By construction, $F_n^{\text{reg}}(w)$ remains finite as $w \to w_n$, with a well-defined value $F_n^{\text{reg}}(w_n)$ that includes the contribution from all other vortices. Similarly, $\chi(\boldsymbol{s}) = \Re\{F(w)\}$ in the vicinity of $\boldsymbol{s}_n$ separates into a singular part $q_n \log|\boldsymbol{s} - \boldsymbol{s}_n|$ and a regular part

$$\chi_n^{\text{reg}}(\boldsymbol{s}) = \sum_{m \neq n} q_m \chi_m(\boldsymbol{s}) + q_n \left[\chi_n(\boldsymbol{s}) - \log|\boldsymbol{s} - \boldsymbol{s}_n|\right] \tag{8.79}$$

where $\chi_m(\boldsymbol{s}) = \Re\{F(w, w_m)\}$. As for the complex potential, Eq. (8.79) includes the contribution from all the other vortices. For a flow field described by such a stream function $\chi(\boldsymbol{s})$, the associated hydrodynamic velocity field is

$$\mathbf{w}(\boldsymbol{s}) = \frac{\hbar}{m_B} \frac{1}{\lambda(\boldsymbol{s})} \hat{\boldsymbol{n}} \times \tilde{\boldsymbol{\nabla}} \chi(\boldsymbol{s}), \tag{8.80}$$

where $\tilde{\boldsymbol{\nabla}} = \boldsymbol{u}\,\partial_u + \boldsymbol{v}\,\partial_v$, as in Eq. (8.59).

Near the vortex core at $\boldsymbol{s}_n$, we write $\hat{\boldsymbol{n}} \times \tilde{\boldsymbol{\nabla}}\chi(\boldsymbol{s}) = q_n \hat{\boldsymbol{n}} \times (\boldsymbol{s} - \boldsymbol{s}_n)/|\boldsymbol{s} - \boldsymbol{s}_n|^2 + \hat{\boldsymbol{n}} \times \tilde{\boldsymbol{\nabla}}\chi_n^{\mathrm{reg}}(\boldsymbol{s})$. An expansion of $\mathbf{w}(\boldsymbol{s})$ in powers of $\boldsymbol{s} - \boldsymbol{s}_n$ gives

$$\begin{aligned}\mathbf{w}(\boldsymbol{s}) =& \frac{\hbar}{m_B}\left[\frac{1}{\lambda(\boldsymbol{s}_n)} + \tilde{\boldsymbol{\nabla}}\left(\frac{1}{\lambda(\boldsymbol{s})}\right)_{\boldsymbol{s}\to\boldsymbol{s}_n} \cdot (\boldsymbol{s} - \boldsymbol{s}_n)\right] \times \\ & \times \left[q_n \frac{\hat{\boldsymbol{n}} \times (\boldsymbol{s} - \boldsymbol{s}_n)}{|\boldsymbol{s} - \boldsymbol{s}_n|^2} + \hat{\boldsymbol{n}} \times \tilde{\boldsymbol{\nabla}}\chi_n^{\mathrm{reg}}(\boldsymbol{s}_n)\right] + \mathcal{O}(\boldsymbol{s} - \boldsymbol{s}_n). \end{aligned} \tag{8.81}$$

Introducing the normalized vector $\hat{\boldsymbol{s}} = (\boldsymbol{s} - \boldsymbol{s}_n)/|\boldsymbol{s} - \boldsymbol{s}_n|$, we have the leading terms

$$\begin{aligned}\mathbf{w}(\boldsymbol{s}) =& \frac{\hbar}{m_B}\frac{1}{\lambda(\boldsymbol{s}_n)}\hat{\boldsymbol{n}} \times \left[q_n \frac{\hat{\boldsymbol{s}}}{|\boldsymbol{s} - \boldsymbol{s}_n|} + \tilde{\boldsymbol{\nabla}}\chi_n^{\mathrm{reg}}(\boldsymbol{s}_n)\right. \\ & \left. - q_n \frac{\hat{\boldsymbol{s}}}{\lambda(\boldsymbol{s}_n)}\left(\tilde{\boldsymbol{\nabla}}\lambda(\boldsymbol{s}_n) \cdot \hat{\boldsymbol{s}}\right)\right] + \mathcal{O}(\boldsymbol{s} - \boldsymbol{s}_n). \end{aligned} \tag{8.82}$$

Now, we can apply the average $\langle \mathbf{w} \rangle_{s_n}$ defined in Eq. (7.42) to properly regularize the local velocity.

This angular average can be applied term by term to Eq. (8.82). The first term vanishes because $\langle \hat{s}_k \rangle = 0$, the second term is simply a constant, and the identity $\langle \hat{s}_k \hat{s}_l \rangle = \frac{1}{2}\delta_{kl}$ simplifies the last term. In this way we find the final result for the translational velocity

$$\begin{aligned}\mathbf{w}_n =& \frac{\hbar}{m_B}\frac{1}{\lambda(\boldsymbol{s}_n)}\hat{\boldsymbol{n}} \times \left[\tilde{\boldsymbol{\nabla}}\chi_n^{\mathrm{reg}}(\boldsymbol{s}) - \frac{q_n}{2\lambda(\boldsymbol{s}_N)}\tilde{\boldsymbol{\nabla}}\lambda(\boldsymbol{s})\right]_{\boldsymbol{s}\to\boldsymbol{s}_n} \\ =& \frac{\hbar}{m_B}\frac{1}{\lambda(\boldsymbol{s}_n)}\hat{\boldsymbol{n}} \times \left[\tilde{\boldsymbol{\nabla}}\left(\chi_n^{\mathrm{reg}}(\boldsymbol{s}) - \frac{q_n}{2}\log\lambda(\boldsymbol{s})\right)\right]_{\boldsymbol{s}\to\boldsymbol{s}_n}. \end{aligned} \tag{8.83}$$

A useful equivalent form is

$$\begin{aligned}\mathbf{w}_n =& \frac{\hbar}{m_B}\frac{1}{\lambda(\boldsymbol{s}_n)} \\ & \times \left[\left(\boldsymbol{v}\frac{\partial}{\partial u} - \boldsymbol{u}\frac{\partial}{\partial v}\right)\left(\chi_n^{\mathrm{reg}}(\boldsymbol{s}) - \frac{q_n}{2}\log\lambda(\boldsymbol{s})\right)\right]_{\boldsymbol{s}\to\boldsymbol{s}_n}. \end{aligned} \tag{8.84}$$

Application to a torus

For a torus, the regular part of the complex potential reads

$$\bar{F}_n^{\mathrm{reg}}(w) = \sum_{m\neq n} q_m \log\vartheta_1\left(\frac{w - w_m}{2c}, q\right) - \sum_m \frac{q_m u_m w}{2\pi b c}. \tag{8.85}$$

Correspondingly, the regular part of the stream function can be taken as $\bar{\chi}_n^{\mathrm{reg}}(\boldsymbol{s}) = \Re\{\bar{F}_n^{\mathrm{reg}}(w)\}$ The two real vector components in Eq. (8.84) can be combined to give the rather compact complex expression

$$\begin{aligned}\Omega_n =& \mathbf{w}_{n,v} + i\mathbf{w}_{n,u} \\ =& \frac{\hbar}{m_B}\frac{1}{\lambda(v_n)}\left(\sum_{m\neq n} q_m f(w_n, w_m)\right. \\ & \left. + i\frac{q_n}{2}\frac{\lambda'(v_n)}{\lambda(v_n)} - q_n\frac{u_n}{2\pi b c}\right), \end{aligned} \tag{8.86}$$

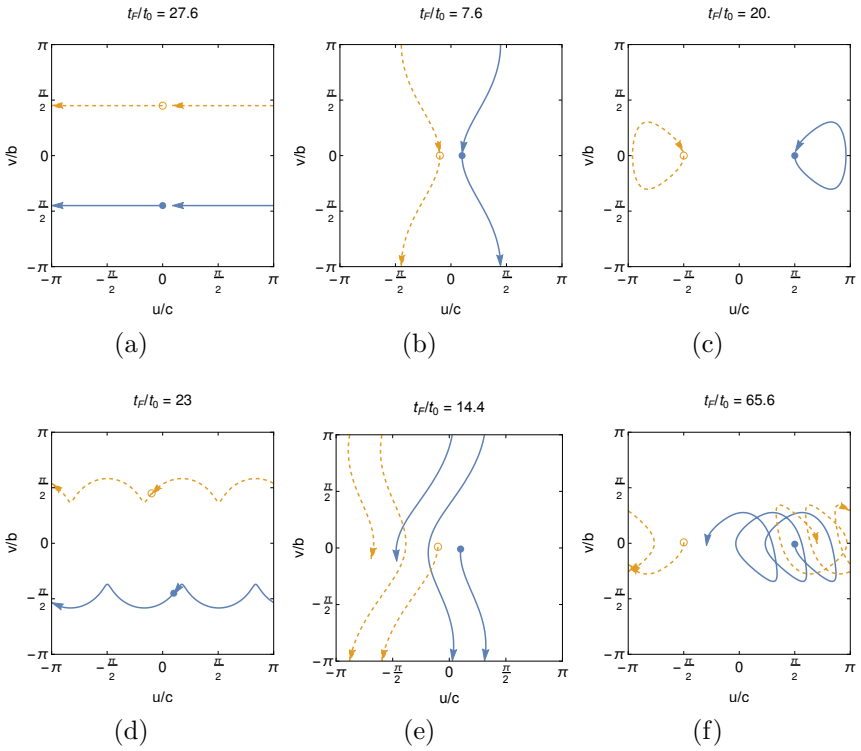

Figure 8.12: Trajectories of a vortex dipole on the surface of 3D torus shown in the u, v plane. Initially a vortex is set at position $z_{1,0}$ (blue dot) and an anti-vortex at position $z_{2,0}$ (orange dot), their trajectories (blue and orange arrows respectively) are then integrated according to Eq. (8.87), up to a final time t_F, measured in units $t_0 = m_B b^2/\hbar$. *Symmetric toroidal configuration:* The vortex dipole moves rigidly in a straight line perpendicular to the dipole axis (8.12a). *Symmetric poloidal configuration:* The curvature and quantum terms in Eq. (8.76) initially drive the dipole apart in circling the torus in the poloidal direction (8.12b). For larger separations, they alter the motion into closed loops on the outer side of the torus (8.12c). *Asymmetric configurations:* dipoles not aligned symmetrically around either axis experience a hybrid trajectory. Configurations close to the symmetric cases lead to a combination of both types of trajectories on separated time scales, as shown in (8.12d to 8.12f).

with $f(w_n, w_m)$ defined by Eq. (8.68). Note that Eq. (8.86) is the physical velocity of the vortex. In the curvilinear coordinate set $\boldsymbol{s} = \{u, v\}$, however, the equations of motion for each vortex take the form $\dot{u}_n = \Im\{\Omega_n\}/\lambda_n$ and $\dot{v}_n = \Re\{\Omega_n\}/\lambda_n$, where $\lambda_n = \lambda(\boldsymbol{s}_n)$.

Kirchhoff [157] introduced the Hamiltonian formulation for classical point vortices on a plane (see also Sec. 157 of [138]) and Refs. [158, 159] extended the description to include more general planar geometries. Here, a detailed analysis shows that vortex dynamics on a torus can also be recast in a Hamiltonian form, where the coordinates u_n and v_n serve as conjugate variables and Eq. (8.75) gives the energy function:

$$\begin{aligned} n_0 \hbar\, 2\pi q_n\, \dot{u}_n &= \frac{1}{\lambda_n^2} \frac{\partial}{\partial v_n} E_{\rm tot}(\boldsymbol{s}_1, \ldots, \boldsymbol{s}_N) \\ n_0 \hbar\, 2\pi q_n\, \dot{v}_n &= -\frac{1}{\lambda_n^2} \frac{\partial}{\partial u_n} E_{\rm tot}(\boldsymbol{s}_1, \ldots, \boldsymbol{s}_N), \end{aligned} \tag{8.87}$$

This formulation ensures that the time evolution conserves the energy in Eq. (8.75), as it must, because the system has no dissipation.

The first set of terms in Eq. (8.86) describes the velocity induced by all other vortices at the position of the nth vortex core. The second term corresponds to the curvature term E_{curv} in Eq. (8.76); it induces a purely toroidal motion. The last term is the effect of the quantum term E_{quant} in Eq. (8.76) of the nth vortex on itself, inducing a purely poloidal motion.

In a flat two-dimensional plane, vortex dipoles always move rigidly in the direction perpendicular to the dipole axis given by the right-hand rule. On the torus, however, the possible trajectories are much more complicated, as depicted in Fig. 8.12, where Eq. (8.87) was integrated numerically for a representative sample of initial vortex positions. The "classical" rigid dipole motion occurs only for a "poloidal" initial vortex dipole aligned along the poloidal axis and symmetric with respect to the $v = 0$ line in the $\{u, v\}$ plane as shown in Fig. 8.12a. In this case, the motion is purely toroidal, analogous to that on an infinite cylinder. In contrast, the poloidal movement of a toroidal dipole induces stretching of the toroidal distance between vortices (Fig. 8.12b) due to the v dependence of the curvature terms Eq. (8.76). Indeed, the vortices can even execute counter-rotating loops (Fig. 8.12c) for sufficiently large initial separation. The remainder of Fig. 8.12 illustrates various other initial configurations. Of interest are also static dipole configurations, where $\Omega_{1,2} = 0$. Symmetric configurations with either a purely toroidal or poloidal dipole axis allow for such solutions, depending on the geometric scales a and b. Interestingly, for a "classical" fluid without the E_{quant} term, a toroidal dipole would be static in the case of $w_1 = w_2 = \pm\pi c/2$, when the vortex cores are separated by the maximal distance possible on the torus. The quantum term E_{quant} however forces this configuration to move (see Fig. 8.12c) and the equilibrium distance varies.

8.6 Generalized toroidal surfaces of revolution

The discussion above can be extended to surfaces similar to the torus by finding an appropriate isothermal coordinate set where the complex potential formalism applies. Consider a two-dimensional curve, described parametrically as $\boldsymbol{f}(\eta) = \{f_1(\eta), f_2(\eta)\}$, $\eta \in \{-\pi, \pi\}$, such that f is closed and never crosses itself. A corresponding surface of revolution has the parametrization [compare Eq. (8.50)]

$$\boldsymbol{s}(\phi, \eta) = \begin{cases} x = [a + f_1(\eta)] \cos\phi \\ y = [a + f_1(\eta)] \sin\phi \\ z = f_2(\eta) \end{cases} \qquad \phi, \eta \in \{-\pi, \pi\}, \tag{8.88}$$

where we restrict to cases $a + \min_\eta f_1(\eta) > 0$, such that the resulting surface has a central hole and hence is multiply connected. Such surfaces are known as toroids. The line element corresponding to Eq. (8.88) is

$$ds^2 = \underbrace{[a + f_1(\eta)]^2}_{\lambda_\phi(\eta)^2} d\phi^2 + \underbrace{\left[f_1'(\eta)^2 + f_2'(\eta)^2\right]}_{\lambda_\eta(\eta)^2} d\eta^2, \tag{8.89}$$

defining λ_ϕ and λ_η. When $\boldsymbol{f}$ describes a circle with radius b, these expressions yield the parametrization of a torus in Eq. (8.50).

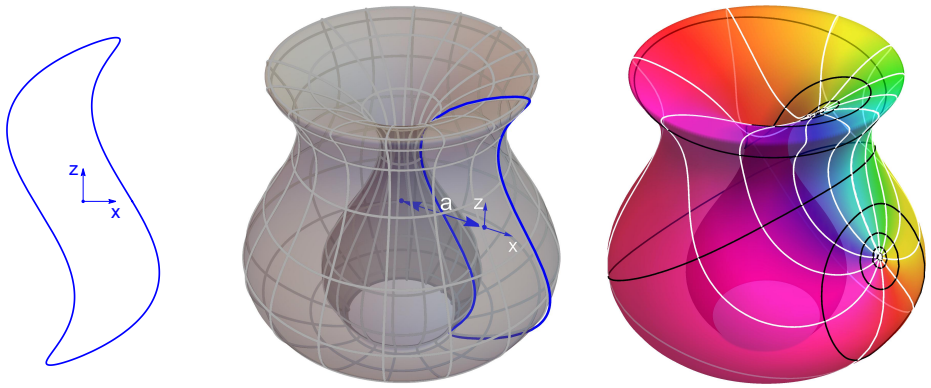

Figure 8.13: *Left panel:* a closed line in the x, z plane described by $\boldsymbol{f}(\eta) = d\{4\cos\eta - \cos 2\eta, 10\sin\eta - 2\sin 3\eta\}$, where d is a length that sets the physical size of the surfaces. *Center panel:* toroid generated by rotating the curve $\boldsymbol{f}$ around a central axis with $a = 6\gamma$, see Eq. (8.88). *Right panel:* The phase pattern induced by a vortex dipole on the surface, via the mapping Eq. (8.92), with $\gamma = d$, and the flow potential Eq. (8.94).

8.6.1 Isothermal coordinate set

As before, for a description of a flow field via a complex potential, we must find an isothermal coordinate set. Let us define $\{u, v\}$ such that $\eta(u, v) = \eta(v)$ only and $\phi(u, v) = \phi(u)$ only. Inserting this ansatz into Eq. (8.89), we find

$$ds^2 = \lambda_\phi^2 \left(\frac{d\phi}{du}\right)^2 \left(du^2 + \frac{\lambda_\eta^2 \left(\frac{d\eta}{dv}\right)^2}{\lambda_\phi^2 \left(\frac{d\phi}{du}\right)^2} dv^2\right). \tag{8.90}$$

For the coordinate set $\{u, v\}$ to be isothermal, the factor in the second term in Eq. (8.90) must equal unity:

$$\lambda_\phi(\eta)\frac{d\phi}{du} = \lambda_\eta(\eta)\frac{d\eta}{dv}. \tag{8.91}$$

Since $\lambda_\phi, \lambda_\eta$ depend on η only, we assume $\phi = u/\gamma$, with γ some arbitrary length scale. Then Eq. (8.91) can be solved for $v(\eta)$ by separation of variables

$$\frac{\lambda_\eta(\eta)}{\lambda_\phi(\eta)} d\eta = \frac{1}{\gamma}\, dv, \quad \text{which gives}$$

$$v(\eta) = \gamma \int_0^\eta \frac{\sqrt{f_1'(\eta')^2 + f_2'(\eta')^2}}{a + f_1(\eta')} d\eta'. \tag{8.92}$$

The resulting line element is

$$ds^2 = \lambda_f(v)^2 \left(du^2 + dv^2\right), \; \lambda_f(v) = \frac{a + f_1[\eta(v)]}{\gamma} \tag{8.93}$$

where $\eta(v)$ is the inversion of Eq. (8.92). The integrand in Eq. (8.92) is always positive, so that $v(\eta)$ is bijective and the inverse $\eta(v)$ well defined. In practice, as long as the length $\int_{-\pi}^{\pi} |\boldsymbol{f}(\eta)'| d\eta$ is finite, both $v(\eta)$ and $\eta(v)$ can easily be evaluated numerically.

For a standard torus with $\boldsymbol{f}(\eta) = b\{\cos\eta, \sin\eta\}$ and $\gamma = c = \sqrt{a^2 - b^2}$, one recovers Kirchhoff's transformation Eq. (8.53).

8.6.2 Flow potential

In the $\{u, v\}$ coordinate set, the toroidal surface of revolution is a doubly periodic cell with dimensions $2\pi\gamma \times \Delta v$, with $\Delta v = v(\pi) - v(-\pi)$. Considering a superfluid confined to the surface described by Eq. (8.88), the problem of finding the flow potential of vortex configurations in the $\{u, v\}$ plane is identical to that of the torus: s

$$\begin{aligned} F_f(w) &= \sum_n q_n F_f(w, w_n) \\ F_f(w, w_n) &= \log \vartheta_1 \left(\frac{w - w_n}{2\gamma}, p_f \right) - \frac{\Re\{w_n\}}{\gamma \Delta v} w, \end{aligned} \tag{8.94}$$

with $p_f = \exp(-\Delta v / 2\gamma)$.

All results obtained in the previous section still apply, with the generalized scaling factor λ_f in Eq. (8.93) replacing the scaling factor $\lambda(v)$. Fig. 8.13 gives an example of a toroidal surface of revolution and the corresponding phase pattern of a vortex dipole on its surface. Eq. (8.84) can then used to determine the movement of the cores.

Chapter 9

Conclusion

A thin superfluid film on a cylindrical surface of radius R allows for closed paths around the circumference of the cylinder as well as those around a vortex. As discussed in section 8.2, this condition requires that a single vortex on an infinite cylinder moves in the azimuthal direction with uniform velocity $\pm\pi\hbar/2m_BR$ as the simplest of many allowed quantized speeds. Clearly, the topology of an infinite cylinder differs from that of a plane, yielding these quantized translational motions. For a finite cylinder of length L, the boundary conditions require pairing with an image vortex on either end of the cylinder. The resulting vortex dipole (the original positive vortex and a negative image) automatically ensures that the phase φ properly winds around the cylinder and gives the appropriate translational velocity of the original vortex, where the choice of image (top or bottom) determines the broken symmetry and the sense of circumferential motion around the cylinder.

The dynamics on a torus prove even more intricate. Interestingly, here the additional quantization condition leads to an additional term in the dynamics for vortex dipoles, that differentiates it strongly from a classical perfect fluid. A particularly striking example is shown in Fig. 8.12c, where a classical dipole could be completely stationary. Following our discussion in section 8.6, we expect the quantum effect on vortex dynamics to be robust with regards to the specific shape of the trap geometry, as long as it is toroidal.

A superfluid film on such complicated surfaces raises many experimental challenges. In the case of a cylinder, the geometry is fortunately mappable to a superfluid on a planar annulus, which was also studied in detail in connection with three-dimensional superfluid ^{4}He [160, 161]. More recently, the study of cold atoms has made dramatic progress in preparing superfluid annuli with various dimensions [162, 163, 164, 165, 166], leading to the creation of very thin planar annuli with closely controlled radii [167]. These measurements rely on interferometric techniques to study the superfluid velocity induced by various quenches. Experimentally, the realization of a toroidal superfluid seems more difficult. BECs have been created in a multitude of trap shapes with unprecedented control over the geometry [168, 16, 169]. Toroidal shell traps can be engineered for the gas, but the effect of gravity may lead to inhomogeneities in the thickness of the fluid. A possible approach would be to do the experiment under microgravity. Such conditions may be obtained, for example, in a free-falling "Einstein elevator" [170], or aboard the International Space Station, where a cold-atom experiment was recently deployed. Current proposals indeed envision the creation of a thin ellipsoidal shell of BEC in

space [169].

It has also proven possible to study the time-resolved dynamics of vortices [171], with a time-resolution of $\sim 90ms$, which were nucleated by rapid thermal quenching. Alternatively, vortices may also be created by merging multiple independent condensates [172]. Various techniques for optical imprinting of vortices have also been proposed [173, 174]. It seems straight forward to apply these techniques to nucleate vortices in a planar annulus, and it should be possible to adapt them to cylindrical and toroidal surfaces. Especially thermal quenching seems a suitable candidate for the nucleation of vortices independent of the superfluid geometry. Since an imprinting beam will always pierce the BEC twice in a cylindrical configuration and at least twice in a toroidal configuration, it will create a vortex anti-vortex pair in both cases. On the toroidal surface, this is consistent with the condition of zero net vorticity, however on a cylindrical surface the nucleation of an interesting single vortex state would be excluded.

A way to observe such a state might be preparing a superflow around the cylinder circumference, or even the planar annulus, in an easily variable trap geometry. Consider preparing uniform superflow with a single quantum first and then expanding the cylinder radius R or annulus radii adiabatically, that is at rates much smaller than the speed of sound in the BEC. Assuming the system cannot lose energy, it is still required to flow slower due to the decreasing speed quantum. An exciting scenario would be the nucleation of a single vortex, acting as a barrier between a region with flow of one elementary speed quantum and one with two. Upon increasing the radius, said vortex would move from the cylinder boundary higher up the axis to keep the kinetic energy conserved. A similar approach might also be usable to controllably create vortex-antivortex pairs on toroids.

Beyond the intrinsic interest of vortex dynamics, the study of such vortices on cylindrical, toroidal or more complicated closed surfaces might prove interesting for various fields of study. The inter-vortex energy plays a large role in the transition to the superfluid phase at low temperatures, which is of Berezinskii-Kosterlitz-Thouless (BKT) type in two dimensions [175]. As shown in the last chapter, this interaction energy is altered significantly on the surfaces discussed. This implies a possible modification of the BKT dynamics, so thermodynamics of vortex excitations in multiply connected geometries merits further study (see [152]). Since the quantization of point vortices requires phase coherence on a length scale much shorter than that required for the quantization of flow around the torus or cylinder circumferences, the vortices on such surfaces might prove interesting for studying finite-temperature effects and the predicted coherence length in BKT-type superfluids.

More generally, superfluid vortices are the building blocks for quantum turbulence, which is speculated to behave very differently at smaller length scales [176]. Studying vortex dynamics in different geometries such as the closed surfaces considered here might allow for additional insights. Especially the toroidal surface might prove interesting, since it has no boundary, making the decay of vortices via phonon-shedding only possible in terms of vortex-antivortex annihilation.

An interesting feature is that the quantization of vortex movement provides a gyroscopic sensor: In a given reference frame one would prepare a cylindrical superfluid film, with a single vortex on its surface. If one would observe a vortex at rest, the reference frame one resides in therefore *must* rotate. As a macroscopic object which can be imaged in-situ without destroying it (at least partially, see [171]),

long-time measurements of the circulation time might be possible in the future. The likely many systematic effects existing in any real experiment make measurements probably quite inaccurate, and it remains to be seen whether flow quantization effects as discussed in chapter 8 can be harnessed in any robust way.

Bibliography

[1] N.-E. Guenther, P. Massignan, and A. L. Fetter, "Quantized superfluid vortex dynamics on cylindrical surfaces and planar annuli," *Phys. Rev. A*, vol. 96, p. 063608, Dec. 2017.

[2] N.-E. Guenther, P. Massignan, M. Lewenstein, and G. M. Bruun, "Bose polarons at finite temperature and strong coupling," *Phys. Rev. Lett.*, vol. 120, p. 050405, Feb. 2018.

[3] N.-E. Guenther, P. Massignan, and A. L. Fetter, "Superfluid vortex dynamics on a torus and other toroidal surfaces of revolution," *Phys. Rev. A*, vol. 101, p. 053606, May 2020.

[4] N.-E. Guenther, R. Schmidt, G. M. Bruun, V. Gurarie, and P. Massignan, "Mobile impurity in a Bose-Einstein condensate and the orthogonality catastrophe," *Phys. Rev. A*, vol. 103, p. 013317, Jan 2021.

[5] S. P. Rath and R. Schmidt, "Field-theoretical study of the Bose polaron," *Phys. Rev. A*, vol. 88, Nov. 2013.

[6] J. Schrieffer, *Theory Of Superconductivity*. Advanced Books Classics, Avalon Publishing, 1999.

[7] M. Lewenstein, A. Sanpera, V. Ahufinger, B. Damski, A. Sen(De), and U. Sen, "Ultracold atomic gases in optical lattices: mimicking condensed matter physics and beyond," *Advances in Physics*, vol. 56, pp. 243–379, Mar. 2007.

[8] R. P. Feynman *Prog. Low Temp. Phys.*, vol. 1, p. 17, 1955.

[9] R. P. Feynman, "Quantum mechanical computers," *Foundations of Physics*, vol. 16, no. 6, pp. 507–531, 1986.

[10] W. D. Phillips, "Nobel lecture: Laser cooling and trapping of neutral atoms," *Rev. Mod. Phys.*, vol. 70, pp. 721–741, Jul 1998.

[11] M. H. Anderson, J. R. Ensher, M. R. Matthews, C. E. Wieman, and E. A. Cornell, "Observation of Bose-Einstein condensation in a dilute atomic vapor," *Science*, vol. 269, no. 5221, pp. 198–201, 1995.

[12] K. B. Davis, M.-O. Mewes, M. A. Joffe, M. R. Andrews, and W. Ketterle, "Evaporative cooling of sodium atoms," *Phys. Rev. Lett.*, vol. 74, pp. 5202–5205, Jun 1995.

[13] R. P. Feynman, *The Feynman lectures on physics*. Reading, Mass. : Addison-Wesley Pub. Co., c1963-1965.

[14] L. Landau and E. Lifshits, *Quantum Mechanics: Non-Relativistic Theory*. A-W series in advanced physics, Oxford: Pergamon Press, 1977.

[15] K. B. Davis, M. O. Mewes, M. R. Andrews, N. J. van Druten, D. S. Durfee, D. M. Kurn, and W. Ketterle, "Bose-Einstein condensation in a gas of sodium atoms," *Physical Review Letters*, vol. 75, p. 3969–3973, 1995.

[16] A. L. Gaunt, T. F. Schmidutz, I. Gotlibovych, R. P. Smith, and Z. Hadzibabic, "Bose-Einstein condensation of atoms in a uniform potential," *Phys. Rev. Lett.*, vol. 110, p. 200406, May 2013.

[17] I. Bloch, "Ultracold quantum gases in optical lattices," *Nature Physics*, vol. 1, no. 1, pp. 23–30, 2005.

[18] M. Lewenstein, A. Sanpera, and V. Ahufinger, *Ultracold Atoms in Optical Lattices: Simulating quantum many-body systems*. Oxford University Press, 2012.

[19] D. S. Hall, M. R. Matthews, J. R. Ensher, C. E. Wieman, and E. A. Cornell, "Dynamics of component separation in a binary mixture of Bose-Einstein Condensates," *Phys. Rev. Lett.*, vol. 81, pp. 1539–1542, Aug 1998.

[20] A. Browaeys and T. Lahaye, *Interacting Cold Rydberg Atoms: A Toy Many-Body System*, pp. 177–198. Cham: Springer International Publishing, 2016.

[21] S. Ronen, D. C. E. Bortolotti, and J. L. Bohn, "Radial and angular rotons in trapped dipolar gases," *Phys. Rev. Lett.*, vol. 98, p. 030406, Jan 2007.

[22] L. Tanzi, C. R. Cabrera, J. Sanz, P. Cheiney, M. Tomza, and L. Tarruell, "Feshbach resonances in potassium Bose-Bose mixtures," *Phys. Rev. A*, vol. 98, p. 062712, Dec. 2018.

[23] E. Wille, F. M. Spiegelhalder, G. Kerner, D. Naik, A. Trenkwalder, G. Hendl, F. Schreck, R. Grimm, T. G. Tiecke, J. T. M. Walraven, S. J. J. M. F. Kokkelmans, E. Tiesinga, and P. S. Julienne, "Exploring an ultracold fermi-fermi mixture: Interspecies feshbach resonances and scattering properties of ^{6}Li and ^{40}K," *Phys. Rev. Lett.*, vol. 100, p. 053201, Feb 2008.

[24] J. W. Park, C.-H. Wu, I. Santiago, T. G. Tiecke, S. Will, P. Ahmadi, and M. W. Zwierlein, "Quantum degenerate Bose-Fermi mixture of chemically different atomic species with widely tunable interactions," *Phys. Rev. A*, vol. 85, p. 051602, May 2012.

[25] N. Bogolyubov, "On the theory of superfluidity," *J. Phys. (USSR)*, vol. 11, pp. 23–32, 1947.

[26] J. Bardeen, L. N. Cooper, and J. R. Schrieffer, "Theory of superconductivity," *Phys. Rev.*, vol. 108, pp. 1175–1204, Dec 1957.

[27] W. Zwerger, *The BCS-BEC Crossover and the Unitary Fermi Gas*. Lecture Notes in Physics, Springer Berlin Heidelberg, 2011.

[28] C. R. Cabrera, L. Tanzi, J. Sanz, B. Naylor, P. Thomas, P. Cheiney, and L. Tarruell, "Quantum liquid droplets in a mixture of Bose-Einstein condensates," *Science*, vol. 359, no. 6373, pp. 301–304, 2018.

[29] F. Böttcher, J.-N. Schmidt, M. Wenzel, J. Hertkorn, M. Guo, T. Langen, and T. Pfau, "Transient supersolid properties in an array of dipolar quantum droplets," *Phys. Rev. X*, vol. 9, p. 011051, Mar 2019.

[30] L. Tanzi, E. Lucioni, F. Famà, J. Catani, A. Fioretti, C. Gabbanini, R. N. Bisset, L. Santos, and G. Modugno, "Observation of a dipolar quantum gas with metastable supersolid properties," *Phys. Rev. Lett.*, vol. 122, p. 130405, Apr 2019.

[31] L. Chomaz, D. Petter, P. Ilzhöfer, G. Natale, A. Trautmann, C. Politi, G. Durastante, R. M. W. van Bijnen, A. Patscheider, M. Sohmen, M. J. Mark, and F. Ferlaino, "Long-lived and transient supersolid behaviors in dipolar quantum gases," *Phys. Rev. X*, vol. 9, p. 021012, Apr 2019.

[32] G. V. Chester, "Speculations on Bose-Einstein condensation and quantum crystals," *Phys. Rev. A*, vol. 2, pp. 256–258, Jul 1970.

[33] M. Greiner, O. Mandel, T. Esslinger, T. W. Hänsch, and I. Bloch, "Quantum phase transition from a superfluid to a mott insulator in a gas of ultracold atoms," *Nature*, vol. 415, no. 6867, pp. 39–44, 2002.

[34] G. Mahan, *Many-Particle Physics*. Kluwer Academic/Plenum Publishers, 2000.

[35] M. E. Gershenson, V. Podzorov, and A. F. Morpurgo, "*Colloquium* : Electronic transport in single-crystal organic transistors," *Rev. Mod. Phys.*, vol. 78, pp. 973–989, Sept. 2006.

[36] G. Baym and C. Pethick, *Landau Fermi-Liquid Theory: Concepts and Applications*. Wiley-VCH, 1991.

[37] E. Dagotto, "Correlated electrons in high-temperature superconductors," *Rev. Mod. Phys.*, vol. 66, pp. 763–840, July 1994.

[38] W. F. Vinen and D. Shoenberg, "The detection of single quanta of circulation in liquid helium ii," *Proc. R. Soc. Lond. A*, vol. 260, no. 1301, pp. 218–236, 1961.

[39] K. W. Madison, F. Chevy, W. Wohlleben, and J. Dalibard, "Vortex formation in a stirred Bose-Einstein condensate," *Phys. Rev. Lett.*, vol. 84, pp. 806–809, Jan 2000.

[40] A. M. Turner, V. Vitelli, and D. R. Nelson, "Vortices on curved surfaces," *Rev. Mod. Phys.*, vol. 82, pp. 1301–1348, Apr. 2010.

[41] I. Bloch, J. Dalibard, and W. Zwerger, "Many-body physics with ultracold gases," *Rev. Mod. Phys.*, vol. 80, pp. 885–964, July 2008.

[42] G. F. Gribakin and V. V. Flambaum, "Calculation of the scattering length in atomic collisions using the semiclassical approximation," *Phys. Rev. A*, vol. 48, pp. 546–553, July 1993.

[43] C. Chin, R. Grimm, P. Julienne, and E. Tiesinga, "Feshbach resonances in ultracold gases," *Rev. Mod. Phys.*, vol. 82, pp. 1225–1286, Apr. 2010.

[44] C. Pethick and H. Smith, *Bose-Einstein Condensation in Dilute Gases*. Cambridge: Cambridge Univ. Press, 2 ed., 2008.

[45] A. Messiah, *Quantum Mechanics*. Dover books on physics, Dover Publications, 1999.

[46] E. T. Whittaker and G. N. Watson, *A Course of Modern Analysis*. Cambridge: Cambridge University Press, 4 ed., 1996.

[47] H. Bethe, R. Peierls, and D. R. Hartree, "Quantum theory of the diplon," *Proceedings of the Royal Society of London. Series A - Mathematical and Physical Sciences*, vol. 148, no. 863, pp. 146–156, 1935.

[48] H. A. Bethe, "Theory of the effective range in nuclear scattering," *Phys. Rev.*, vol. 76, pp. 38–50, July 1949.

[49] U. Fano, "Effects of configuration interaction on intensities and phase shifts," *Phys. Rev.*, vol. 124, pp. 1866–1878, Dec. 1961.

[50] A. Viel and A. Simoni, "Feshbach resonances and weakly bound molecular states of boson-boson and boson-fermion nak pairs," *Phys. Rev. A*, vol. 93, p. 042701, Apr. 2016.

[51] I. Tanihata, "Neutron halo nuclei," *Journal of Physics G: Nuclear and Particle Physics*, vol. 22, pp. 157–198, feb 1996.

[52] A. S. Jensen, K. Riisager, D. V. Fedorov, and E. Garrido, "Structure and reactions of quantum halos," *Rev. Mod. Phys.*, vol. 76, pp. 215–261, Feb. 2004.

[53] P. Jeszenszki, A. Y. Cherny, and J. Brand, "s-wave scattering length of a gaussian potential," *Phys. Rev. A*, vol. 97, p. 042708, Apr. 2018.

[54] P. O. Fedichev, M. W. Reynolds, and G. V. Shlyapnikov, "Three-body recombination of ultracold atoms to a weakly bound s level," *Phys. Rev. Lett.*, vol. 77, pp. 2921–2924, Sept. 1996.

[55] J. Stenger, S. Inouye, M. R. Andrews, H.-J. Miesner, D. M. Stamper-Kurn, and W. Ketterle, "Strongly enhanced inelastic collisions in a Bose-Einstein condensate near Feshbach resonances," *Phys. Rev. Lett.*, vol. 82, pp. 2422–2425, Mar. 1999.

[56] R. S. Bloom, M.-G. Hu, T. D. Cumby, and D. S. Jin, "Tests of universal three-body physics in an ultracold Bose-Fermi mixture," *Phys. Rev. Lett.*, vol. 111, p. 105301, Sept. 2013.

[57] D. S. Petrov, "Three-body problem in Fermi gases with short-range interparticle interaction," *Phys. Rev. A*, vol. 67, p. 010703, Jan. 2003.

[58] P. Makotyn, C. E. Klauss, D. L. Goldberger, E. A. Cornell, and D. S. Jin, "Universal dynamics of a degenerate unitary Bose gas," *Nature Physics*, vol. 10, no. 2, pp. 116–119, 2014.

[59] M. Gattobigio, M. Göbel, H.-W. Hammer, and A. Kievsky, "More on the universal equation for Efimov states," *Few-Body Systems*, vol. 60, May 2019.

[60] E. Braaten and H.-W. Hammer, "Universality in few-body systems with large scattering length," *Physics Reports*, vol. 428, no. 5, pp. 259–390, 2006.

[61] P. Naidon and S. Endo, "Efimov physics: a review," *Reports on Progress in Physics*, vol. 80, p. 056001, Mar. 2017.

[62] V. Efimov, "Energy levels arising from resonant two-body forces in a three-body system," *Physics Letters B*, vol. 33, no. 8, pp. 563–564, 1970.

[63] E. Braaten, H.-W. Hammer, and M. Kusunoki, "Universal equation for Efimov states," *Phys. Rev. A*, vol. 67, p. 022505, Feb. 2003.

[64] A. O. Gogolin, C. Mora, and R. Egger, "Analytical solution of the bosonic three-body problem," *Physical Review Letters*, vol. 100, Apr. 2008.

[65] R. Chapurin, X. Xie, M. J. Van de Graaff, J. S. Popowski, J. P. D'Incao, P. S. Julienne, J. Ye, and E. A. Cornell, "Precision test of the limits to universality in few-body physics," *Phys. Rev. Lett.*, vol. 123, p. 233402, Dec. 2019.

[66] L. D. Landau, "Über die Bewegung der Elektronen in Kristalgitter," *Phys. Z. Sowjetunion*, vol. 3, p. 644, 1933.

[67] S. I. Pekar, "Autolocalization of the electron in an inertially polarizable dielectric medium," *Zh. Eksp. Teor. Fiz.*, vol. 16, p. 335, 1946.

[68] L. D. Landau and S. Pekar, "The effective mass of the polaron," *Zh. Eksp. Teor. Fiz.*, vol. 18, p. 419–423, 1948.

[69] H. Fröhlich, H. Pelzer, and S. Zienau, "Xx. properties of slow electrons in polar materials," *Philosophical Magazine Series 7*, vol. 41, no. 314, pp. 221–242, 1950.

[70] H. Fröhlich, "Electrons in lattice fields," *Adv. Phys.*, vol. 3, no. 11, pp. 325–361, 1954.

[71] T.-D. Lee and D. Pines, "Interaction of a nonrelativistic particle with a scalar field with application to slow electrons in polar crystals," *Phys. Rev.*, vol. 92, pp. 883–889, Nov. 1953.

[72] R. P. Feynman, "Slow electrons in a polar crystal," *Phys. Rev.*, vol. 97, pp. 660–665, Feb. 1955.

[73] T. Holstein, "Studies of polaron motion: Part i. the molecular-crystal model," *Annals of Physics*, vol. 8, no. 3, pp. 325–342, 1959.

[74] D. Emin, *Polarons*. Cambridge University Press, 2012.

[75] V. G. Storchak, O. E. Parfenov, J. H. Brewer, P. L. Russo, S. L. Stubbs, R. L. Lichti, D. G. Eshchenko, E. Morenzoni, T. G. Aminov, V. P. Zlomanov, A. A. Vinokurov, R. L. Kallaher, and S. von Molnár, "Direct observation of the magnetic polaron," *Phys. Rev. B*, vol. 80, p. 235203, Dec. 2009.

[76] T. J. Smart, A. C. Cardiel, F. Wu, K.-S. Choi, and Y. Ping, "Mechanistic insights of enhanced spin polaron conduction in cuo through atomic doping," *npj Computational Materials*, vol. 4, no. 1, p. 61, 2018.

[77] G.-m. Zhao, *Polarons in Colossal Magnetoresistive and High-Temperature Superconducting Materials*, pp. 569–597. 01 2007.

[78] M. Petty, "Molecular electronics from principles to practice," 01 2008.

[79] N. Lu, L. Li, D. Geng, and M. Liu, "A review for polaron dependent charge transport in organic semiconductor," *Organic Electronics*, vol. 61, pp. 223–234, 2018.

[80] L. B. Tan, O. Cotlet, A. Bergschneider, R. Schmidt, P. Back, Y. Shimazaki, M. Kroner, and A. m. c. İmamoğlu, "Interacting polaron-polaritons," *Phys. Rev. X*, vol. 10, p. 021011, Apr. 2020.

[81] C. W. Tang and S. A. VanSlyke, "Organic electroluminescent diodes," *Applied Physics Letters*, vol. 51, no. 12, pp. 913–915, 1987.

[82] K. Hoang and M. D. Johannes, "Defect physics in complex energy materials," *Journal of Physics: Condensed Matter*, vol. 30, p. 293001, June 2018.

[83] S. Nascimbène, N. Navon, K. J. Jiang, L. Tarruell, M. Teichmann, J. McKeever, F. Chevy, and C. Salomon, "Collective oscillations of an imbalanced Fermi gas: Axial compression modes and polaron effective mass," *Phys. Rev. Lett.*, vol. 103, p. 170402, Oct. 2009.

[84] F. Chevy and C. Mora, "Ultra-cold polarized Fermi gases," *Rep. Progr. Phys.*, vol. 73, p. 112401, Nov. 2010.

[85] R. Schmidt, M. Knap, D. A. Ivanov, J.-S. You, M. Cetina, and E. Demler, "Universal many-body response of heavy impurities coupled to a Fermi sea: A review of recent progress," *Rep. Prog. Phys.*, vol. 81, no. 2, p. 024401, 2018.

[86] P. Massignan, M. Zaccanti, and G. M. Bruun, "Polarons, dressed molecules and itinerant ferromagnetism in ultracold Fermi gases," *Rep. Progr. Phys.*, vol. 77, no. 3, p. 034401, 2014.

[87] N. B. Jørgensen, L. Wacker, K. T. Skalmstang, M. M. Parish, J. Levinsen, R. S. Christensen, G. M. Bruun, and J. J. Arlt, "Observation of attractive and repulsive polarons in a Bose-Einstein condensate," *Phys. Rev. Lett.*, vol. 117, p. 055302, July 2016.

[88] M.-G. Hu, M. J. Van de Graaff, D. Kedar, J. P. Corson, E. A. Cornell, and D. S. Jin, "Bose polarons in the strongly interacting regime," *Phys. Rev. Lett.*, vol. 117, p. 055301, July 2016.

[89] Z. Z. Yan, Y. Ni, C. Robens, and M. W. Zwierlein, "Bose polarons near quantum criticality," *Science*, vol. 368, no. 6487, pp. 190–194, 2020.

[90] L. A. Peña Ardila and S. Giorgini, "Impurity in a Bose-Einstein condensate: Study of the attractive and repulsive branch using quantum Monte Carlo methods," *Phys. Rev. A*, vol. 92, p. 033612, 2015.

[91] L. A. Peña Ardila, N. B. Jörgensen, T. Pohl, S. Giorgini, G. M. Bruun, and J. J. Arlt, "Analyzing the Bose Polaron Across Resonant Interactions," *arXiv:1812.04609*, Dec. 2018.

[92] J. Tempere, W. Casteels, M. K. Oberthaler, S. Knoop, E. Timmermans, and J. T. Devreese, "Feynman path-integral treatment of the BEC-impurity polaron," *Phys. Rev. B*, vol. 80, p. 184504, Nov. 2009.

[93] J. Levinsen, M. M. Parish, and G. M. Bruun, "Impurity in a Bose-Einstein condensate and the Efimov effect," *Phys. Rev. Lett.*, vol. 115, p. 125302, Sept. 2015.

[94] R. S. Christensen, J. Levinsen, and G. M. Bruun, "Quasiparticle properties of a mobile impurity in a Bose-Einstein condensate," *Phys. Rev. Lett.*, vol. 115, p. 160401, Oct. 2015.

[95] Y. E. Shchadilova, R. Schmidt, F. Grusdt, and E. Demler, "Quantum dynamics of ultracold Bose polarons," *Phys. Rev. Lett.*, vol. 117, p. 113002, Sept. 2016.

[96] S. M. Yoshida, S. Endo, J. Levinsen, and M. M. Parish, "Universality of an impurity in a Bose-Einstein condensate," *Phys. Rev. X*, vol. 8, p. 011024, Feb. 2018.

[97] J. Levinsen, M. M. Parish, R. S. Christensen, J. J. Arlt, and G. M. Bruun, "Finite-temperature behavior of the Bose polaron," *Phys. Rev. A*, vol. 96, p. 063622, Dec. 2017.

[98] B. Field, J. Levinsen, and M. M. Parish, "Fate of the Bose polaron at finite temperature," *Phys. Rev. A*, vol. 101, p. 013623, Jan. 2020.

[99] S. Weinberg, *The Quantum Theory of Fields*, vol. 1. Cambridge University Press, 1995.

[100] A. Fetter and J. Walecka, *Quantum Theory of Many-particle Systems*. Dover Books on Physics, Dover Publications, 2003.

[101] E. E. Salpeter and H. A. Bethe, "A relativistic equation for bound-state problems," *Phys. Rev.*, vol. 84, pp. 1232–1242, Dec. 1951.

[102] A. Fetter and J. Walecka, *Quantum Theory of Many-Particle Systems*. Dover Books on Physics Series, Dover Publications, 1971.

[103] A. Guidini, G. Bertaina, D. E. Galli, and P. Pieri, "Condensed phase of Bose-Fermi mixtures with a pairing interaction," *Phys. Rev. A*, vol. 91, p. 023603, Feb. 2015.

[104] P. Massignan, C. J. Pethick, and H. Smith, "Static properties of positive ions in atomic Bose-Einstein condensates," *Phys. Rev. A*, vol. 71, p. 023606, Feb. 2005.

[105] P. W. Anderson, "Infrared catastrophe in Fermi gases with local scattering potentials," *Phys. Rev. Lett.*, vol. 18, p. 1049, June 1967.

[106] J. Goold, T. Fogarty, N. Lo Gullo, M. Paternostro, and T. Busch, "Orthogonality catastrophe as a consequence of qubit embedding in an ultracold Fermi gas," *Phys. Rev. A*, vol. 84, p. 063632, Dec. 2011.

[107] M. Cetina, M. Jag, R. S. Lous, I. Fritsche, J. T. M. Walraven, R. Grimm, J. Levinsen, M. M. Parish, R. Schmidt, M. Knap, and E. Demler, "Ultrafast many-body interferometry of impurities coupled to a Fermi sea," *Science*, vol. 354, no. 6308, pp. 96–99, 2016.

[108] S. I. Mistakidis, G. C. Katsimiga, G. M. Koutentakis, T. Busch, and P. Schmelcher, "Quench dynamics and orthogonality catastrophe of Bose polarons," *Phys. Rev. Lett.*, vol. 122, p. 183001, May 2019.

[109] M. Drescher, M. Salmhofer, and T. Enss, "Theory of a resonantly interacting impurity in a Bose-Einstein condensate," *Phys. Rev. Research*, vol. 2, p. 032011, July 2020.

[110] D. Dzsotjan, R. Schmidt, and M. Fleischhauer, "Dynamical variational approach to Bose polarons at finite temperatures," *Phys. Rev. Lett.*, vol. 124, p. 223401, June 2020.

[111] E. Gross, "Motion of foreign bodies in boson systems," *Ann. of Phys.*, vol. 19, no. 2, p. 234, 1962.

[112] C. Chin, R. Grimm, P. Julienne, and E. Tiesinga, "Feshbach resonances in ultracold gases," *Rev. Mod. Phys.*, vol. 82, pp. 1225–1286, Apr. 2010.

[113] P. Massignan, N. Yegovtsev, and V. Gurarie, "Universal aspects of a strongly interacting impurity in a dilute Bose condensate," *Phys. Rev. Lett.*, vol. 126, p. 123403, Mar 2021.

[114] W. Casteels and M. Wouters, "Polaron formation in the vicinity of a narrow Feshbach resonance," *Phys. Rev. A*, vol. 90, p. 043602, Oct. 2014.

[115] L. A. Peña Ardila and S. Giorgini, "Bose polaron problem: Effect of mass imbalance on binding energy," *Phys. Rev. A*, vol. 94, p. 063640, Dec. 2016.

[116] R. Schmidt, T. Enss, V. Pietilä, and E. Demler, "Fermi polarons in two dimensions," *Phys. Rev. A*, vol. 85, p. 021602, Feb. 2012.

[117] J. J. Zirbel, K.-K. Ni, S. Ospelkaus, J. P. D'Incao, C. E. Wieman, J. Ye, and D. S. Jin, "Collisional stability of fermionic Feshbach molecules," *Phys. Rev. Lett.*, vol. 100, p. 143201, Apr. 2008.

[118] S. Tan, "Energetics of a strongly correlated Fermi gas," *Ann. Phys.*, vol. 323, no. 12, pp. 2952–2970, 2008.

[119] S. Tan, "Large momentum part of a strongly correlated Fermi gas," *Ann. Phys.*, vol. 323, no. 12, pp. 2971–2986, 2008.

[120] E. Braaten, M. Kusunoki, and D. Zhang, "Scattering models for ultracold atoms," *Annals of Physics*, vol. 323, pp. 1770–1815, July 2008.

[121] E. Braaten, "Universal Relations for Fermions with Large Scattering Length," p. 43, Aug. 2010.

[122] F. Werner and Y. Castin, "General relations for quantum gases in two and three dimensions. ii. bosons and mixtures," *Phys. Rev. A*, vol. 86, p. 053633, Nov. 2012.

[123] W. Yi and X. Cui, "Polarons in ultracold Fermi superfluids," *Phys. Rev. A*, vol. 92, p. 013620, July 2015.

[124] G. A. Fiete, G. Zaránd, and K. Damle, "Effective hamiltonian for $ga_{1-x}mn_xAs$ in the dilute limit," *Phys. Rev. Lett.*, vol. 91, p. 097202, Aug. 2003.

[125] V. V. Klimov, "Collective excitations in a hot quark gluon plasma," *Soviet Phys. JETP*, vol. 55, p. 199, 1982. [Zh. Eksp. Teor. Fiz. **82**, 336 (1982)].

[126] H. A. Weldon, "Effective fermion masses of order gT in high-temperature gauge theories with exact chiral invariance," *Phys. Rev. D*, vol. 26, pp. 2789–2796, Nov. 1982.

[127] H. A. Weldon, "Dynamical holes in the quark-gluon plasma," *Phys. Rev. D*, vol. 40, pp. 2410–2420, Oct. 1989.

[128] G. Baym, J.-P. Blaizot, and B. Svetitsky, "Emergence of new quasiparticles in quantum electrodynamics at finite temperature," *Phys. Rev. D*, vol. 46, pp. 4043–4051, Nov. 1992.

[129] E. Braaten, "Neutrino emissivity of an ultrarelativistic plasma from positron and plasmino annihilation," *The Astrophysical Journal*, vol. 392, pp. 70–73, June 1992.

[130] Z. Yan, P. B. Patel, B. Mukherjee, R. J. Fletcher, J. Struck, and M. W. Zwierlein, "Boiling a Unitary Fermi Liquid," *arXiv:1811.00481*, Nov. 2018.

[131] B. Field, J. Levinsen, and M. M. Parish, "Fate of the Bose polaron at finite temperature," *Phys. Rev. A*, vol. 101, p. 013623, Jan 2020.

[132] C. Kohstall, M. Zaccanti, M. Jag, A. Trenkwalder, P. Massignan, G. M. Bruun, F. Schreck, and R. Grimm, "Metastability and coherence of repulsive polarons in a strongly interacting Fermi mixture," *Nature*, vol. 485, pp. 615–618, May 2012.

[133] M. Cetina, M. Jag, R. S. Lous, J. T. M. Walraven, R. Grimm, R. S. Christensen, and G. M. Bruun, "Decoherence of impurities in a Fermi sea of ultracold atoms," *Phys. Rev. Lett.*, vol. 115, p. 135302, Sept. 2015.

[134] Y. Ashida, R. Schmidt, L. Tarruell, and E. Demler, "Many-body interferometry of magnetic polaron dynamics," *Phys. Rev. B*, vol. 97, p. 060302, Feb. 2018.

[135] A. Camacho-Guardian, L. A. Peña Ardila, T. Pohl, and G. M. Bruun, "Bipolarons in a Bose-Einstein condensate," *Phys. Rev. Lett.*, vol. 121, p. 013401, July 2018.

[136] L. B. Tan, O. Cotlet, A. Bergschneider, R. Schmidt, P. Back, Y. Shimazaki, M. Kroner, and A. İmamoğlu, "Interacting polaron-polaritons," *Phys. Rev. X*, vol. 10, p. 021011, Apr. 2020.

[137] L. Pitaevskii and S. Stringari, *Bose-Einstein Condensation and Superfluidity*. Oxford: Oxford Univ. Press, 2 ed., 2016.

[138] H. Lamb, *Hydrodynamics*. New York: Dover publications, 6 ed., 1945.

[139] S. Beliaev, "Application of the methods of quantum field theory to a system of bosons," *ZhETF*, vol. 34, no. 2, p. 417, 1958.

[140] E. P. Gross, "Structure of a quantized vortex in boson systems," *Nuovo Cimento*, vol. 20, p. 453, 1961.

[141] L. P. Pitaevskii, "Vortex lines in an imperfect Bose gas," *Sov. Phys. JETP*, vol. 13, p. 451, 1961.

[142] E. M. Wright, D. F. Walls, and J. C. Garrison, "Collapses and revivals of Bose-Einstein condensates formed in small atomic samples," *Phys. Rev. Lett.*, vol. 77, pp. 2158–2161, Sep 1996.

[143] M. Lewenstein and L. You, "Quantum phase diffusion of a Bose-Einstein condensate," *Phys. Rev. Lett.*, vol. 77, pp. 3489–3493, Oct 1996.

[144] G. Baym and C. J. Pethick, "Ground-state properties of magnetically trapped Bose-condensed rubidium gas," *Physical Review Letters*, vol. 76, pp. 6–9, 1996.

[145] V. M. Pérez-García, H. Michinel, J. I. Cirac, M. Lewenstein, and P. Zoller, "Low energy excitations of a Bose-Einstein condensate: a variational analysis," *Physical Review Letters*, vol. 77, p. 5230, 1996.

[146] L. Onsager, "Statistical hydrodynamics," *Il Nuovo Cimento (1943-1954)*, vol. 6, no. 2, pp. 279–287, 1949.

[147] A. L. Fetter, "Rotating trapped Bose-Einstein condensates," *Rev. Mod. Phys.*, vol. 81, pp. 647–691, May 2009.

[148] V. Ginsburg and L. Pitaevskii, "On the theory of superfluidity," *JETP*, vol. 7, p. 858, November 1958.

[149] A. J. Majda and A. L. Bertozzi, *Vorticity and Incompressible Flow*. Cambridge Texts in Applied Mathematics, Cambridge University Press, 2001.

[150] A. Gray, *Modern Differential Geometry of Curves and Surfaces*. CRC Press, 1993.

[151] T.-L. Ho and B. Huang, "Spinor condensates on a cylindrical surface in synthetic gauge fields," *Phys. Rev. Lett.*, vol. 115, p. 155304, Oct. 2015.

[152] J. Machta and R. A. Guyer, "Superfluid films on a cylindrical surface," *Journal of Low Temperature Physics*, vol. 74, pp. 231–261, Feb. 1989.

[153] E. T. Whittaker and G. N. Watson, *A Course of Modern Analysis*. Cambridge: Cambridge University Press, 4 ed., 1996.

[154] M. Turner, A, V. Vitelli, and D. R. Nelson, "Vortices on curved surfaces," *Rev. Mod. Phys.*, vol. 82, no. 1301, 2010.

[155] G. Kirchhoff, "Über die stationären elektrischen Strömungen in einer gekrümmten leitenden Fläche," *Monatsbericht der Akademie der Wissenschaften zu Berlin vom 19. July 1875, pages 56-66*, 1875.

[156] P. W. Anderson, "Considerations on the Flow of Superfluid Helium," *Rev. Mod. Phys.*, vol. 38, pp. 298–310, Apr. 1966.

[157] G. R. Kirchhoff, *Vorlesungen über mathematische Physik, Bd. 1: Mechanik*. Teubner, 1876.

[158] C. C. Lin, "On the motion of vortices in two dimensions - i. existence of the kirchhoff-routh function," *Proc. Nat. Acad. Sci.*, vol. 27, no. 12, pp. 570–575, 1941.

[159] C. C. Lin, "On the motion of vortices in two dimensions - ii. some further investigations on the kirchhoff-routh function," *Proc. Nat. Acad. Sci.*, vol. 27, no. 12, pp. 575–577, 1941.

[160] A. L. Fetter, "Low-lying superfluid states in a rotating annulus," *Phys. Rev.*, vol. 153, pp. 285–296, Jan. 1967.

[161] P. J. Bendt, "Superfluid helium critical velocities in a rotating annulus," *Phys. Rev.*, vol. 127, pp. 1441–1445, Sep 1962.

[162] C. Ryu, M. F. Andersen, P. Cladé, V. Natarajan, K. Helmerson, and W. D. Phillips, "Observation of persistent flow of a Bose-Einstein condensate in a toroidal trap," *Phys. Rev. Lett.*, vol. 99, p. 260401, Dec 2007.

[163] S. Moulder, S. Beattie, R. P. Smith, N. Tammuz, and Z. Hadzibabic, "Quantized supercurrent decay in an annular Bose-Einstein condensate," *Phys. Rev. A*, vol. 86, p. 013629, Jul 2012.

[164] L. Corman, L. Chomaz, T. Bienaimé, R. Desbuquois, C. Weitenberg, S. Nascimbène, J. Dalibard, and J. Beugnon, "Quench-induced supercurrents in an annular Bose gas," *Phys. Rev. Lett.*, vol. 113, p. 135302, Sep 2014.

[165] S. Eckel, F. Jendrzejewski, A. Kumar, C. J. Lobb, and G. K. Campbell, "Interferometric measurement of the current-phase relationship of a superfluid weak link," *Phys. Rev. X*, vol. 4, p. 031052, Sep 2014.

[166] J. L. Ville, T. Bienaimé, R. Saint-Jalm, L. Corman, M. Aidelsburger, L. Chomaz, K. Kleinlein, D. Perconte, S. Nascimbène, J. Dalibard, and J. Beugnon, "Loading and compression of a single two-dimensional Bose gas in an optical accordion," *Phys. Rev. A*, vol. 95, p. 013632, Jan 2017.

[167] M. Aidelsburger, J. L. Ville, R. Saint-Jalm, S. Nascimbène, J. Dalibard, and J. Beugnon, "Relaxation dynamics in the merging of n independent condensates," *Phys. Rev. Lett.*, vol. 119, p. 190403, Nov 2017.

[168] A. Chakraborty, S. R. Mishra, S. P. Ram, S. K. Tiwari, and H. S. Rawat, "A toroidal trap for cold ^{87} rb atoms using an rf-dressed quadrupole trap," *J. Phys. B*, vol. 49, p. 075304, Mar. 2016.

[169] N. Lundblad, R. A. Carollo, C. Lannert, M. J. Gold, X. Jiang, D. Paseltiner, N. Sergay, and D. C. Aveline, "Shell potentials for microgravity Bose-Einstein condensates," *npj Microgravity*, vol. 5, Dec. 2019.

[170] G. Condon, M. Rabault, B. Barrett, L. Chichet, R. Arguel, H. Eneriz-Imaz, D. Naik, A. Bertoldi, B. Battelier, P. Bouyer, and A. Landragin, "All-optical Bose-Einstein condensates in microgravity," *Phys. Rev. Lett.*, vol. 123, p. 240402, Dec. 2019.

[171] D. V. Freilich, D. M. Bianchi, A. M. Kaufman, T. K. Langin, and D. S. Hall, "Real-time dynamics of single vortex lines and vortex dipoles in a Bose-Einstein condensate," *Science*, vol. 329, no. 5996, pp. 1182–1185, 2010.

[172] D. R. Scherer, C. N. Weiler, T. W. Neely, and B. P. Anderson, "Vortex formation by merging of multiple trapped Bose-Einstein condensates," *Phys. Rev. Lett.*, vol. 98, p. 110402, Mar 2007.

[173] Ł. Dobrek, M. Gajda, M. Lewenstein, K. Sengstock, G. Birkl, and W. Ertmer, "Optical generation of vortices in trapped Bose-Einstein condensates," *Phys. Rev. A*, vol. 60, p. R3381, Nov. 1999.

[174] G. Nandi, R. Walser, and W. P. Schleich, "Vortex creation in a trapped Bose-Einstein condensate by stimulated raman adiabatic passage," *Phys. Rev. A*, vol. 69, p. 063606, June 2004.

[175] P. Minnhagen, "The two-dimensional coulomb gas, vortex unbinding, and superfluid-superconducting films," *Rev. Mod. Phys.*, vol. 59, pp. 1001–1066, Oct. 1987.

[176] W. F. Vinen and J. J. Niemela, "Quantum turbulence," *Journal of Low Temperature Physics*, vol. 128, no. 5, pp. 167–231, 2002.

Appendix

Appendix A

Diagrammatic ladder approximation

A.1 The regularized pair propagator Π

The regularized Pair propagator $\Pi(\Omega, \mathbf{q})$ is defined by Eq. (4.29) together with Eqs. (4.6) and (4.16) for the propagators:

$$\Pi(\Omega, \mathbf{q}) = \int \frac{d^3k}{(2\pi)^3} \left(\int \frac{d\omega}{2\pi} G_0(\omega, \mathbf{k}) G_B(\Omega - \omega, \mathbf{q} - \mathbf{k}) + \frac{2m_r}{\hbar k^2} \right), \tag{A.1}$$

$$G_0(\omega, \mathbf{k}) = \frac{1}{\omega - \mathcal{E}_\mathbf{k}/\hbar + i0^+}, \tag{A.2}$$

$$G_B(\omega, \mathbf{k}) = \frac{u_\mathbf{k}^2}{\omega - E_\mathbf{k}/\hbar + i0^+} - \frac{v_\mathbf{k}^2}{\omega + E_\mathbf{k}/\hbar - i0^+}, \tag{A.3}$$

, where 0^+ always indicates an infinitesimal and positive real number, and

$$\mathcal{E}_\mathbf{k} = \frac{\hbar^2 k^2}{2m_I} \quad , \quad \epsilon_\mathbf{k} = \frac{\hbar^2 k^2}{2m_B}, \quad \mu_B = n_0 \frac{4\pi\hbar^2 a_B}{m_B}$$
$$E_\mathbf{k}^2 = \epsilon_\mathbf{k}(\epsilon_\mathbf{k}^2 + 2\mu_B), \; u_\mathbf{k}^2 = \frac{1}{2}\left(\frac{\epsilon_\mathbf{k} + \mu_B}{E_\mathbf{k}} + 1\right), \; v_\mathbf{k}^2 = \frac{1}{2}\left(\frac{\epsilon_\mathbf{k} + \mu_B}{E_\mathbf{k}} + 1\right). \tag{A.4}$$

The integrals appearing in the definition of the pair propagator in (A.1) can be performed analytically, as first derived in [5]. A derivation closely following the approach presented there is discussed here for the sake of completeness:

The frequency integral in the first term in Eq. (A.1) can be performed via the residue theorem:
The integrand can be extended analytically to the complex plane by replacing $\omega \to z$, with $z = \omega + i\nu$ complex. For large $|z|$, the integrand scales as $\sim z^{-2}$ such that the line integral can be extended to a Bromwich contour in the positive half-plane. The only pole in the upper half plane is a simple pole corresponding to the first term in Eq. (A.3), giving after some basic rearrangement

$$\Pi(\Omega, \mathbf{q}) = \int \frac{d^3k}{(2\pi)^3} \left(\frac{u_\mathbf{k}^2}{\Omega - \mathcal{E}_{\mathbf{k}+\mathbf{q}}/\hbar - E_\mathbf{k}/\hbar + i0^+} + \frac{2m_r}{\hbar k^2} \right). \tag{A.5}$$

Performing the angular integral is straight-forward and yields

$$\Pi(\Omega,\mathbf{q}) = \int_0^\infty \frac{dk}{(2\pi)^2}\left(\frac{4m_r}{\hbar} + \right. \\ \left. + u_{\mathbf{k}}^2 \frac{m_I}{\hbar}\frac{k}{q}\log\left[\frac{(k-q)^2-(\Omega+i0^+-E_{\mathbf{k}}/\hbar)(2m_I/\hbar)}{(k+q)^2-(\Omega+i0^+-E_{\mathbf{k}}/\hbar)(2m_I/\hbar)}\right]\right). \tag{A.6}$$

The remaining integration in the radial part requires careful treatment due to the complicated square root dependence of $E_{\mathbf{k}}$ and $u_{\mathbf{k}}$ on k. Introducing $\delta = \mu_B m_B/\hbar^2$, a useful change of variable is $k \to \sqrt{\delta}(x - 1/x)$, since $E_{\mathbf{k}}$ transforms as

$$E_{\mathbf{k}} \to \frac{\hbar^2\delta}{2m_B}\left(x^2 - 1/x^2\right), \tag{A.7}$$

eliminating the square root from the integrand. Especially

$$k u_{\mathbf{k}}^2 dk \to \delta x dx. \tag{A.8}$$

transforms particularly simple. The resulting integral reads

$$\Pi(\Omega,\mathbf{q}) = \frac{m_I\sqrt{\delta}}{\hbar}\int_1^\infty \frac{dx}{(2\pi)^2}\left(\frac{4\gamma}{1+\gamma}\left(1/x^2+1\right) + \right. \\ \left. + \frac{x}{\kappa}\log\left[\frac{x^4-\kappa a x^3+bx^2+\kappa a x+c}{x^4+\kappa a x^3+bx^2-\kappa a x+c}\right]\right) \tag{A.9}$$

where $\kappa = q/\delta$ and $\gamma = mB/mI$ is the mass ratio and the argument of the logarithm is directly ordered as a 4th-order polynomial in x, with coefficients

$$a = \frac{2\gamma}{1+\gamma}, \tag{A.10}$$

$$b = \frac{\gamma}{1+\gamma}\left(\kappa^2 - 2 - \frac{\Omega+i0^+}{\hbar\delta/2m_I}\right), \tag{A.11}$$

$$c = \frac{\gamma-1}{\gamma+1}. \tag{A.12}$$

It is straight forward to integrate the first term in the first line of Eq. (A.9). The second and third term together behave as $\sim x^{-3}$ for large x but diverge individually. It is convenient to rearrange the polynomial in terms of its roots x_i with $i \in \{1,2,3,4\}$, which have analytical if unyielding expressions in terms of the coefficients in Eq. (A.10):

$$\frac{\Pi(\Omega,\mathbf{q})}{m_I\sqrt{\delta}/\hbar} = \frac{1}{\pi^2}\frac{\gamma}{1+\gamma} + \int_1^\infty \frac{dx}{(2\pi)^2}\left(\frac{4\gamma}{1+\gamma} + \frac{x}{\kappa}\log\left[\prod_{i=1}^4 \frac{x-x_i}{x+x_i}\right]\right). \tag{A.13}$$

Note that $\sum_i x_i = a\kappa$, such that $4\gamma/(1+\gamma) = 2\sum_i x_i/\kappa$. We can separate the integral in Eq. (A.13) such that

$$\frac{\Pi(\Omega,\mathbf{q})}{m_I\sqrt{\delta}/\hbar} = \frac{1}{\pi^2}\frac{\gamma}{1+\gamma} + \frac{1}{\kappa}\sum_i^4 \int_1^\infty \frac{dx}{(2\pi)^2}\left(x\log\left[\frac{x-x_i}{x+x_i}\right] + 2x_i\right), \tag{A.14}$$

since the integrals in Eq. (A.14) converge individually. The expression can be solved analytically via the well-known anti-derivatives of $\log(x)$ and $x\log(x)$:

$$\int_1^\infty dx \left(x \log\left[\frac{x-x_i}{x+x_i}\right] + 2x_i \right) = \operatorname{atanh}(x_i)\left(1-x_i^2\right) - x_i. \tag{A.15}$$

Collecting the single terms and inserting $\sum_i x_i = a\kappa$, we find

$$\frac{\Pi(\Omega,\mathbf{q})}{m_I\sqrt{\delta}/\hbar} = \frac{1}{2\pi^2}\left(\frac{\gamma}{1+\gamma} + \sum_i^4 \frac{1-x_i^2}{2}\operatorname{atanh}(x_i) \right) \tag{A.16}$$

A.2 Weak coupling and low temperature analysis

To get a deeper understanding of the subtle transition from one quasiparticle to two at non-zero temperatures, let us focus on temperatures $T \ll T_c$, and study in detail the contribution Σ_1 to the self-energy Σ. To simplify the analysis, we assume a very weakly interacting BEC, so that the approximations $E_\mathbf{k} \approx \epsilon_\mathbf{k}^B + \mu_B$, $u_\mathbf{k}^2 \approx 1$, and $v_\mathbf{k}^2 \approx 0$, hold for most of the relevant momenta. We then obtain

$$\Sigma_1(\omega) \approx \int \frac{d^3k}{(2\pi)^3} \frac{f_\mathbf{k}}{\mathcal{T}_v^{-1} - \Pi(\mathbf{k},\omega+E_\mathbf{k}) - \frac{n_0}{\omega+E_\mathbf{k}-\epsilon_\mathbf{k}}}. \tag{A.17}$$

Before proceeding further let us note that, due to the presence of the Bose distribution, the integrand vanishes at zero temperature, whereas it is sharply peaked at low momenta for finite T. Moreover, the denominator of $\tilde{\mathcal{T}}$ appearing in the last equation vanishes whenever $\omega + E_\mathbf{k} = \epsilon_\mathbf{k} + n_0/[\mathcal{T}_v^{-1} - \Pi(\mathbf{k},\omega+E_\mathbf{k})] = \epsilon_\mathbf{k} + \Sigma_0(\mathbf{k},\omega+E_\mathbf{k})$, i.e., whenever $\omega + E_\mathbf{k}$ coincides with the energy of a polaron with momentum $\mathbf{k}$, dressed by condensate excitations [compare the thick dashed line in Fig. 4.4 (d)]. This feature is allowed by the presence of a dressed propagator inside the last diagram shown in Fig. 4.4 (c), and is therefore a purely non-perturbative effect. It implies that, for small but non-zero temperatures and small boson-boson interactions, Σ_1 develops a resonant feature at zero momentum and at an energy coinciding with the energy of the polaron at zero temperature.

We may proceed by noting that, at small temperatures and couplings, the pair propagator Π provides only a small contribution to Σ, so that the polaron energy at zero temperature is to a great accuracy given by $\omega^{(0)} \equiv n_0\mathcal{T}_v$, and we may neglect Π in Eq. (A.17). This leaves us with

$$\begin{aligned}\Sigma_1(\omega) &\approx \int \frac{d^3k}{(2\pi)^3} \frac{f_\mathbf{k}}{\mathcal{T}_v^{-1} - \frac{n_0}{\omega+n_0\mathcal{T}_B+\mathbf{k}^2(1/2m_B-1/2m_F)}} \\ &= \frac{\omega+n_0\mathcal{T}_B}{\omega-n_0(\mathcal{T}_v-\mathcal{T}_B)} n_{\mathrm{ex}}\mathcal{T}_v,\end{aligned} \tag{A.18}$$

where for simplicity we assumed $m_B = m_F$, such that the remaining integral became immediately proportional to thermal depletion of the condensate density,

$$n_{\mathrm{ex}} = \int \frac{d^3k}{(2\pi)^3} f_\mathbf{k}(u_\mathbf{k}^2 + v_\mathbf{k}^2) \approx \int \frac{d^3k}{(2\pi)^3} f_\mathbf{k}. \tag{A.19}$$

Even for unequal masses, the kinetic terms in the denominator of Eq. (A.18) are not important, since at low temperatures they are cut-off by the Bose distribution. Eq. (A.18) shows that the self-energy has a pole at $\omega_{\rm crit} = n_0(\mathcal{T}_v - \mathcal{T}_B)$. This pole position is plotted in Fig. 4.9 as vertical dotted lines (the color of each line indicating the corresponding value of $k_n a_B$). We note that the pole structure of $\Sigma_1(\omega)$ in (A.18) is a result of the approximations made. In particular, a finite a_B changes the infrared divergence of $f_{\mathbf{k}}$ from $1/k^2$ to $1/k$ and the pole changes into a resonance, as can be seen in Fig. 4.9. However, the position of the resonance structure is close to the predicted value $\omega_{\rm crit} = n_0(\mathcal{T}_v - \mathcal{T}_B)$.

The energy splitting may now be computed by solving the self-consistent equation

$$\omega = \omega^{(0)} + (\omega - \omega^{(0)})\Sigma_0' + \Sigma_1(\omega), \tag{A.20}$$

with the shorthand notation $\Sigma_0' \equiv \partial_\omega \Sigma_0(\omega)|_{\omega=\omega^{(0)}}$. For Σ_1 we will use the approximate form derived in Eq. (A.17), evaluated at $\omega \approx \omega^{(0)}$. In the limit $\mathcal{T}_v \ll \mathcal{T}_B$, one finds the single solution

$$\omega_\uparrow = (n_0 + Z_0 n_{\rm ex})\mathcal{T}_v \approx n\mathcal{T}_v, \tag{A.21}$$

thereby recovering the expected mean-field result from first order perturbation theory, which is in particular independent of temperature. In the opposite limit $\mathcal{T}_v \gg \mathcal{T}_B$ one instead finds two solutions,

$$\omega_{\uparrow,\downarrow} = \omega_0 \left(1 \pm \sqrt{Z_0 n_{\rm ex}/n_0}\right) \tag{A.22}$$

and

$$Z_\uparrow = Z_\downarrow = Z_0/2, \tag{A.23}$$

indicating that the two quasiparticles split symmetrically around the zero-temperature solution, and that each carries half of the residue of the zero temperature polaron, $Z_0 \equiv (1 - \Sigma_0')^{-1}$.

Note that our theory predicts that there are always two polaron solutions as $T \to T_c^-$. The reason is that the Bogoliubov dispersion softens at $\mathbf{k} \sim 0$ and that $\Sigma_1(\omega)$ therefore develops a proper pole, so that two polaron solutions appear. However, the residue of the upper polaron is negligible just below T_c. Moreover, this occurs in the critical region $|T - T_c|/T_c \lesssim n^{1/3} a_B$ where diagrammatic perturbation theory breaks down precisely due to the infrared divergences we encounter[1]. Further studies are needed to understand this region in detail.

[1] See, e.g., the discussion in the following papers: H. Shi and A. Griffin, *Finite-temperature excitations in a dilute Bose-condensed gas*, Phys. Rep. **304**, 1 (1998); J. O. Andersen, *Theory of the weakly interacting Bose gas*, Rev. Mod. Phys. **76**, 599 (2004).

Appendix B

Coherent state ansatz

B.1 Derivation of the modified GP equation

We start by presenting a step-by-step derivation of the expectation value of the grand potential,

$$\hat{\Omega} = \int d^3r \left[\hat{b}^\dagger_{\boldsymbol{r}} \left(-\frac{\hbar^2 \nabla^2_{\boldsymbol{r}}}{2m_B} + \frac{\mathcal{T}_B}{2} \hat{b}^\dagger_{\boldsymbol{r}} \hat{b}_{\boldsymbol{r}} - \mu \right) \hat{b}_{\boldsymbol{r}} + \hat{a}^\dagger_{\boldsymbol{r}} \left(-\frac{\hbar^2 \nabla^2_{\boldsymbol{r}}}{2m_I} \right) \hat{a}_{\boldsymbol{r}} + \hat{b}^\dagger_{\boldsymbol{r}} \hat{b}_{\boldsymbol{r}} U(\boldsymbol{r}-\boldsymbol{s}) \hat{a}^\dagger_{\boldsymbol{s}} \hat{a}_{\boldsymbol{s}} \right], \tag{B.1}$$

upon the ansatz state

$$|\Psi\rangle = \int \frac{d^3r}{\sqrt{V}}\, \hat{a}^\dagger_{\boldsymbol{r}} \exp\left(\int d^3s\ \phi(\boldsymbol{r}-\boldsymbol{s}) \hat{b}^\dagger_{\boldsymbol{s}} - c.c. \right) |0\rangle = \int \frac{d^3r}{\sqrt{V}} |\boldsymbol{r}\rangle |\phi(\boldsymbol{r})\rangle. \tag{B.2}$$

The result contains three contributions, coming from the bath, the impurity, and their mutual interaction. The contribution from the bath is very simple. Using $\langle \boldsymbol{r}|\boldsymbol{r}'\rangle = \delta(\boldsymbol{r}-\boldsymbol{r}')$ and $\hat{b}_{\boldsymbol{s}}|\phi(\boldsymbol{r})\rangle = \phi(\boldsymbol{r}-\boldsymbol{s})|\phi(\boldsymbol{r})\rangle$, one finds:

$$\begin{aligned} \langle \hat{\Omega}_B \rangle &= \int \frac{d^3r\ d^3s}{V} \phi^*(\boldsymbol{r}-\boldsymbol{s}) \left[-\frac{\hbar^2 \nabla^2_{\boldsymbol{s}}}{2m_B} + \frac{\mathcal{T}_B}{2} |\phi(\boldsymbol{r}-\boldsymbol{s})|^2 - \mu \right] \phi(\boldsymbol{r}-\boldsymbol{s}) \\ &= \int d^3r\ \phi^*(\boldsymbol{r}) \left[-\frac{\hbar^2 \nabla^2_{\boldsymbol{r}}}{2m_B} + \frac{\mathcal{T}_B}{2} |\phi(\boldsymbol{r})|^2 - \mu \right] \phi(\boldsymbol{r}). \end{aligned} \tag{B.3}$$

Similarly, the bath-impurity interaction term gives:

$$\begin{aligned} \langle \hat{\Omega}_{\text{int}} \rangle &= \int \frac{d^3r\ d^3s}{V}\ U(\boldsymbol{r}-\boldsymbol{s}) \langle \phi(\boldsymbol{r}) | \hat{b}^\dagger_{\boldsymbol{s}} \hat{b}_{\boldsymbol{s}} | \phi(\boldsymbol{r}) \rangle \\ &= \int \frac{d^3r\ d^3s}{V} U(\boldsymbol{r}-\boldsymbol{s}) |\phi(\boldsymbol{r}-\boldsymbol{s})|^2 \\ &= \int d^3r\ U(\boldsymbol{r}) |\phi(\boldsymbol{r})|^2. \end{aligned} \tag{B.4}$$

To study the impurity sector, care must be taken when evaluating the Laplacian. A possible approach is working explicitly with a difference quotient

$$\nabla^2_{\boldsymbol{r}} \hat{a}_{\boldsymbol{r}} = \lim_{d\to 0} \sum_{i=(1,2,3)} \frac{\hat{a}_{\boldsymbol{r}+d\mathbf{e}_i} + \hat{a}_{\boldsymbol{r}-d\mathbf{e}_i} - 2\hat{a}_{\boldsymbol{r}}}{d^2}, \tag{B.5}$$

and taking the limit $d \to 0$ at the end. Here $\mathbf{e}_i$ is any orthonormal basis set. This gives

$$\begin{aligned}\langle \hat{\Omega}_I \rangle &= -\frac{\hbar^2}{2m_I} \int d^3r \lim_{d\to 0} \sum_{i=(1,2,3)} \langle \hat{a}^\dagger_{\boldsymbol{r}} \frac{\hat{a}_{\boldsymbol{r}+d\mathbf{e}_i} + \hat{a}_{\boldsymbol{r}-d\mathbf{e}_i} - 2\hat{a}_{\boldsymbol{r}}}{d^2} \rangle \\ &= -\frac{\hbar^2}{2m_I} \lim_{d\to 0} \int \frac{d^3r}{Vd^2} \sum_{i=(1,2,3)} \Big(\langle \phi(\boldsymbol{r})|\phi(\boldsymbol{r}+d\mathbf{e}_i)\rangle + \langle \phi(\boldsymbol{r})|\phi(\boldsymbol{r}-d\mathbf{e}_i)\rangle - 2\underbrace{\langle \phi(\boldsymbol{r})|\phi(\boldsymbol{r})\rangle}_{1} \Big).\end{aligned} \tag{B.6}$$

The overlap between different coherent states is

$$\langle \phi_1|\phi_2\rangle = \exp\left[\int d^3r \left(\phi_1^*(\boldsymbol{r})\phi_2(\boldsymbol{r}) - \frac{|\phi_1(\boldsymbol{r})|^2}{2} - \frac{|\phi_2(\boldsymbol{r})|^2}{2}\right)\right]. \tag{B.7}$$

Applied to the last line in Eq. (B.6), this gives

$$\begin{aligned}\langle \phi(\boldsymbol{r})|\phi(\boldsymbol{r}\pm d\mathbf{e}_i)\rangle =& \exp\left[\int d^3s \Big(\phi^*(\boldsymbol{r}-\boldsymbol{s})\phi(\boldsymbol{r}\pm d\mathbf{e}_i-\boldsymbol{s}) - \frac{|\phi(\boldsymbol{r}-\boldsymbol{s})|^2}{2} \right. \\ & \left. - \frac{|\phi(\boldsymbol{r}\pm d\mathbf{e}_i-\boldsymbol{s})|^2}{2}\Big)\right] \\ =& \exp\left[\int d^3s \left(\phi^*(\boldsymbol{s})\phi(\boldsymbol{s}\mp d\mathbf{e}_i) - |\phi(\boldsymbol{s})|^2\right)\right] \qquad \text{(B.8)} \\ =& 1 \mp d \underbrace{\int d^3s\ \phi^*(\boldsymbol{s})\partial_i\phi(\boldsymbol{s})}_{=0} \\ & + \frac{d^2}{2}\left[\int d^3s\ \phi^*(\boldsymbol{s})\partial_i^2\phi(\boldsymbol{s}) \underbrace{\left(\int d^3s\ \phi^*(\boldsymbol{s})\partial_i\phi(\boldsymbol{s})\right)^2}_{=0}\right] + \mathcal{O}(d^3), \qquad \text{(B.9)}\end{aligned}$$

where the first and last term vanish because $\phi^*(\boldsymbol{s})\partial_i\phi(\boldsymbol{s})$ is antisymmetric in s_i due to ϕ being a central function, $\phi(\boldsymbol{s}) = \phi(s)$. Plugging this expression into (B.6) gives:

$$\langle \hat{\Omega}_I \rangle = \int d^3r\ \phi^*(\boldsymbol{r}) \left(-\frac{\hbar^2\nabla^2_{\boldsymbol{r}}}{2m_I}\right)\phi(\boldsymbol{r}). \tag{B.10}$$

Combining all terms, the expectation value of $\hat{\Omega}$ over the coherent ansatz $|\Psi\rangle$ reads:

$$\langle \hat{\Omega} \rangle = \int d^3r\ \phi^*(\boldsymbol{r}) \left(-\frac{\hbar^2\nabla^2_{\boldsymbol{r}}}{2m_r} + U(\boldsymbol{r}) + \frac{\mathcal{T}_B}{2}|\phi(\boldsymbol{r})|^2 - \mu\right)\phi(\boldsymbol{r}), \tag{B.11}$$

where $m_r^{-1} = m_B^{-1} + m_I^{-1}$ is the reduced mass for one bath boson and one impurity. By minimizing (B.11) with respect to ϕ^*, one recovers the equation introduced in the text,

$$\left[-\frac{\hbar^2\nabla^2_{\boldsymbol{r}}}{2m_r} + U(r) + \mathcal{T}_B|\phi(\boldsymbol{r})|^2\right]\phi(\boldsymbol{r}) = \mu\phi(\boldsymbol{r}), \tag{B.12}$$

which is a modified GP equation (due to the presence of the reduced mass m_r) describing the coherent dressing of a mobile impurity when it is immersed in a weakly-interacting BEC.

Bibliography

[1] N.-E. Guenther, P. Massignan, and A. L. Fetter, "Quantized superfluid vortex dynamics on cylindrical surfaces and planar annuli," *Phys. Rev. A*, vol. 96, p. 063608, Dec. 2017.

[2] N.-E. Guenther, P. Massignan, M. Lewenstein, and G. M. Bruun, "Bose polarons at finite temperature and strong coupling," *Phys. Rev. Lett.*, vol. 120, p. 050405, Feb. 2018.

[3] N.-E. Guenther, P. Massignan, and A. L. Fetter, "Superfluid vortex dynamics on a torus and other toroidal surfaces of revolution," *Phys. Rev. A*, vol. 101, p. 053606, May 2020.

[4] N.-E. Guenther, R. Schmidt, G. M. Bruun, V. Gurarie, and P. Massignan, "Mobile impurity in a Bose-Einstein condensate and the orthogonality catastrophe," *Phys. Rev. A*, vol. 103, p. 013317, Jan 2021.

[5] S. P. Rath and R. Schmidt, "Field-theoretical study of the Bose polaron," *Phys. Rev. A*, vol. 88, Nov. 2013.

[6] J. Schrieffer, *Theory Of Superconductivity*. Advanced Books Classics, Avalon Publishing, 1999.

[7] M. Lewenstein, A. Sanpera, V. Ahufinger, B. Damski, A. Sen(De), and U. Sen, "Ultracold atomic gases in optical lattices: mimicking condensed matter physics and beyond," *Advances in Physics*, vol. 56, pp. 243–379, Mar. 2007.

[8] R. P. Feynman *Prog. Low Temp. Phys.*, vol. 1, p. 17, 1955.

[9] R. P. Feynman, "Quantum mechanical computers," *Foundations of Physics*, vol. 16, no. 6, pp. 507–531, 1986.

[10] W. D. Phillips, "Nobel lecture: Laser cooling and trapping of neutral atoms," *Rev. Mod. Phys.*, vol. 70, pp. 721–741, Jul 1998.

[11] M. H. Anderson, J. R. Ensher, M. R. Matthews, C. E. Wieman, and E. A. Cornell, "Observation of Bose-Einstein condensation in a dilute atomic vapor," *Science*, vol. 269, no. 5221, pp. 198–201, 1995.

[12] K. B. Davis, M.-O. Mewes, M. A. Joffe, M. R. Andrews, and W. Ketterle, "Evaporative cooling of sodium atoms," *Phys. Rev. Lett.*, vol. 74, pp. 5202–5205, Jun 1995.

[13] R. P. Feynman, *The Feynman lectures on physics*. Reading, Mass. : Addison-Wesley Pub. Co., c1963-1965.

[14] L. Landau and E. Lifshits, *Quantum Mechanics: Non-Relativistic Theory*. A-W series in advanced physics, Oxford: Pergamon Press, 1977.

[15] K. B. Davis, M. O. Mewes, M. R. Andrews, N. J. van Druten, D. S. Durfee, D. M. Kurn, and W. Ketterle, "Bose-Einstein condensation in a gas of sodium atoms," *Physical Review Letters*, vol. 75, p. 3969–3973, 1995.

[16] A. L. Gaunt, T. F. Schmidutz, I. Gotlibovych, R. P. Smith, and Z. Hadzibabic, "Bose-Einstein condensation of atoms in a uniform potential," *Phys. Rev. Lett.*, vol. 110, p. 200406, May 2013.

[17] I. Bloch, "Ultracold quantum gases in optical lattices," *Nature Physics*, vol. 1, no. 1, pp. 23–30, 2005.

[18] M. Lewenstein, A. Sanpera, and V. Ahufinger, *Ultracold Atoms in Optical Lattices: Simulating quantum many-body systems*. Oxford University Press, 2012.

[19] D. S. Hall, M. R. Matthews, J. R. Ensher, C. E. Wieman, and E. A. Cornell, "Dynamics of component separation in a binary mixture of Bose-Einstein Condensates," *Phys. Rev. Lett.*, vol. 81, pp. 1539–1542, Aug 1998.

[20] A. Browaeys and T. Lahaye, *Interacting Cold Rydberg Atoms: A Toy Many-Body System*, pp. 177–198. Cham: Springer International Publishing, 2016.

[21] S. Ronen, D. C. E. Bortolotti, and J. L. Bohn, "Radial and angular rotons in trapped dipolar gases," *Phys. Rev. Lett.*, vol. 98, p. 030406, Jan 2007.

[22] L. Tanzi, C. R. Cabrera, J. Sanz, P. Cheiney, M. Tomza, and L. Tarruell, "Feshbach resonances in potassium Bose-Bose mixtures," *Phys. Rev. A*, vol. 98, p. 062712, Dec. 2018.

[23] E. Wille, F. M. Spiegelhalder, G. Kerner, D. Naik, A. Trenkwalder, G. Hendl, F. Schreck, R. Grimm, T. G. Tiecke, J. T. M. Walraven, S. J. J. M. F. Kokkelmans, E. Tiesinga, and P. S. Julienne, "Exploring an ultracold fermi-fermi mixture: Interspecies feshbach resonances and scattering properties of ^{6}Li and ^{40}K," *Phys. Rev. Lett.*, vol. 100, p. 053201, Feb 2008.

[24] J. W. Park, C.-H. Wu, I. Santiago, T. G. Tiecke, S. Will, P. Ahmadi, and M. W. Zwierlein, "Quantum degenerate Bose-Fermi mixture of chemically different atomic species with widely tunable interactions," *Phys. Rev. A*, vol. 85, p. 051602, May 2012.

[25] N. Bogolyubov, "On the theory of superfluidity," *J. Phys. (USSR)*, vol. 11, pp. 23–32, 1947.

[26] J. Bardeen, L. N. Cooper, and J. R. Schrieffer, "Theory of superconductivity," *Phys. Rev.*, vol. 108, pp. 1175–1204, Dec 1957.

[27] W. Zwerger, *The BCS-BEC Crossover and the Unitary Fermi Gas*. Lecture Notes in Physics, Springer Berlin Heidelberg, 2011.

[28] C. R. Cabrera, L. Tanzi, J. Sanz, B. Naylor, P. Thomas, P. Cheiney, and L. Tarruell, "Quantum liquid droplets in a mixture of Bose-Einstein condensates," *Science*, vol. 359, no. 6373, pp. 301–304, 2018.

[29] F. Böttcher, J.-N. Schmidt, M. Wenzel, J. Hertkorn, M. Guo, T. Langen, and T. Pfau, "Transient supersolid properties in an array of dipolar quantum droplets," *Phys. Rev. X*, vol. 9, p. 011051, Mar 2019.

[30] L. Tanzi, E. Lucioni, F. Famà, J. Catani, A. Fioretti, C. Gabbanini, R. N. Bisset, L. Santos, and G. Modugno, "Observation of a dipolar quantum gas with metastable supersolid properties," *Phys. Rev. Lett.*, vol. 122, p. 130405, Apr 2019.

[31] L. Chomaz, D. Petter, P. Ilzhöfer, G. Natale, A. Trautmann, C. Politi, G. Durastante, R. M. W. van Bijnen, A. Patscheider, M. Sohmen, M. J. Mark, and F. Ferlaino, "Long-lived and transient supersolid behaviors in dipolar quantum gases," *Phys. Rev. X*, vol. 9, p. 021012, Apr 2019.

[32] G. V. Chester, "Speculations on Bose-Einstein condensation and quantum crystals," *Phys. Rev. A*, vol. 2, pp. 256–258, Jul 1970.

[33] M. Greiner, O. Mandel, T. Esslinger, T. W. Hänsch, and I. Bloch, "Quantum phase transition from a superfluid to a mott insulator in a gas of ultracold atoms," *Nature*, vol. 415, no. 6867, pp. 39–44, 2002.

[34] G. Mahan, *Many-Particle Physics*. Kluwer Academic/Plenum Publishers, 2000.

[35] M. E. Gershenson, V. Podzorov, and A. F. Morpurgo, "*Colloquium* : Electronic transport in single-crystal organic transistors," *Rev. Mod. Phys.*, vol. 78, pp. 973–989, Sept. 2006.

[36] G. Baym and C. Pethick, *Landau Fermi-Liquid Theory: Concepts and Applications*. Wiley-VCH, 1991.

[37] E. Dagotto, "Correlated electrons in high-temperature superconductors," *Rev. Mod. Phys.*, vol. 66, pp. 763–840, July 1994.

[38] W. F. Vinen and D. Shoenberg, "The detection of single quanta of circulation in liquid helium ii," *Proc. R. Soc. Lond. A*, vol. 260, no. 1301, pp. 218–236, 1961.

[39] K. W. Madison, F. Chevy, W. Wohlleben, and J. Dalibard, "Vortex formation in a stirred Bose-Einstein condensate," *Phys. Rev. Lett.*, vol. 84, pp. 806–809, Jan 2000.

[40] A. M. Turner, V. Vitelli, and D. R. Nelson, "Vortices on curved surfaces," *Rev. Mod. Phys.*, vol. 82, pp. 1301–1348, Apr. 2010.

[41] I. Bloch, J. Dalibard, and W. Zwerger, "Many-body physics with ultracold gases," *Rev. Mod. Phys.*, vol. 80, pp. 885–964, July 2008.

[42] G. F. Gribakin and V. V. Flambaum, "Calculation of the scattering length in atomic collisions using the semiclassical approximation," *Phys. Rev. A*, vol. 48, pp. 546–553, July 1993.

[43] C. Chin, R. Grimm, P. Julienne, and E. Tiesinga, "Feshbach resonances in ultracold gases," *Rev. Mod. Phys.*, vol. 82, pp. 1225–1286, Apr. 2010.

[44] C. Pethick and H. Smith, *Bose-Einstein Condensation in Dilute Gases*. Cambridge: Cambridge Univ. Press, 2 ed., 2008.

[45] A. Messiah, *Quantum Mechanics*. Dover books on physics, Dover Publications, 1999.

[46] E. T. Whittaker and G. N. Watson, *A Course of Modern Analysis*. Cambridge: Cambridge University Press, 4 ed., 1996.

[47] H. Bethe, R. Peierls, and D. R. Hartree, "Quantum theory of the diplon," *Proceedings of the Royal Society of London. Series A - Mathematical and Physical Sciences*, vol. 148, no. 863, pp. 146–156, 1935.

[48] H. A. Bethe, "Theory of the effective range in nuclear scattering," *Phys. Rev.*, vol. 76, pp. 38–50, July 1949.

[49] U. Fano, "Effects of configuration interaction on intensities and phase shifts," *Phys. Rev.*, vol. 124, pp. 1866–1878, Dec. 1961.

[50] A. Viel and A. Simoni, "Feshbach resonances and weakly bound molecular states of boson-boson and boson-fermion nak pairs," *Phys. Rev. A*, vol. 93, p. 042701, Apr. 2016.

[51] I. Tanihata, "Neutron halo nuclei," *Journal of Physics G: Nuclear and Particle Physics*, vol. 22, pp. 157–198, feb 1996.

[52] A. S. Jensen, K. Riisager, D. V. Fedorov, and E. Garrido, "Structure and reactions of quantum halos," *Rev. Mod. Phys.*, vol. 76, pp. 215–261, Feb. 2004.

[53] P. Jeszenszki, A. Y. Cherny, and J. Brand, "s-wave scattering length of a gaussian potential," *Phys. Rev. A*, vol. 97, p. 042708, Apr. 2018.

[54] P. O. Fedichev, M. W. Reynolds, and G. V. Shlyapnikov, "Three-body recombination of ultracold atoms to a weakly bound s level," *Phys. Rev. Lett.*, vol. 77, pp. 2921–2924, Sept. 1996.

[55] J. Stenger, S. Inouye, M. R. Andrews, H.-J. Miesner, D. M. Stamper-Kurn, and W. Ketterle, "Strongly enhanced inelastic collisions in a Bose-Einstein condensate near Feshbach resonances," *Phys. Rev. Lett.*, vol. 82, pp. 2422–2425, Mar. 1999.

[56] R. S. Bloom, M.-G. Hu, T. D. Cumby, and D. S. Jin, "Tests of universal three-body physics in an ultracold Bose-Fermi mixture," *Phys. Rev. Lett.*, vol. 111, p. 105301, Sept. 2013.

[57] D. S. Petrov, "Three-body problem in Fermi gases with short-range interparticle interaction," *Phys. Rev. A*, vol. 67, p. 010703, Jan. 2003.

[58] P. Makotyn, C. E. Klauss, D. L. Goldberger, E. A. Cornell, and D. S. Jin, "Universal dynamics of a degenerate unitary Bose gas," *Nature Physics*, vol. 10, no. 2, pp. 116–119, 2014.

[59] M. Gattobigio, M. Göbel, H.-W. Hammer, and A. Kievsky, "More on the universal equation for Efimov states," *Few-Body Systems*, vol. 60, May 2019.

[60] E. Braaten and H.-W. Hammer, "Universality in few-body systems with large scattering length," *Physics Reports*, vol. 428, no. 5, pp. 259–390, 2006.

[61] P. Naidon and S. Endo, "Efimov physics: a review," *Reports on Progress in Physics*, vol. 80, p. 056001, Mar. 2017.

[62] V. Efimov, "Energy levels arising from resonant two-body forces in a three-body system," *Physics Letters B*, vol. 33, no. 8, pp. 563–564, 1970.

[63] E. Braaten, H.-W. Hammer, and M. Kusunoki, "Universal equation for Efimov states," *Phys. Rev. A*, vol. 67, p. 022505, Feb. 2003.

[64] A. O. Gogolin, C. Mora, and R. Egger, "Analytical solution of the bosonic three-body problem," *Physical Review Letters*, vol. 100, Apr. 2008.

[65] R. Chapurin, X. Xie, M. J. Van de Graaff, J. S. Popowski, J. P. D'Incao, P. S. Julienne, J. Ye, and E. A. Cornell, "Precision test of the limits to universality in few-body physics," *Phys. Rev. Lett.*, vol. 123, p. 233402, Dec. 2019.

[66] L. D. Landau, "Über die Bewegung der Elektronen in Kristalgitter," *Phys. Z. Sowjetunion*, vol. 3, p. 644, 1933.

[67] S. I. Pekar, "Autolocalization of the electron in an inertially polarizable dielectric medium," *Zh. Eksp. Teor. Fiz.*, vol. 16, p. 335, 1946.

[68] L. D. Landau and S. Pekar, "The effective mass of the polaron," *Zh. Eksp. Teor. Fiz.*, vol. 18, p. 419–423, 1948.

[69] H. Fröhlich, H. Pelzer, and S. Zienau, "Xx. properties of slow electrons in polar materials," *Philosophical Magazine Series 7*, vol. 41, no. 314, pp. 221–242, 1950.

[70] H. Fröhlich, "Electrons in lattice fields," *Adv. Phys.*, vol. 3, no. 11, pp. 325–361, 1954.

[71] T.-D. Lee and D. Pines, "Interaction of a nonrelativistic particle with a scalar field with application to slow electrons in polar crystals," *Phys. Rev.*, vol. 92, pp. 883–889, Nov. 1953.

[72] R. P. Feynman, "Slow electrons in a polar crystal," *Phys. Rev.*, vol. 97, pp. 660–665, Feb. 1955.

[73] T. Holstein, "Studies of polaron motion: Part i. the molecular-crystal model," *Annals of Physics*, vol. 8, no. 3, pp. 325–342, 1959.

[74] D. Emin, *Polarons*. Cambridge University Press, 2012.

[75] V. G. Storchak, O. E. Parfenov, J. H. Brewer, P. L. Russo, S. L. Stubbs, R. L. Lichti, D. G. Eshchenko, E. Morenzoni, T. G. Aminov, V. P. Zlomanov, A. A. Vinokurov, R. L. Kallaher, and S. von Molnár, "Direct observation of the magnetic polaron," *Phys. Rev. B*, vol. 80, p. 235203, Dec. 2009.

[76] T. J. Smart, A. C. Cardiel, F. Wu, K.-S. Choi, and Y. Ping, "Mechanistic insights of enhanced spin polaron conduction in cuo through atomic doping," *npj Computational Materials*, vol. 4, no. 1, p. 61, 2018.

[77] G.-m. Zhao, *Polarons in Colossal Magnetoresistive and High-Temperature Superconducting Materials*, pp. 569–597. 01 2007.

[78] M. Petty, "Molecular electronics from principles to practice," 01 2008.

[79] N. Lu, L. Li, D. Geng, and M. Liu, "A review for polaron dependent charge transport in organic semiconductor," *Organic Electronics*, vol. 61, pp. 223–234, 2018.

[80] L. B. Tan, O. Cotlet, A. Bergschneider, R. Schmidt, P. Back, Y. Shimazaki, M. Kroner, and A. m. c. İmamoğlu, "Interacting polaron-polaritons," *Phys. Rev. X*, vol. 10, p. 021011, Apr. 2020.

[81] C. W. Tang and S. A. VanSlyke, "Organic electroluminescent diodes," *Applied Physics Letters*, vol. 51, no. 12, pp. 913–915, 1987.

[82] K. Hoang and M. D. Johannes, "Defect physics in complex energy materials," *Journal of Physics: Condensed Matter*, vol. 30, p. 293001, June 2018.

[83] S. Nascimbène, N. Navon, K. J. Jiang, L. Tarruell, M. Teichmann, J. McKeever, F. Chevy, and C. Salomon, "Collective oscillations of an imbalanced Fermi gas: Axial compression modes and polaron effective mass," *Phys. Rev. Lett.*, vol. 103, p. 170402, Oct. 2009.

[84] F. Chevy and C. Mora, "Ultra-cold polarized Fermi gases," *Rep. Progr. Phys.*, vol. 73, p. 112401, Nov. 2010.

[85] R. Schmidt, M. Knap, D. A. Ivanov, J.-S. You, M. Cetina, and E. Demler, "Universal many-body response of heavy impurities coupled to a Fermi sea: A review of recent progress," *Rep. Prog. Phys.*, vol. 81, no. 2, p. 024401, 2018.

[86] P. Massignan, M. Zaccanti, and G. M. Bruun, "Polarons, dressed molecules and itinerant ferromagnetism in ultracold Fermi gases," *Rep. Progr. Phys.*, vol. 77, no. 3, p. 034401, 2014.

[87] N. B. Jørgensen, L. Wacker, K. T. Skalmstang, M. M. Parish, J. Levinsen, R. S. Christensen, G. M. Bruun, and J. J. Arlt, "Observation of attractive and repulsive polarons in a Bose-Einstein condensate," *Phys. Rev. Lett.*, vol. 117, p. 055302, July 2016.

[88] M.-G. Hu, M. J. Van de Graaff, D. Kedar, J. P. Corson, E. A. Cornell, and D. S. Jin, "Bose polarons in the strongly interacting regime," *Phys. Rev. Lett.*, vol. 117, p. 055301, July 2016.

[89] Z. Z. Yan, Y. Ni, C. Robens, and M. W. Zwierlein, "Bose polarons near quantum criticality," *Science*, vol. 368, no. 6487, pp. 190–194, 2020.

[90] L. A. Peña Ardila and S. Giorgini, "Impurity in a Bose-Einstein condensate: Study of the attractive and repulsive branch using quantum Monte Carlo methods," *Phys. Rev. A*, vol. 92, p. 033612, 2015.

[91] L. A. Peña Ardila, N. B. Jörgensen, T. Pohl, S. Giorgini, G. M. Bruun, and J. J. Arlt, "Analyzing the Bose Polaron Across Resonant Interactions," *arXiv:1812.04609*, Dec. 2018.

[92] J. Tempere, W. Casteels, M. K. Oberthaler, S. Knoop, E. Timmermans, and J. T. Devreese, "Feynman path-integral treatment of the BEC-impurity polaron," *Phys. Rev. B*, vol. 80, p. 184504, Nov. 2009.

[93] J. Levinsen, M. M. Parish, and G. M. Bruun, "Impurity in a Bose-Einstein condensate and the Efimov effect," *Phys. Rev. Lett.*, vol. 115, p. 125302, Sept. 2015.

[94] R. S. Christensen, J. Levinsen, and G. M. Bruun, "Quasiparticle properties of a mobile impurity in a Bose-Einstein condensate," *Phys. Rev. Lett.*, vol. 115, p. 160401, Oct. 2015.

[95] Y. E. Shchadilova, R. Schmidt, F. Grusdt, and E. Demler, "Quantum dynamics of ultracold Bose polarons," *Phys. Rev. Lett.*, vol. 117, p. 113002, Sept. 2016.

[96] S. M. Yoshida, S. Endo, J. Levinsen, and M. M. Parish, "Universality of an impurity in a Bose-Einstein condensate," *Phys. Rev. X*, vol. 8, p. 011024, Feb. 2018.

[97] J. Levinsen, M. M. Parish, R. S. Christensen, J. J. Arlt, and G. M. Bruun, "Finite-temperature behavior of the Bose polaron," *Phys. Rev. A*, vol. 96, p. 063622, Dec. 2017.

[98] B. Field, J. Levinsen, and M. M. Parish, "Fate of the Bose polaron at finite temperature," *Phys. Rev. A*, vol. 101, p. 013623, Jan. 2020.

[99] S. Weinberg, *The Quantum Theory of Fields*, vol. 1. Cambridge University Press, 1995.

[100] A. Fetter and J. Walecka, *Quantum Theory of Many-particle Systems*. Dover Books on Physics, Dover Publications, 2003.

[101] E. E. Salpeter and H. A. Bethe, "A relativistic equation for bound-state problems," *Phys. Rev.*, vol. 84, pp. 1232–1242, Dec. 1951.

[102] A. Fetter and J. Walecka, *Quantum Theory of Many-Particle Systems*. Dover Books on Physics Series, Dover Publications, 1971.

[103] A. Guidini, G. Bertaina, D. E. Galli, and P. Pieri, "Condensed phase of Bose-Fermi mixtures with a pairing interaction," *Phys. Rev. A*, vol. 91, p. 023603, Feb. 2015.

[104] P. Massignan, C. J. Pethick, and H. Smith, "Static properties of positive ions in atomic Bose-Einstein condensates," *Phys. Rev. A*, vol. 71, p. 023606, Feb. 2005.

[105] P. W. Anderson, "Infrared catastrophe in Fermi gases with local scattering potentials," *Phys. Rev. Lett.*, vol. 18, p. 1049, June 1967.

[106] J. Goold, T. Fogarty, N. Lo Gullo, M. Paternostro, and T. Busch, "Orthogonality catastrophe as a consequence of qubit embedding in an ultracold Fermi gas," *Phys. Rev. A*, vol. 84, p. 063632, Dec. 2011.

[107] M. Cetina, M. Jag, R. S. Lous, I. Fritsche, J. T. M. Walraven, R. Grimm, J. Levinsen, M. M. Parish, R. Schmidt, M. Knap, and E. Demler, "Ultrafast many-body interferometry of impurities coupled to a Fermi sea," *Science*, vol. 354, no. 6308, pp. 96–99, 2016.

[108] S. I. Mistakidis, G. C. Katsimiga, G. M. Koutentakis, T. Busch, and P. Schmelcher, "Quench dynamics and orthogonality catastrophe of Bose polarons," *Phys. Rev. Lett.*, vol. 122, p. 183001, May 2019.

[109] M. Drescher, M. Salmhofer, and T. Enss, "Theory of a resonantly interacting impurity in a Bose-Einstein condensate," *Phys. Rev. Research*, vol. 2, p. 032011, July 2020.

[110] D. Dzsotjan, R. Schmidt, and M. Fleischhauer, "Dynamical variational approach to Bose polarons at finite temperatures," *Phys. Rev. Lett.*, vol. 124, p. 223401, June 2020.

[111] E. Gross, "Motion of foreign bodies in boson systems," *Ann. of Phys.*, vol. 19, no. 2, p. 234, 1962.

[112] C. Chin, R. Grimm, P. Julienne, and E. Tiesinga, "Feshbach resonances in ultracold gases," *Rev. Mod. Phys.*, vol. 82, pp. 1225–1286, Apr. 2010.

[113] P. Massignan, N. Yegovtsev, and V. Gurarie, "Universal aspects of a strongly interacting impurity in a dilute Bose condensate," *Phys. Rev. Lett.*, vol. 126, p. 123403, Mar 2021.

[114] W. Casteels and M. Wouters, "Polaron formation in the vicinity of a narrow Feshbach resonance," *Phys. Rev. A*, vol. 90, p. 043602, Oct. 2014.

[115] L. A. Peña Ardila and S. Giorgini, "Bose polaron problem: Effect of mass imbalance on binding energy," *Phys. Rev. A*, vol. 94, p. 063640, Dec. 2016.

[116] R. Schmidt, T. Enss, V. Pietilä, and E. Demler, "Fermi polarons in two dimensions," *Phys. Rev. A*, vol. 85, p. 021602, Feb. 2012.

[117] J. J. Zirbel, K.-K. Ni, S. Ospelkaus, J. P. D'Incao, C. E. Wieman, J. Ye, and D. S. Jin, "Collisional stability of fermionic Feshbach molecules," *Phys. Rev. Lett.*, vol. 100, p. 143201, Apr. 2008.

[118] S. Tan, "Energetics of a strongly correlated Fermi gas," *Ann. Phys.*, vol. 323, no. 12, pp. 2952–2970, 2008.

[119] S. Tan, "Large momentum part of a strongly correlated Fermi gas," *Ann. Phys.*, vol. 323, no. 12, pp. 2971–2986, 2008.

[120] E. Braaten, M. Kusunoki, and D. Zhang, "Scattering models for ultracold atoms," *Annals of Physics*, vol. 323, pp. 1770–1815, July 2008.

[121] E. Braaten, "Universal Relations for Fermions with Large Scattering Length," p. 43, Aug. 2010.

[122] F. Werner and Y. Castin, "General relations for quantum gases in two and three dimensions. ii. bosons and mixtures," *Phys. Rev. A*, vol. 86, p. 053633, Nov. 2012.

[123] W. Yi and X. Cui, "Polarons in ultracold Fermi superfluids," *Phys. Rev. A*, vol. 92, p. 013620, July 2015.

[124] G. A. Fiete, G. Zaránd, and K. Damle, "Effective hamiltonian for $ga_{1-x}mn_xAs$ in the dilute limit," *Phys. Rev. Lett.*, vol. 91, p. 097202, Aug. 2003.

[125] V. V. Klimov, "Collective excitations in a hot quark gluon plasma," *Soviet Phys. JETP*, vol. 55, p. 199, 1982. [Zh. Eksp. Teor. Fiz. **82**, 336 (1982)].

[126] H. A. Weldon, "Effective fermion masses of order gT in high-temperature gauge theories with exact chiral invariance," *Phys. Rev. D*, vol. 26, pp. 2789–2796, Nov. 1982.

[127] H. A. Weldon, "Dynamical holes in the quark-gluon plasma," *Phys. Rev. D*, vol. 40, pp. 2410–2420, Oct. 1989.

[128] G. Baym, J.-P. Blaizot, and B. Svetitsky, "Emergence of new quasiparticles in quantum electrodynamics at finite temperature," *Phys. Rev. D*, vol. 46, pp. 4043–4051, Nov. 1992.

[129] E. Braaten, "Neutrino emissivity of an ultrarelativistic plasma from positron and plasmino annihilation," *The Astrophysical Journal*, vol. 392, pp. 70–73, June 1992.

[130] Z. Yan, P. B. Patel, B. Mukherjee, R. J. Fletcher, J. Struck, and M. W. Zwierlein, "Boiling a Unitary Fermi Liquid," *arXiv:1811.00481*, Nov. 2018.

[131] B. Field, J. Levinsen, and M. M. Parish, "Fate of the Bose polaron at finite temperature," *Phys. Rev. A*, vol. 101, p. 013623, Jan 2020.

[132] C. Kohstall, M. Zaccanti, M. Jag, A. Trenkwalder, P. Massignan, G. M. Bruun, F. Schreck, and R. Grimm, "Metastability and coherence of repulsive polarons in a strongly interacting Fermi mixture," *Nature*, vol. 485, pp. 615–618, May 2012.

[133] M. Cetina, M. Jag, R. S. Lous, J. T. M. Walraven, R. Grimm, R. S. Christensen, and G. M. Bruun, "Decoherence of impurities in a Fermi sea of ultracold atoms," *Phys. Rev. Lett.*, vol. 115, p. 135302, Sept. 2015.

[134] Y. Ashida, R. Schmidt, L. Tarruell, and E. Demler, "Many-body interferometry of magnetic polaron dynamics," *Phys. Rev. B*, vol. 97, p. 060302, Feb. 2018.

[135] A. Camacho-Guardian, L. A. Peña Ardila, T. Pohl, and G. M. Bruun, "Bipolarons in a Bose-Einstein condensate," *Phys. Rev. Lett.*, vol. 121, p. 013401, July 2018.

[136] L. B. Tan, O. Cotlet, A. Bergschneider, R. Schmidt, P. Back, Y. Shimazaki, M. Kroner, and A. İmamoğlu, "Interacting polaron-polaritons," *Phys. Rev. X*, vol. 10, p. 021011, Apr. 2020.

[137] L. Pitaevskii and S. Stringari, *Bose-Einstein Condensation and Superfluidity*. Oxford: Oxford Univ. Press, 2 ed., 2016.

[138] H. Lamb, *Hydrodynamics*. New York: Dover publications, 6 ed., 1945.

[139] S. Beliaev, "Application of the methods of quantum field theory to a system of bosons," *ZhETF*, vol. 34, no. 2, p. 417, 1958.

[140] E. P. Gross, "Structure of a quantized vortex in boson systems," *Nuovo Cimento*, vol. 20, p. 453, 1961.

[141] L. P. Pitaevskii, "Vortex lines in an imperfect Bose gas," *Sov. Phys. JETP*, vol. 13, p. 451, 1961.

[142] E. M. Wright, D. F. Walls, and J. C. Garrison, "Collapses and revivals of Bose-Einstein condensates formed in small atomic samples," *Phys. Rev. Lett.*, vol. 77, pp. 2158–2161, Sep 1996.

[143] M. Lewenstein and L. You, "Quantum phase diffusion of a Bose-Einstein condensate," *Phys. Rev. Lett.*, vol. 77, pp. 3489–3493, Oct 1996.

[144] G. Baym and C. J. Pethick, "Ground-state properties of magnetically trapped Bose-condensed rubidium gas," *Physical Review Letters*, vol. 76, pp. 6–9, 1996.

[145] V. M. Pérez-García, H. Michinel, J. I. Cirac, M. Lewenstein, and P. Zoller, "Low energy excitations of a Bose-Einstein condensate: a variational analysis," *Physical Review Letters*, vol. 77, p. 5230, 1996.

[146] L. Onsager, "Statistical hydrodynamics," *Il Nuovo Cimento (1943-1954)*, vol. 6, no. 2, pp. 279–287, 1949.

[147] A. L. Fetter, "Rotating trapped Bose-Einstein condensates," *Rev. Mod. Phys.*, vol. 81, pp. 647–691, May 2009.

[148] V. Ginsburg and L. Pitaevskii, "On the theory of superfluidity," *JETP*, vol. 7, p. 858, November 1958.

[149] A. J. Majda and A. L. Bertozzi, *Vorticity and Incompressible Flow*. Cambridge Texts in Applied Mathematics, Cambridge University Press, 2001.

[150] A. Gray, *Modern Differential Geometry of Curves and Surfaces*. CRC Press, 1993.

[151] T.-L. Ho and B. Huang, "Spinor condensates on a cylindrical surface in synthetic gauge fields," *Phys. Rev. Lett.*, vol. 115, p. 155304, Oct. 2015.

[152] J. Machta and R. A. Guyer, "Superfluid films on a cylindrical surface," *Journal of Low Temperature Physics*, vol. 74, pp. 231–261, Feb. 1989.

[153] E. T. Whittaker and G. N. Watson, *A Course of Modern Analysis*. Cambridge: Cambridge University Press, 4 ed., 1996.

[154] M. Turner, A, V. Vitelli, and D. R. Nelson, "Vortices on curved surfaces," *Rev. Mod. Phys.*, vol. 82, no. 1301, 2010.

[155] G. Kirchhoff, "Über die stationären elektrischen Strömungen in einer gekrümmten leitenden Fläche," *Monatsbericht der Akademie der Wissenschaften zu Berlin vom 19. July 1875, pages 56-66*, 1875.

[156] P. W. Anderson, "Considerations on the Flow of Superfluid Helium," *Rev. Mod. Phys.*, vol. 38, pp. 298–310, Apr. 1966.

[157] G. R. Kirchhoff, *Vorlesungen über mathematische Physik, Bd. 1: Mechanik*. Teubner, 1876.

[158] C. C. Lin, "On the motion of vortices in two dimensions - i. existence of the kirchhoff-routh function," *Proc. Nat. Acad. Sci.*, vol. 27, no. 12, pp. 570–575, 1941.

[159] C. C. Lin, "On the motion of vortices in two dimensions - ii. some further investigations on the kirchhoff-routh function," *Proc. Nat. Acad. Sci.*, vol. 27, no. 12, pp. 575–577, 1941.

[160] A. L. Fetter, "Low-lying superfluid states in a rotating annulus," *Phys. Rev.*, vol. 153, pp. 285–296, Jan. 1967.

[161] P. J. Bendt, "Superfluid helium critical velocities in a rotating annulus," *Phys. Rev.*, vol. 127, pp. 1441–1445, Sep 1962.

[162] C. Ryu, M. F. Andersen, P. Cladé, V. Natarajan, K. Helmerson, and W. D. Phillips, "Observation of persistent flow of a Bose-Einstein condensate in a toroidal trap," *Phys. Rev. Lett.*, vol. 99, p. 260401, Dec 2007.

[163] S. Moulder, S. Beattie, R. P. Smith, N. Tammuz, and Z. Hadzibabic, "Quantized supercurrent decay in an annular Bose-Einstein condensate," *Phys. Rev. A*, vol. 86, p. 013629, Jul 2012.

[164] L. Corman, L. Chomaz, T. Bienaimé, R. Desbuquois, C. Weitenberg, S. Nascimbène, J. Dalibard, and J. Beugnon, "Quench-induced supercurrents in an annular Bose gas," *Phys. Rev. Lett.*, vol. 113, p. 135302, Sep 2014.

[165] S. Eckel, F. Jendrzejewski, A. Kumar, C. J. Lobb, and G. K. Campbell, "Interferometric measurement of the current-phase relationship of a superfluid weak link," *Phys. Rev. X*, vol. 4, p. 031052, Sep 2014.

[166] J. L. Ville, T. Bienaimé, R. Saint-Jalm, L. Corman, M. Aidelsburger, L. Chomaz, K. Kleinlein, D. Perconte, S. Nascimbène, J. Dalibard, and J. Beugnon, "Loading and compression of a single two-dimensional Bose gas in an optical accordion," *Phys. Rev. A*, vol. 95, p. 013632, Jan 2017.

[167] M. Aidelsburger, J. L. Ville, R. Saint-Jalm, S. Nascimbène, J. Dalibard, and J. Beugnon, "Relaxation dynamics in the merging of n independent condensates," *Phys. Rev. Lett.*, vol. 119, p. 190403, Nov 2017.

[168] A. Chakraborty, S. R. Mishra, S. P. Ram, S. K. Tiwari, and H. S. Rawat, "A toroidal trap for cold ^{87} rb atoms using an rf-dressed quadrupole trap," *J. Phys. B*, vol. 49, p. 075304, Mar. 2016.

[169] N. Lundblad, R. A. Carollo, C. Lannert, M. J. Gold, X. Jiang, D. Paseltiner, N. Sergay, and D. C. Aveline, "Shell potentials for microgravity Bose-Einstein condensates," *npj Microgravity*, vol. 5, Dec. 2019.

[170] G. Condon, M. Rabault, B. Barrett, L. Chichet, R. Arguel, H. Eneriz-Imaz, D. Naik, A. Bertoldi, B. Battelier, P. Bouyer, and A. Landragin, "All-optical Bose-Einstein condensates in microgravity," *Phys. Rev. Lett.*, vol. 123, p. 240402, Dec. 2019.

[171] D. V. Freilich, D. M. Bianchi, A. M. Kaufman, T. K. Langin, and D. S. Hall, "Real-time dynamics of single vortex lines and vortex dipoles in a Bose-Einstein condensate," *Science*, vol. 329, no. 5996, pp. 1182–1185, 2010.

[172] D. R. Scherer, C. N. Weiler, T. W. Neely, and B. P. Anderson, "Vortex formation by merging of multiple trapped Bose-Einstein condensates," *Phys. Rev. Lett.*, vol. 98, p. 110402, Mar 2007.

[173] Ł. Dobrek, M. Gajda, M. Lewenstein, K. Sengstock, G. Birkl, and W. Ertmer, "Optical generation of vortices in trapped Bose-Einstein condensates," *Phys. Rev. A*, vol. 60, p. R3381, Nov. 1999.

[174] G. Nandi, R. Walser, and W. P. Schleich, "Vortex creation in a trapped Bose-Einstein condensate by stimulated raman adiabatic passage," *Phys. Rev. A*, vol. 69, p. 063606, June 2004.

[175] P. Minnhagen, "The two-dimensional coulomb gas, vortex unbinding, and superfluid-superconducting films," *Rev. Mod. Phys.*, vol. 59, pp. 1001–1066, Oct. 1987.

[176] W. F. Vinen and J. J. Niemela, "Quantum turbulence," *Journal of Low Temperature Physics*, vol. 128, no. 5, pp. 167–231, 2002.